A SEARCH FOR DARK MATTER WITH THE ATLAS EXPERIMENT

Rebecca H Pickles
The School of Physics and Astronomy

2019

A thesis submitted to the University of Manchester
for the degree of Doctor of Philosophy
in the Faculty of Science and Engineering

Contents

Word count 27064

A search for dark matter with the ATLAS experiment

A thesis submitted to the University of Manchester
for the degree of Doctor of Philosophy
in the Faculty of Science and Engineering

Rebecca H Pickles
The School of Physics and Astronomy
2019

Abstract

This thesis presents a calibration of the ATLAS calorimeter response to jets, a detector-corrected measurement of missing transverse momentum in association with jets, and the first model-independent beyond-the-Standard-Model interpretation of that detector-corrected measurement.

The calibration of the jet energy resolution in the forward region of the ATLAS calorimeter is performed using dijet events in 36.1 fb^{-1} of $\sqrt{s} = 13$ TeV proton-proton collision data collected in 2015 and 2016. The dijet-balance methodology, used in this measurement, is described for events produced in the ATLAS detector forward region ($0.8 < |\eta| < 3.2$) relative to a central region ($|\eta| < 0.8$).

Dark matter is motivated by cosmological experiments and remains one of the great mysteries of the Universe. Among the possible approaches to investigate this elusive type of matter are searches for missing transverse momentum at particle colliders. This thesis describes one such search. The ratio of the fiducial cross-sections of $p_{\text{T}}^{\text{miss}}$ + jets to $\ell^+\ell^-$ + jets is measured at $\sqrt{s} = 13$ TeV with 3.2 fb^{-1} of proton-proton collision data collected by the ATLAS detector in 2015. This study is conducted using variables corrected for detector effects in two kinematic regions and four differential distributions. The consequence of using the ratio is the cancellation of a number of significant systematic uncertainties and detector effects. Expected and observed exclusion limits at the 95 % confidence level are set on three dark matter models using these distributions and the correlations between them.

Declaration

No portion of the work referred to in the thesis has been submitted in support of an application for another degree or qualification of this or any other university or other institute of learning.

Rebecca H Pickles

Copyright statement

i. The author of this thesis (including any appendices and/or schedules to this thesis) owns certain copyright or related rights in it (the “Copyright”) and she has given The University of Manchester certain rights to use such Copyright, including for administrative purposes.

ii. Copies of this thesis, either in full or in extracts and whether in hard or electronic copy, may be made **only** in accordance with the Copyright, Designs and Patents Act 1988 (as amended) and regulations issued under it or, where appropriate, in accordance with licensing agreements which the University has from time to time. This page must form part of any such copies made.

iii. The ownership of certain Copyright, patents, designs, trade marks and other intellectual property (the “Intellectual Property”) and any reproductions of copyright works in the thesis, for example graphs and tables (“Reproductions”), which may be described in this thesis, may not be owned by the author and may be owned by third parties. Such Intellectual Property and Reproductions cannot and must not be made available for use without the prior written permission of the owner(s) of the relevant Intellectual Property and/or Reproductions.

iv. Further information on the conditions under which disclosure, publication and commercialisation of this thesis, the Copyright and any Intellectual Property and/or Reproductions described in it may take place is available in the University IP Policy (see http://documents.manchester.ac.uk/DocuInfo.aspx?DocID=24420), in any relevant Thesis restriction declarations deposited in the University Library, The University Library’s regulations (see http://www.library.manchester.ac.uk/about/regulations/) and in The University’s Policy on Presentation of Theses.

Acknowledgements

My research and the completion of this thesis would have been impossible without the aid and support of many people. First and foremost, I would like to thank my supervisor, Darren Price, for all his patient guidance and invaluable advice throughout my PhD. He provided me with enthusiasm and direction when I needed it, but also allowed me follow my own interests. Thanks also to Stefan Soldner-Rembold for his quiet encouragement and support, and for convincing me to stay in Manchester for my PhD.

Thank you to everyone in the Manchester particle physics group for making the last three and a half years a thoroughly enjoyable experience. I have especially appreciated all the tea and cake.

I would also like to thank to everyone I have worked with in the $E_{\mathrm{T}}^{\mathrm{miss}}+\mathrm{jet(s)}$ unfolded analysis group during my PhD. My visits to Heidelberg and London were always filled with fun, and often wine, which was always appreciated.

I am profoundly grateful to my friends from all around the globe that I met at CERN, who made my life over there the adventure I had only hoped to have. They are far too numerous to name, but they know who they are. I doubt I will ever be able to repay them for the impact they've made on my life.

Finally, the most important thanks goes to my family, for their unwavering love and support. They have always provided respite when I need it and that extra little push when I'm lacking motivation. Thank you for always encouraging my pursuits and believing in my path, even when I find it hard to see myself.

Preface

The work presented in this thesis was performed as part of the ATLAS collaboration where the contributions of the author are detailed as follows.

The calibration work in Chapter 5 was performed alongside the Jet-$E_{\mathrm{T}}^{\mathrm{miss}}$ working group. The author was responsible for the studies related to the dijet imbalance of jets in the forward region of the ATLAS detector. The work presented on the in-situ jet energy resolution calibration for dijet events with 2015 and 2016 data with a bunch spacing of 25 ns is entirely the work of the author.

The dark matter search using ratio measurements presented in Chapters 7 and 8 was performed in an analysis team with contributions from a number of institutes across the world. The author was responsible for the investigation of the optimal particle-level definition of the fiducial kinematic region, the studies relating to the beyond-the-Standard-Model interpretation of the numerator of the ratio (measurement of events containing missing transverse momentum produced in association with jets), and for setting 95 % $\mathrm{CL_s}$ exclusion limits on three beyond-the-Standard-Model theoretical frameworks. In addition, the author was solely responsible for performing tests of the dependence of the limits on the systematic correlations, statistical precision, and signal injection tests.

Chapter 1

Introduction

The Standard Model (SM) of particle physics is a quantum field theory which describes with extreme accuracy the behaviour of fundamental particles as they interact with the strong, electromagnetic and weak forces [1]. Although the Standard Model has had many successes—the discovery of the Higgs Boson in 2012 [2, 3] seemingly the most apt example—it is unable to explain some of the more conspicuous observed physical phenomena in the Universe. For example, the Standard Model theory cannot provide an explanation for the many astrophysical and cosmological observations that indicate vast quantities of invisible matter [4]. The existence of this dark matter (DM) has long been accepted due to these studies and persists as one of most confounding mysteries within the field.

Accordingly, one of the main objectives of the physics programme at the Large Hadron Collider (LHC) [5] is to detect and study dark matter. However, this elusive type of matter cannot be identified by standard detection methods in particle-collider experiments, such as the ATLAS experiment [6]. This is because dark matter does not partake in the strong or electromagnetic forces, by which Standard Model particles interact with the detector—as evidenced by the lack of observation of dark matter interactions with normal matter in astrophysics. Therefore, in order to identify its existence in a detector, searches require the assumption that dark matter interacts with the Standard Model via some other path. The effect on the Standard Model particles produced in the detector can then be measured. For this, an additional force other than gravity is required for the DM–SM interaction: the Standard Model electroweak force is assumed to fill this demand. Due to the lack of direct detection, the signature of dark matter is of the same type as that of neutrinos: missing transverse momentum ($p_{\mathrm{T}}^{\mathrm{miss}}$) and associated Standard Model particles. This thesis presents a search for $p_{\mathrm{T}}^{\mathrm{miss}}$ in association with common detector objects, known as hadronic jets.

These narrow collimated cones of hadrons (jets), permeate the modern particle-collider experiment landscape; a variety of jet measurements contribute to the analysis of a vast assortment of physics phenomena taking place in the ATLAS detector—including new physics searches. It is therefore of vital importance that they are well-understood. The calibration of the jet energy resolution, discussed in this thesis, endeavors to measure the response of the ATLAS detector when encountering dijet events.

The measurements taken in the presented dark matter analysis are corrected for the effects of detector efficiency and resolution, allowing the comparison of beyond-the-Standard-Model (BSM) predictions without the need for detector simulations. This is the first time this has been done in the context of a dedicated dark matter search. Differential distributions also further the cause of setting constraints on BSM theoretical models, and are here constructed from a ratio of cross-sections,

$$R^{\mathrm{miss}} = \frac{\sigma_{\mathrm{fid}}(p_{\mathrm{T}}^{\mathrm{miss}} + \mathrm{jets})}{\sigma_{\mathrm{fid}}(\ell^{+}\ell^{-} + \mathrm{jets})}. \tag{1.1}$$

Both systematic uncertainties and detector effects are significantly reduced via the use of this ratio. The definitions of the kinematic regions in which the numerator and denominator are measured allow some uncertainties to cancel, increasing the sensitivity of the search.

The dominant Standard Model contributions to both the numerator ($Z \to \nu\bar{\nu}$) and denominator ($Z \to \ell^{+}\ell^{-}$) arise from the decay of the Z boson. This allows for the extremely precise prediction of these Standard Model cross-sections. Therefore, any dark matter contribution would be seen from any additional enhancement in the numerator and R^{miss}.

The remainder of this thesis is laid out as follows. An overview of the theoretical framework of Standard Model and BSM physics is delivered in Chapter 2. The experimental setup, including design and performance information, of the LHC and ATLAS is then discussed in Chapter 3. Chapter 4 examines the reconstruction and calibration of physics objects produced in the ATLAS detector. The jet energy calibration of jets in dijet events produced in the forward region of the ATLAS calorimeter is then discussed in Chapter 5. Chapters 7 and 8 represent the main portion of this thesis: an in-depth description of the dark matter search in the unfolded cross-section ratio analysis using the 2015 dataset collected by the ATLAS detector. These chapters contain a discussion of all main aspects of the analysis, but the contributions of the author of this thesis are the focus in Chapter 8. A future outlook is given in Chapter 9. Lastly, a summary and conclusions are given in Chapter 10.

Chapter 2

Theoretical framework

2.1 Standard Model of particle physics

The Standard Model (SM) of particle physics [1, 7] is the theoretical framework describing the phenomenology of fundamental constituents of matter and their interactions, excluding the gravitational interaction.

2.1.1 Fundamental particles and forces

There are two main categories of ordinary matter that are defined by particle properties: particles that interact (fermions) and particles that mediate forces (bosons):

Fermions: Fermions are half-integer spin particles that obey the Pauli exclusion principle and Fermi-Dirac statistics.

Bosons: Bosons are integer spin particles that are governed by Bose-Einstein statistics.

The strong, weak, and electromagnetic (EM) interactions are three forces described by the Standard Model; these forces are mediated by force-carrying gauge bosons. The spin-1 gauge bosons mediating each interaction are: the gluon (g) for the strong force, three weak bosons ($W^{\pm}$, Z^0) for the weak force, and the photon (γ) for the electromagnetic force.

Gluons: Gluons are colour-charged mediator particles. They are electrically neutral and massless.

Generation	1st	2nd	3rd
Quarks	$\begin{pmatrix} u \\ d \end{pmatrix}$	$\begin{pmatrix} c \\ s \end{pmatrix}$	$\begin{pmatrix} t \\ b \end{pmatrix}$
Leptons	$\begin{pmatrix} e \\ \nu_e \end{pmatrix}$	$\begin{pmatrix} \mu \\ \nu_\mu \end{pmatrix}$	$\begin{pmatrix} \tau \\ \nu_\tau \end{pmatrix}$

Table 2.1: The three generations of quarks and leptons.

Weak bosons ($W^{\pm}, Z^0$): The bosons responsible for the weak interaction obtain their mass through spontaneous symmetry breaking (Section 2.1.4).

Photons: Photons are electrically neutral and massless.

Matter is composed of fermions: six quarks and six leptons with half-integer spin. Quarks participate in all three fundamental interactions, whereas leptons only interact via the electromagnetic and weak forces. The six flavours of quarks and leptons are split up into three generations, shown in Table 2.1, where the first generation consists of up and down quarks as well as the electron and electron neutrino.

Quarks: Quarks exist in pairs in one of three generations. Each pair consists of an up component with an electric charge $Q = +2/3$ e and isospin $I = +1/2$, and a down component with $Q = -1/3$ e and $I = -1/2$, where e is the unit of electron charge.

Leptons: Leptons also exist in two components in each generation. Each pair consists of one charged lepton and one electrically-neutral weakly-interacting neutrino. The Standard Model treats neutrinos as massless particles, however, experimental observations of neutrino oscillations have demonstrated the non-zero value of the neutrino masses.

Every fermion has an associated antiparticle with the same mass but opposite quantum numbers, known as anti-matter. Standard Model particles receive their mass due to their interactions with the scalar Higgs field [8–13]—the associated spin-0 Higgs boson was discovered in 2012 [2, 3].

The Standard Model itself is a quantum field theory (QFT) [14] based on inherent symmetries theorised and experimentally observed. The strong, weak, and electromagnetic interactions can be described in this formalism by the gauge symmetry $\mathrm{SU}(3)_C \times \mathrm{SU}(2)_L \times \mathrm{U}(1)_Y$, where:

- $\mathrm{SU}(3)_C$ is the symmetry group associated with the strong force,
- $\mathrm{SU}(2)_L$ is the symmetry group associated with the weak force, and,
- $\mathrm{U}(1)_Y$ is the symmetry group associated with the electromagnetic force.

The requirement of gauge invariance under local transformations implies the presence of gauge bosons. The number of these bosons can be determined from the appropriate unitarity group.

2.1.2 Quantum electrodymanics

Quantum electrodynamics (QED) was the first relativistic quantum field theory developed [14, 15] and was proposed to describe electromagnetic interactions. The Lagrangian, given in Equation 2.1, describes the interaction of a charged spin-$1/2$ field Ψ with mass m and the electromagnetic field.

$$\mathcal{L} = -\frac{1}{4}F_{\mu\nu}F^{\mu\nu} + \bar{\Psi}(i\gamma^{\mu}D_{\mu} - m)\Psi, \tag{2.1}$$

where F is the electromagnetic field tensor, defined as a function of the covariant four-potential of the electromagnetic field, A_{μ}:

$$F_{\mu\nu} = \partial_{\mu}A_{\nu} - \partial_{\nu}A_{\mu}, \tag{2.2}$$

where ∂_{μ} is the partial derivative $\partial/\partial x_{\mu}$. D_{μ} is the gauge covariant derivative, given by:

$$D_{\mu} = \partial_{\mu} + iqA_{\mu}, \tag{2.3}$$

where q is the electric charge of the charged spin-1/2 field Ψ. QED is invariant under the local transformation of the unitarity gauge group U(1). The group U(1) is Abelian: all generators of the group commute. The mass term of the electromagnetic field A_{μ} is not invariant under local transformations: the consequence of which is the massless photon which is observed.

2.1.3 Quantum chromodynamics

Quantum chromodynamics (QCD) is the quantum field theory that describes strong interactions between quarks and gluons. In the Standard Model, each quark has one of three colour charges (conventionally named red, green, and blue):

$$\mathbf{q} = \begin{pmatrix} q_r \\ q_g \\ q_b \end{pmatrix}. \tag{2.4}$$

The strong interaction is governed by the $\mathrm{SU}(3)_C$ symmetry group and these quark colour triplets are invariant under such transformations. The QCD group is non-Abelian (generators do not commute) which means the resulting terms in the Lagrangian then represent self-interaction of gluons. Assuming a one-loop approximation, the field strength in QCD ($g_s^2 = 4\pi\alpha_s$) is a function of the energy scale, Q^2, as:

$$\alpha_s(Q^2) \approx \frac{1}{\beta_0 \ln(Q^2/\Lambda^2)}, \tag{2.5}$$

where $\beta_0 = 1/[12\pi(33-2N_f)]$ when N_f is the number of quark flavours, and Λ is the scale of QCD. The consequences of this give an important feature of QCD: at low energies the coupling strength is extremely high and confines coloured particles to a bound state, but at high energies the coupling strength is weak enough for perturbation theory to give a good approximation to final states.

2.1.4 Electroweak interactions, spontaneous symmetry breaking, and the Higgs boson

Producing a formulation of a quantum field theory for the weak interaction is more challenging than for QED and QCD due to its parity violating nature and short range ($\sim 10^{-17}$ m) [7, 15], which results in massive gauge boson mediator particles (known as $W^{\pm}$ and Z^0 bosons). Though these bosons were investigated theoretically, they suffered from inherent problems such as a lack of gauge invariance [14, 16]. Theories then considered a hidden gauge invariance, caused by the breaking of the associated symmetry at the observable energy scale. The $\mathrm{SU}(2)_L \times \mathrm{U}(1)_Y$ symmetry group represents this hidden gauge invariance and corresponds to the unified electroweak theory. Here, SU(2) and U(1) represent the weak and electromagnetic interactions respectively. The Y is in reference to the weak hypercharge and the L to the handedness, known as the chirality, of the weak interaction. The $\mathrm{SU}(2)_L \times \mathrm{U}(1)_Y$

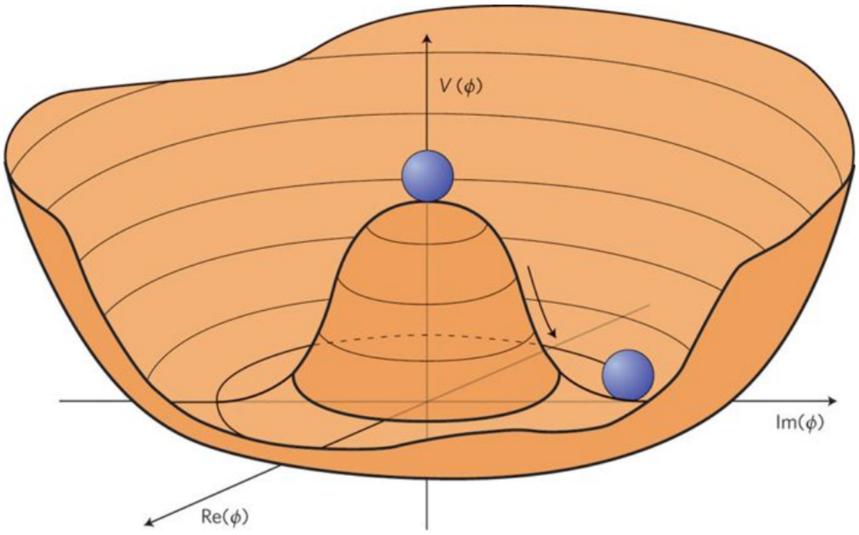

Figure 2.1: Interpretive image of the Higgs potential $V(\phi)$ in the complex plane. Any randomly chosen position at a minimum potential corresponds to the vacuum and any movement to this position from the centre of potential represents a massive scalar Higgs boson. Image taken from Reference [17].

symmetry group has four associated gauge bosons: W_μ^a, $a = 1, 2, 3$, and B_μ which all mix to produce the mediator bosons that are observed ($W^\pm$, Z^0, γ).

One example of spontaneous symmetry breaking is found in the Higgs mechanism, which preserves gauge invariance while allowing the fermions and gauge bosons to obtain mass. Consistency with the Standard Model is maintained by introducing the Higgs field as a complex scalar doublet with four degrees of freedom, implied from its four real components. The potential of the field, pictured in Figure 2.1, has a non-zero vacuum expectation value which breaks the symmetry of the SU(2) group. This spontaneous symmetry breaking is represented by the arrow pointing away from the centre of potential. Interaction of the Higgs field with the $\mathrm{SU}(2)\times\mathrm{U}(1)$ gauge fields at this vacuum expectation value results in the three W_μ^a fields obtaining mass. The final gauge field, B_μ, remains massless as a photon. The consequence of this for the Higgs field is to become a spinless scalar: a massive Higgs boson.

The $W^\pm$, Z^0, and γ gauge fields correspond to mixing between the W_μ^a and B_μ fields:

$$W_\mu^\pm = \frac{W_\mu^1 \mp iW_\mu^2}{\sqrt{2}}, \tag{2.6}$$

$$Z_\mu = W_\mu^3 \cos\theta_W - B_\mu \sin\theta_W, \tag{2.7}$$

$$A_\mu = W_\mu^3 \sin\theta_W + B_\mu \cos\theta_W, \tag{2.8}$$

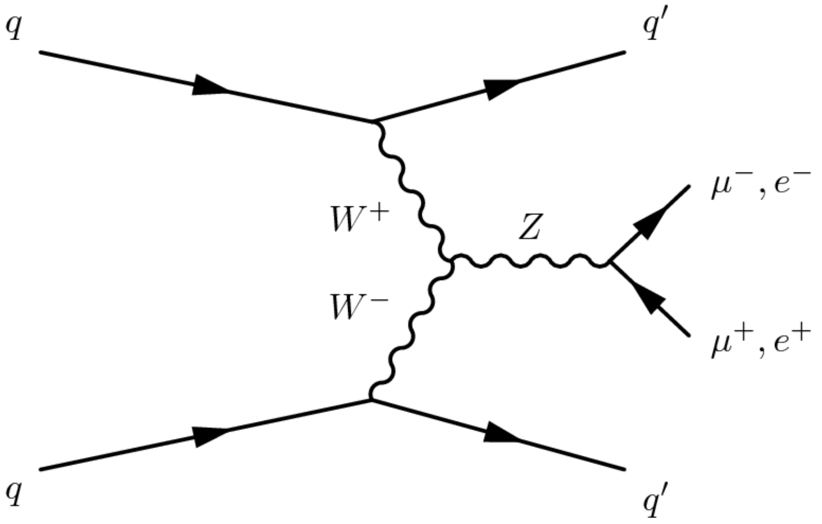

Figure 2.2: Feynman diagram of the process of vector boson fusion. In this example, the vector bosons fuse to produce another vector boson.

where θ_W is the Weinberg weak mixing angle. The fermions gain their mass through interactions with the Higgs boson after electroweak symmetry breaking has taken effect.

Vector boson fusion

These electroweak gauge bosons can participate in a process called *vector boson fusion* (VBF), as shown in Figure 2.2. In a proton collider, two quarks can radiate virtual electroweak gauge bosons ($W^{\pm}$,Z^0) from the interacting protons, which can then fuse to produce another particle, such as another vector boson, or a Higgs boson. This topology is used in later chapters and is a vital part of the analysis discussed in this thesis.

2.2 The dark matter mystery

Dark matter (DM) represents one of the greatest puzzles in modern physics. Astrophysical observations including galaxy formation and gravitational lensing have indicated that the Universe is made predominantly of this completely unknown substance. Precise measurements predict that approximately 85 % of the mass of the Universe consists dark matter [18], which has thus far been mostly invisible to our detection methods. The only exceptions being the detection of its gravitational effect on matter and its influence on the energy-density of the Universe. Yet, it has not been directly observed, which implies a lack of ability to interact electromagnetically. In this section, the evidence for dark matter, as well as several

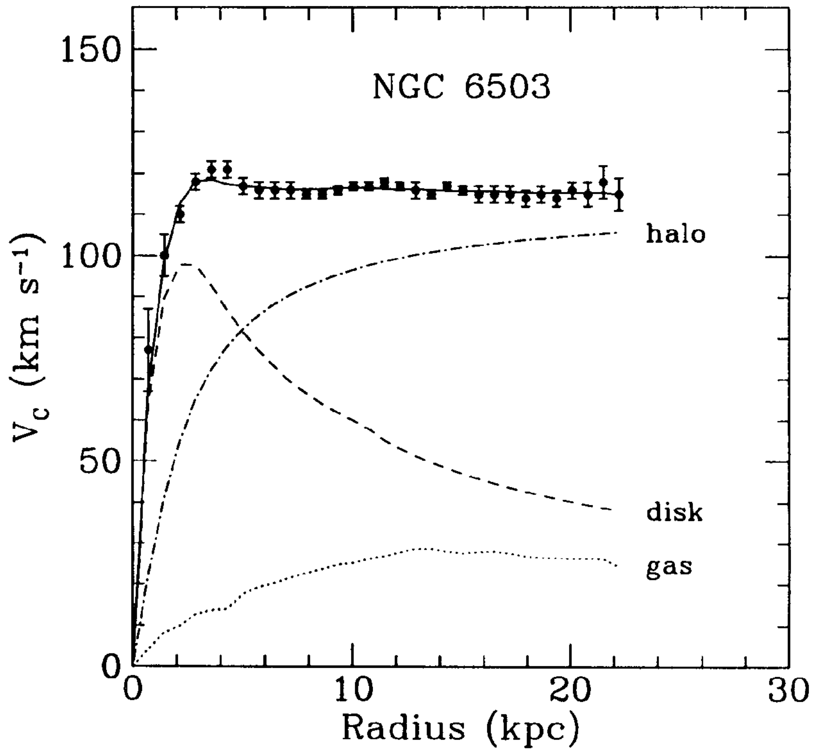

Figure 2.3: The rotation curve of the galaxy NGC 6503 is shown. The data distribution is explained theoretically by a dark halo. The black points show the data and the lines describe the contribution from each part of the galaxy. The *disk* is the baryonic, or normal matter expected from the Standard Model, the *gas* is interstellar gas, and the *halo* is the theorised dark matter. Image taken from Reference [19].

potential theoretical models, are discussed.

2.2.1 Evidence for dark matter

The experimental evidence for dark matter is most prominent in the field of cosmology. A large variety of independent studies have concluded the existence of a type of matter that interacts via the gravitational, but not the electromagnetic, force. Discrepancies in measurements made as early as the 1930s [20, 21] have retroactively been attributed to the unaccounted-for presence of dark matter. It was more confidently identified in the 1970s by Vera Rubin in observation of its gravitational effect on galactic rotation curves [22]. It was found that red-shift analyses on stars of galaxies do not ascribe to the expected velocity distribution as a function of the distance from the centre of the galaxy, r. Newtonian physics predicts that the velocity distribution would fall as $\sqrt{1/r}$; however, observed velocities are seemingly constant once outside the central region. The hypothesis posed to explain this behaviour depicts a *halo* of dark matter on the outskirts of galaxies [19, 23]. Figure 2.3

shows an example of how a galaxy rotation curve cannot be explained by visible matter alone. The orbital velocities of visible stars or gas in the galaxy of interest are plotted versus their radial distance from the galactic centre. If a dark matter halo is added to the theoretical calculations, the data is matched well by expectation.

Other observational evidence was gathered through gravitational lensing studies [24]. Gravitational lensing refers to the effect of a distribution of matter, between a source and an observer, bending the light from the source [4]. This effect can be used to measure the masses of galaxy clusters. In this case, the mass of the directly observed baryonic matter does not account for the gravitational lensing effect found for a number of galaxy clusters. The most famous example is the galaxy cluster 1E 0657-558 [25], known as the *bullet cluster*. It is currently the most direct observational evidence for the existence of dark matter. Figure 2.4 shows the presence of two galaxy clusters, which have separated after a past collision between the two smaller constituent clusters. The gas and baryonic matter component of the clusters slows and remains around the point of impact due to electromagnetic interactions between these particles, whereas, the dark matter continues on along its path almost uninterrupted.

Further evidence comes from data collected concerning the radiation from the cosmic microwave background (CMB). The CMB was produced approximately 300 000 years after the Big Bang in the cosmological era of recombination. Detailed measurements show this to be almost completely isotropic at a temperature of 2.7 K. However, on a smaller scale, temperature differences have been observed—first by the Cosmic Background Explorer (CoBE) satellite in 1989 [26]. These differences, shown in the cosmic microwave background image in Figure 2.5, are due to matter clumps that are at a slightly increased or decreased temperature from the average. It is possible to base cosmological models of the Universe on these discrepancies. The effect on the rate of growth of different proportions of ordinary matter and dark matter can be calculated and compared with observation. Figure 2.6 shows the power spectrum of the temperature anisotropy of the cosmic microwave background as measured by the Wilkinson Microwave Anisotropy Probe (WMAP) [27]. It is given as a function of the angular scale and describes the relative brightness of the high temperature areas to their size. Each peak in the spectrum indicates different physical phenomena: the size of the first peak sets limits of the curvature of the Universe; the second is indicative of the baryon density; and the third provides information on the dark matter density. The current

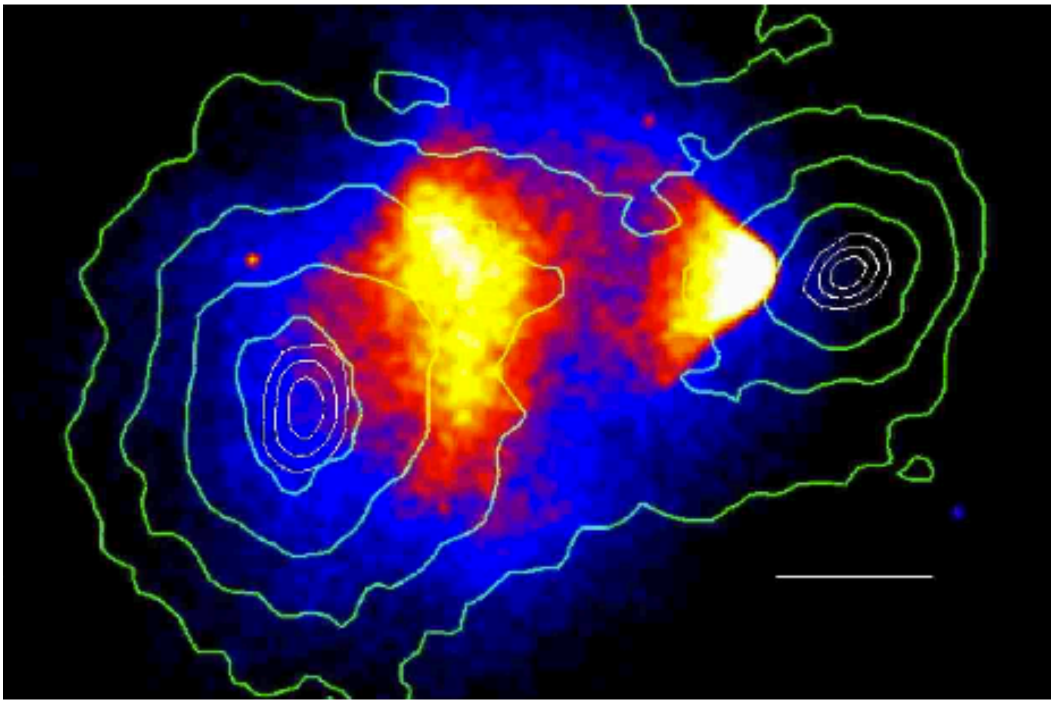

Figure 2.4: The separation of light and dark matter in the bullet cluster. The white bar provides a scale indicating 200 kpc at the distance of the cluster. The green contours are the weak lensing κ reconstruction starting with the outer-most contour having a level of $\kappa = 0.16$ and increasing in increments of 0.07. The white to blue gradient shows the position of the mass centres of the gas clouds. Image taken from Reference [25].

Standard Model of Cosmology includes the presence of cold (non-relativistic) dark matter and is known as the ΛCDM model [28]. Here, Λ represents the cosmological constant. In order to fit this model to the data, the energy density of the Universe must be distributed as follows: 4.9 % baryonic matter, 68.3 % dark energy, and 26.8 % dark matter [29].

The existence of dark matter has long been established and accepted by the scientific community due to the above evidence, but its particle properties are still mostly a mystery. The Standard Model of particle physics does not account for such a particle, nor is it able to explain the above observations.

2.2.2 Dark matter models

Many dark matter models have been theorised in the last century to explain the discrepancies mentioned previously. Limits are set on three benchmark models in Chapter 8: a simplified WIMP model, an effective field theory (EFT) characterising weak boson fusion interactions, and invisible decays of the Higgs boson to dark matter pairs. Few assumptions are made in the construction of these models, other than the existence of a dark matter particle that

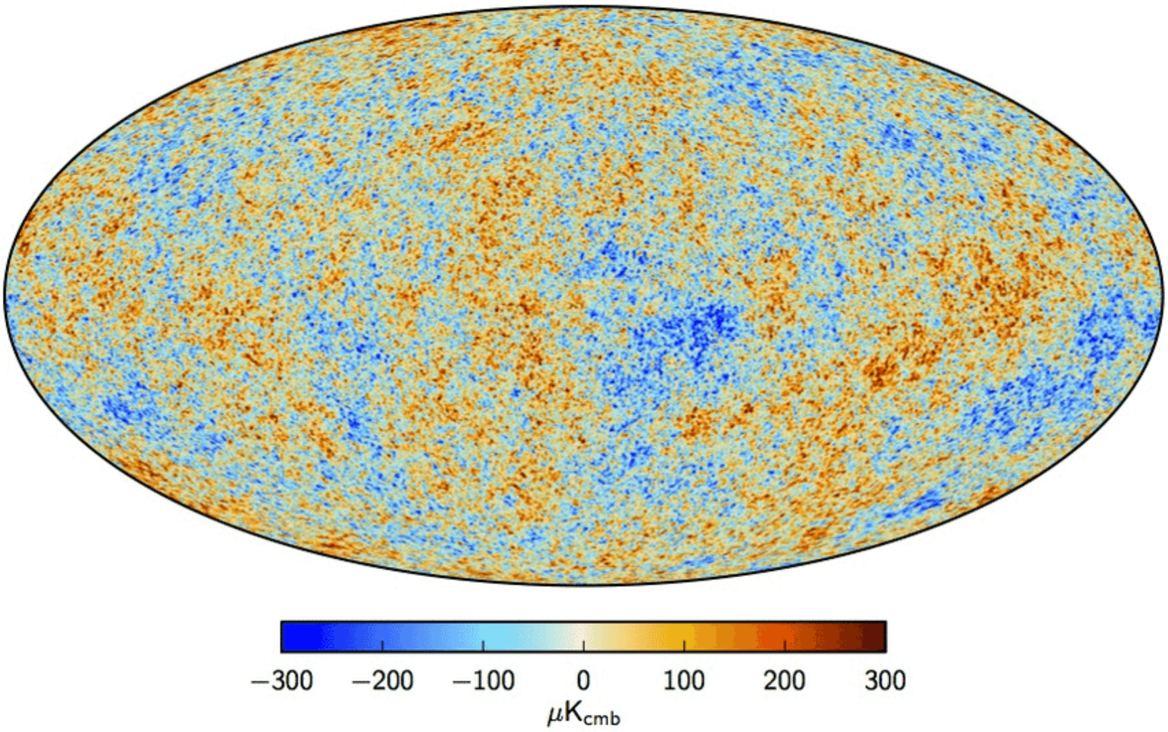

Figure 2.5: The anisotropic temperature distribution within the cosmic microwave background as measured by Planck in 2018. The temperature varies around the average of 2.7 K. Image taken from Reference [18].

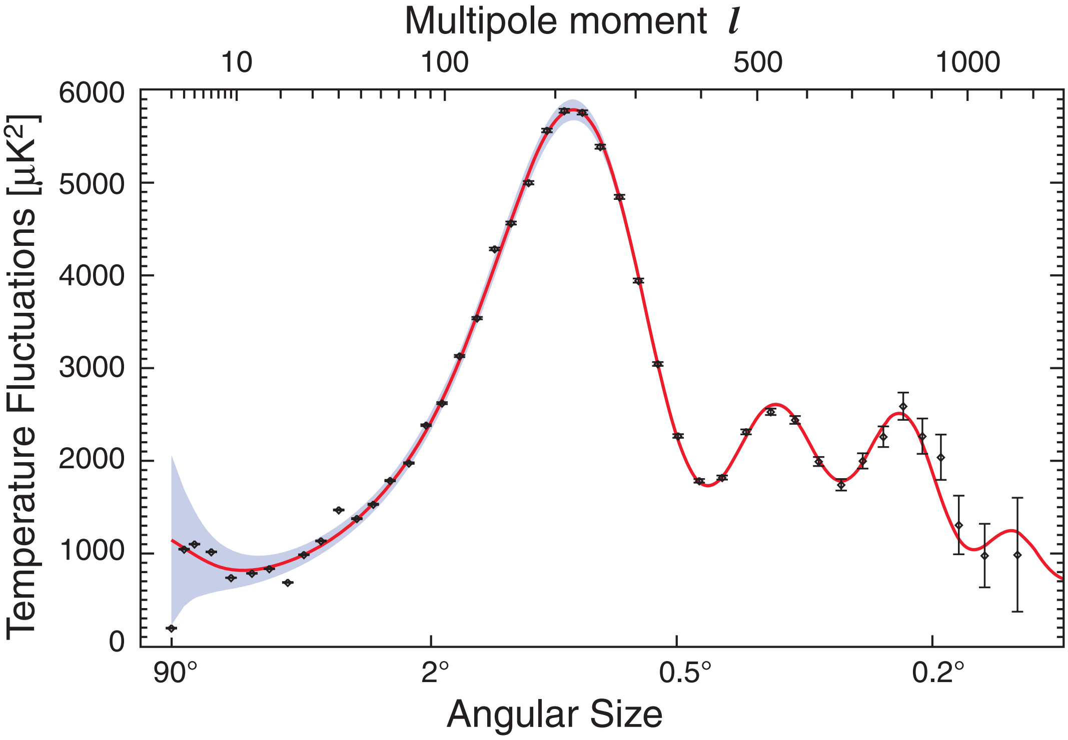

Figure 2.6: The power spectrum of the temperature anisotropy of the cosmic microwave background as measured over seven years by WMAP during the period 2003–2010. Image taken from Reference [27].

couples to the Standard Model. This section details these models. However, these specific examples are only used to highlight the possibilities for the new methodology discussed in Chapters 7 and 8; many other dark matter theoretical models remain to be studied further. A few examples of other models include axions, MACHOS and supersymmetry.

Axions

Axions are hypothetical elementary particles with low masses, in the range of 10^{-6} eV–1 eV, and no electromagnetic interactions [4]. They also have very low interaction cross-sections for the strong and weak forces. They were originally postulated as a solution to the strong CP problem [30], which arises from the difference in CP violation in strong and weak interactions. A solution to this was to introduce the axion as a new particle in the Standard Model. If this newly postulated particle is very light, it would interact so weakly that it would be close to impossible to detect—and would be a very convincing candidate for dark matter. The amount produced could also be reconciled with the expected dark matter proportion of the Universe.

The Axion Dark Matter Experiment (ADMX) [31] aims to search for evidence of this particle in the galactic dark matter halo using a resonant microwave cavity within a superconducting magnet. The experiment has thus far had success in eliminating some energy ranges within a number of benchmark models.

MACHOS

Massive Compact Halo Objects (MACHOS) are massive cosmological objects (i.e black holes) that satisfy the requirements for cold dark matter [32]. They are composed of non-luminous baryonic matter travelling through interstellar space. They are difficult to detect due to their lack of radiation emission.

Although MACHOS are attractive candidates to explain the abundance of non-luminous matter in the Universe, it is widely accepted that they are unable to account for the amount of dark matter measured in astrophysical experiments. It is not possible for the Big Bang to have produced enough baryonic matter to account for the dark matter discrepancy and also remain consistent with observations of elemental abundances. Furthermore, the fraction of baryonic matter of the total observed matter in the Universe shows the necessity of a large abundance of non-baryonic matter, regardless of whether MACHOS are present or not [33].

Supersymmetry

The supersymmetric model is an extension to the Standard Model which aims to explain observed discrepancies. The theoretical framework predicts an additional partner particle for every Standard Model particle. Some forms of the supersymmetry hypothesis imply the lightest neutral supersymmetric particle is a dark matter candidate [4, 34]. This is due to its properties of stability, electrical neutrality, and weakness of interaction.

Two of the largest general-purpose detector experiments at the LHC (ATLAS and CMS—described in Chapter 3) provide recommendations for the investigation of a number of models which nominate weakly interacting massive particles (WIMPs) as their dark matter candidate [35]. The idea of WIMPs evolved with the postulation of a relic dark matter particle from the early Universe. At this time a state of thermal equilibrium would have prevailed, causing dark matter particles to both form and annihilate with their antiparticles. The lighter particles produced in the annihilation process would have gradually cooled with the expansion of the Universe, eventually decreasing to an energy which cannot form a dark matter particle-antiparticle pair. The annihilation process would also cease once the number density reached a low enough value and so the number of dark matter particles across the Universe would remain approximately constant. The length of time that annihilation would continue for would be directly related to the interaction cross-section. With the current estimation of the quantity of dark matter in the Universe, the limit of the interaction cross-section for dark matter particle-antiparticle annihilation is that of the weak scale. This is approximately what would be expected for a new $\sim$ 100 GeV particle associated with the electroweak interaction. Some extensions to the Standard Model in supersymmetry predict a particle with these properties and this coincidence has been named the WIMP *miracle*. However, evidence for this particle has yet to be presented and null results from direct detection and collider experiments suggest that supersymmetry is not the answer.

It is still possible that WIMPs exist outside of the supersymmetric framework and the first model discussed in this section is one of the ATLAS and CMS benchmarks WIMP scenarios.

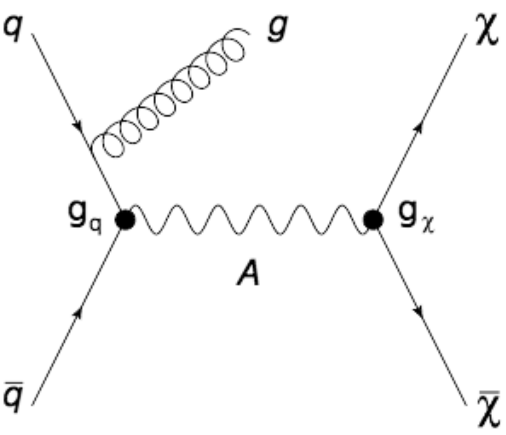

Figure 2.7: Feynman diagram for a simplified WIMP axial-vector model production of Dirac fermion dark matter in association with a gluon originating from initial state radiation.

Simplified WIMP axial-vector mediator model

Simplified models are designed to include as few new particles and interactions as possible [36]. Often, simplified models are the product of integrating out most particles from a more general new physics model. For collider physics, many of these models only include the relevant parameters: particle masses, decay widths, production cross-sections, branching fractions, and a particular dominant interaction type.

The model discussed here is a small extension of the Standard Model [35] that adds a U(1) gauge symmetry, under which a dark matter particle obtains charge. This is only useful for collider searches as it is also assumed that some Standard Model particles are also charged under this group, allowing a new gauge boson mediator particle for DM–SM interactions. For this case, depicted in Figure 2.7, a Dirac fermion dark matter particle, χ, of mass m_χ, is pair-produced by a spin-1 mediator particle, A, of mass m_A. Both vector and axial-vector couplings between the mediator particle and the dark matter fields are often considered. However, due to the choice of couplings only having a very minor effect on cross-sections and p_T distributions, one is chosen for this study based on the variety of other experiments also conducting analyses on it: axial-vector. An axial vector particle has even parity, which affects its mass due to the orientation of its spin when coupling. This construction of the model is now considered a benchmark for ATLAS dark matter searches.

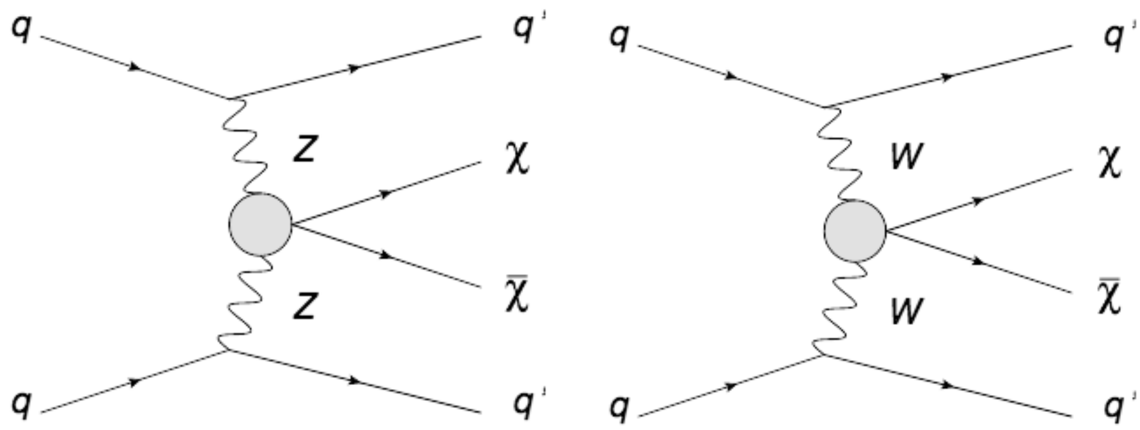

(a) (b)

Figure 2.8: Feynman diagrams for two vector boson fusion dark matter production channels. The vector bosons radiated in the proton-proton collision are shown here as (a) Z bosons, and (b) W bosons, which each interact to produce a pair of dark matter particles.

Effective field theory weak boson dark matter production model

An effective field theory (EFT) is an approximation for a fully-described underlying physical theory. In particle physics an effective field theory is used to generalise quantum field theories. They include only the necessary degrees of freedom to describe the physical interactions, while ignoring any information regarding their substructure. To this end, the minimum number of assumptions possible are made—for this purpose the theorised dark matter particle is the only new particle that is kinematically possible to create at the LHC outside of the Standard Model. Despite the attractive option of model-independence that an effective field theory provides, LHC searches often disregarded them since they can violate perturbative unitarity and can make predictions that are unphysical for large momentum interactions [37].

The effective field theory models studied in this thesis use contact interactions in place of the DM–SM mediator particle paradigm present in simplified models, as shown in Figure 2.8.

Invisible Higgs-boson decay model

The Higgs boson decay to invisible particles in the Standard Model proceeds via $H \to ZZ \to \nu\bar{\nu}\nu\bar{\nu}$. The branching fraction for this process is small at $\sim 0.1\,\%$ [38, 39], and so is too small for measurements at the LHC with the current experimental set-up [40]. However, if

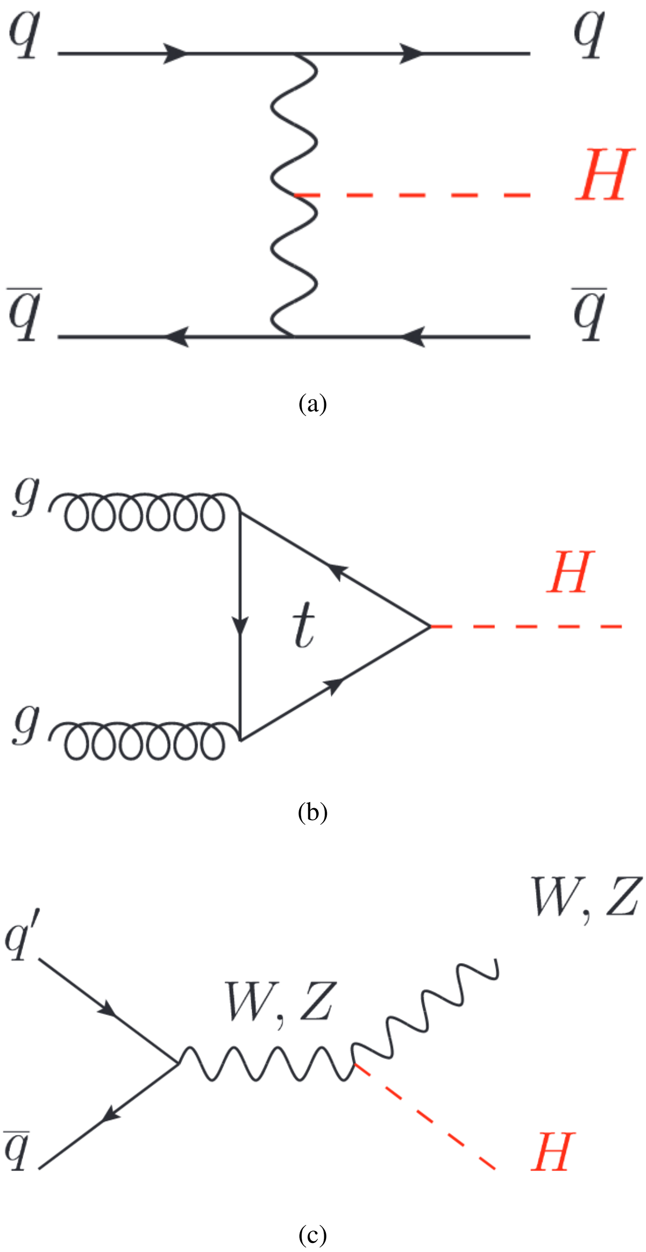

(a)

(b)

(c)

Figure 2.9: Feynman diagram depicting three production channels of the Higgs boson where it could subsequently decay into a dark matter particle-antiparticle pair. The processes are (a) vector boson fusion (b) gluon-gluon fusion, and (c) associated production with a vector boson.

this branching fraction is larger due to the addition of the Higgs boson decaying to two dark matter particles, or a new mediator particle, the LHC could potentially make a measurement. Three of these potential processes can be seen in the vector boson fusion (VBF), gluon-gluon fusion, and associated production Feynman diagrams in Figure 2.9. The vector boson fusion production channel contributes the most to the signal, but the other two are also included in the analysis described in this thesis.

Chapter 3

Experimental facilities

In this chapter the relevant features of the Large Hadron Collider (LHC), built at the European Organisation for Nuclear Research (Conseil Europeen pour la Research Nucleaire—CERN), and the main features and functionalities of the ATLAS detector, are described.

3.1 The Large Hadron Collider

The Large Hadron Collider [5] is currently the largest and most powerful accelerator on Earth. It has a circumference of 26.7 km and is situated approximately 100 m below the border of France and Switzerland at CERN. It is a particle accelerator built with the intention of probing the constituents of proton-proton, proton-lead and lead-lead collisions with unrivaled high energies and luminosities [41]: from 2015 to 2018 the LHC collided bunches of protons at a centre-of-mass energy of $\sqrt{s} = 13$ TeV [42], surpassing the energy range of every experiment that has come before.

The LHC is the last stage in a multi-phase accelerator complex [43, 44], depicted in Figure 3.1. The starting point is a cylinder of hydrogen gas, from which the electrons are stripped in an electric field to output protons. Once produced, these protons enter the linear accelerator LINAC2 to begin the first phase of acceleration up to an energy of 50 MeV. They are then injected into the Proton Synchrotron Booster (PSB) before being transferred to the Proton Synchrotron (PS), where they subsequently reach energies of 1.4 GeV and 25 GeV in respective circular accelerators. After running through the Transfer Tunnels (TTs) these protons are passed to the Super Proton Synchrotron (SPS), which is the final stage before they are injected into the LHC; the SPS ramps up the energy of the protons to 450 GeV. The

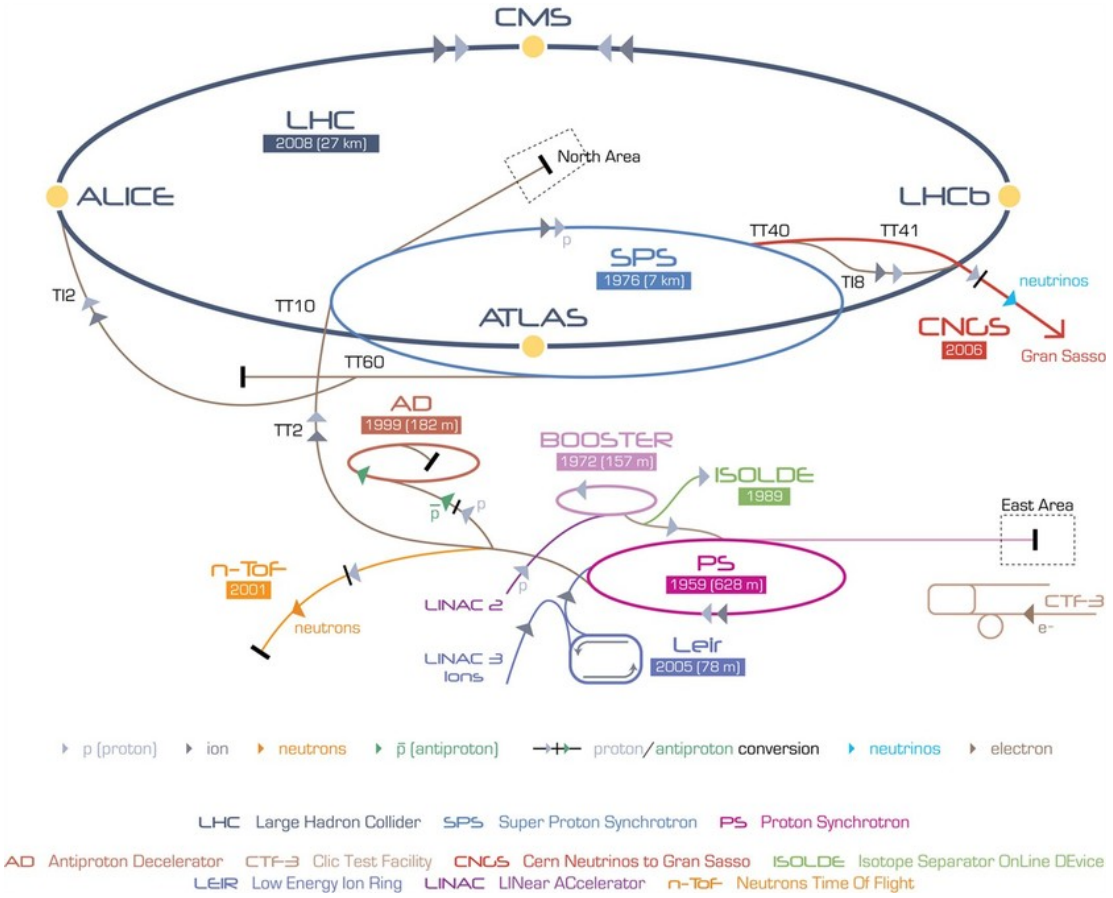

Figure 3.1: A schematic overview of the layout of the CERN accelerator complex. Image taken from Reference [43].

final acceleration takes place in the LHC—using radio frequency cavities to bring the beam energy up to 6.5 TeV.

The LHC ring is arranged in eight sections of arcs and linear segments. Bending dipole magnets are used in the arc sections to curve the beam, leaving the linear sections primarily for the purpose of beam control and manipulation (i.e injection, acceleration, cleaning, collision, or dumping of the beam). The four interaction points around the ring are placed at the sites of the four largest experiments: ATLAS (A Toroidal LHC ApparatuS) [6], CMS (The Compact Muon Solenoid) [45], LHCb (LHC Beauty) [46], and ALICE (A Large Ion Collider Experiment) [47] arranged at interaction points schematized in Figure 3.2. The ATLAS and CMS experiments are general-purpose detectors devised with the intention of probing a large variety of new physics phenomena. Between ATLAS and CMS stands the forward-spectrometer LHCb experiment which specialises in heavy flavour physics. The ALICE experiment, on the opposite side of ATLAS and CMS, studies the physics phenomena occurring from heavy ion collisions.

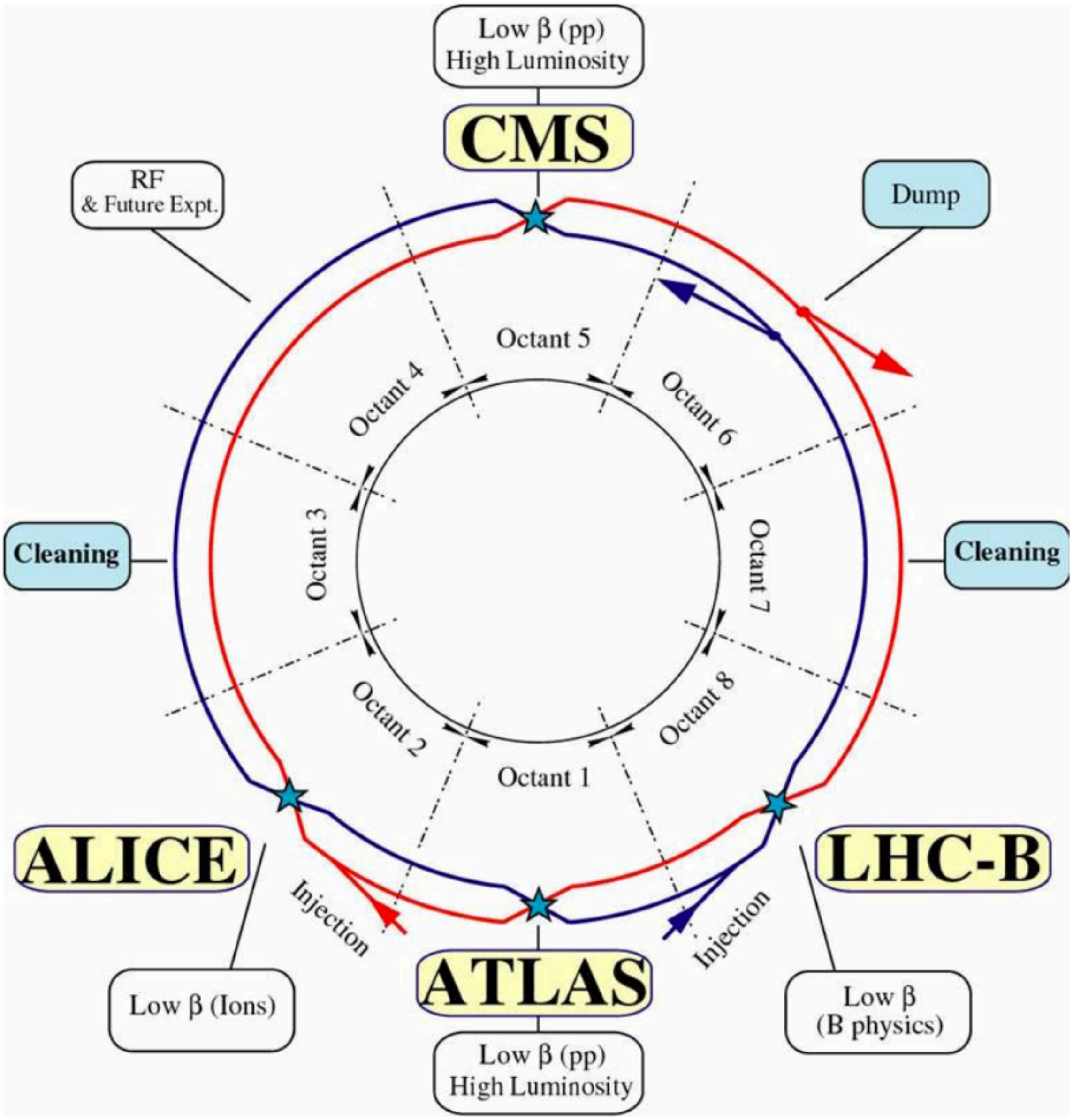

Figure 3.2: A schematic of the layout of the Large Hadron Collider. It is arranged in eight sections of arcs and linear segments with a low beam amplitude function, β, at each interaction point. Image taken from Reference [5].

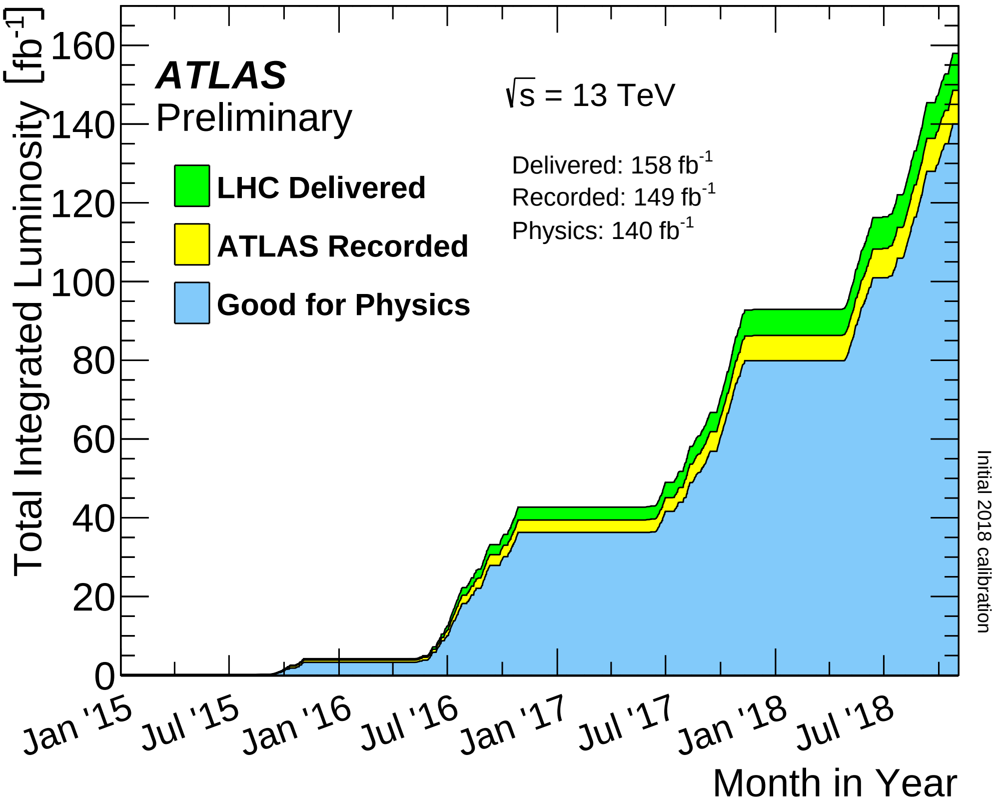

Figure 3.3: Total integrated luminosity as a function of time, from 2015 to 2018, (green) delivered to, (yellow) recorded by, and (blue) used as *good data* for the ATLAS detector experiment for proton-proton collisons [48].

At the LHC, proton beam collisions occur between bunches, with each bunch containing $\sim 10^{11}$ protons and each beam comprising of up to 2808 bunches. One of the principal aims of the LHC is to reach a high frequency of collisions in order to increase the volume of data and subsequently the rate of interesting physics phenomena. The measure of this rate of collisions is known as the instantaneous luminosity, $\mathcal{L}$, which is given by:

$$\mathcal{L} = \frac{n_b f_r n_1 n_2}{2\pi \sum_x \sum_y}, \tag{3.1}$$

where n_b is the number of bunches in a beam, f_r is the bunch revolution frequency in the LHC, and n_1 and n_2 are the number of protons within each bunch in beams 1 and 2 respectively. $\sum_x$ and $\sum_y$ describe the interaction width of the two beams across the x and y axes. For physics analysis, the interesting quantity is the integrated luminosity, $\mathrm{L} = \int \mathcal{L}(t)\mathrm{d}t$, calculated by integrating the instantaneous luminosity over a period of data-taking.

In October 2008 construction of the LHC was finished and was running successfully only a month later. It is situated in the tunnel previously used by the Large Electron-Positron Collider (LEP) [49, 50]. After slowly increasing energies to a collision energy of 7 TeV and bunch rates to 20 MHz, the Run 1 period of data collection began in 2010. This continued until 2012 when the collision energy was increased to 8 TeV and was followed by the first long shutdown which spanned 2013–2015. Run 2 commenced in June 2015 with a centre-of-mass collision energy of 13 TeV and a bunch spacing rate of 20 MHz, which has since been increased to 40 MHz. This data taking period continued until 2018 and had a mean number of interactions per crossing (pileup) of 33.7. Pileup can cause problems when reconstructing the final state of a collision.

The total integrated luminosity delivered by the LHC from 2015 to 2018 ($158\,\text{fb}^{-1}$) is compared in Figure 3.3 with the total integrated luminosity received by the ATLAS detector ($149\,\text{fb}^{-1}$) and that which was successfully collected as *good* data for physics analyses ($140\,\text{fb}^{-1}$). The future plan for the upgrade is to increase the energy of the LHC up to the design energy of $\sqrt{s} = 14$ TeV, and to further increase the luminosity.

3.2 Physics of hadron colliders

Experiments aiming to test the validity of the Standard Model, or of BSM theoretical frameworks, predominantly consist of the investigation of high energy collisions of particles, such as the colliding of protons at the LHC. These protons are composed of quarks and gluons, known as partons, which each carry a fraction of the total proton energy. The parton distribution function (PDF), $f_i(x,Q^2)$ is the probability of a parton i carrying a fraction x of the momentum of the proton at a energy scale Q. The parton distribution function is calculated using measurements from deep inelastic scattering experiments [51], before being extrapolated to the energy scale at the LHC. They are the first step in determining cross-sections.

Cross-sections are vital in predictions for which interactions are likely to take place in a given event. They are quantities that give the ability to test theoretical predictions of particle phenomena. The production cross-section for a hadron, X, in proton-proton collisions is given by:

$$\sigma_{pp\to X} = \int dx_a f_a(x_a,Q^2) \int dx_b f_b(x_b,Q^2)\hat{\sigma}_{ab\to X}, \tag{3.2}$$

where $f_{a,b}$ are the parton distribution functions for the constituents of each of the colliding proton, and $\hat{\sigma}_{ab\to X}$ is the cross-section for the partons in the process, known as the partonic cross-section. This cross-section and the integrated luminosity given in Equation 3.1 are related via:

$$\langle N \rangle = \sigma_{pp\to X} \cdot \mathcal{L}_{\mathrm{int}}, \tag{3.3}$$

which gives the expected mean number of events N in the hadronic final state X.

The momentum of the colliding partons will not always be balanced and so the longitudinal momentum cannot be known. Therefore, the transverse momentum p_{T} is used.

3.3 The ATLAS detector

3.3.1 Overview

The ATLAS detector is a multipurpose experiment developed to study an extensive physics programme at the LHC [6]. This programme ranges from precision measurements of the Standard Model to searches for new physics phenomena up to the TeV scale. At 44 m long, with a 25 m radius, and a weight of $\sim$ 7000 t, it is the largest detector ever constructed for use with a particle collider. The cylindrical shape allows for a solid angle coverage of approximately 4π sr, which maximises the number of particles detected in the aftermath of collisions. The axis of the cylinder is aligned with the LHC beams, which are directed to intersect at the centre of the detector. The motivation for such large coverage of this device is to measure the properties of as many particles produced in an interaction as possible; measurements of the charge, trajectory, momentum, energy, and type of each particle allow for the reconstruction of an event. This is most vital in analyses where full event information is necessary for understanding the physics behind an interaction.

The ATLAS detector apparatus is comprised of four main subsystems arranged in layers around the point of interaction: the magnet system which is responsible for the curvature of charged particles; the inner detector, which tracks the trajectories of a variety of charged particles; the calorimeters, which identify showers and jets of particles with high efficiency; and the muon spectrometer, which achieves high performance in the identification of muons and the measurement of their momenta and charge. A schematic overview of the ATLAS detector with labelled subsystems is displayed in Figure 3.4. Further descriptions of the ATLAS subsystems are given in the following sections.

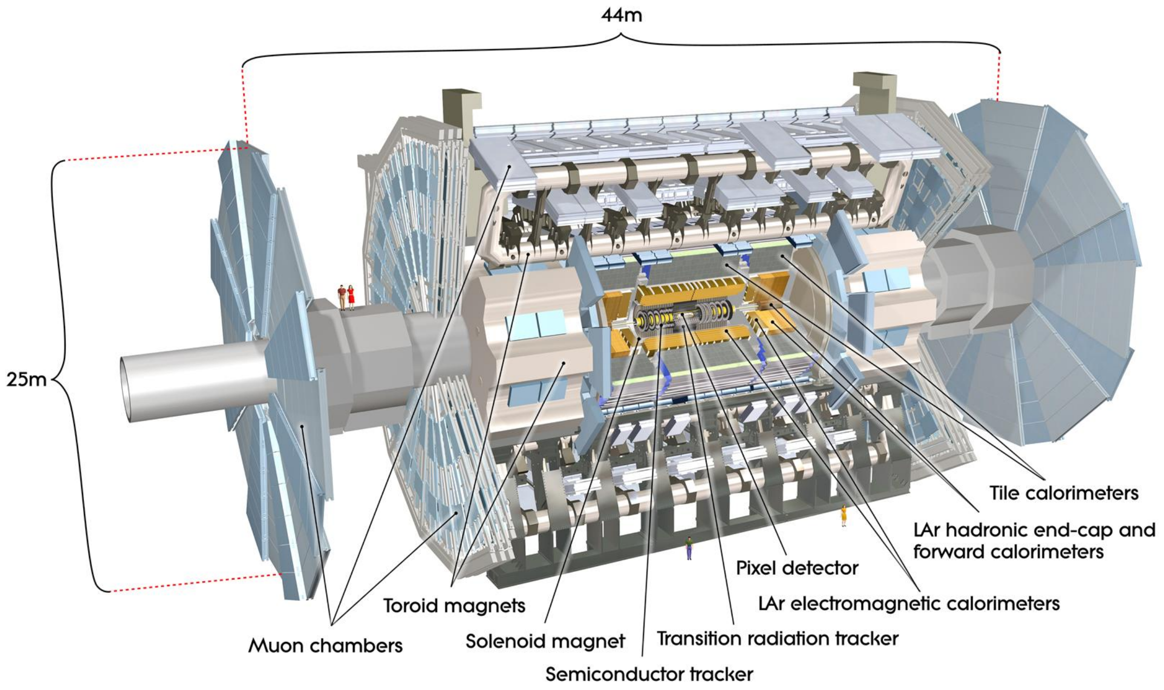

Figure 3.4: A schematic of the ATLAS detector and subsystems. The graphic has been cut away to allow all subsystems to be seen. Image taken from Reference [6].

Coordinate system

The coordinate system used in this report follows the standard ATLAS definition [6] and is schematised in Figure 3.5. The nominal interaction point is defined as the origin of the coordinate system. The beam direction defines the z-axis, and the x-y plane is transverse to the beam direction. The positive x-axis is defined as pointing from the interaction point to the centre of the LHC ring and the positive y-axis is defined as pointing upwards. The transverse momentum p_{T}, the transverse energy E_{T} and the missing transverse energy $\not{E}_{\mathrm{T}}$ are defined in the x-y plane, transverse to the beamline. The azimuthal angle ϕ is measured around the beam axis and the polar angle θ is the angle from the beam axis. The rapidity is defined as $y = 1/2 \cdot \ln\left[(E+p_z)/(E-p_z)\right]$, where $y \to \pm\infty$ along the beam pipe and $y \to 0$ perpendicular to the beam pipe. For a highly relativistic particle (close to a limit of zero particle mass) the rapidity tends towards the pseudorapidity, $\eta = -\ln(\tan(\theta/2))$. The distance ΔR in the η–ϕ space is defined as $\Delta R = \sqrt{\Delta\eta^2 + \Delta\phi^2}$.

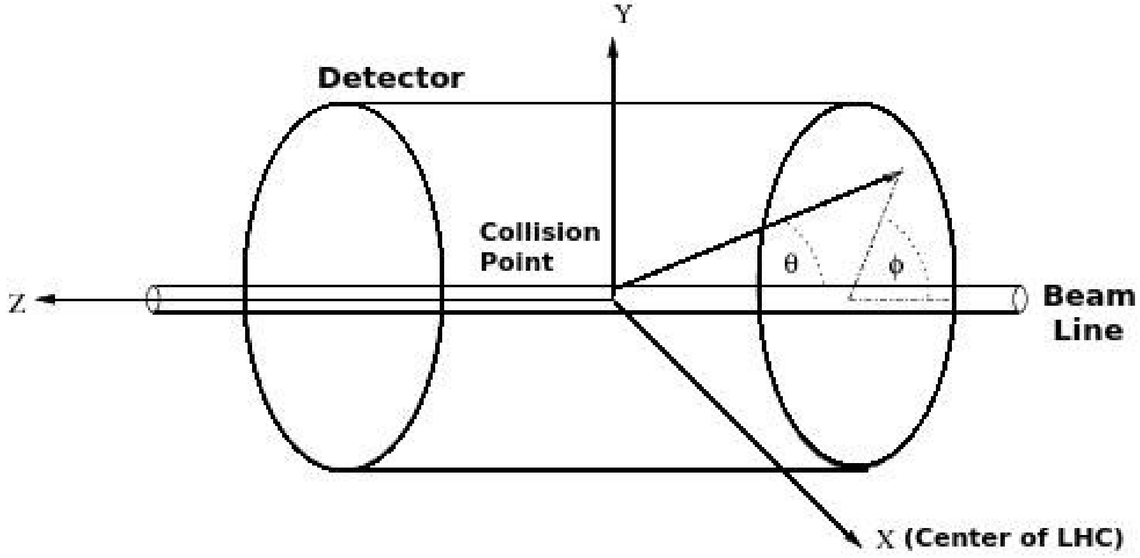

Figure 3.5: A schematic of the ATLAS coordinate system.

3.3.2 Magnet system

The ATLAS detector depends heavily on the magnet system for particle identification [52] as it induces curvature in the trajectories of charged particles—which is crucial for momentum measurements. The magnet complex is comprised of three different types of superconducting magnet system, shown in Figure 3.6.

Central solenoid: The central solenoid produces a magnetic field of 2 T parallel to the beam—crucial for the tracking system mechanism of determining the momenta of a charged particle leaving the interaction point.

Barrel toroid: The barrel toroid is cylindrical and symmetric around the beam axis allowing for the generation of a 0.5 T magnetic field along the central zone of the muon spectrometer.

End-cap toroids: The end-cap toroids are a pair of smaller toroids placed as to ensure a 1 T magnetic field in the forward region of the muon spectrometer.

3.3.3 Tracking system

The inner detector (ID) [53, 54] is designed to measure the trajectory and momenta of charged particles produced in a proton-proton collision event. It is the closest part of the

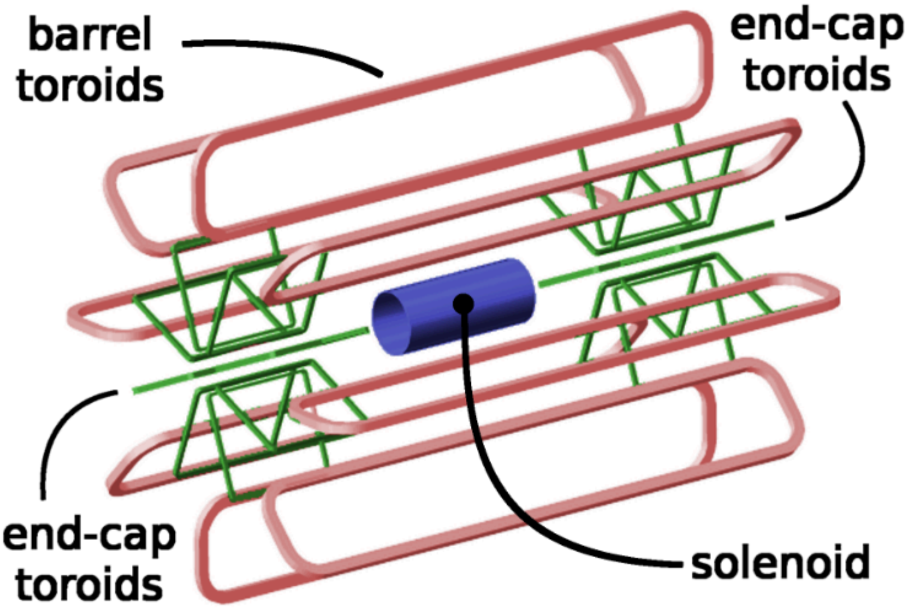

Figure 3.6: A schematic of the ATLAS Magnet System. The barrel toroidal magnets are shown in red, the central solenoid in blue, and the end-cap toroidal magnets in green. Image taken from Reference [52].

ATLAS apparatus to the interaction point and spans the region $|\eta| < 2.5$ with full azimuthal coverage. The solenoid magnet surrounding this part of the detector generates a 2 T magnetic field which induces bending in the paths of the charged particles; the curvature in the charged particles tracks allows the precise calculation of their charge and momenta with a resolution of $\sigma_{p_{\mathrm{T}}}/p_{\mathrm{T}} = 0.05\% \cdot p_{\mathrm{T}} \oplus 1\%$ GeV. The inner detector is also able to provide both primary and secondary vertex reconstruction, as well as electron identification at the high level of luminosity in the LHC. The inner detector is composed of three independent and complementary detectors, displayed in Figure 3.7. These systems allow the reconstruction of tracks of charged particles with energies as low as 0.4 GeV.

Silicon pixel detector

The silicon detector [56] apparatus is arranged in three concentric cylinders around the beam axis in the barrel, and three wheels in the end-caps. It is comprised of 1744 sensor modules which each contain $\sim 47\,000$ pixels of size $50 \times 400\,\mu\mathrm{m}^2$, summing to a total of 80 million read-out channels covering the range $|\eta| < 2.5$.

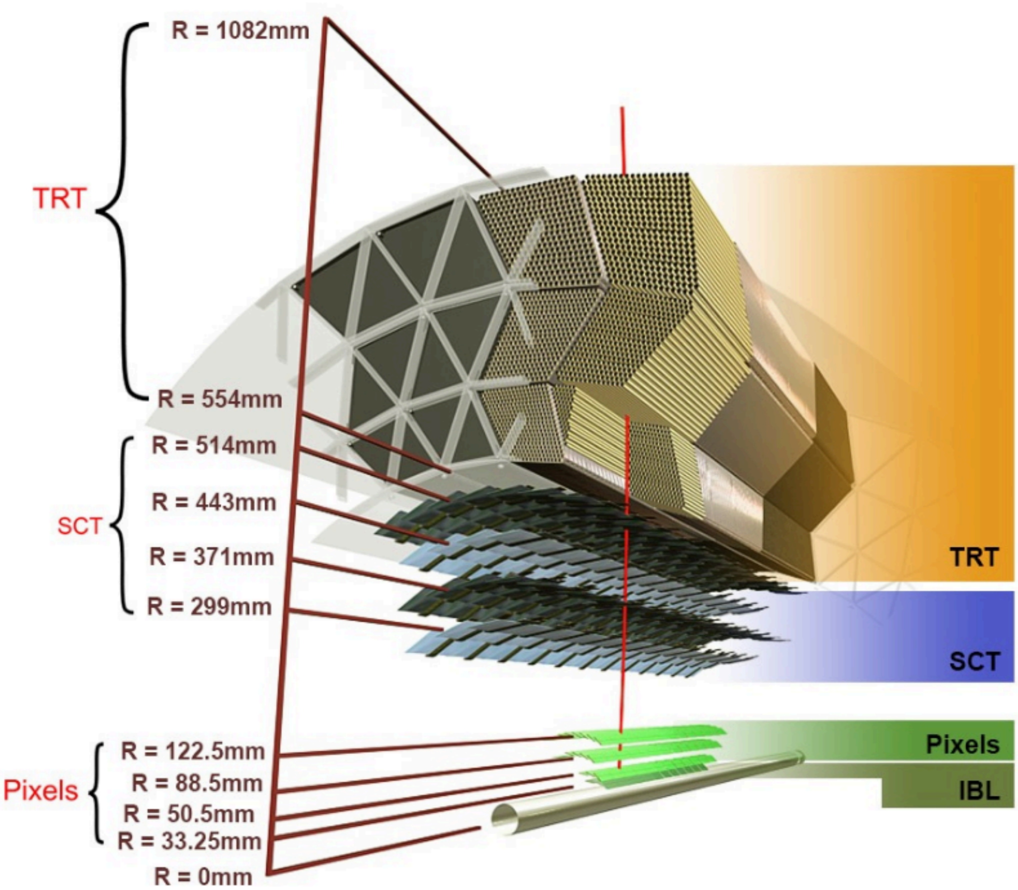

Figure 3.7: Schematic showing the composition of the ATLAS inner detector, including the new insertable B-layer (IBL). Image taken from Reference [55].

During the first long shutdown of the LHC a new tracking sub-detector layer, the insertable B-layer (IBL) [57], was installed at a radius of 33.3 mm, between the beam pipe and pixel detector. This increases the number of pixel read-out channels in the system by 12 million. The high granularity and fine reconstruction resolution of the pixel detector allows for track and vertex reconstruction of very short-lived particles.

Including the IBL, the pixel detector consists of four separate layers of pixels in the barrel region, and three in the end-caps. These layers use silicon sensor modules to identify the position of hits in order to reconstruct tracks. Particles travelling through the sensors ionise the silicon, creating free *electron* and *hole* pairs. With a voltage applied across the silicon modules, the electrons (holes) are attracted (repulsed) to the cathode (anode)—this induces a current that is logged and cataloged by the electronics.

Semiconductor tracker

The semiconductor tracker (SCT) is comprised of 15912 micro-strip sensors which each contain 768 strips of silicon, instead of pixel modules like those used in the pixel detector. These are arranged in four layers, cylindrically around the beam axis in the barrel and symmetrically pointing along the radius of each wheel from the beam axis in the end-caps. The entire semiconductor tracker amounts to over 6 million read-out channels, which allows for a spatial resolution of 17 µm for the range $|\eta| < 2.5$.

Transition radiation tracker

In contrast to the other two components of the tracking system, the transition radiation tracker (TRT) [58] does not use silicon-based technology. It instead consists of 370 000 drift tubes filled with a gaseous mixture of xenon (70 %), carbon dioxide (27 %) and oxygen (3 %). These tubes are kept at high voltage and contain anode wires along their central axis. Particles travelling through the tubes ionise the xenon gas, producing electrons and ions that drift and cause a current, which is measured and recorded. The drift tubes are interleaved with polypropylene fibres. The difference in dielectric constant between the two materials allows the production of X-ray transition radiation, which is responsible for the ionisation in the drift tubes. The TRT is the outermost layer of the ATLAS tracker system and envelopes the other apparatus with a barrel region and two end-caps. The range covered by this subsystem is $|\eta| < 2.0$.

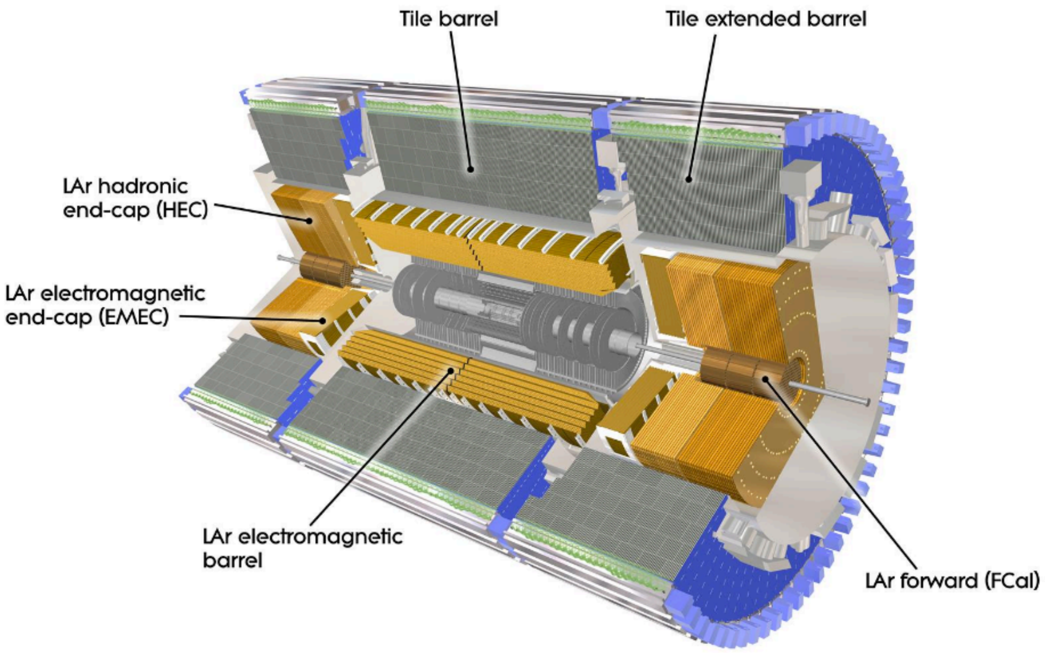

Figure 3.8: A cut-out schematic of the ATLAS calorimeter system. Image taken from Reference [6].

3.3.4 Calorimeter system

The ATLAS calorimeters [59] are used in the identification and energy measurement of incident particles through their electromagnetic or strong interactions. The calorimeters use a sampling system composed of active material layered with a high-density absorbing material. The absorber layers cause showers of particles in the calorimeter which subsequently deposit energy in the active detection material within $|\eta| < 4.9$. This allows the identification and measurement of the original incident particle. The ATLAS calorimetry system has two main components: the electromagnetic calorimeter and the hadronic calorimeter.

Precision measurements of electrons and photons can be made within the region $|\eta| < 2.5$ owing, in part, to the fine granularity of the electromagnetic calorimeter. The coarser granularity of the hadronic calorimeter is well-suited for its design purpose of jet reconstruction and measurements of missing transverse momentum. A cut-out schematic of the ATLAS calorimetry system is shown in Figure 3.8. Despite having charge, muons are expected to pass through the calorimeters due to their minimally ionising properties.

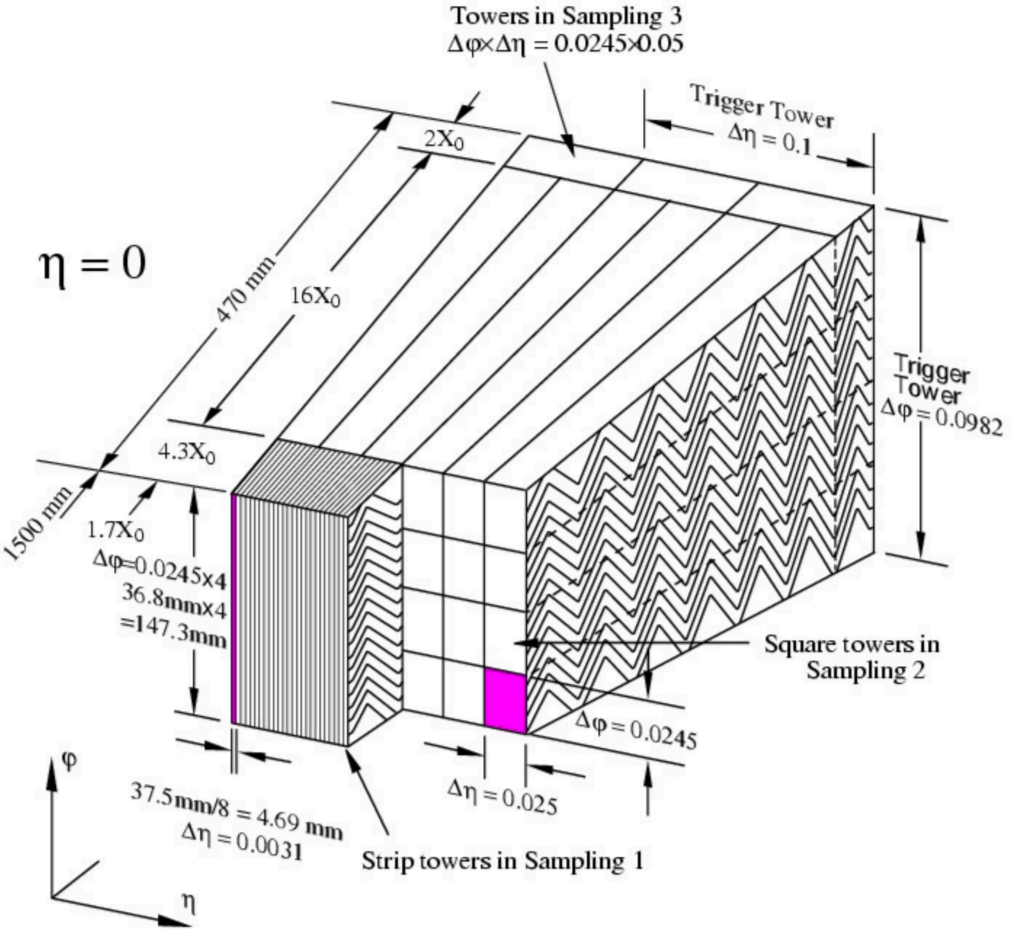

Figure 3.9: Schematic of a slice of the ATLAS electromagnetic calorimeter. Image taken from Reference [6].

Electromagnetic calorimeter

The electromagnetic (EM) calorimeter [60] is the part of the detector responsible for the reconstruction of electromagnetic showers. It consists of two half-barrels covering the region $|\eta| < 1.475$, known as the electromagnetic barrel, and two disc-shaped end-caps which cover the space $1.375 < |\eta| < 3.2$, known as the electromagnetic end-caps. The ATLAS electromagnetic calorimeter samples with a lead absorber layered with a liquid argon (LAr) [61] active medium. The kapton electrodes are folded in an accordion-like geometry parallel to the incident particle trajectories. This provides complete azimuthal coverage, as can be seen in Figure 3.9. The energy resolution of the electromagnetic calorimeter is $\sigma_E/E = 10\%/\sqrt{E} \oplus 0.7\%$, where E is in GeV.

The electromagnetic calorimeter has three longitudinal sections:

First sampling layer: The first sampling layer of the barrel comprises compact strip cells of $\Delta\eta \times \Delta\phi = 0.003 \times 0.01$, which allows for the design feature of identifying and distinguishing photons produced in the process: $\pi^0 \to \gamma\gamma$.

Second sampling layer: The second sampling layer is segmented in cells of size $\Delta\eta \times \Delta\phi = 0.025 \times 0.025$. This is the thickest electromagnetic sampling layer so far following the line along the incident particle trajectory and most of the energy is deposited here.

Third sampling layer: The third sampling layer is twice as wide as the second sampling layer ($\Delta\eta \times \Delta\phi = 0.05 \times 0.025$), with a designated purpose of measuring electrons and photons with high energies which cause wider clusters.

Hadronic calorimeter

The hadronic calorimeter (HCal) [62] is responsible for the measurement of the energy and trajectory of hadronic jets resulting from the hadronisation of quarks and gluons. The choice to locate the ATLAS hadronic calorimeter outside of the electromagnetic calorimeter was made due to hadronic showers producing longer and wider profiles than electromagnetic ones. It is comprised of a tile calorimeter [62] in the barrel region $|\eta| < 1.7$, and end-cap liquid argon calorimeters [61] in the region $1.5 < |\eta| < 3.2$. The overall energy resolution for $|\eta| < 3.1$ is $\sigma_E/E = 50\%/\sqrt{E} \oplus 3\%$, where E is in GeV.

The tile sampling calorimeter uses steel as an absorber material alongside tiles of plastic scintillating material which act as the active medium. The main barrel region covers the region $|\eta| < 0.8$, with two identical barrel extensions covering the region $0.8 < |\eta| < 1.7$.

The hadronic liquid argon end-cap calorimeter interleaves the scintillating liquid argon with copper plates, covering a range $1.5 < |\eta| < 3.2$. This is required to stop all showers of particles before they reach the muon spectrometer. To this end, the total barrel region has a radial depth of almost 2 m.

Forward calorimeter

The forward calorimeter (FCal) [6] provides coverage of the region $3.1 < |\eta| < 4.9$ for energy measurements of both electromagnetic and hadronic showers. It consists of three modules in the end-cap regions: one module is optimised for electromagnetic measurements by using copper and liquid argon; and the other two modules are hadronic tungsten-liquid argon calorimeters. The ATLAS forward calorimeter has an energy resolution of $\sigma_E/E = 100\%/\sqrt{E} \oplus 10\%$, where E is in GeV.

3.3.5 Muon spectrometer

The ATLAS muon spectrometer (MS) [63, 64] is located in the outer regions of the detector. This is due to the ability of muons to pass through most matter while preserving most of their initial energy. It measures the trajectory and momentum of muons in the magnetic field generated by the toroid magnets. This allows for high-precision track reconstruction. The muon spectrometer apparatus is arranged in three cylindrical layers of chambers around the beam axis in the barrel, and in three wheels in each end-cap region, as shown in Figure 3.10.

Each chamber is composed of four different, but complementary, technologies:

The monitored drift tubes: The monitored drift tubes (MDTs) [66] are aluminium tubes, of diameter 30 mm and thickness 400 μm, containing a pressurised mixture of argon and carbon dioxide gas. A Tungsten-Rhenium wire of 50 μm diameter runs along the central axis at high voltage with the tube walls—a muon signature is evidenced by the electrical pulses produced in the tubes from electrons and holes, produced in ionisation, drifting and causing a current. They provide a resolution of $\sim 35\,\mu$m for the full $|\eta| < 2.7$ range of the muon spectrometer to ensure precise tracking measurements.

The cathode strip chambers: The cathode strip chambers (CSCs) [67] provide precision track measurement in the region $2.0 < |\eta| < 2.7$ with higher granularity than the MDTs. They consist of multi-wire proportional chambers with cathodes arranged in strips. This set-up is able to achieve a spatial resolution of $\sim 40\,\mu$m in the radial direction. They use similar technology to drift tubes; the difference arises from individual positive and negative wires interspersed within a larger chamber of gas. The cathode strips run perpendicular to the wires to improve dimensional position resolution.

Resistive plate chambers: The resistive plate chambers (RPCs) [68] are parallel electrode-plate detectors filled with a gaseous mixture of $C_2H_2F_4$ and SF_6. These chambers provide extremely fast track identification and trigger measurements (Section 3.3.6) for the barrel

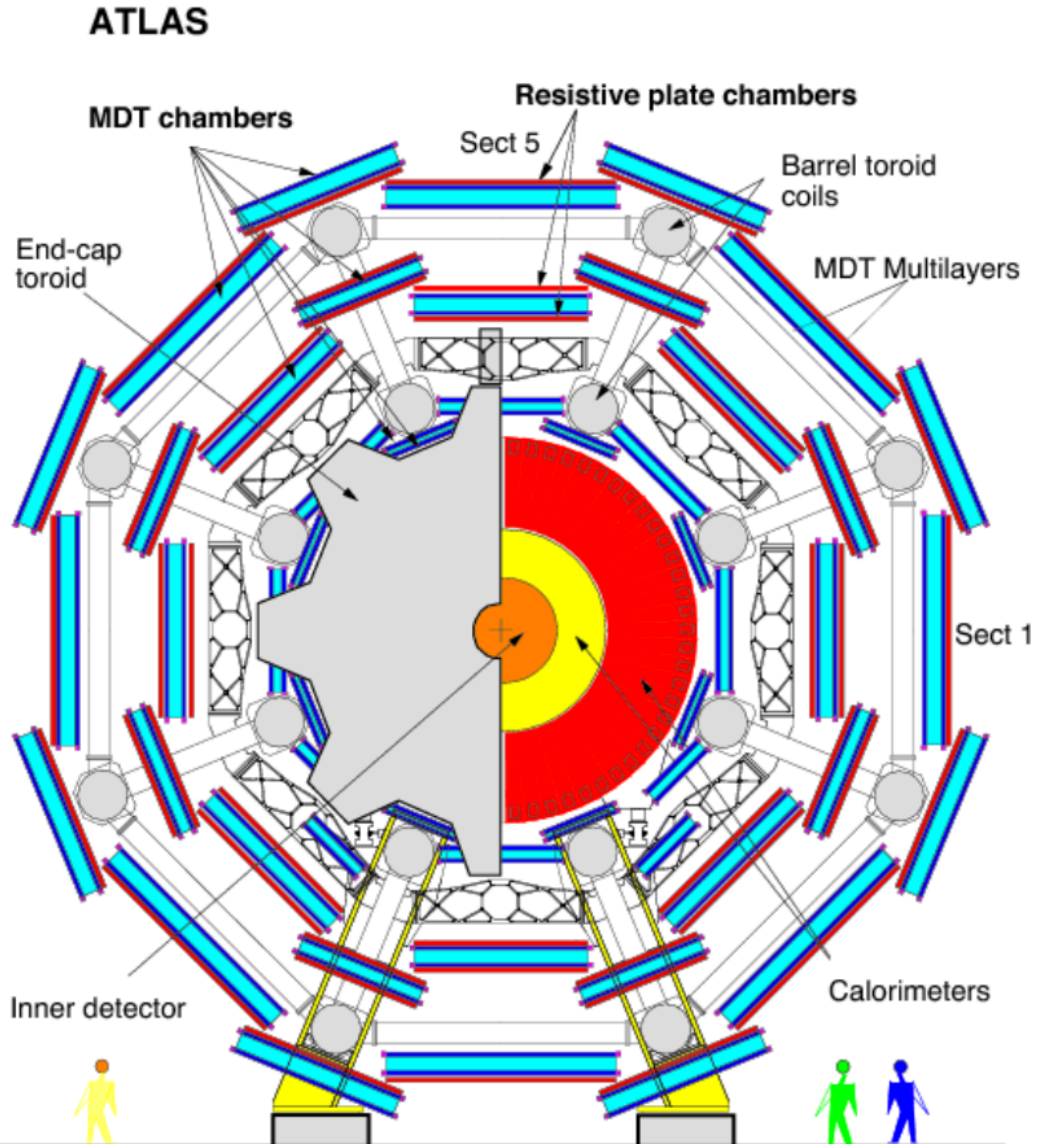

Figure 3.10: Schematic of a transverse view of the muon spectrometer. Image taken from Reference [65].

region, $|\eta| < 1.05$. They use two parallel resistive plates to maintain the electric field within the gas volume during ionisation.

Thin gap chambers: The thin gap chambers (TGCs) are multi-wire proportional chambers filled with a gaseous mixture of carbon dioxide and n-pentane (n-C_5H_{12}). They provide tracking and triggering coverage for the end-cap regions, $1.05 < |\eta| < 2.4$.

3.3.6 Trigger and data acquisition system

During Run 2 the LHC had a bunch-crossing rate of 40 MHz. The ATLAS detector is not capable of reading out and recording events at this frequency—this necessitates a method of retaining interesting physics data while keeping a feasible rate of information stored. The ATLAS trigger and data acquisition system (TDAQ) [69–71] is responsible for identifying the presence of physically-interesting signatures in the event. These signatures often undergo a process known as prescaling, where only $1/N$ events are accepted when the prescale is set to N, with the aim of decreasing bandwidth. The TDAQ consists of several tiers of increasingly fine filters. This is in order to refine the data and reduce the speed requirements by which events are processed. These tiers can be grouped into two trigger levels: Level-1 which is hardware based, and the High-Level trigger which is software based.

Level-1: The Level-1 (L1) trigger makes decisions using information from the calorimeter, muon spectrometer and fast, specialised hardware. It defines the regions-of-interest (RoIs) where signatures have been recognised as interesting—cutting the data rate down to $\sim 100\,\text{kHz}$ with a latency of $< 2.5\,\mu\text{s}$. High-p_T objects and large missing transverse energy E_T^{miss} are interesting signatures that the L1 trigger identifies, or *triggers* on. Objects that have been identified in the calorimeter systems by the L1 trigger are recorded as clusters. These provide the region-of-interest for those signatures. The p_T of muons can be measured using a dedicated muon L1 trigger with low granularity.

High-Level trigger: The High-Level trigger (HLT) was created from the merging of the Level-2 and the Event Filter trigger levels used in Run 1. It uses dedicated software algorithms to access data within the regions of interest before reducing the data rate further to $\sim 1\,\text{kHz}$. The High-Level trigger uses the full detector information for the reconstruction of objects detected. The decision-making algorithms used to do this have a latency of up to $\sim 300\,\mathrm{ms}$. Full event reconstruction can be achieved with the High-Level trigger. Events are subsequently saved in a number of different channels for different purposes: detector monitoring and calibration, physics analysis, and trigger-level analysis.

Worldwide LHC computing grid

After this filtering process, collision data is handled and stored by the worldwide LHC computing grid (wLCG) [72]. This international project encompasses over 170 computing facilities around the globe in a grid-based computer network, built with the purpose of handling the large volume of data produced by ATLAS and the other LHC experiments.

3.4 Monte Carlo event generators

Monte Carlo (MC) event generators provide simulations of Standard Model and BSM scattering processes in high energy particle collisions with $O(100–1000)$ final-state particles per collision [73]. As this becomes more complicated with every additional process, the event simulation is split into a number of stages.

The first step considers the *hard scatter* matrix element of a particle collision up to a certain order, depending on the generator. Most modern event generators provide event simulations up to leading order (LO) or next-to-leading order (NLO). Some BSM physics processes can be simulated given that the required Feynman rules have been activated, often by using the FeynRules programme [74].

Parton showering (PS) algorithms are the next step in the chain and aim to simulate the final stages of an event with additional parton radiation. Only some event generators provide this additional step in their software, and so dedicated parton showering generators also exist to fill this gap. After the parton showering stage, hadronisation takes place, i.e. any coloured partons are converted into colourless hadrons that can be observed. Unlike previous steps in the process, this is not achieved by calculation—hadronisation models are used, such as the cluster model [75] and the Lund string model [76].

The final stage of the event generator chain is detector simulation. This involves a highly-detailed software, built to imitate the the ATLAS detector. It provides a simulation of how each sub-detector would behave when an object from the previous stage in the simulation passes through, including inefficiencies and thresholds. Geant4 [77] is used to simulate the ATLAS detector.

Further details of the MC generators used for the analyses in this thesis are included in the preamble of each respective chapter.

3.5 Rivet Toolkit

The Robust Independent Validation of Experiment and Theory (Rivet) toolkit [78] is an analysis software system which allows for the preservation of analysis code from experiments at high-energy particle colliders. It is used for the validation and comparison of MC event generators with data. Rivet is used in the analysis presented in Chapter 7.

Chapter 4

Event and physics object reconstruction

Events that are to be used in data analyses are required to pass quality criteria that determine if there are any incomplete events or data integrity problems. The data that passes these selections is listed on the *Good Runs List*. The accurate identification and reconstruction of physics objects in each event is vital for all physics analyses in the ATLAS collaboration. Techniques to this end are outlined in this chapter.

4.1 Electrons

Electrons are identified and reconstructed with the measurement of energy deposits, known as clusters, in the electromagnetic calorimeter, and matching tracks in the inner detector (ID) [79]. Electron candidates are distinguished from background objects during reconstruction by electron identification algorithms. These algorithms use both the matching of inner detector tracks to electromagnetic calorimeter clusters and the matching of the origin of the vertex to the primary interaction at the collision point. The electron is reconstructed from the cluster by summing the energy deposited in the calorimeter cells. This is done within a rectangle in η–ϕ space of 3×7 cells in the barrel region and 5×5 cells in the end-cap region. Fake electrons are rejected using selection criteria involving the properties of the shower, matching of the inner detector tracks to electromagnetic calorimeter clusters, and the track quality. These criteria can be set at different levels (*loose*, *medium*, or *tight*) in order to find an appropriate selection efficiency. Each level of selection criteria is defined by a likelihood discriminant based on the same variables; electrons selected by the *tight* level criteria are also selected by the *medium* and *loose* criteria.

In order to further reduce backgrounds, electron candidates are required to be isolated in the inner detector and calorimeter. This isolation energy is calculated from the sum of the energy deposited in every cell within a cone-shaped range of $\Delta R < 0.4$ around the central track. This accounts for 95 % of the electron energy. The leakage of the electron energy outside of the cone is taken into account in correction calculations. Other calibrations in effect are required to correct for pileup and the effect of the underlying event.

4.2 Photons

Like electrons, photons are reconstructed using energy deposits in the electromagnetic calorimeter [80, 81]. An energy deposit in the electromagnetic calorimeter that has no associated track in the inner detector is known as an *unconverted* photon. Clusters with associated inner detector tracks may have been produced by an electron or photon producing an electron-positron pair in the detector—these are known as *converted* photons. If the inner detector track originates from a vertex in the interaction point region the object is reconstructed as an electron. Candidate photons are produced from the sum of energy deposits in calorimeter cells. The restrictions on these are set in η–ϕ space: an area in the barrel region of 3×7 and 3×5 cells for converted and unconverted photons respectively; and 5×5 in the end-cap regions for both.

Selection criteria are defined using the properties of the electromagnetic shower cluster in the calorimeter. The two identification layers of criteria used are *loose* and *tight*. The variables used to discriminate between selections are based on both the shower shape in the electromagnetic calorimeter and the proportion of energy leakage into the hadronic calorimeter. *Loose* and *tight* selections are different for converted and unconverted photons.

As with electrons, photons are required to be isolated in the inner detector and electromagnetic calorimeter. This is in order to distinguish background photons from prompt photons. A cone of size $\Delta R = 0.4$ gives the boundary for the isolation energy calculation of a candidate photon.

4.3 Muons

Muons are identified and reconstructed using three detector systems—namely the inner detector, the calorimeter, and the muon spectrometer [82]. A number of different algorithms combine the information from the three systems using a variety of methods. The primary muon reconstruction methodology, known as the *combined* algorithm, incorporates independently measured track information from the inner detector and muon spectrometer. Muons reconstructed with the segment-tagged algorithm have higher acceptance than combined muons due to the extrapolation from the inner detector to the muon spectrometer only requiring one track segment in the latter apparatus.

Selection criteria for muon candidates includes quality track information found during reconstruction, as well as isolation requirements like those of the electron.

4.4 Jets

Jets are showers of particles produced in a cone-like formation travelling away from the interaction point through the detector. They are created by the fragmentation of quarks and gluons, or electrons and photons. Jets are identified and reconstructed from the combination of energy deposits in the calorimeters and high multiplicity tracks in the inner detector [83]. These energy deposits, known as topological clusters or topo-clusters, are constructed using the topological clustering algorithm. This algorithm identifies the output of hard-scatter physics processes and suppresses background signals resulting from inefficiencies of the detector or pileup. A three-stage classification is used to build the topo-clusters known as the ATLAS 4-2-0 topo-cluster threshold scheme:

1. Seed cells: Calorimeter cells with large relative energies are identified with $E_{\text{cell}} > 4\sigma_{\text{cell}}$, where E_{cell} is the energy of the chosen cell and σ_{cell} is the expected background noise of that cell.

2. Secondary cells: Calorimeter cells adjacent to seed cells or secondary cells that have already been found with an energy of $E_{\text{cell}} > 2\sigma_{\text{cell}}$.

3. Tertiary cells: Calorimeter cells adjacent to seed cells or secondary cells with energy $E_{\text{cell}} > 0$.

The three-dimensional property of this constructuction allows topo-clusters to span across the different calorimeters.

The constructed topo-clusters are calibrated at the electromagnetic scale where electronic signals from the calorimeter are recovered and interpreted into energy values. The actual energy of the shower is then estimated using the energy deposit measurements and the sampling fraction of the calorimeter. Although this scheme is accurate for electromagnetic processes, it has variable efficiency for hadronic processes due to dependencies on other factors. In order to account for these other dependencies, the energies of topo-clusters can be further refined using the local cluster weight (LCW) scheme [84]. This scheme classifies each cluster under electromagnetic-like or hadronic-like showers.

4.4.1 The anti-k_t jet algorithm

Once all jet inputs have been defined, the information gathered from topo-clusters, truth particles, tracks, and other objects is used in a jet-finding algorithm to form jets. The jet-finding methodology used for the vast majority of purposes in ATLAS is the anti-k_t jet algorithm [85]. In this algorithm the distance d_{ij} between jet constituents i and j, and the distance d_{iB} between jet constituent i and the beam, are given by:

$$d_{ij} = \min(k_{ti}^{-2}, k_{tj}^{-2})\frac{\Delta_{ij}^2}{R^2}, \tag{4.1}$$

$$d_{iB} = k_{ti}^{-2}, \tag{4.2}$$

where $\Delta_{ij}^2 = (y_i - y_j)^2 + (\phi_i - \phi_j)^2$ and k_{ti} is the transverse momentum, y_i is the rapidity and ϕ_i is the azimuthal angle of the i^{th} jet constituent. For each constituent, the smallest distance parameter is calculated; if the result is d_{ij}, the i^{th} and j^{th} constituents are grouped, or if d_{iB} is smaller the j^{th} constituent is categorized as an independent jet. This process is repeated from a seed with the highest p_{T} constituent in the event to the one with the lowest.

4.4.2 Jet calibration overview

Jets are subject to a variety of calibration stages in order to account for inefficiencies and known problems in the detector.

The jet origin correction is the first stage of jet calibration. This correction adjusts the direction of the jet to point back to the primary interaction vertex. This is applied before the jet energy scale (JES) calibration due to the dependence on η. As well as affecting the

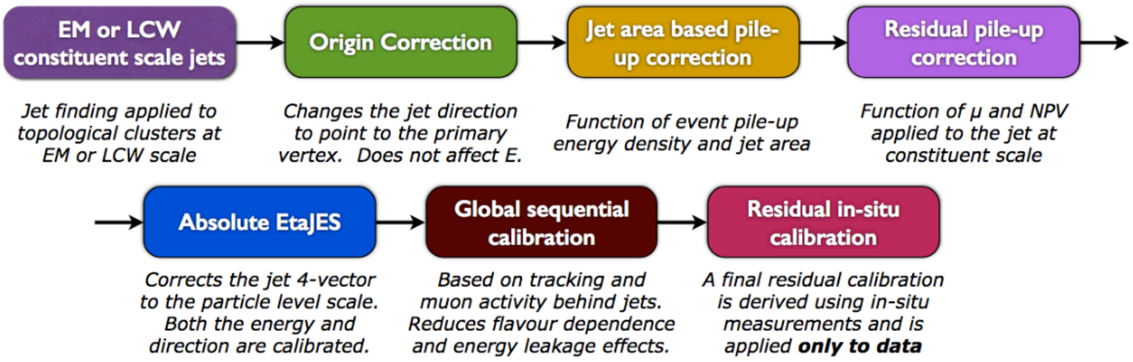

Figure 4.1: Overview of the jet calibration work-flow in ATLAS. Image taken from Reference [86].

jet energy scale calibration, this adjustment significantly improves the jet energy resolution (JER).

Corrections are then implemented to suppress the effect of additional interactions. The contributions from pileup can increase the energy of the jets under scrutiny and also produce additional jet multiplicity. These contributions are corrected for on an event-by-event basis.

Particle-level (truth) jets from MC simulation are used to further calibrate the jet four-vectors. The anti-k_t jet algorithm is used to form particle-level jets from MC samples, only excluding muons and neutrinos. This calibration is produced as a function of the energy of the jet, E_{jet}, and the pseudorapidity η_{det}. It is derived from the relationship between these parameters in the reconstructed (reco) data jet information and the MC simulated truth jet information. The ratio of the jet energy at reco- to truth-level ($E^{\text{reco}}/E^{\text{truth}}$) is known as the jet energy response.

The global sequential calibration is the next stage in the calibration chain and accounts for the variability of jets produced from different sources, namely quark- and gluon-initiated jets. This calibration stage also provides a correction for high-p_{T} jets which *punch-through* the ATLAS apparatus into the muon detector system. It is applied on a jet-by-jet sequential basis, which conserves the overall jet energy.

The last stage in the chain to calibrate jets uses data-driven (in-situ) measurements. These measurements are employed to validate corrections using MC simulated samples and also to produce further corrections to the jet energy scale in data. As transverse momentum must be balanced in an event, any apparent imbalance can be calculated and used with in-situ techniques to find the necessary correction. The first of these is the dijet η-intercalibration in which the comparison of the well-understood central region ($|\eta_{\mathrm{det}}| < 0.8$) jets and forward region ($0.8 < |\eta_{\mathrm{det}}| < 4.5$) is utilized to remove the dependence of the jet response on the pseudorapidity. After the dijet η-intercalibration is applied, the jet energy scale in the central region is calibrated by balancing jets against other objects and jets. Finally, the jet energy resolution correction, which quantifies the precision of the jet energy, is applied. It is calculated for a number of different jet events, including γ-jet and Z-jet events. Chapter 5 further details the jet energy resolution measurement and application.

4.5 Missing transverse momentum

The momentum imbalance in the transverse plane can be measured once all other objects have been identified and reconstructed. The terms $E_{\mathrm{T}}^{\mathrm{miss}}$ and $p_{\mathrm{T}}^{\mathrm{miss}}$ are regularly considered to be synonyms and are referred to in the same context. The missing transverse energy ($E_{\mathrm{T}}^{\mathrm{miss}}$), calculated using the momentum imbalance, indicates the presence of neutrinos, or different weakly- or non-interacting particles. The momentum imbalance is calculated from the negative sum of the momenta of each constituent object of the final state [87, 88]:

$$E_{x(y)}^{\mathrm{miss}} = E_{x(y)}^{\mathrm{miss},e} + E_{x(y)}^{\mathrm{miss},\gamma} + E_{x(y)}^{\mathrm{miss},\tau} + E_{x(y)}^{\mathrm{miss,jets}} + E_{x(y)}^{\mathrm{miss},\mu} + E_{x(y)}^{\mathrm{miss,soft}}, \tag{4.3}$$

where $E_{\mathrm{T}} = \sqrt{(E_x^{\mathrm{miss}})^2 + (E_y^{\mathrm{miss}})^2}$ and $E_{x(y)}^{\mathrm{miss}} = -E_{x(y)}$ for each of the respective calibrated objects. The soft term originates from all the unidentified contributions detected in the inner detector and calorimeters; it is calculated from reconstructed tracks of charged particles associated with the primary vertex in the interaction, but not a specifically defined object.

Chapter 5

Jet energy resolution calibration

A large proportion of ATLAS measurements and searches rely heavily on jets and their accurate reconstruction. Therefore, knowledge of any mismeasurement of jet energy in the calorimeters is vital to allow precise calibration of jet properties to the true values. Both Monte Carlo (MC) simulation and data-driven (in-situ) techniques are implemented to extract these calibrations.

In this chapter, the derivation of the in-situ jet energy resolution calibration for dijet events is presented. The dijet-balance method is described for events produced in the ATLAS detector forward region ($0.8 < |\eta| < 3.2$) relative to a central region ($|\eta| < 0.8$), with a p_{T} of 55–760 GeV. The data used in this study originates from proton-proton collisions at $\sqrt{s} = 13$ TeV recorded by the ATLAS detector during the period 2015–2016. The previous iteration of the dijet jet energy resolution calibration was made public in Reference [89] using 2012 data.

5.1 The dijet-balance method

In dijet events at leading order in QCD the two jets are expected to conserve transverse momentum [90]. Imbalances in p_{T} can be attributed to some regions of the calorimeter responding unexpectedly. This can be a result of incorrect calibration in MC-simulation due to an incomplete description of the ATLAS detector. Specifically, the use of a variety of detector materials and technologies and the complex geometry of the detector affect the resulting value of the energy of a measured jet.

The jet p_{T} imbalance is used in the dijet-balance method to measure the relative response of the calorimeter to jets in a probe region versus those in a reference region, in which the response of the calorimeter is well understood. The dijet-balance can be characterised by the asymmetry of the two jets:

$$\mathcal{A} = \frac{p_{\mathrm{T}}^{\mathrm{probe}} - p_{\mathrm{T}}^{\mathrm{ref}}}{p_{\mathrm{T}}^{\mathrm{avg}}}, \tag{5.1}$$

where $p_{\mathrm{T}}^{\mathrm{probe}}$ is the transverse momentum of a jet in the probe region under investigation, $p_{\mathrm{T}}^{\mathrm{ref}}$ is the transverse momentum of a jet in the reference region, and $p_{\mathrm{T}}^{\mathrm{avg}}$ is the average dijet p_{T}. The full-width-half-maximum (width), $\sigma(\mathcal{A})$, of this asymmetry distribution can be used to determine the jet energy resolution:

$$\sigma(\mathcal{A}^{\mathrm{probe}}) = \frac{\sqrt{\sigma^2(p_{\mathrm{T}}^{\mathrm{ref}}) + \sigma^2(p_{\mathrm{T}}^{\mathrm{probe}})}}{p_{\mathrm{T}}^{\mathrm{avg}}} = \sqrt{\frac{\sigma^2(p_{\mathrm{T}}^{\mathrm{ref}})}{(p_{\mathrm{T}}^{\mathrm{avg}})^2} + \frac{\sigma^2(p_{\mathrm{T}}^{\mathrm{probe}})}{(p_{\mathrm{T}}^{\mathrm{avg}})^2}}, \tag{5.2}$$

where $\sigma(p_{\mathrm{T}}^{\mathrm{probe}})$ and $\sigma(p_{\mathrm{T}}^{\mathrm{ref}})$ are the fractional jet energy resolutions for the jets in the probe and reference regions respectively.

The width is calculated by fitting a Gaussian curve to the core of the asymmetry distribution. The study of the jet energy resolution adopts the reference region of $|\eta_{\mathrm{det}}| < 0.8$ from previous iterations and η-intercalibration methodology. This choice was made in consideration of the tile sampling calorimeter range in the barrel region. It is derived as a function of $p_{\mathrm{T}}^{\mathrm{avg}}$ and η_{det}. For two jets in the reference region, the width can be directly calculated from the fit of the asymmetry distribution:

$$\sigma(\mathcal{A}_{(i,i)}) = \frac{\sqrt{2\sigma^2(p_{\mathrm{T}}^{i})}}{p_{\mathrm{T}}^{\mathrm{avg}}} = \frac{\sqrt{2\sigma^2(p_{\mathrm{T}}^{i})}}{p_{\mathrm{T}}^{i}}, \tag{5.3}$$

where the transverse momentum of the two leading jets can be equated. The jets have previously been calibrated according to the jet energy scale correction factors, and $p_{\mathrm{T}}^{\mathrm{avg}}$ is the average of these. Alternatively, if one of the two jets is outside the reference region, the jet energy resolution is calculated using:

$$\sigma(\mathcal{A}_{(i,j)}) = \sqrt{\frac{\sigma^2(p_{\mathrm{T}}^{\mathrm{ref}})}{(p_{\mathrm{T}}^{\mathrm{ref}})^2} + \frac{\sigma^2(p_{\mathrm{T}}^{\mathrm{probe}})}{(p_{\mathrm{T}}^{\mathrm{probe}})^2}} = \sqrt{\frac{\sigma^2(A_{(i,i)})}{2} + \frac{\sigma^2(p_{\mathrm{T}}^{\mathrm{probe}})}{(p_{\mathrm{T}}^{\mathrm{probe}})^2}}, \tag{5.4}$$

and therefore,

$$\frac{\sigma(p_{\mathrm{T}}^{\mathrm{probe}})}{(p_{\mathrm{T}}^{\mathrm{probe}})} = \sqrt{\sigma^2(\mathcal{A}_{(i,i)}) - \frac{1}{2}\sigma^2(\mathcal{A}_{(i,j)})}. \tag{5.5}$$

The transverse momentum balance in a dijet event can be affected by additional radiation, hadronisation, and particle mis-identification. For each event generator used, particle-level asymmetry distributions are produced and the widths calculated. The detector resolution is derived from subtracting, in quadrature, the weighted average of these particle-level widths from the asymmetry widths of the reconstructed MC-simulated and detector-level data.

5.2 Data selection and Monte Carlo simulation

The dataset used in this calibration is derived from 36.1 fb^{-1} [91] of proton-proton collision data at a centre-of-mass energy of $\sqrt{s} = 13$ TeV recorded by the ATLAS detector from June 2015 to the end of data taking in 2016. All sub-detectors in the ATLAS experiment are required to be fully operational, and events are rejected if data quality issues are present.

Jet triggers in the *central* ($|\eta| \leq 3.2$) and *forward* ($|\eta| > 3.2$) regions of the ATLAS detector are used in a logical-OR combination during event collection. The central and forward trigger are combined to give a design efficiency of > 99 % for selecting dijet events above a $p_{\mathrm{T}}^{\mathrm{avg}}$ threshold. Prescales for the forward jet trigger are typically smaller than those for the central region due to the cross-section of jet production decreasing as a function of η_{det}. Weights are applied to events according to the luminosity and prescale of the trigger. Trigger combinations are used to match trigger decisions. The trigger combinations used for 2015 and 2016 data are given in Table 5.1. For example, the trigger used for jets in the $p_{\mathrm{T}}^{\mathrm{avg}}$ range 175–220 GeV requires at least one reconstructed primary vertex with $p_{\mathrm{T}} > 110$ GeV (HLT_j110) in the central region, or (HLT_j110_320eta490) in the forward region. Any events with incomplete detector information, or corrupted data in the calorimeters, are rejected.

The Monte Carlo samples, which simulate inclusive dijet events, use three event generators: POWHEG+PYTHIA v8.186 [92], SHERPA v2.1 [93], and PYTHIA v8.186 [94].

For the POWHEG+PYTHIA samples, POWHEGBOX v2 [95] is used to simulate next-to-leading order accuracy in perturbative QCD. The initial hard scatter simulation uses the CT10 PDF set [96]. PYTHIA v8.186 showers the dijet events alongside the simulation of additional radiation with the NNPDF2.3lo PDF set [97]. The parameters for this simulation are in accordance with the A14 event tune [98]. PYTHIA v8.186 also simulates the hard scatter for the pure PYTHIA samples using the same PDF set and event tune.

SHERPA v2.1 is used to simulate dijet events for the purpose of studying the systematic uncertainties associated with the event generation. The CT10 PDF set is again used with the dedicated SHERPA event tune.

The energy measured from a hard scattered or reconstructed jet could be altered due to

Average p_{T} (GeV)	Triggers
55–85	HLT_j35 OR HLT_j35_320eta490
85–115	HLT_j60 OR HLT_j60_320eta490
115–145	HLT_j60 OR HLT_j60_320eta490
145–175	HLT_j110 OR HLT_j110_320eta490
175–220	HLT_j110 OR HLT_j110_320eta490
220–270	HLT_j175 OR HLT_j175_320eta490
270–330	HLT_j175 OR HLT_j175_320eta490
330–400	HLT_j260 OR HLT_j260_320eta490
400–525	HLT_j360 OR HLT_j360_320eta490
525–760	HLT_j360 OR HLT_j360_320eta490

Table 5.1: Trigger combination for 25 ns bunch spacing, $\sqrt{s} = 13$ TeV data. HLT_j(p_{T}^{i}) requires a jet with $p_{\mathrm{T}} > p_{\mathrm{T}}^{i}$ GeV in the central region. HLT_j(p_{T}^{i})_320eta490 requires a jet with $p_{\mathrm{T}} > p_{\mathrm{T}}^{i}$ GeV in the forward region.

pileup interactions within the current or neighboring bunch crossing. The effects caused by pileup are modeled using PYTHIA v8.186, according to the distribution expected in the specified period of data taking.

An ATLAS detector simulation in Geant4 [77] is run over the generated events in order to account for the interaction of particles with the detector.

5.3 Derivation of the jet energy resolution correction

In this section, the dijet-balance method is described in order to calculate the jet energy resolution correction. As previously mentioned, the fractional resolutions for three MC-generators, POWHEG+PYTHIA v8.186, SHERPA v2.1, and PYTHIA v8.186, are studied alongside data collected by the ATLAS experiment in 2015 and 2016.

5.3.1 Dijet-balance asymmetry

The asymmetry defined in Equation 5.1 is used as a measure of the imbalance of the two leading jets in a dijet event. A Gaussian fit is applied to the asymmetry distribution, from which the width is calculated to produce the fractional resolution. The asymmetry distributions and Gaussian fits for jets in the reference region with a mid-range transverse momentum ($175 \leq p_{\mathrm{T}}^{\mathrm{avg}} \leq 220$ GeV) are shown in Figure 5.1 for (a) data, and the three MC-simulated samples: (b) POWHEG+PYTHIA, (c) SHERPA, and (d) PYTHIA.

5.3.2 Mismeasured-jet bias studies

Single-jet or multijet events can imitate real dijet events through mismeasurement in the calorimeter, or mis-reconstruction. A fake jet with $p_{\mathrm{T}} > 25$ GeV, which is measured alongside a real jet with approximately equivalent p_{T}, can be reconstructed as a dijet event. A three-jet event may mimic a dijet event if one of the jets is missed; a jet is not reconstructed if the $p_{\mathrm{T}} < 25$ GeV, or if the trajectory is along the beam-line or through a broken region of the detector. A real dijet event can also be missed if the trajectory of either jet follows the beam-line. If there is an excess of such fake or missing jets in a particular region of the calorimeter, a relative difference in the asymmetry distribution can be observed. Figure 5.2 (a) shows how a Gaussian fitting does not capture the true shape of the asymmetry distribution. Extra criteria are implemented to identify and remove this effect as shown in Figure 5.2 (b). The distribution depicts the resulting Gaussian fit after removing reconstructed jets that are not matched to particle-level jets with a cut-off of $\Delta\mathrm{R} < 0.4$.

The difference in the width given in the two figures as σ in pink shows the reduced asymmetry after the extra selection criteria is applied and the fake dijet events are excluded.

5.3.3 Fractional jet energy resolution

The fractional jet energy resolution is calculated from the Gaussian fitting of the asymmetry distributions. Equation 5.3 is used for dijet events where both jets are contained in the reference region ($|\eta| < 0.8$). Equation 5.4 is used for dijet events containing one jet observed in the reference region and the other jet in the event observed in the probe region.

Intrinsic MC-simulated resolution

The intrinsic MC-simulated jet energy resolution is derived directly using the width of a Gaussian fitting to a distribution measuring the asymmetry between particle-level and reconstructed-level jet events. This intrinsic MC-simulated asymmetry is defined by:

$$\mathcal{A}^{\mathrm{MC}} = \frac{p_{\mathrm{T}}^{\mathrm{reco}} - p_{\mathrm{T}}^{\mathrm{truth}}}{p_{\mathrm{T}}^{\mathrm{reco}}}, \tag{5.6}$$

and shown in Figure 5.3 as a function of η_{det} and $p_{\mathrm{T}}^{\mathrm{avg}}$.

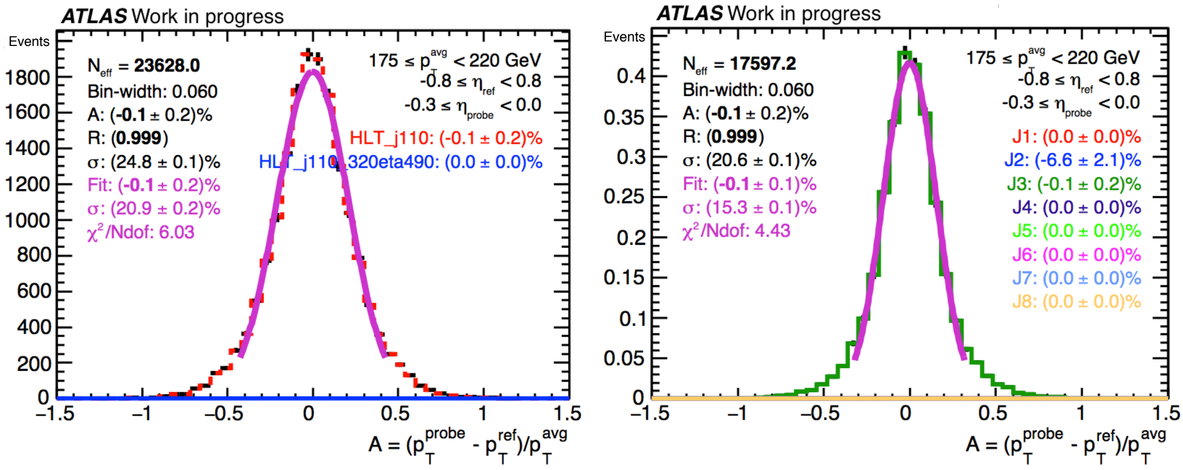

(a) Data 2016

(b) POWHEG+PYTHIA

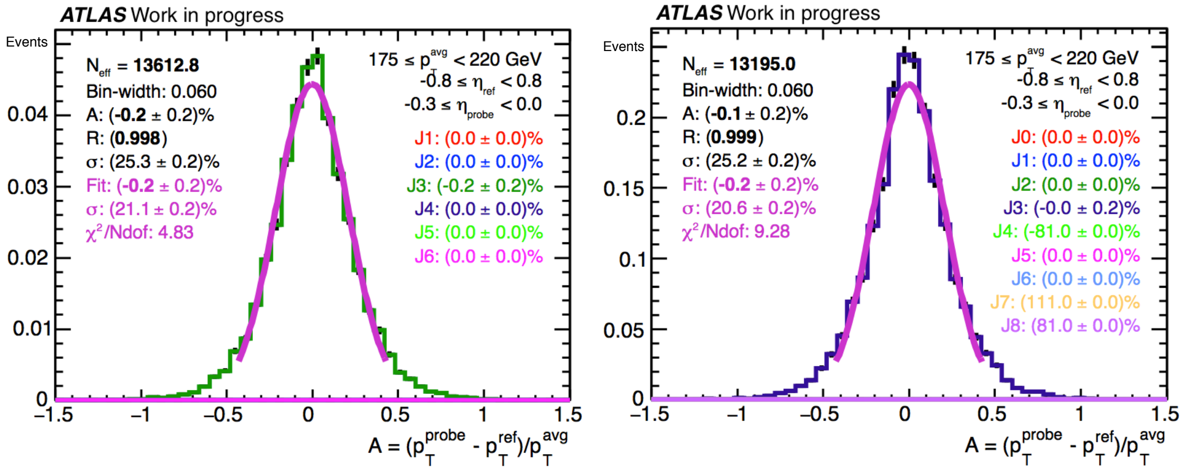

(c) SHERPA

(d) PYTHIA

Figure 5.1: Asymmetry distributions for the two leading jets produced in a dijet event for (a) data, and samples from the event generators: (b) POWHEG+PYTHIA, (c) SHERPA, and (d) PYTHIA. These distributions display the kinematic region: $175 \leq p_{\mathrm{T}}^{\mathrm{avg}} \leq 220$ GeV, $-0.3 \leq \eta_{\mathrm{probe}} \leq 0.0$. The J(1,2,...,etc.) components represent the relative jet slices for the MC distributions. The trigger specifications are displayed for data. The Gaussian fit and the width σ are given in pink.

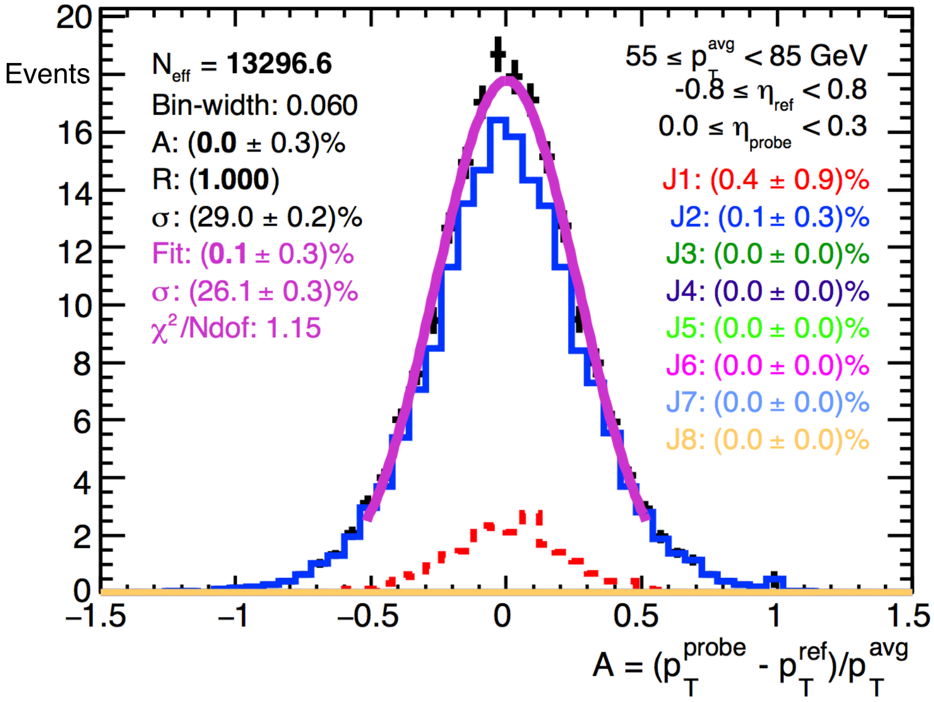

(a) Original

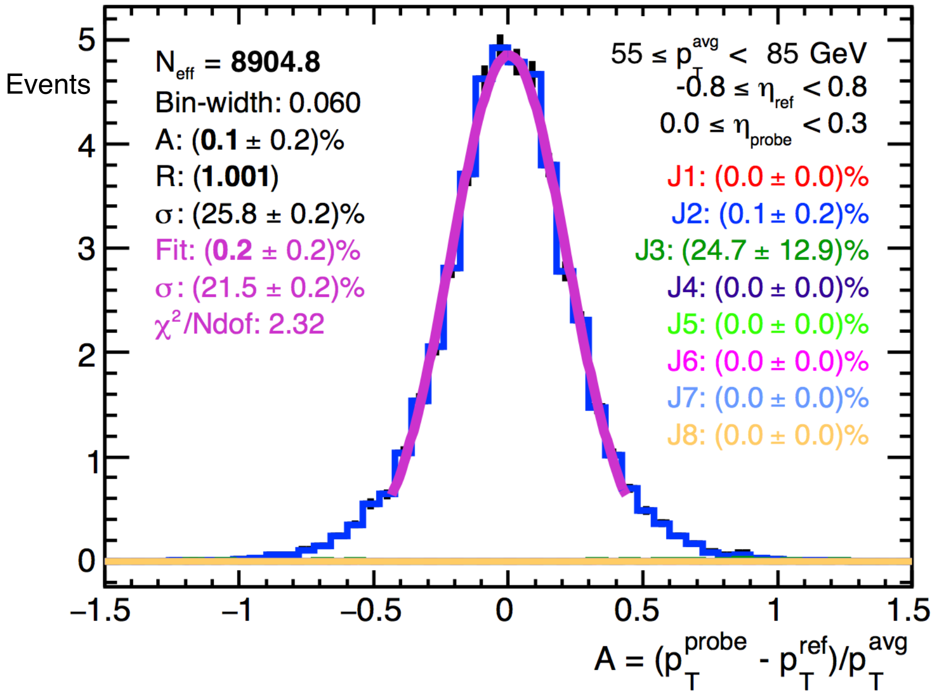

(b) $\Delta R \leq 0.4$

Figure 5.2: Asymmetry distribution for POWHEG+PYTHIA in a problem bin as an example of the non-Gaussian behaviour of some asymmetry distributions being studied: (a) the bin before any restrictions, and (b) the bin once the ΔR-matching on the truth and reconstructed jets is applied.

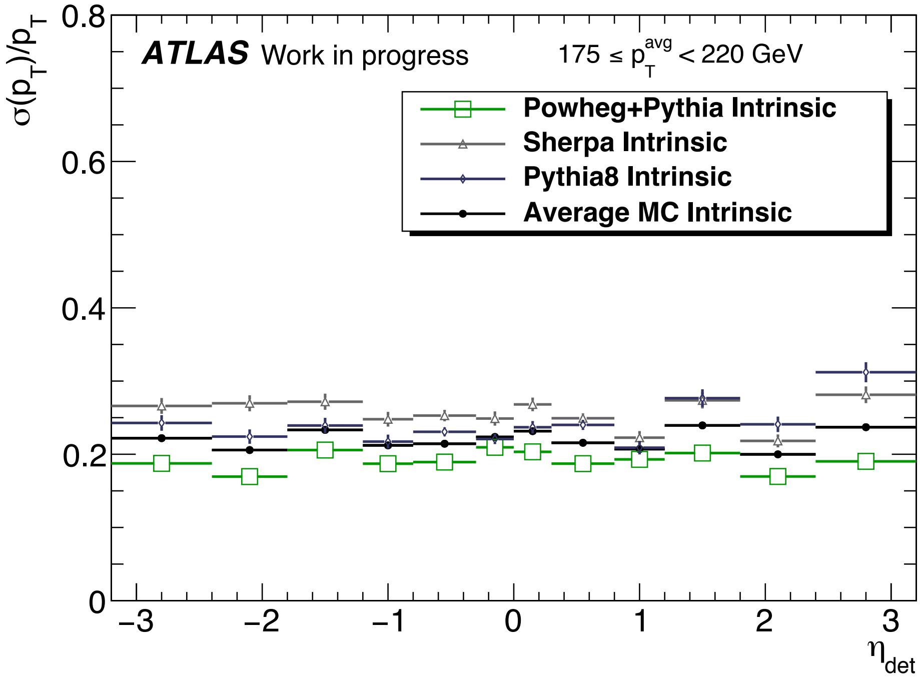

(a)

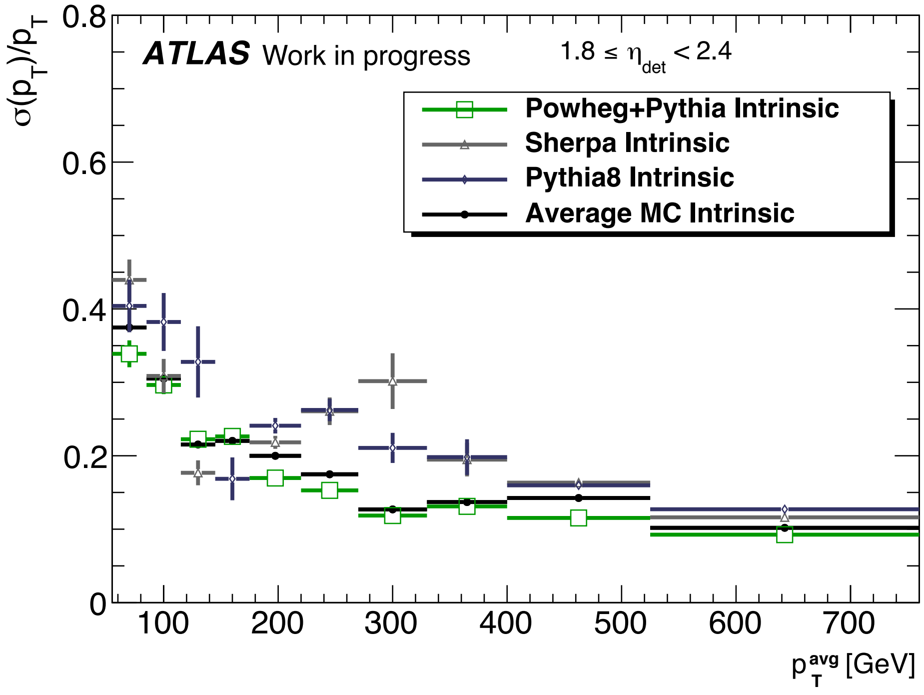

(b)

Figure 5.3: Intrinsic MC-simulated jet energy resolution distributions for an example range of (a) $p_{\mathrm{T}}^{\mathrm{avg}}$, and (b) η_{det}—calculated via Equation 5.6—for event generators: POWHEG+PYTHIA in green, SHERPA in light grey, PYTHIA in dark blue, and the weighted average in black.

Distributions for the three event generators, (green) POWHEG+PYTHIA, (grey) SHERPA, and (dark blue) PYTHIA, are displayed alongside (black) the weighted average of all three. The relative statistical uncertainties are taken into account in the contributions of each generator to the final weighted average. The POWHEG+PYTHIA MC-simulated sample contributes the most to the weighted average due to the low associated statistical uncertainty. The intrinsic MC-simulated jet energy resolution ranges from ~ 0.40 at low $p_{\mathrm{T}}^{\mathrm{avg}}$ to ~ 0.13 at high-$p_{\mathrm{T}}^{\mathrm{avg}}$. This rise at low p_{T} is due to increased difficulty triggering in p_{T} regions more susceptible to pileup. The η_{det} distribution is largely consistent at ~ 0.23 across the range due to the implementation of the jet energy scale calibration. It does, however, rise slightly at high-$|\eta_{\mathrm{det}}|$, due to the poorer understanding and worse tracking performance of those regions.

MC-simulated dijet-balance resolution

The MC-simulated dijet-balance jet energy resolution is defined as the difference between the MC-simulated detector-level and the MC-simulated particle-level fractional resolutions, calculated using:

$$\frac{\sigma(p_{\mathrm{T}}^{\mathrm{MC}})}{p_{\mathrm{T}}^{\mathrm{MC}}} = \sqrt{\frac{\sigma^2(p_{\mathrm{T}}^{\mathrm{reco}})}{(p_{\mathrm{T}}^{\mathrm{reco}})^2} - \frac{\sigma^2(p_{\mathrm{T}}^{\mathrm{truth}})}{(p_{\mathrm{T}}^{\mathrm{truth}})^2}}, \tag{5.7}$$

where $\sigma(p_{\mathrm{T}}^{\mathrm{MC}})/p_{\mathrm{T}}^{\mathrm{MC}}$ is the MC-simulated dijet-balance resolution, $\sigma(p_{\mathrm{T}}^{\mathrm{reco}})/(p_{\mathrm{T}}^{\mathrm{reco}})$ is the MC-simulated detector-level resolution, and $\sigma(p_{\mathrm{T}}^{\mathrm{truth}})/(p_{\mathrm{T}}^{\mathrm{truth}})$ is the MC-simulated particle-level resolution. This comparison accounts and corrects for misidentification during jet reconstruction.

The MC-simulated dijet-balance jet energy resolutions are studied for each of the three event generators: POWHEG+PYTHIA, SHERPA, and PYTHIA. Figure 5.4 displays the distribution for each event generator alongside the weighted average of all three event generators for mid-range example distributions of $p_{\mathrm{T}}^{\mathrm{avg}}$ and η_{det}.

The MC-simulated jet energy resolution calculated using the dijet-balance method is found to be smaller than the intrinsic MC-simulated jet energy resolution at low dijet $p_{\mathrm{T}}^{\mathrm{avg}}$. At higher dijet $p_{\mathrm{T}}^{\mathrm{avg}}$ the two distributions give an approximately consistent result.

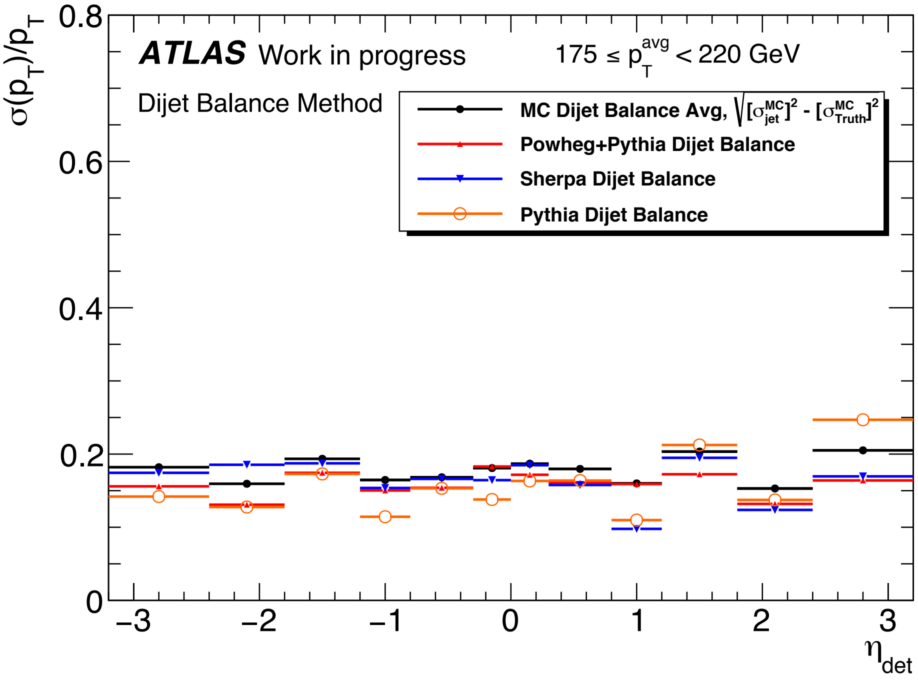

(a)

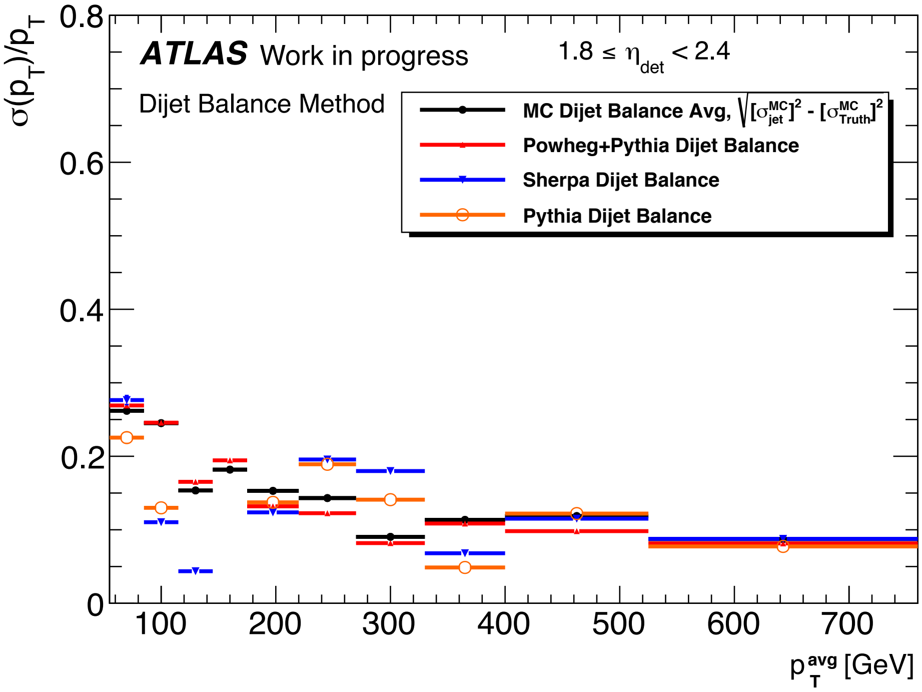

(b)

Figure 5.4: Monte Carlo jet energy resolution calculated using the dijet-balance method for generators: POWHEG+PYTHIA in red, SHERPA in blue, PYTHIA in orange, and the weighted average in black.

5.4 Systematic uncertainties

The systematic uncertainties on the calculated jet energy resolution corrections are evaluated from (i) the uncertainty associated with the modelling of the hadronic activity in dijet events, and (ii) uncertainties raised in the choice of event selection criteria that also impact additional jet emission.

5.4.1 Event generator uncertainties

For the jet energy resolution calibration calculated using 2015 and 2016 data the three event generators used are POWHEG+PYTHIA v8.186, PYTHIA v8.186 and SHERPA v2.1. The former two generators are chosen to evaluate the physics modelling uncertainty for dijet events; the latter generator is chosen as it models the third jet at leading order and so reduces the associated uncertainties.

As detailed previously in Section 5.1, the jet energy resolution in data is determined by subtracting, in quadrature, the weighted average MC-simulated particle-level fractional resolution from the fractional resolution measured at detector-level in data.

The systematic uncertainty associated with the spread of the individual MC-generator particle-level resolutions is evaluated as the root-mean-square difference between the weighted and non-weighted average of the particle-level distributions. This source of uncertainty, displayed in orange in Figure 5.5, is typically quite low at around 0.04, and reaches only 0.09 at low-$p_{\mathrm{T}}^{\mathrm{avg}}$. However, this is relatively high when compared with the previous iteration of this calculation of 0.02 [89].

The impact of implementing the dijet-balance method is evaluated via the non-closure, or quadratic difference, of the simulated dijet-balance jet energy resolution and the intrinsic MC-simulated resolution. Figure 5.6 shows the non-closure to be typically about 0.03, reaching ~ 0.12 in some low-$p_{\mathrm{T}}^{\mathrm{avg}}$ regions.

Some minor theoretical uncertainties are expected from GEANT4 when modelling hadronic physics associated with jet production. However, as part of the intention with this study is to investigate the problems with the entire simulation process, these uncertainties have not been added to avoid double-counting.

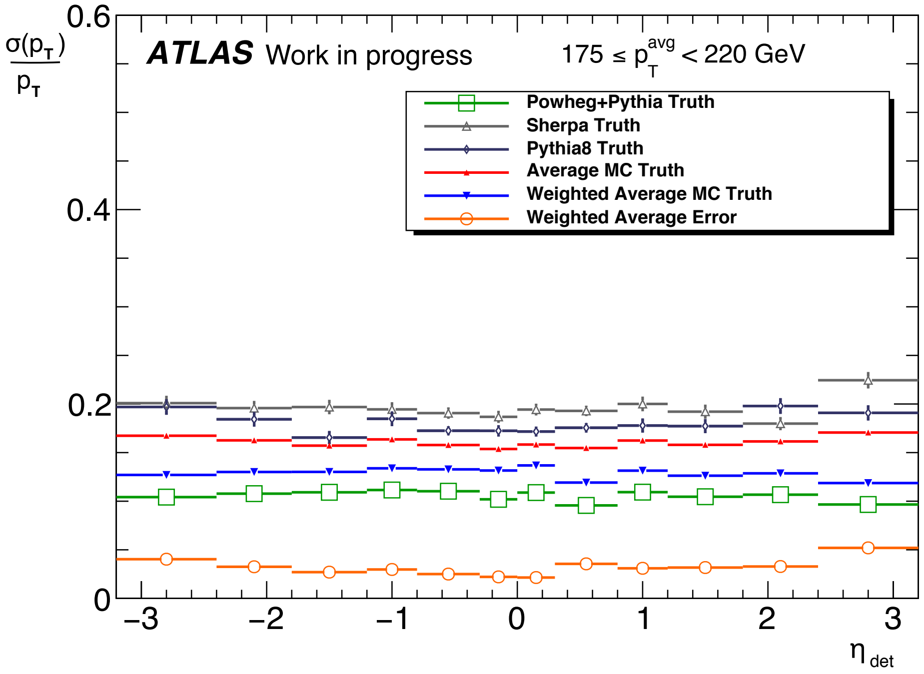

(a)

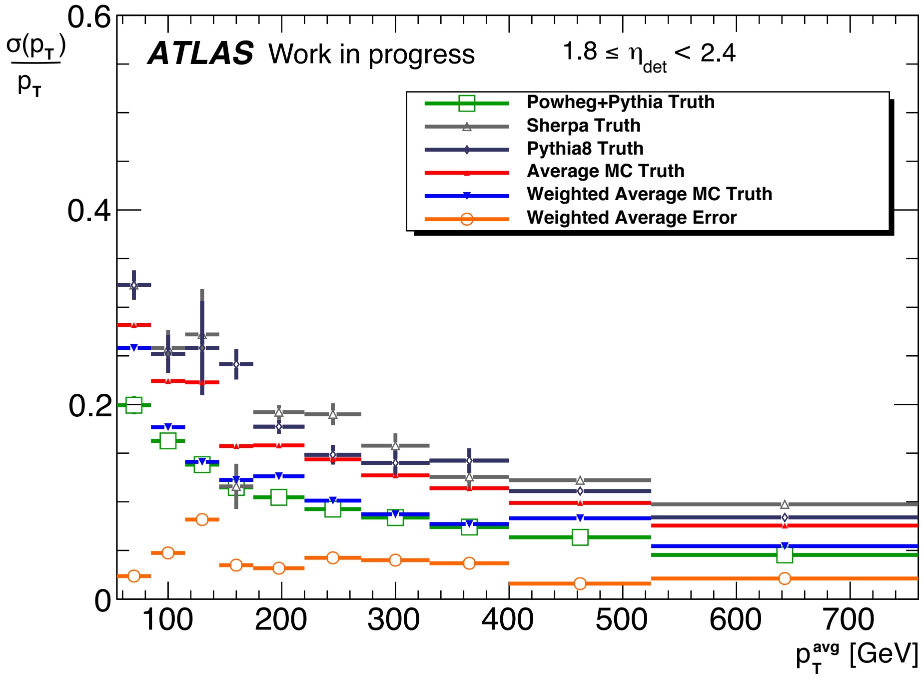

(b)

Figure 5.5: Systematic uncertainty arising from the spread of the three MC-simulated particle-level resolutions when calculating the jet energy resolution from data using the dijet-balance method.

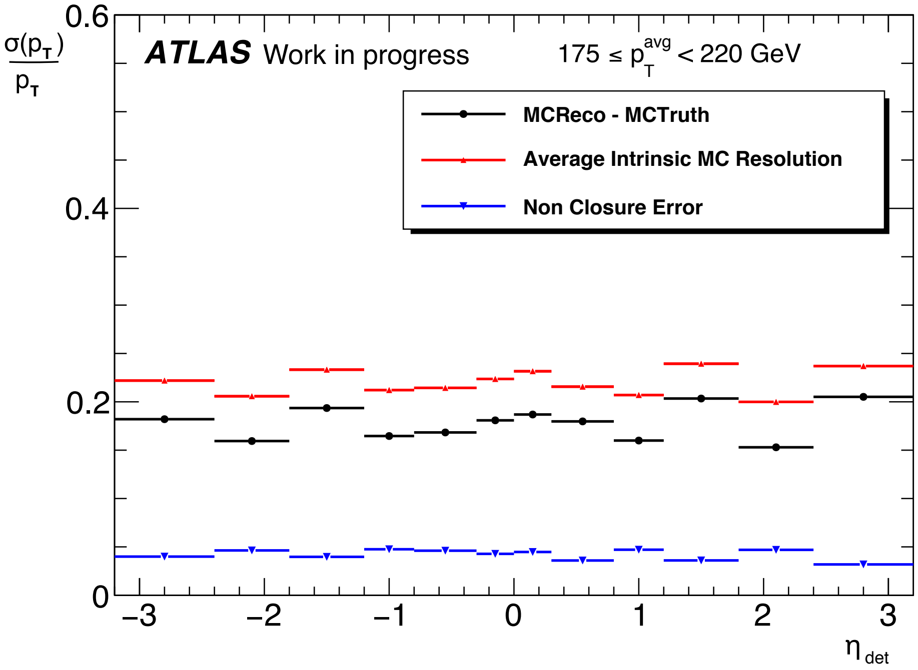

(a)

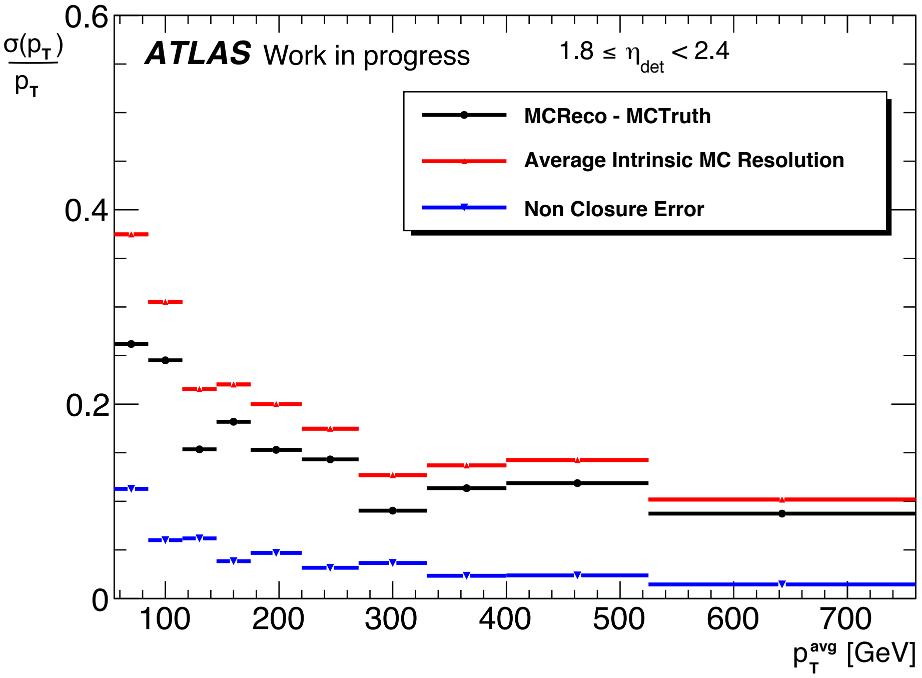

(b)

Figure 5.6: Non-closure of the intrinsic MC-simulated jet energy resolution and the MC-simulated jet energy resolution calculated using the dijet-balance method.

Source of uncertainty	Nominal cut	Shifted cut	Average deviation of $\sigma(p_{\mathrm{T}})/p_{\mathrm{T}}$
JVT (tight)	> 0.59	> 0.92	0.01
$\Delta\phi_{jj}$ (loose)	< 2.5	< 2.8	0.005
$\Delta\phi_{jj}$ (tight)	< 2.5	< 2.2	0.008
3rd jet p_{T} (loose)	$> 0.4p_{\mathrm{T}}^{\mathrm{avg}}$	$> 0.5p_{\mathrm{T}}^{\mathrm{avg}}$	0.06
3rd jet p_{T} (tight)	$> 0.4p_{\mathrm{T}}^{\mathrm{avg}}$	$> 0.3p_{\mathrm{T}}^{\mathrm{avg}}$	0.02

Table 5.2: Summary of the experimental systematic uncertainties in the jet energy resolution calibration.

5.4.2 Experimental uncertainties

Experimental sources of uncertainty also contribute to the final determination of the systematic uncertainties. They arise from the implementation of event selections and are determined by the response of the distribution from the nominal when looser and tighter selections are applied. Table 5.2 displays these sources, the original and shifted selections, and the effective deviation from nominal. An envelope is taken of all the experimental uncertainties for the final value for this source.

The jet vertex tagger (JVT) is required in order to suppress pileup in the jets. The effect of this suppression is investigated by applying a tighter selection of 0.92, oppose to the original 0.59. The impact of additional parton radiation can be assessed by varying the azimuthal angle between the two leading jets. This is because the nominal $\Delta\phi_{jj}$ selection requires that the two leading jets are approximately back-to-back ($\Delta\phi_{jj} < 2.5$). The third jet p_{T} selection ensures that a third jet with significant p_{T}, $p_{\mathrm{T}}^{\mathrm{jet}_3} > 0.4p_{\mathrm{T}}^{\mathrm{avg}}$, is rejected. Figure 5.7 shows the extent of the effect of the experimental systematic uncertainties on the final uncertainties. The envelope is taken as the largest error for each range; for most bins, the 3rd jet p_{T} cut is the largest source of uncertainty.

Jet energy resolution in data

The jet energy resolution in data is derived following the same method as that for generated events, where the MC-simulated detector-level resolution is exchanged for measured data at detector-level, as shown in Figure 5.8. The resolutions in data are calculated by subtracting the weighted average of the three MC-simulated particle-level resolutions from the detector-level data.

The final jet energy resolution in data ranges from ~ 0.40 at low dijet $p_{\mathrm{T}}^{\mathrm{avg}}$ down to

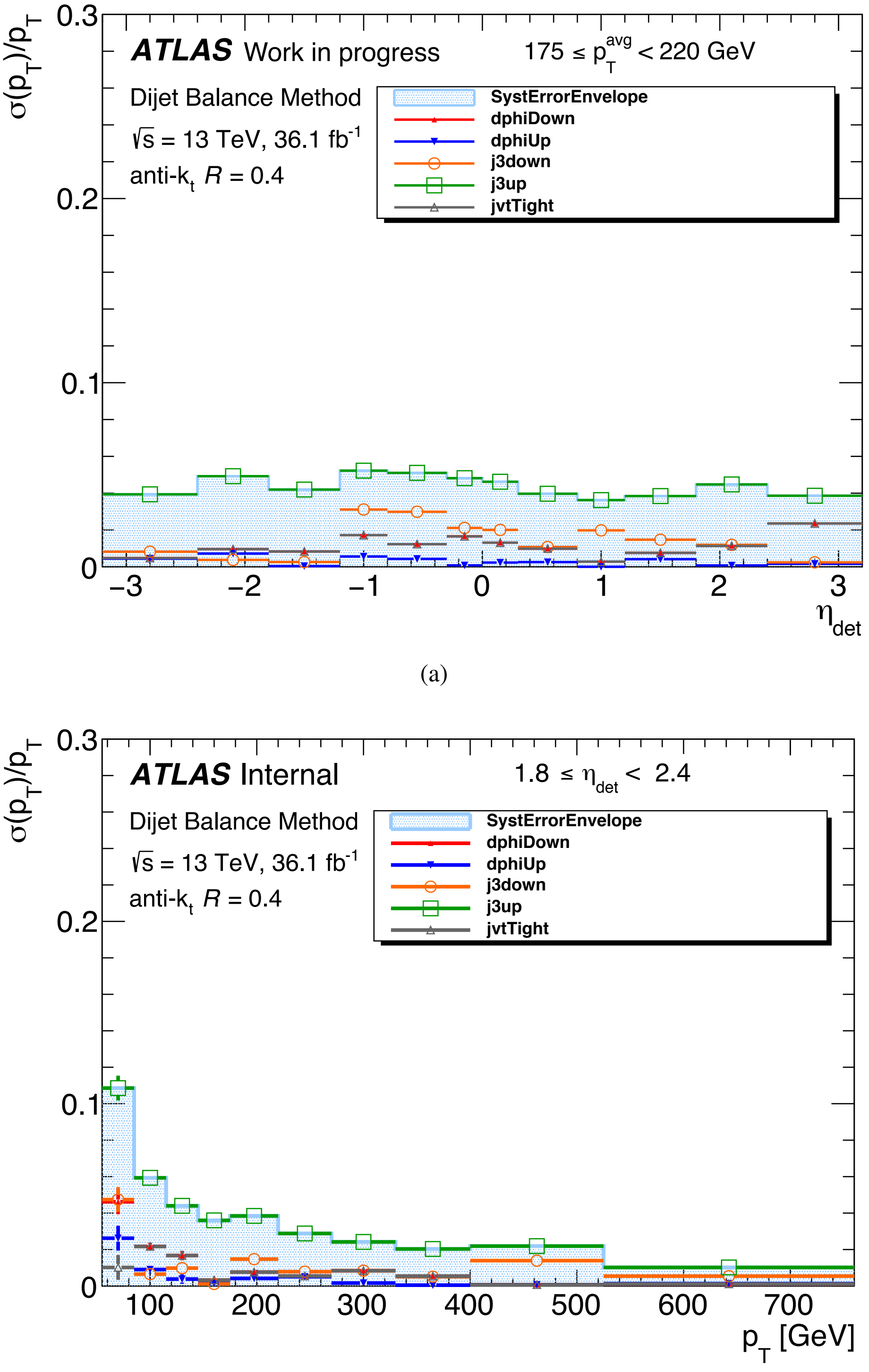

(a)

(b)

Figure 5.7: Experimental systematic uncertainties arising from: (grey) a jet vertex tagger cut, (red & blue) a $\Delta\phi_{jj}$ cut, and (orange & green) a $p_{\mathrm{T}}^{\mathrm{jet}_3}$ cut.

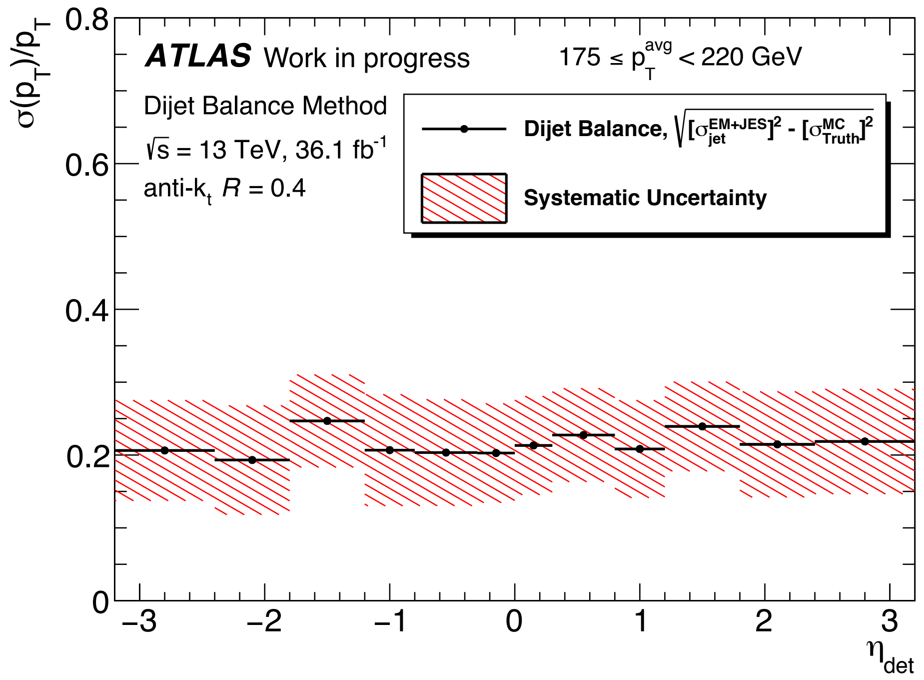

(a)

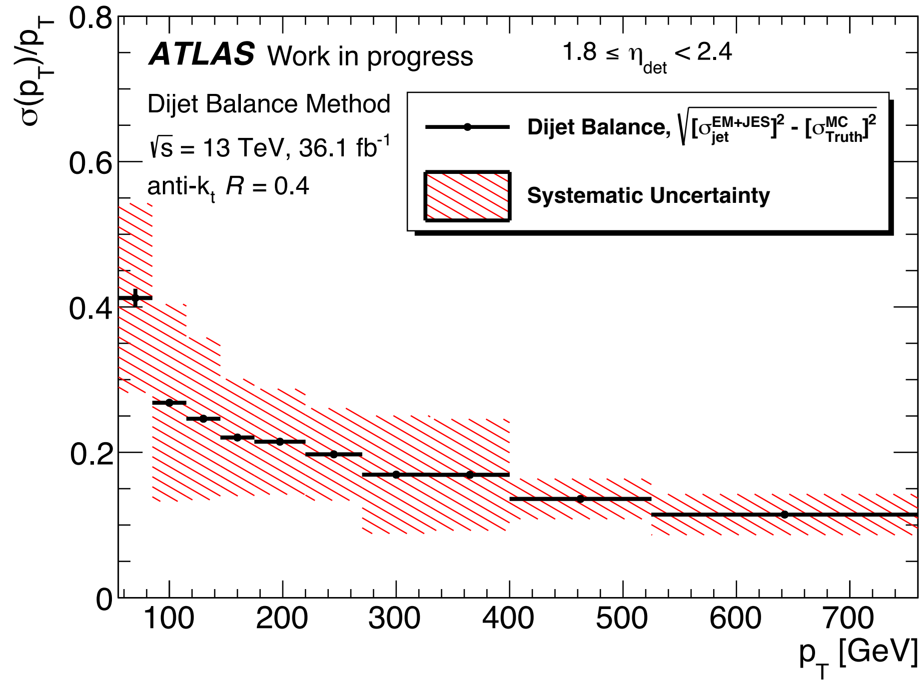

(b)

Figure 5.8: Jet energy resolution calculated using the dijet-balance method with data and particle-level distributions from three MC event generators.

~ 0.15 at higher dijet $p_{\mathrm{T}}^{\mathrm{avg}}$ as shown in Figure 5.8 for a range of $175 \leq p_{\mathrm{T}}^{\mathrm{avg}} \leq 220$ GeV and $1.8 \leq \eta_{\mathrm{det}} < 2.4$.

5.5 Final jet energy resolution correction for dijet events

The measured jet energy resolution is shown in Figures 5.9–5.19 as a function of $p_{\mathrm{T}}^{\mathrm{avg}}$ and η_{det} for electromagnetic jets that are corrected according to the jet energy scale calibration. The results are presented for the dijet-balance method alongside the intrinsic simulation resolution, which is in agreement and shown in blue. The intrinsic MC-simulated jet energy resolution is derived by matching particle- and detector-level jets, and is given by the width of the Gaussian fit to the asymmetry distribution, calculated using Equation 5.6. All distributions investigated are shown here.

5.6 Summary

This chapter describes studies of the in-situ calibration of the jet energy resolution for dijet events measured in the forward region of the ATLAS calorimeter. This calibration is evaluated using the dijet-balance method with $36.1\,\mathrm{fb}^{-1}$ of $\sqrt{s} = 13$ TeV proton-proton data, recorded in 2015 and 2016 with a bunch rate of 40 MHz. It is determined to account for effects not seen in the MC-simulation of reconstructed dijet events in the forward region. The jet energy resolution calibration for dijet events in data is calculated to reside in the range 0.15 to 0.4. This value varies as a function of the transverse momentum and pseudorapidity of the jet. The resolution in data is consistent with the jet energy resolution observed in MC-simulated samples within systematic uncertainties. Previous measurements are slightly lower at around a maximum of 0.15 as shown in Figure 5.20 [89]. The uncertainties on these calibration factors have been evaluated and are typically 0.05, but reach 0.12 at low-$p_{\mathrm{T}}^{\mathrm{avg}}$. The dominant systematic uncertainty associated with this calibration is due to the modelling of the dijet-balance methodology in the MC-simulated resolution. The use of MC-generators at next-to-leading order could improve upon this result in the future as it would provide a better description of the third leading jet.

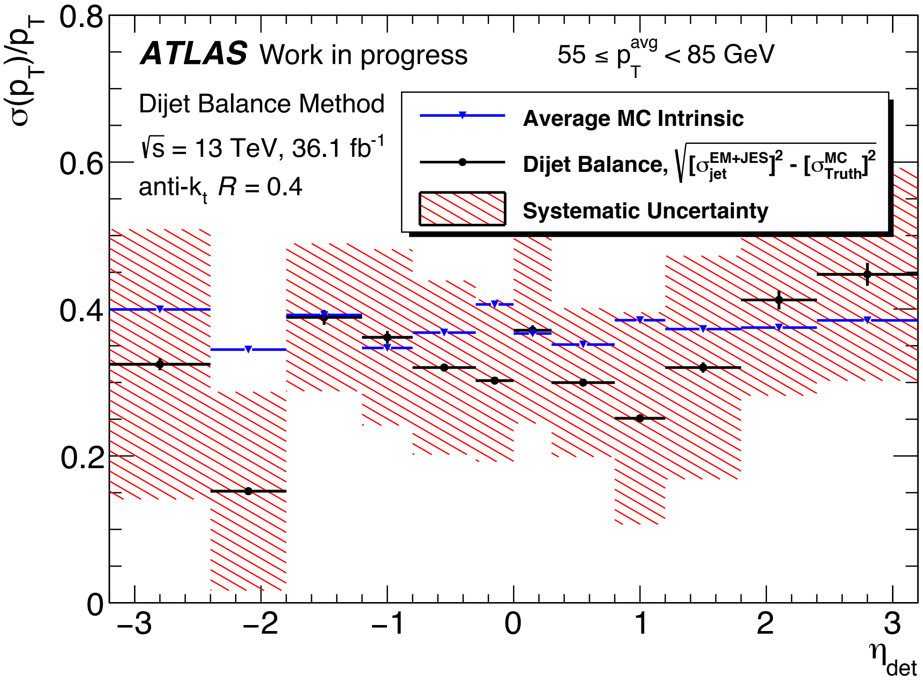

(a)

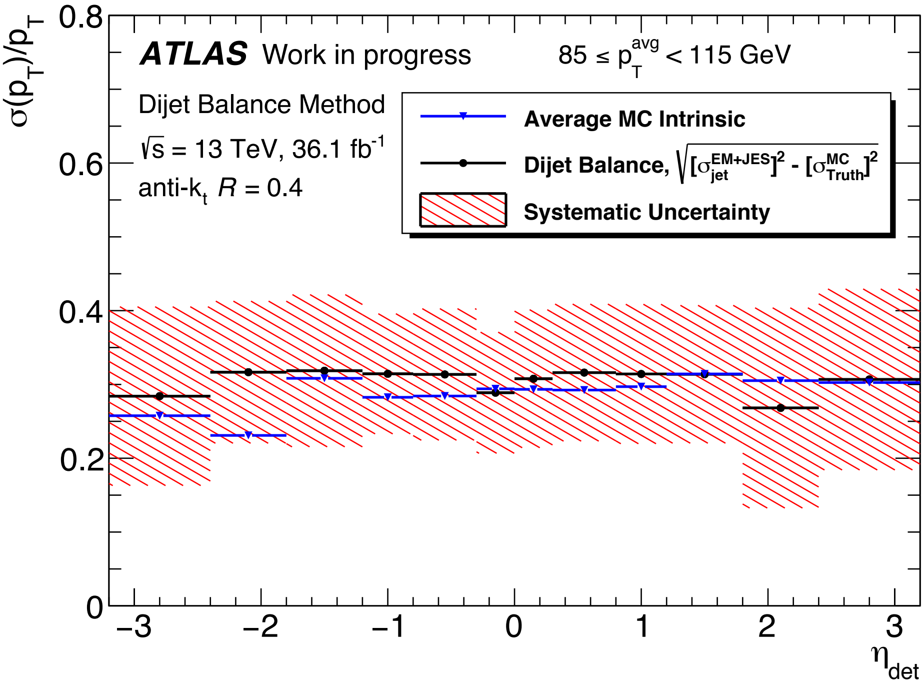

(b)

Figure 5.9: Jet energy resolution calculated using the dijet-balance method with data and the particle-level fractional resolution distributions from the weighted average of three MC event generators for the average transverse momentum ranges: 55 to 85 GeV and 85 to 115 GeV. The intrinsic Monte Carlo jet energy resolution is shown in blue for comparison.

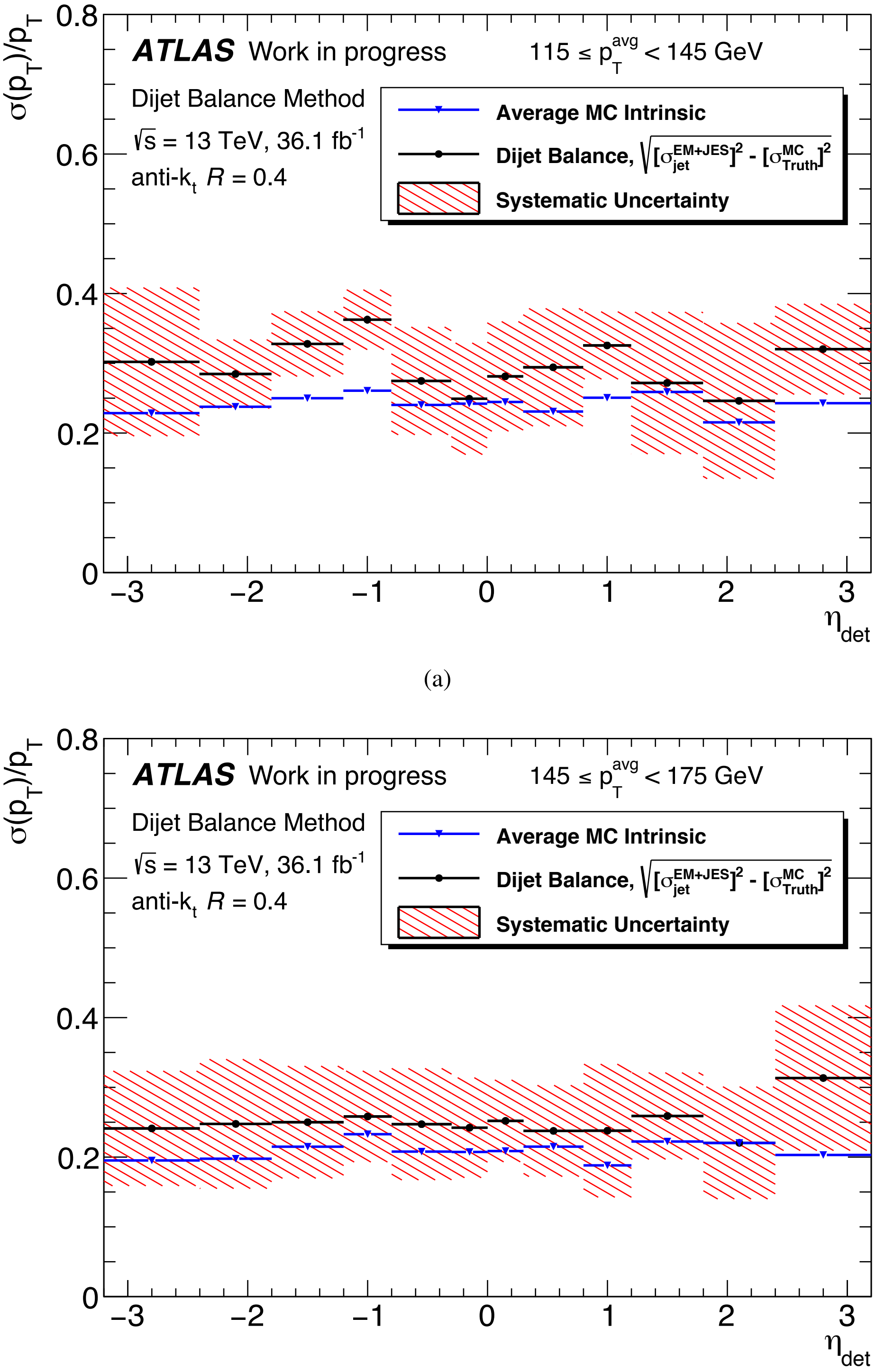

(a)

(b)

Figure 5.10: Jet energy resolution calculated using the dijet-balance method with data and the particle-level fractional resolution distributions from the weighted average of three MC event generators for the average transverse momentum ranges: 115 to 145 GeV and 145 to 175 GeV. The intrinsic Monte Carlo jet energy resolution is shown in blue for comparison.

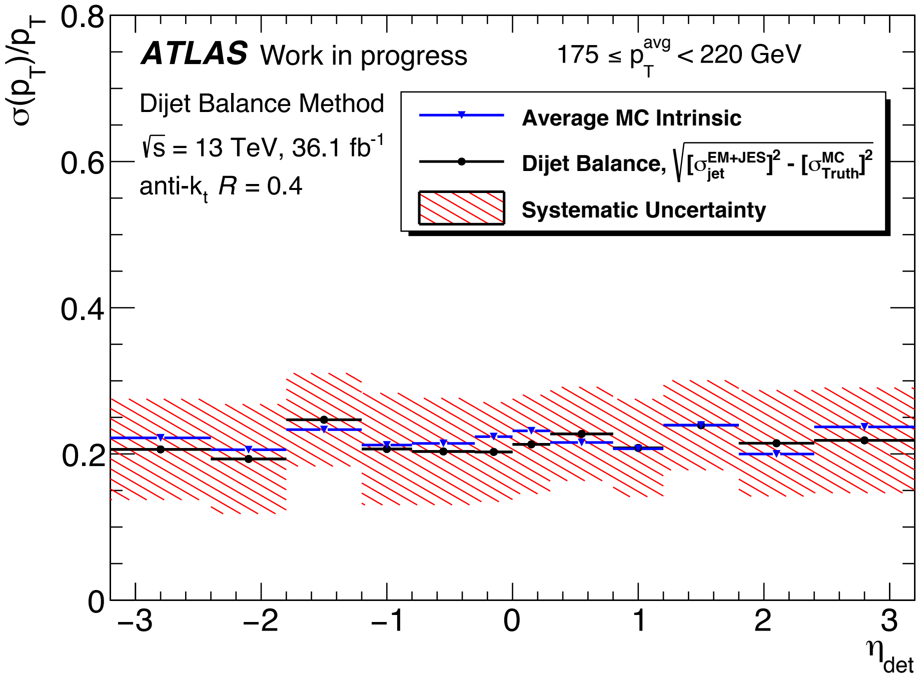

(a)

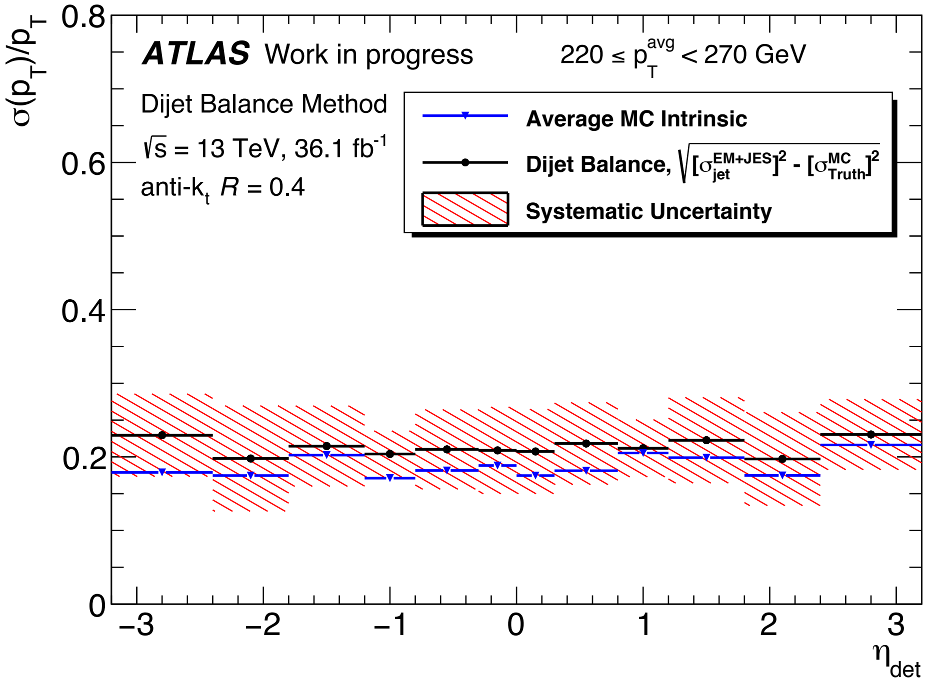

(b)

Figure 5.11: Jet energy resolution calculated using the dijet-balance method with data and the particle-level fractional resolution distributions from the weighted average of three MC event generators for the average transverse momentum ranges: 175 to 220 GeV and 220 to 270 GeV. The intrinsic Monte Carlo jet energy resolution is shown in blue for comparison.

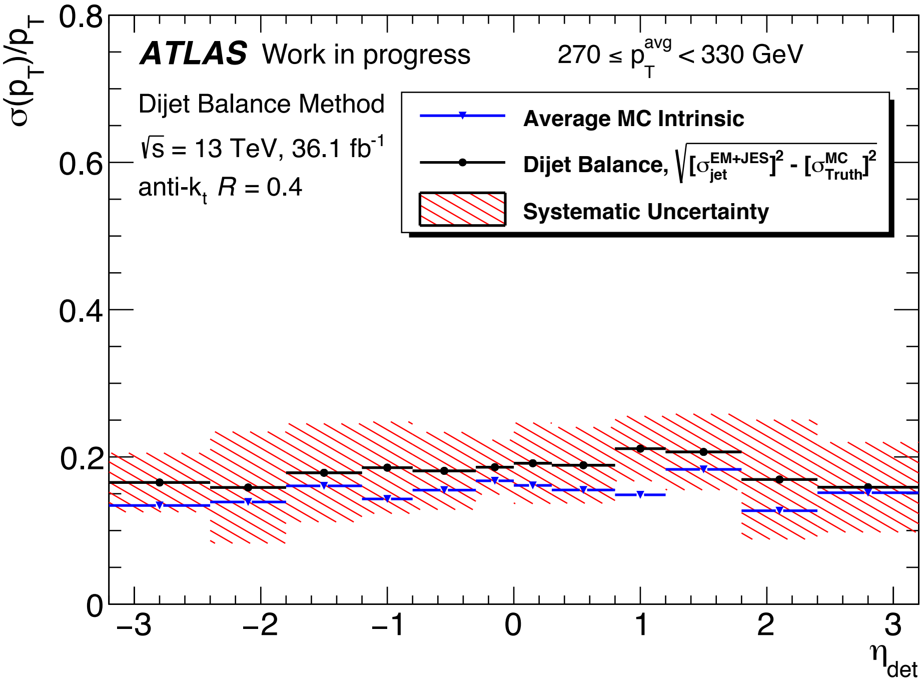

(a)

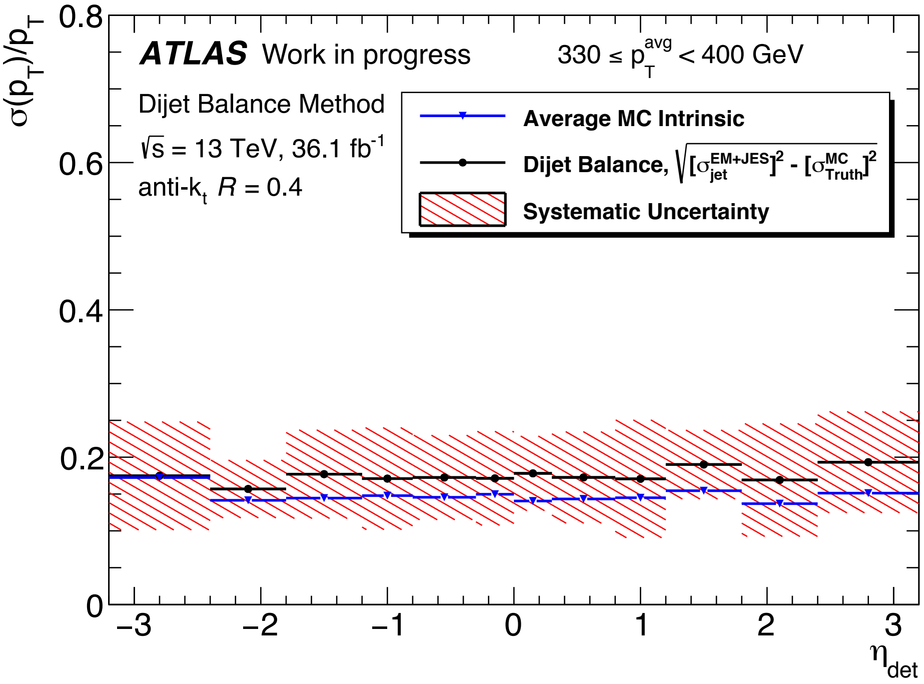

(b)

Figure 5.12: Jet energy resolution calculated using the dijet-balance method with data and the particle-level fractional resolution distributions from the weighted average of three MC event generators for the average transverse momentum ranges: 270 to 330 GeV and 330 to 400 GeV. The intrinsic Monte Carlo jet energy resolution is shown in blue for comparison.

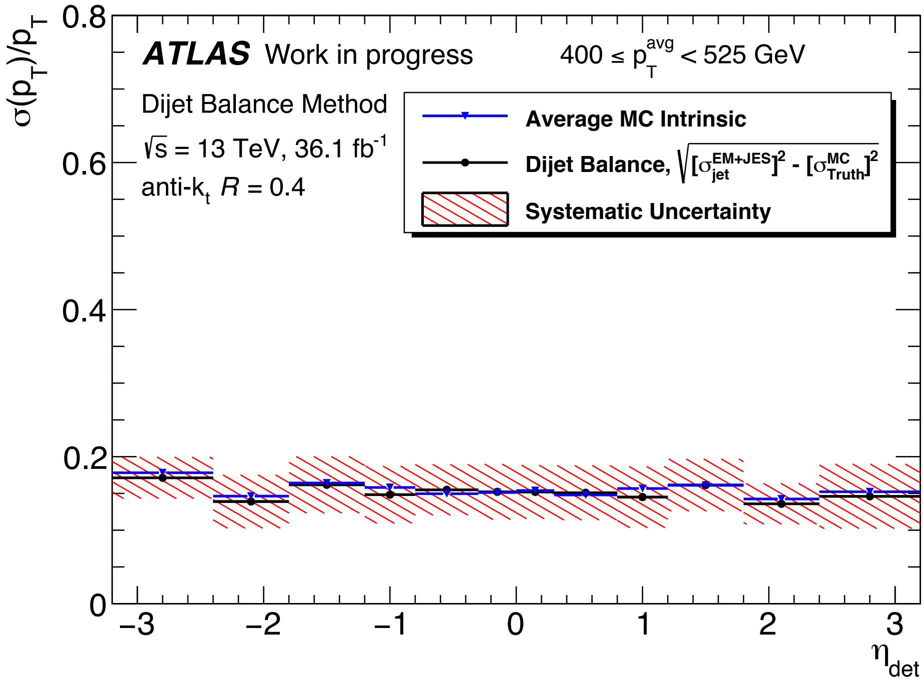

(a)

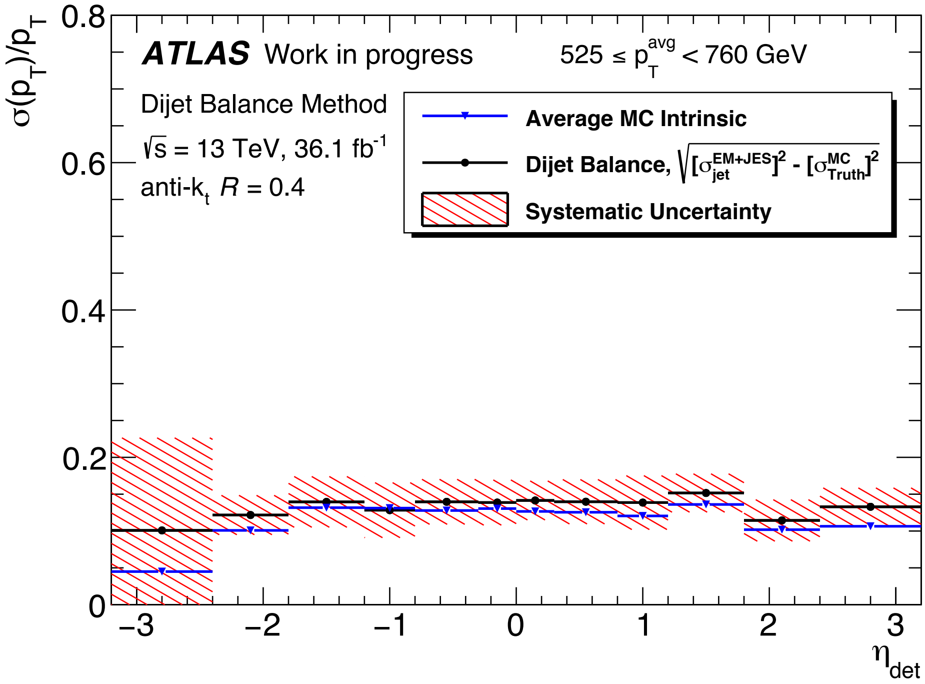

(b)

Figure 5.13: Jet energy resolution calculated using the dijet-balance method with data and the particle-level fractional resolution distributions from the weighted average of three MC event generators for the average transverse momentum ranges: 400 to 525 GeV and 525 to 760 GeV. The intrinsic Monte Carlo jet energy resolution is shown in blue for comparison.

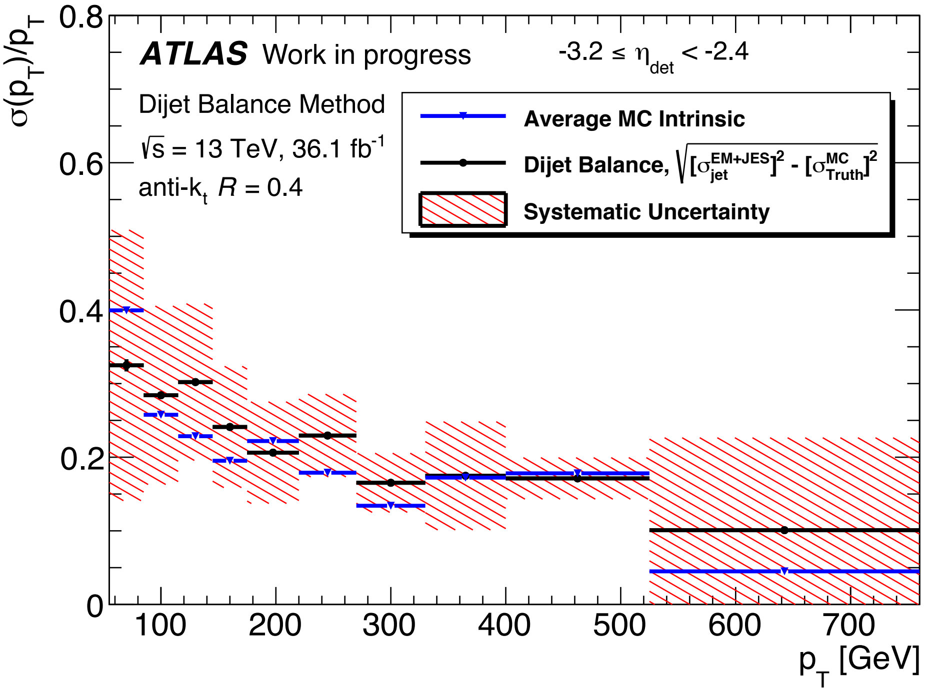

(a)

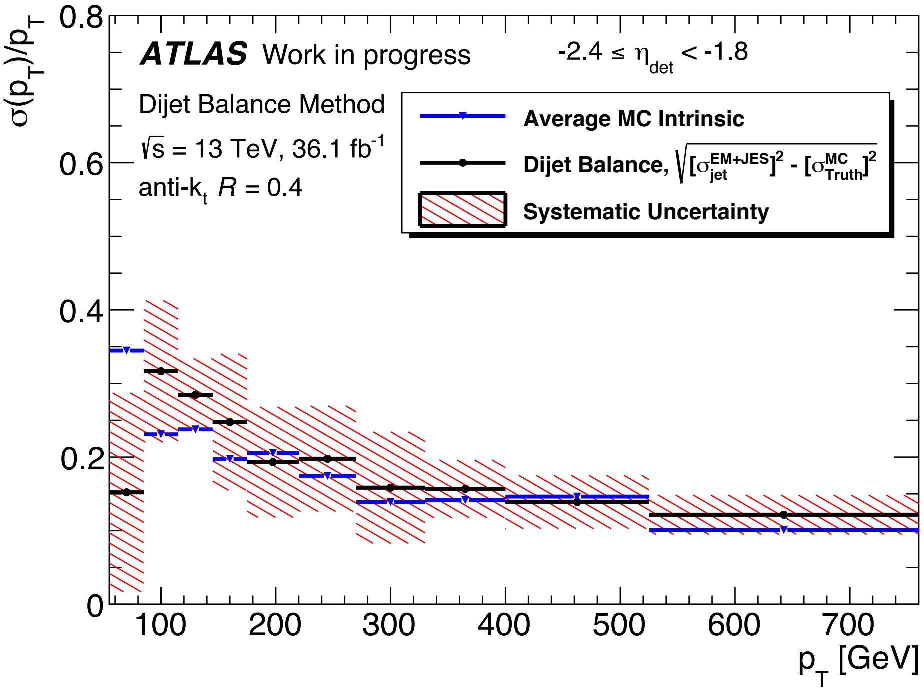

(b)

Figure 5.14: Jet energy resolution calculated using the dijet-balance method with data and the particle-level fractional resolution distributions from the weighted average of three MC event generators for the detector η ranges: -3.2 to -2.4 and -2.4 to -1.8. The intrinsic Monte Carlo jet energy resolution is shown in blue for comparison.

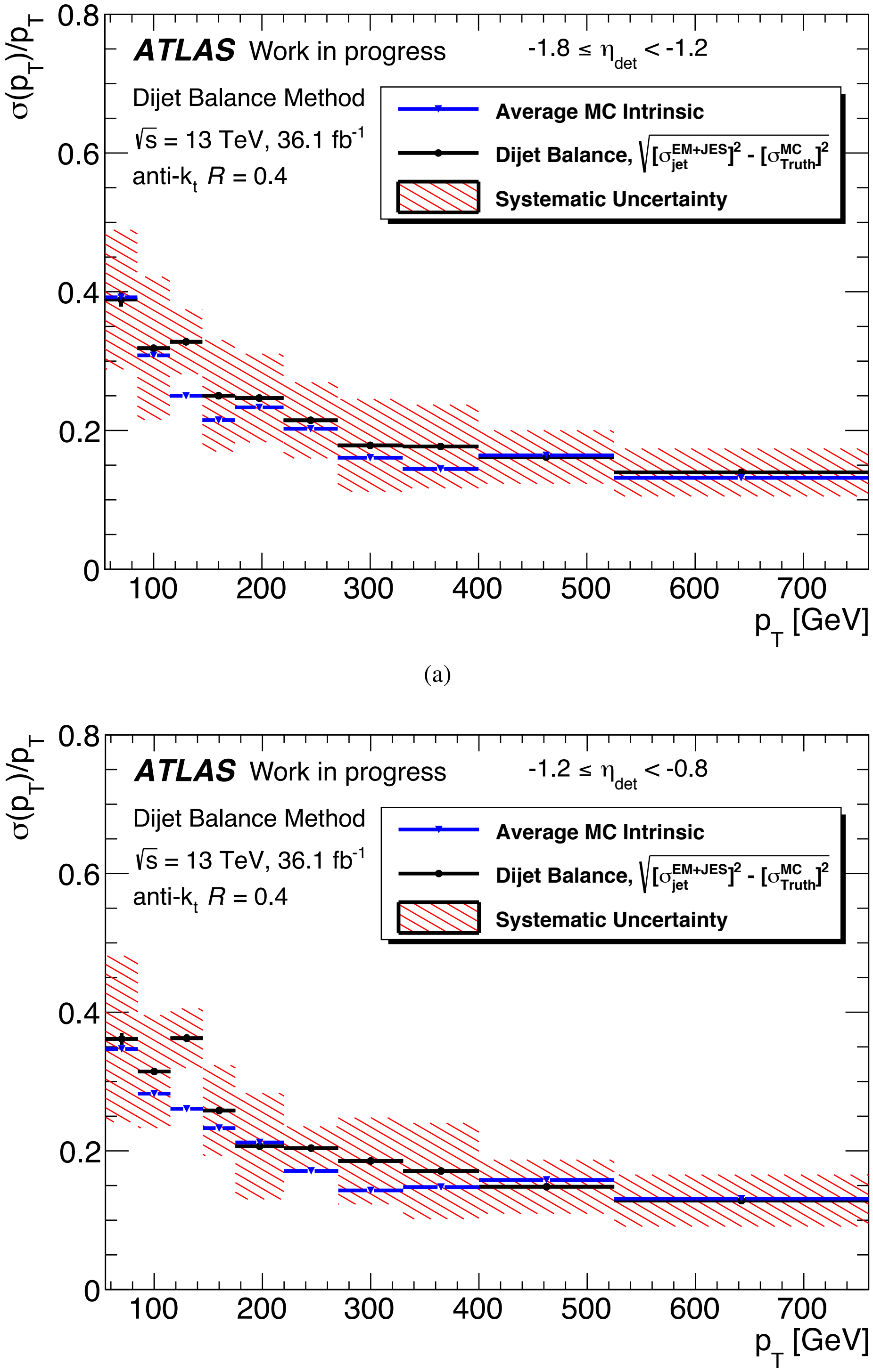

(a)

(b)

Figure 5.15: Jet energy resolution calculated using the dijet-balance method with data and the particle-level fractional resolution distributions from the weighted average of three MC event generators for the detector η ranges: -1.8 to -1.2 and -1.2 to -0.8. The intrinsic Monte Carlo jet energy resolution is shown in blue for comparison.

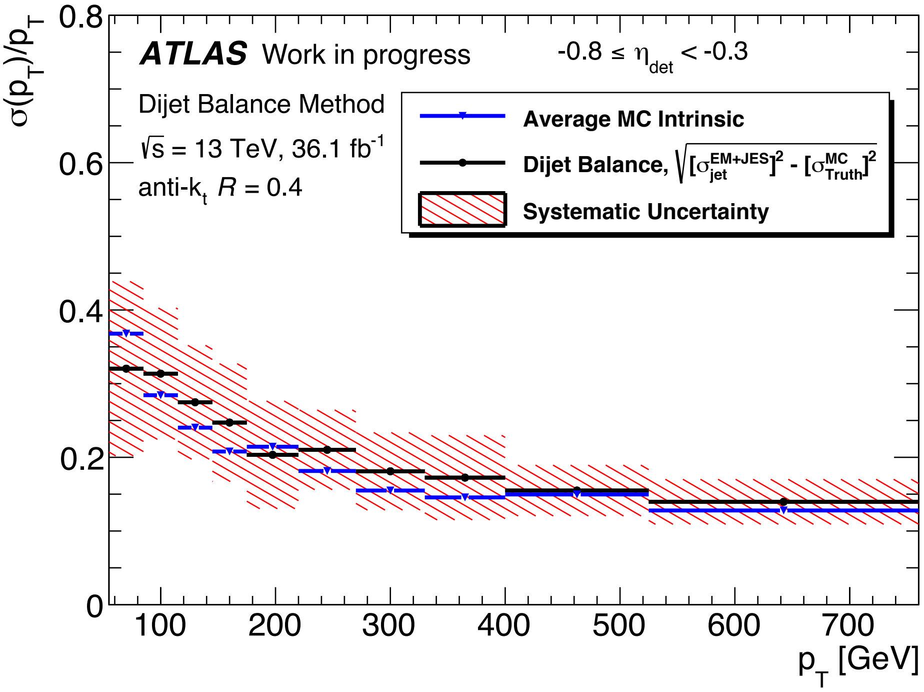

(a)

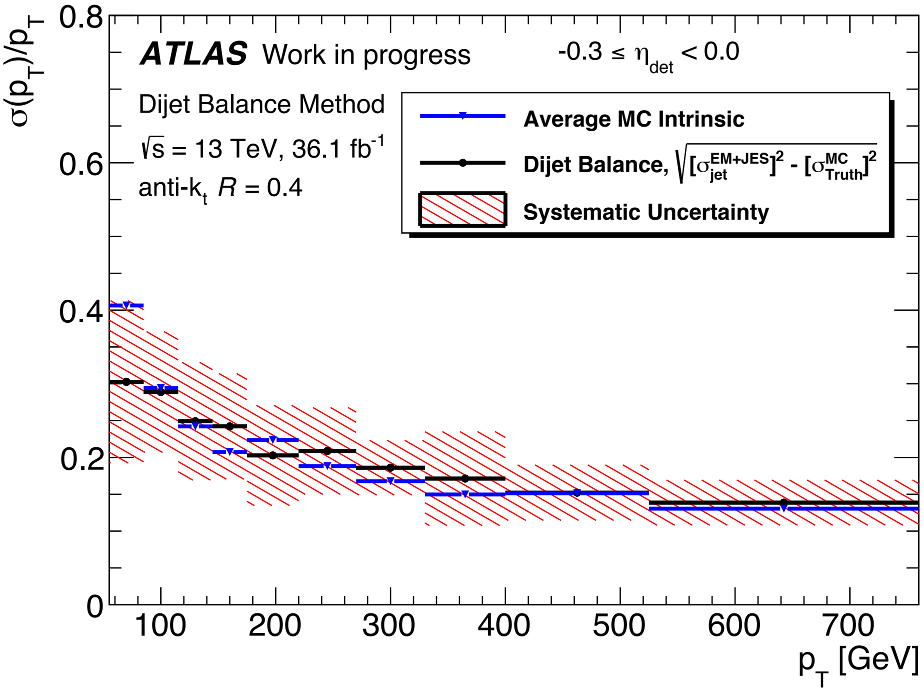

(b)

Figure 5.16: Jet energy resolution calculated using the dijet-balance method with data and the particle-level fractional resolution distributions from the weighted average of three MC event generators for the detector η ranges: -0.8 to -0.3 and -0.3 to 0.0. The intrinsic Monte Carlo jet energy resolution is shown in blue for comparison.

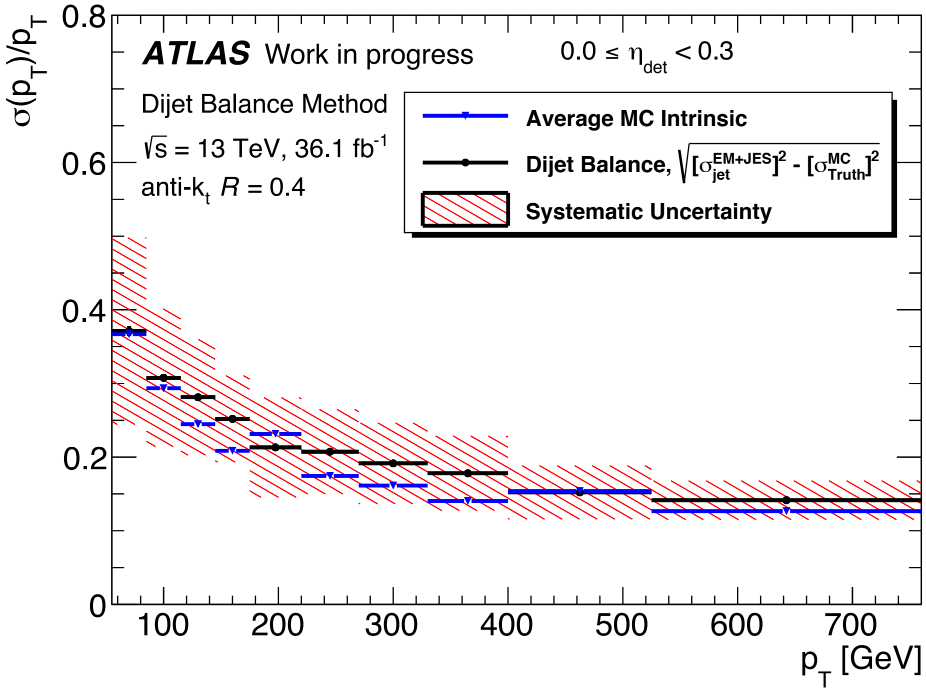

(a)

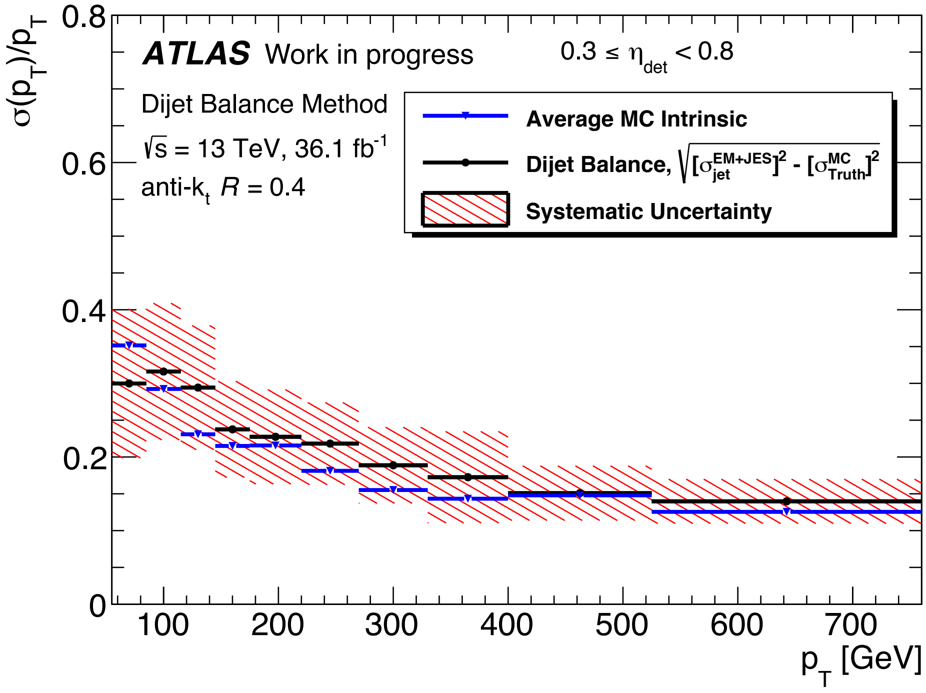

(b)

Figure 5.17: Jet energy resolution calculated using the dijet-balance method with data and the particle-level fractional resolution distributions from the weighted average of three MC event generators for the detector η ranges: 0.0 to 0.3 and 0.3 to 0.8. The intrinsic Monte Carlo jet energy resolution is shown in blue for comparison.

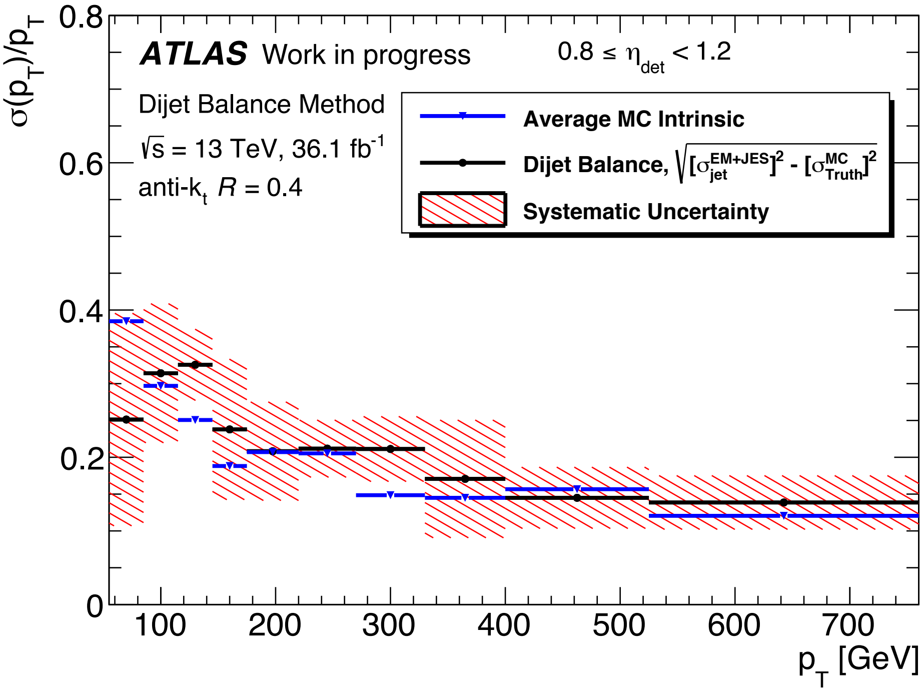

(a)

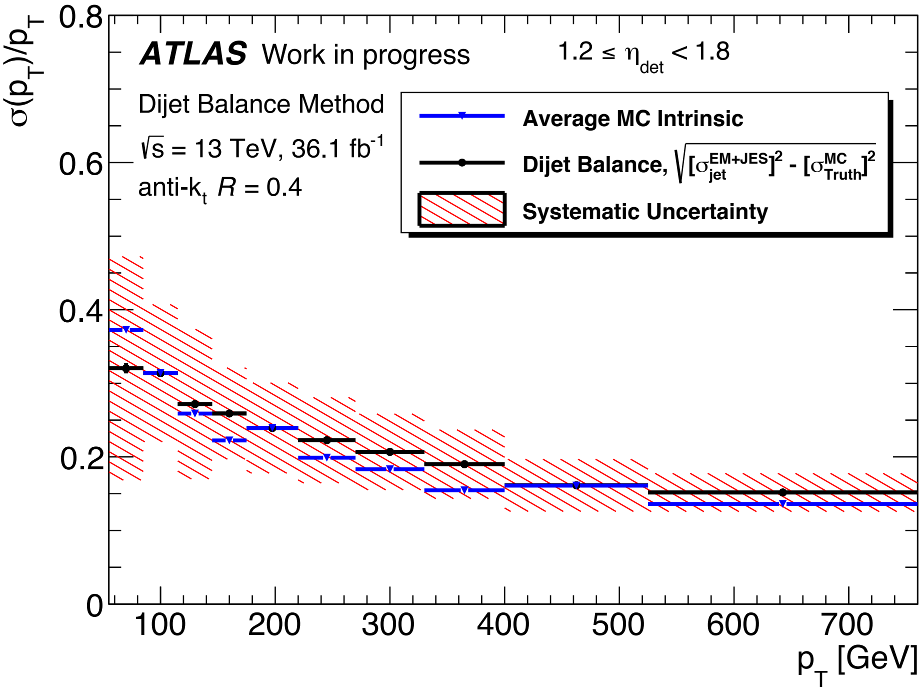

(b)

Figure 5.18: Jet energy resolution calculated using the dijet-balance method with data and the particle-level fractional resolution distributions from the weighted average of three MC event generators for the detector η ranges: 0.8 to 1.2 and 1.2 to 1.8. The intrinsic Monte Carlo jet energy resolution is shown in blue for comparison.

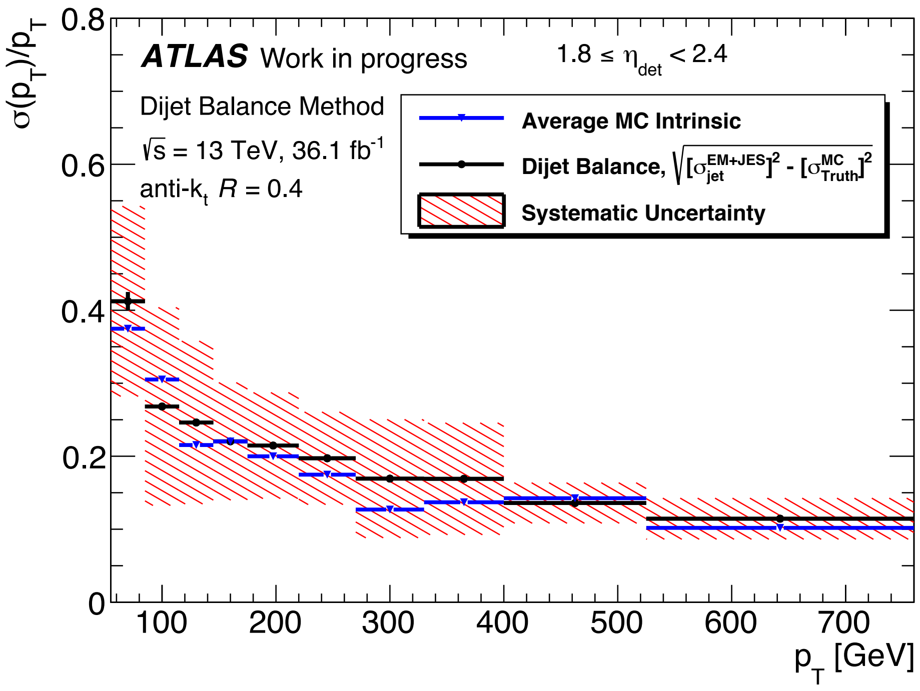

(a)

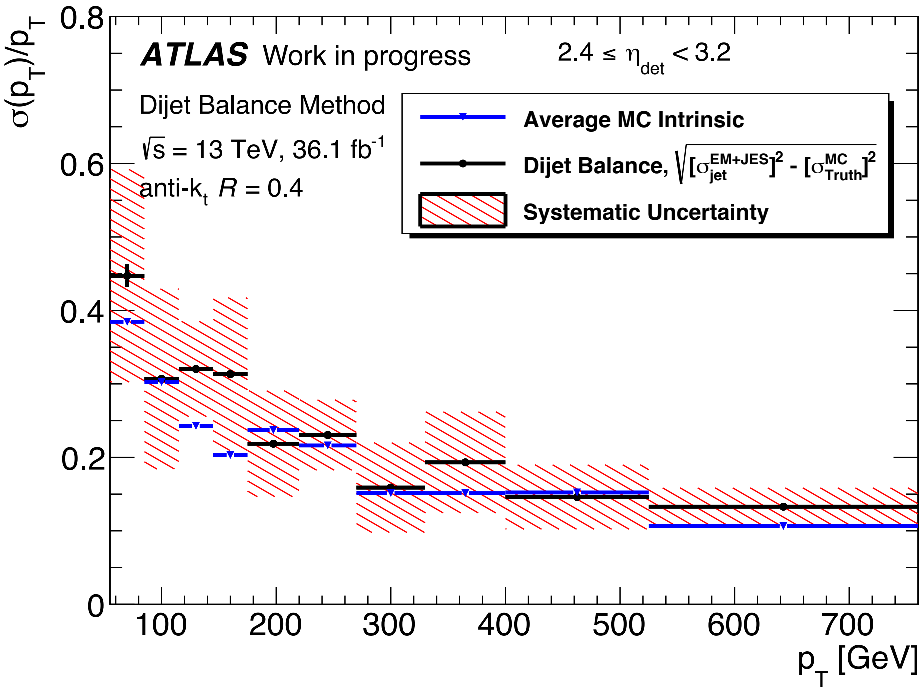

(b)

Figure 5.19: Jet energy resolution calculated using the dijet-balance method with data and the particle-level fractional resolution distributions from the weighted average of three MC event generators for the detector η ranges: 1.8 to 2.4 and 2.4 to 3.2. The intrinsic Monte Carlo jet energy resolution is shown in blue for comparison.

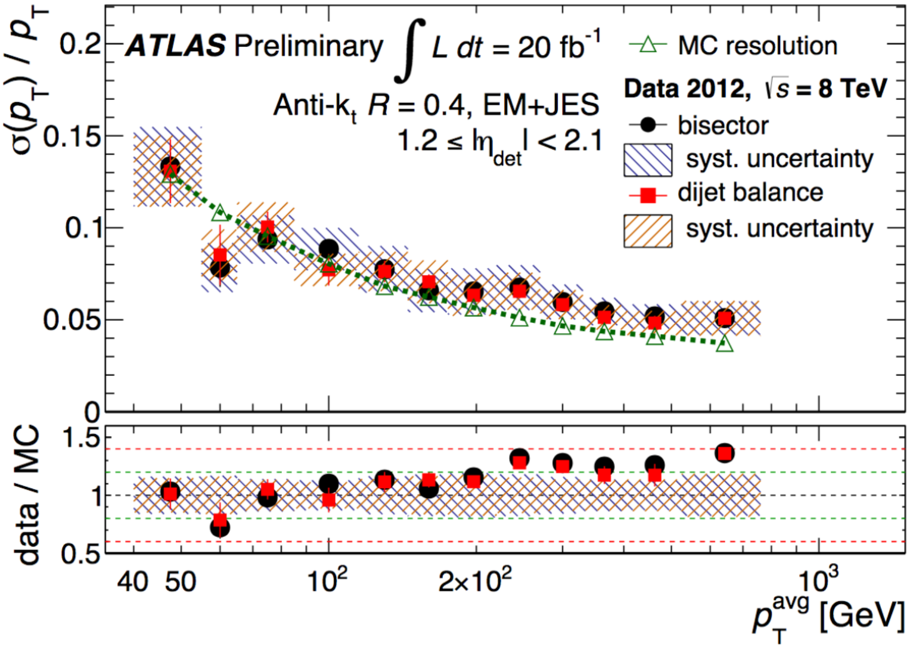

Figure 5.20: Jet energy resolution as a function of the jet transverse momentum in the region $1.2 \leq |\eta_{\mathrm{det}}| < 2.1$ for Run 1. Figure taken from Reference [89].

Chapter 6

Dark matter detection efforts

In order to detect the invisible matter introduced in Chapter 2, interactions with Standard Model particles are assumed. There are, at present, three methodologies implemented in the search for dark matter: indirect, direct and collider detection searches [99], depicted in Figure 6.1. This chapter details these methodologies and the current status of the searches conducted by the experiments using them.

6.1 Direct detection

Direct detection experiments search for low-energy recoils of nuclei produced in scattering events with dark matter particles. The transfer of energy in these interactions is small ($< 100\,\mathrm{keV}$), and as such, detectors must have the capability to measure such low energies. The recoil induces the emission of scintillation light or phonons, or causes ionisation, as nuclei move through the detector. Due to the required high sensitivity of the apparatus, these types of experiments are positioned deep underground to shield against cosmic ray interactions, in order to maintain as small a background as possible. Even with such precautions, some background signal is inevitable; therefore, these techniques must be able to distinguish between background particles, which are primarily involved in scattering interactions with electrons, and dark matter particles, which scatter with nuclei. In order to maximise the energy transfer from the dark matter particles scattering in the detector, nuclei with approximately the same mass as the dark matter particle are used as the active medium.

This category of experiment encompases a number of different methodologies: some notable experiments use noble gas detectors (XENON [101], LUX [102], PandaX [103],

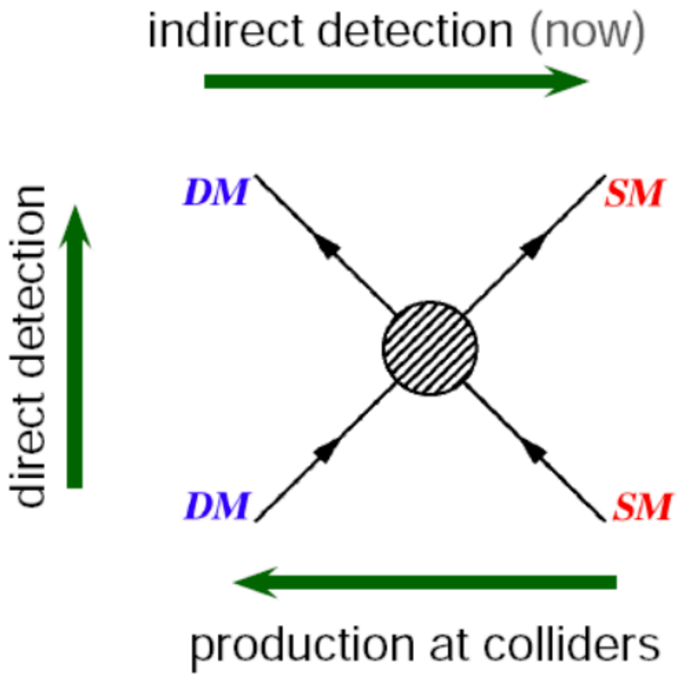

Figure 6.1: The three methodologies for dark matter searches. Image taken from Reference [100].

DarkSide [104]); others use bubble chambers (PICO [105]); germanium detectors (CoGeNT [106]); cryogenic detectors (CRESST-II [107], SuperCDMS [108]); or silicon devices (DAMIC [109]). Limits are set by these experiments on the cross-section of the dark matter–nucleon interaction. Both spin-independent interactions where protons and neutrons contribute to the scattering process equally, and spin-dependent interactions where only unpaired nucleons contribute, are investigated. The spin-dependent case can only be studied using atomic nuclei with an odd number of protons or neutrons. The experiments aim to detect either one, or a combination, of the interaction signatures from: ionisation, scintillation, heat, or annual modulation. Figure 6.2 shows the most recent exclusion limits set on the dark matter–nucleon cross-section by direct detection experiments for spin-independent interactions.

6.2 Indirect detection

Indirect detection experiments search for the annihilation and decay products of dark matter from the local solar system and beyond. These annihilation processes are responsible for producing the dark matter relic density and should still be occurring today in areas of high

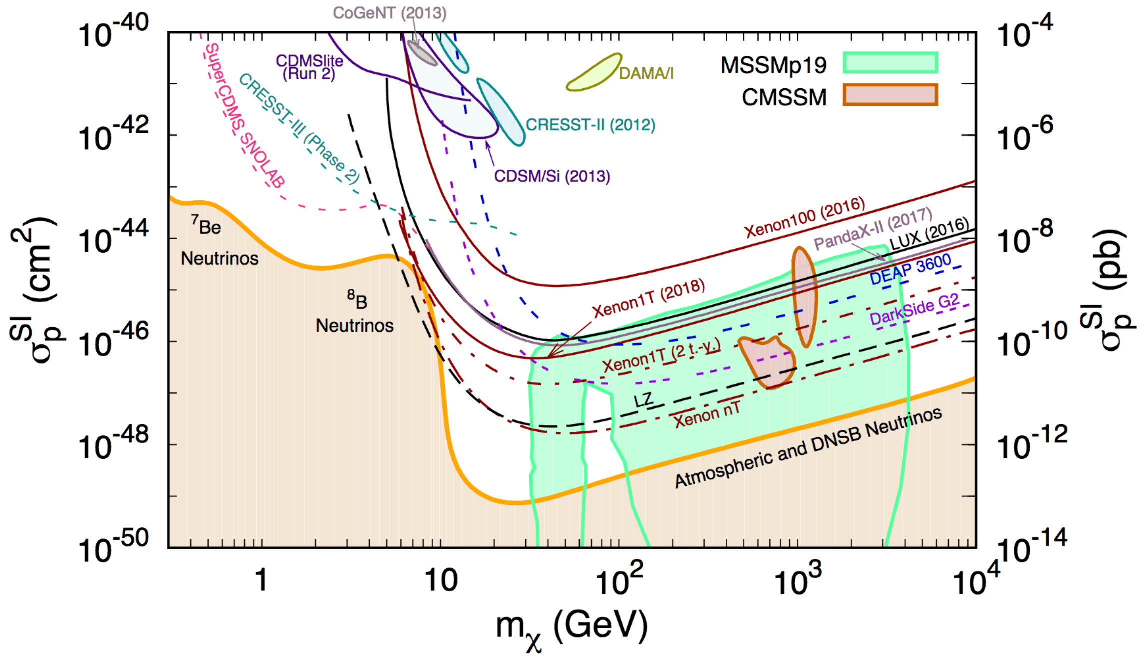

Figure 6.2: Exclusion limits from a number of different direct detection experiments on the cross-section of spin-independent dark matter–nucleon interactions. Current limits and future projections are shown in solid and dashed lines, respectively. Figure taken from Reference [110].

dark matter density. However, ordinary astrophysics produces a background for these types of searches, which is both significant and not always fully understood. One main example of this is the Galactic centre, which would theoretically have the highest signal strength from dark matter annihilations. Unfortunately it also has an almost unconstrained astrophysical background that accounts for all the signal when statistical fluctuations are considered.

There are a number of indirect detection experiments studying various dark matter signatures. For example, the international space station hosts the AMS experiment which measures cosmic rays [111]. The Fermi-LAT [112] experiment is another space-based indirect detection experiment. As was the Payload for Antimatter Matter Exploration and Light-nuclei Astrophysics (PAMELA) experiment [113]: a cosmic ray measurement device which was connected to a satellite orbiting Earth. During its ten years of operation from 2006–2016, PAMELA aspired to detect evidence for dark matter annihilation through the measurement of the matter–antimatter ratio. An excess of positrons found by the experiment appears to support the idea of dark matter annihilation or decays. However, other measurements, such as the contrasting result obtained from proton–antiproton data, casts doubt on a dark matter interpretation. Limits set from this data on a number of effective field theory dark matter models are shown in Chapter 8 alongside the results presented in this thesis.

There are also a number of Earth-based indirect detection experiments: ANTARES [114] and ICECUBE [115], use specialised telescopes to identify neutrinos. They, as well as experiments such as Super-Kamiokande [116], search for neutrinos produced from dark matter annihilation events inside the sun. Figure 6.3 shows the most recent exclusion limits set on the dark matter–nucleon cross-section by indirect detection experiments for both spin-independent and spin-dependent interactions.

Alternative methodology is used by the Very Energetic Radiation Imaging Telescope Array System (VERITAS) experiment [117]. This ground-based gamma-ray observatory aims detect Cherenkov radiation produced from particle cascades created when gamma rays enter the upper atmosphere. These high-energy gamma rays are produced from dwarf galaxies and would indicate the annihilation or decay of dark matter particles. Limits set using data collected by VERITAS are also compared to the reported results in Chapter 8.

6.3 Collider searches

Collider searches aim to produce dark matter particle-antiparticle pairs in association with Standard Model particles. Unlike the other two techniques, colliders do not suffer from the problem of threshold effects in the search for low-mass dark matter as they are able to produce an abundance of light particles. However, above dark matter masses of around hundreds of GeV where direct and indirect searches are more robust, colliders begin to see parton distribution function suppression. The energy constraints of what an accelerator can currently produce also restrict searches at colliders. There is also the matter of whether a dark matter signal observed in a collider would be actually caused by the same dark matter that exists in the Universe, or if it is, in fact, some other new particle that would not be stable in cosmological timescales, but appears stable in the timescales of a collider.

Due to the ability of dark matter particles to escape the experiment unnoticed, detection efforts are centered around interactions where other particles are produced in association with the missing transverse momentum $p_{\mathrm{T}}^{\mathrm{miss}}$ that the dark matter particles take with them. All these searches are discussed here and summarised in Table 6.1. Most of these types of analyses fall under the category of *mono-X* searches, where *X* represents an associated

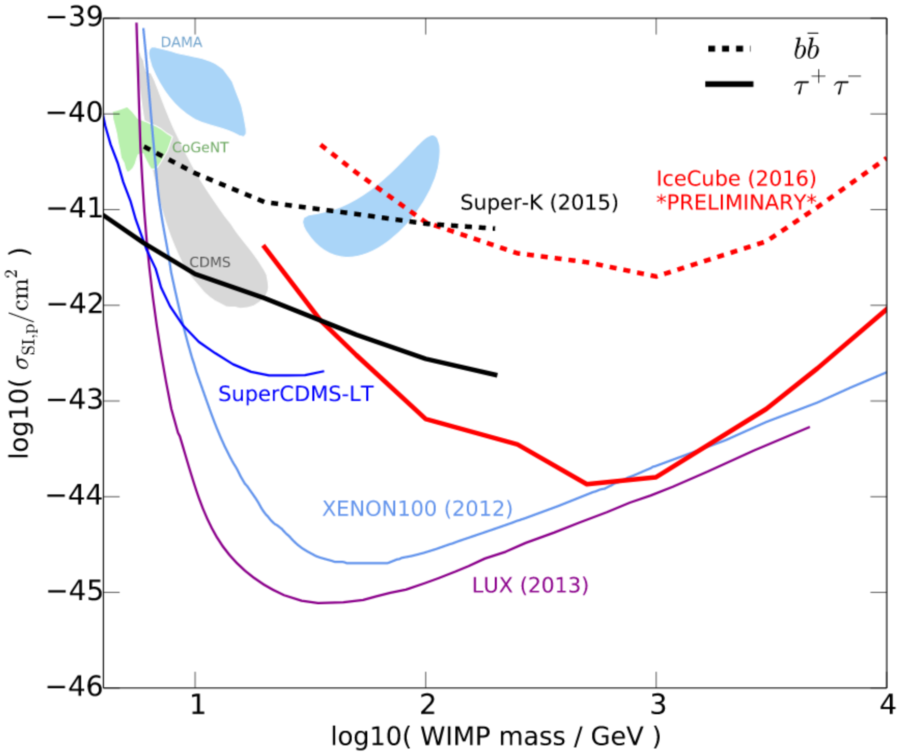

(a) Spin-independent

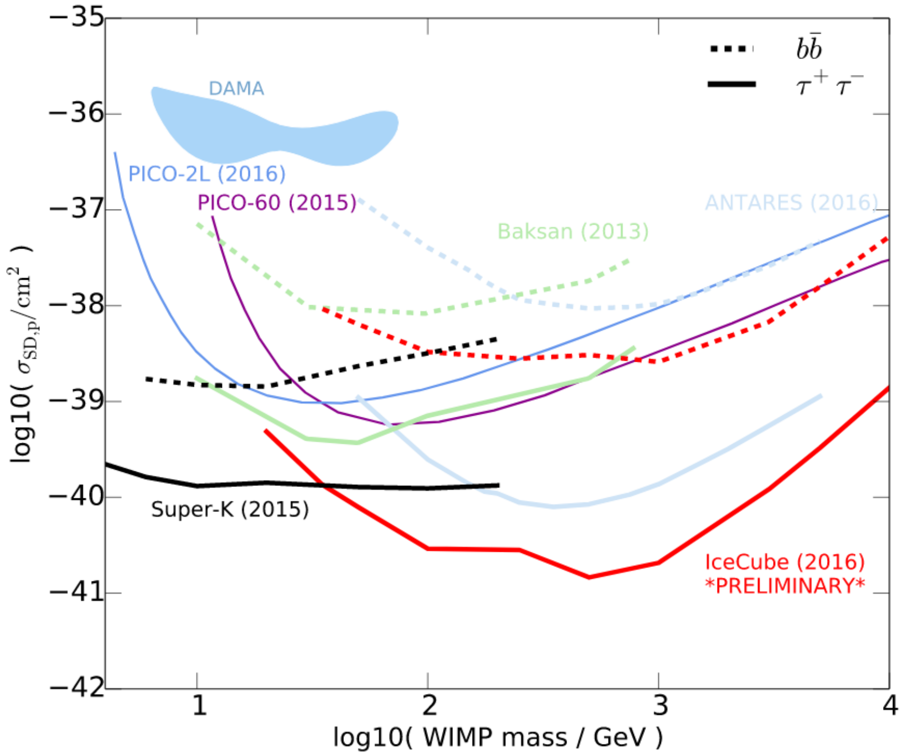

(b) Spin-dependent

Figure 6.3: Exclusion limits from a number of different indirect detection experiments on the cross-section of (a) spin-independent and (b) spin-dependent dark matter–nucleon interactions. Current limits and future projections are shown in solid and dashed lines, respectively. Figures taken from Reference [118].

Channel	Experimental signature	Analytical approach
Mono-X	$E_{\mathrm{T}}^{\mathrm{miss}} + X$	$X =$ jet, $W^{\pm}$, Z, γ, or a Higgs boson.
Invisible Higgs	$E_{\mathrm{T}}^{\mathrm{miss}}+$ jets	Higgs decay to invisible particles.
Resonances	Pair-production	Dijet, $t\bar{t}$, or b-jet pair.

Table 6.1: Overview of collider searches for dark matter discussed in Section 6.3. X represents a Standard Model object produced alongside candidate dark matter ($p_{\mathrm{T}}^{\mathrm{miss}}$): a jet, a vector boson, a photon, or a Higgs boson. The *invisible Higgs* analysis searches for a Higgs boson decaying to invisible particles. Resonances searches look for processes that imply new mediating particles.

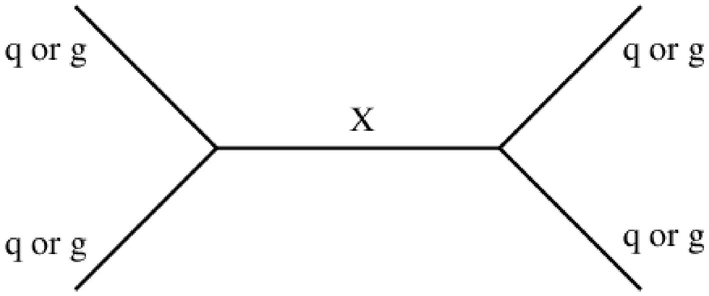

Figure 6.4: Feynman diagram of the interaction resulting in dijet resonance with a dark matter intermediate particle.

Standard Model object, such as a jet, a vector boson, or a Higgs boson. Searches for mono-jet signatures [119, 120] look for the initial state radiation of at least one jet produced in association with dark matter ($p_{\mathrm{T}}^{\mathrm{miss}}$). Mono-$V$ searches investigate the radiation of a vector boson from a quark in the initial state in association with $p_{\mathrm{T}}^{\mathrm{miss}}$. This process is cleaner than the mono-jet search, but has a significantly lower cross-section. Mono-Z [121, 122], where the Z-boson decays leptonically, and mono-γ [123, 124] searches, do not suffer from such high backgrounds and they produce a much cleaner signal. Mono-W [125, 126] searches have a further obstacle when the W decays leptonically due to the additional $p_{\mathrm{T}}^{\mathrm{miss}}$ contribution from the neutrino. This signature mimics dark matter and gives the same experimental signature as an off-shell W boson decaying leptonically. The signatures and analytical approach of the mono-Z and mono-W analyses with hadronic final states [127] are very similar to the mono-jet search; the difference between them exists only in that they use larger leading jet radius criteria and that its mass matches that of a Z or W boson. The mono-Higgs search uses the final states $b\bar{b}$ [128] or $\gamma\gamma$ [129, 130], to look for a Standard Model Higgs boson produced in association with dark matter particles. A search investigating the signature $p_{\mathrm{T}}^{\mathrm{miss}} +$ jet(s) is described in Chapters 7 and 8.

Another popular search at collider experiments is that of the invisible decay of the Higgs

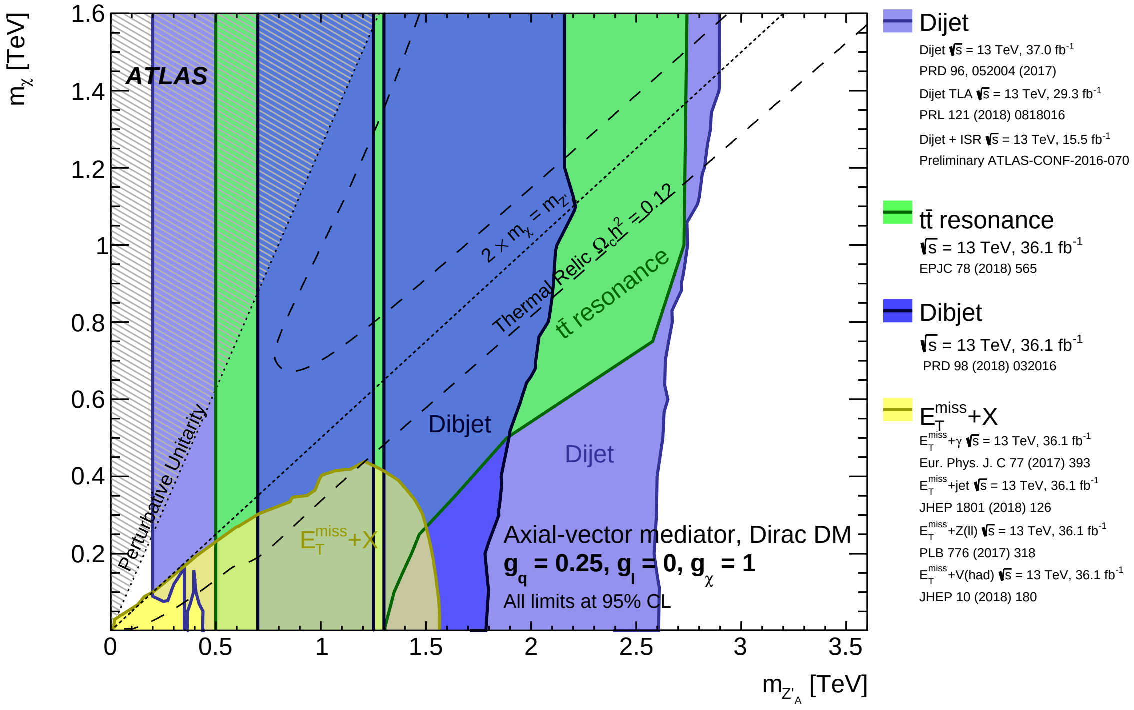

Figure 6.5: ATLAS summary plot for 95% CL exclusion limits for an axial-vector mediator simplified model with Dirac fermion dark matter. Various analyses are shown for comparison [138].

boson [131, 132]. This search looks for the pair-production of dark matter particles produced in the decay $H \to \chi\bar{\chi}$. This measurement is discussed further and used as a benchmark signature in the analysis in Chapter 8. A different approach does not have dark matter particles in the final state, but instead looks for previously unseen resonances in dijet [133–135], $t\bar{t}$ [136], or b-jet pair production [137] events that imply new mediating particles. The advantage of this methodology is the minimal dependence on the dark matter mass due to the absence of dark matter particles in the final states, as shown in Figure 6.4. Dijet searches also have the advantage of a large production cross-section. They are therefore used as fully as possible to set limits on a number of different BSM models.

Figure 6.5 shows how all these ATLAS searches use the dark matter mass–mediator particle mass plane for limit setting on the benchmark simplified WIMP dark matter model. All mono-X searches are labelled in this figure as $E_{\mathrm{T}}^{\mathrm{miss}} + X$. A mediator particle in this context is an intermediate particle that carries forces between particles. The dashed curves correspond to the dark matter and mediator mass values that are consistent with a standard thermal history and a dark matter density of $\Omega h^2 = 0.12$ [139]. The dotted rule following the ($2\times$ dark matter mass $=$ mediator mass) line indicates the threshold where the mediator

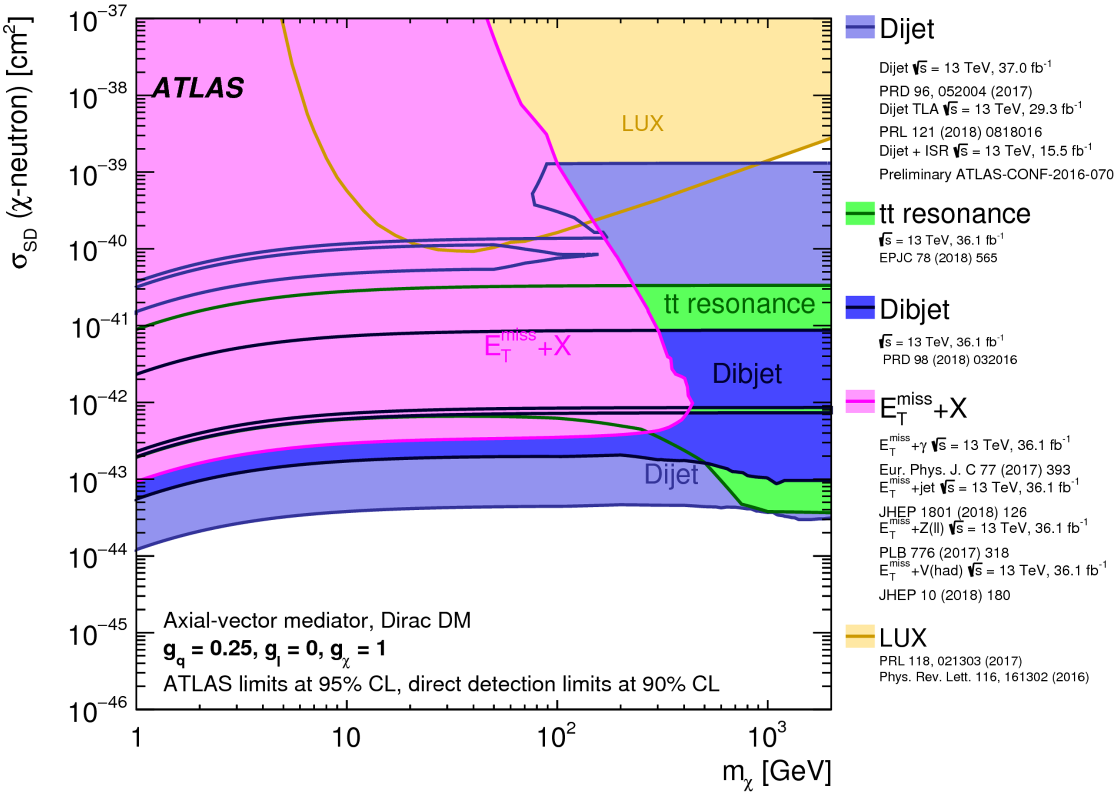

Figure 6.6: ATLAS summary plot for 95 % CL exclusion limits for an axial-vector mediator simplified model with Dirac fermion dark matter. Various analyses are shown for comparison, including direct dark matter search limits at 90 % [138].

mass can decay on-shell to pair-produce dark matter particles. The shaded region in the upper left corner excludes the region that is in disagreement with perturbative unitarity considerations. These exclusions are specifically for the fixed couplings: dark matter coupling, $g_\chi = 1$; quark coupling, $g_q = 0.25$; and lepton coupling, $g_\ell = 0$. These are set as ATLAS and CMS benchmark models [35]—the choice of g_q is driven due to historical limits set by dijet searches, and g_χ to ease re-scaling of rates. The choice of g_ℓ is made to place a leptophobic constraint on the axial-vector mediator as a number of the historically more popular searches are not sensitive to lepton couplings. The choice of couplings dramatically affects the limits that are able to be set by each search. Here, the dijet search appears to dominate and remove the possibility for $E_\mathrm{T}^\mathrm{miss} + X$ searches to expand their sensitivity into kinematic regions that have previously been untouched. However, if the value of g_q is reduced, the dijet limits reduce along the m_{Z_A} axis, but the $E_\mathrm{T}^\mathrm{miss} + X$ remains sensitive. The search discussed in this thesis endevours to set limits that are largely independent of these couplings and models.

In the past, dark matter searches at colliders have looked for strongly-coupled new particles using $p_{\mathrm{T}}^{\mathrm{miss}}$ as the tag for a dark matter candidate. More recently, pair-production rates at colliders have been compared with scattering and annihilation rates in other types of searches. Figure 6.6 shows a summary of the same benchmark simplified WIMP dark matter model discussed previously, including results from the LUX direct detection experiment. In order to include direct detection limits, the limits are set in the dark matter mass–spin-dependent cross-section plane. The dijet results still appear to dominate for this coupling combination in this plane, therefore a search independent of the couplings would be adventageous. In order to explore as many variations of couplings as possible, as few assumptions as possible are made about dark matter: only that it exists, has mass, and is stable.

This can be achieved by using an effective field theory (EFT) framework [140], as discussed previously in Section 2.2.2. This gives an approximation to an underlying theory, including the degrees of freedom appropriate to describe physical phenomena at a specific energy scale, but not specifying substructure and degrees of freedom at higher energies. This methodology is explored further in Chapter 8.

Chapter 7

Measurement of the R^{miss} cross-section ratio

The overwhelming cosmological evidence for dark matter was detailed in Chapter 2. The particle nature of dark matter and the lack of consistency with the Standard Model was also presented. This chapter describes an innovative new methodology for the measurement of differential observables sensitive to events with a final state of one or more hadronic jets and large missing transverse momentum. This analysis uses a detector corrected cross-section ratio measurement to probe as broad a kinematic region as possible. This is in order to generalise the measurement for sensitivity to a range of BSM models, including a number of examples such as processes involving vector boson fusion (VBF). The publication *'Measurement of detector-corrected observables sensitive to the anomalous production of events with jets and large missing transverse momentum in pp collisions at* $\sqrt{s} = 13$ *TeV using the* ATLAS *detector'* [141] details the full endeavour. It provides an approach for the direct comparison of Standard Model and BSM theoretical predictions at particle-level that is the first of its kind. The analysis used 3.2 fb^{-1} of data collected by the ATLAS experiment in 2015 for the proof-of-principle measurement.

7.1 Analysis outline

This analysis incorporates three main adjustments with respect to conventional dark matter searches that measure $p_{\mathrm{T}}^{\mathrm{miss}} + \mathrm{jets}$:

1. Use of a ratio of cross-sections as a function of differential distributions. Many

sources of systematic uncertainty cancel in the ratio due to the equivalent jet requirements placed on both the numerator and denominator.

2. Correcting the data for detector effects (unfolding). This allows the data to be compared to BSM model predictions at particle-level. It is computationally efficient for this analysis and for future reinterpretations as a simulation of the ATLAS detector is unnecessary.

3. Use of correlation information from additional kinematic regions in order to set limits on a number of theoretical models, including processes involving vector boson fusion. This can enhance the statistical sensitivity of the search.

A number of other advancements are made, including changes to the event and object selections, the aim being to investigate a larger kinematic range in order to increase the adaptability for comparisons with future theoretical models.

The measured observables are constructed from the cross-section ratio, defined as,

$$R^{\mathrm{miss}} = \frac{\sigma_{\mathrm{fid}}(p_{\mathrm{T}}^{\mathrm{miss}} + \mathrm{jets})}{\sigma_{\mathrm{fid}}(\ell^+\ell^- + \mathrm{jets})} = \frac{\sigma_{\mathrm{SM}}(Z \to \nu\bar{\nu} + \mathrm{jets}) + \sigma_{\mathrm{BSM}}(p_{\mathrm{T}}^{\mathrm{miss}}(\chi\bar{\chi}) + \mathrm{jets})}{\sigma_{\mathrm{SM}}(Z \to \ell^+\ell^- + \mathrm{jets})}, \tag{7.1}$$

in a fiducial kinematic region where the numerator is the sum of the $p_{\mathrm{T}}^{\mathrm{miss}}$ contributions, and the denominator is defined for a single averaged lepton flavour. The numerator in the ratio is the fiducial cross-section for events with a final state of $p_{\mathrm{T}}^{\mathrm{miss}} + \mathrm{jets}$. In the Standard Model this signature corresponds to the creation of neutrinos in events with inclusive $Z(\to \nu\bar{\nu}) + \mathrm{jets}$ production. The denominator gives the fiducial cross-section of the production of a lepton pair + jets. This pair would be produced as two same-flavour opposite-sign leptons of the first two generations: e^+e^- or $\mu^+\mu^-$. Tau leptons typically pose a challenge in measurement and so are not selected in the denominator for this proof-of-principle analysis. The calculation of this ratio is performed using the formula of the decay rate [142]:

$$\Gamma(Z \to f_1\bar{f}_2) = \frac{g_Z^2}{48\pi}(c_V^2 + c_A^2)M_Z, \tag{7.2}$$

where f_1 and f_2 represent a particle-antiparticle pair of leptons or neutrinos and dictate the values of the vector and axial-vector coupling modifications, c_V and c_A respectively. The value of c_V is $+1/2$ for neutrinos and $-1/2 + 2\sin^2\theta_W (\simeq -0.03)$ for charged leptons; and the value of c_A is $+1/2$ for neutrinos and $-1/2$ for charged leptons. g_Z is the coupling of a Z boson to a pair of fermions, and M_Z is the Z boson mass. The factor $g_Z M_Z/48\pi$ cancels in the ratio and so the final calculation is given as $(c_V^2 + c_A^2)$ for each particle-antiparticle

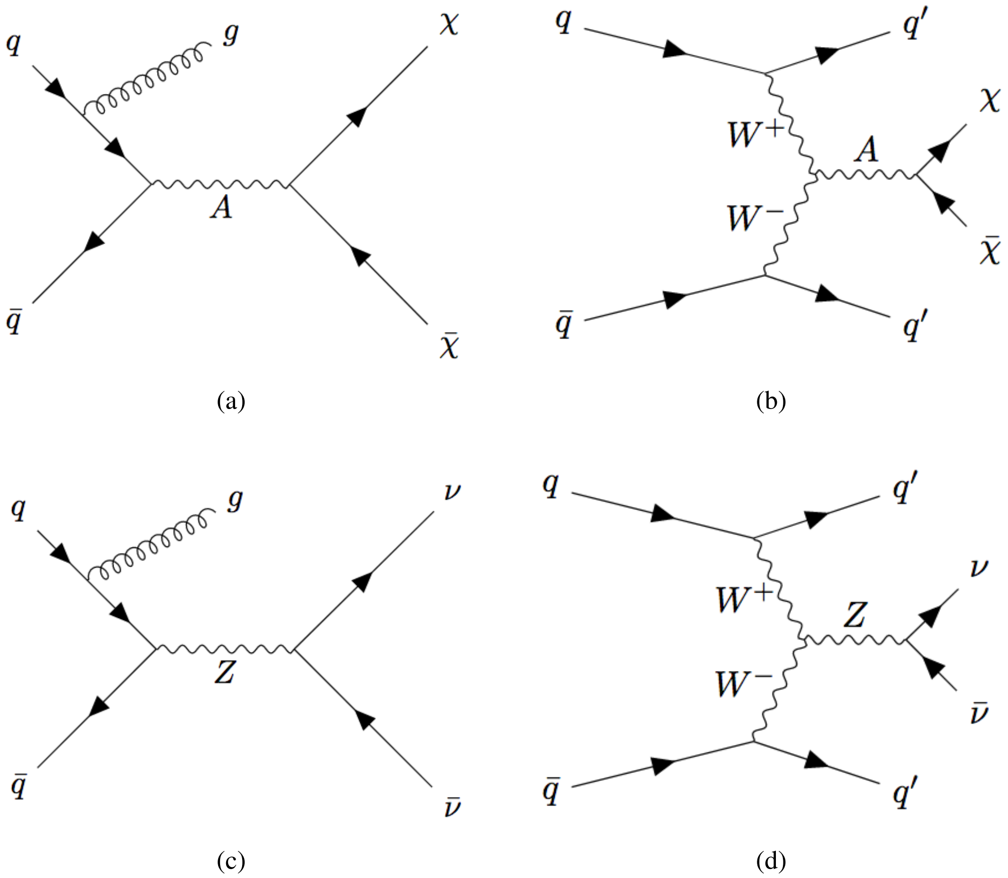

Figure 7.1: (Top) Feynman diagrams detailing WIMP dark matter pair production in association with (a) a single jet, and (b) two jets in vector boson fusion. (Bottom) Feynman diagrams for the equivalent Standard Model processes, producing neutrinos in the place of dark matter particles.

pair considered. As all three lepton channels are considered in the numerator but only two are considered in the denominator, and Z decays to neutrinos have approximately twice the branching fraction of that to leptons, the ratio in the Standard Model is ~ 6.

The jet observable in these processes is necessary for the parallel selection criteria of the numerator and denominator, which allows the partial cancellation of associated effects. This significantly reduces both experimental and theoretical uncertainties, and corrections required during the ensuing uncertainty analysis and unfolding procedure.

Any presence of BSM physics in the numerator would be observed as a discrepancy between the ratio measured in data and that expected from the Standard Model. The two Feynman diagrams in the top row of Figure 7.1 give schematics of potential dark matter production in association with (a) one or (b) two jets.

The advantage of providing detector-corrected distributions lies in the quick comparison

Event channel	MC Generator	Order	Tuning	PDF Set
$V+$ jets	SHERPA v2.2.0	NLO	SHERPA	NNPDF3.0
$V+$ jets (cross-check)	MADGRAPH5 aMC@NLO v2.2.2	LO	A14	NNPDF3.0
$V+$ jets (electroweak)	SHERPA v2.1.1	LO	SHERPA	CT10
Top production ($t\bar{t}$ & t)	POWHEGBOX v2	LO	Perugia 2012	CTEQ6L1
Multijet	PYTHIA v8.186	LO	A14	NNPDF2.3
Simplified WIMP DM	POWHEGBOX v2	LO	A14	NNPDF3.0
Invisible Higgs decay	POWHEGBOX v1	NLO	PYTHIA v8.212	CT10
Effective field theory	MADGRAPH5 aMC@NLO v2.2.3	LO	A14	NNPDF2.3

Table 7.1: Overview of Monte Carlo generators used in this analysis for each event topology under investigation. These are also discussed in the main body of the text in Section 7.2.

of Standard Model and BSM distributions without the complexity of simulating the effects of the ATLAS detector during a specific period of time. This means that new BSM models can be compared to the data as they are theorised. The publication of the kinematic distributions as well as the correlations allows for reinterpretation of the data.

Two kinematic regions are used in this analysis, one of which has not been considered in collider searches before: the VBF region. This selection requires an event containing a minimum of two high-p_{T} hadronic jets, alongside other criteria described in Section 7.3. The second kinematic region is the ≥ 1 jet region, the previous dedicated study for which is described in Reference [119].

The differential distributions measured are $p_{\text{T}}^{\text{miss}}$, m_{jj}, and $\Delta\phi_{jj}$. As both m_{jj} and $\Delta\phi_{jj}$ require events with ≥ 2 jets they are measured in the VBF kinematic region, and only $p_{\text{T}}^{\text{miss}}$ is measured in both. These four distributions were chosen for their sensitivity to a number of dark matter models and their ability to provide complimentary information for optimum limit setting.

7.2 Monte Carlo simulation

A variety of different Monte Carlo generators are used in this analysis. They are summarised in Table 7.1 and discussed in this section.

The SHERPA v2.2.0 event generator is used to generate events which contain W or Z bosons in association with jets ($V+$jets). In this software framework, matrix elements are calculated for up-to-four, and up-to-two, partons at leading order and next-to-leading order, respectively. Comix [143] and OpenLoops [144] are used to do this, before they are merged using the matrix element and parton shower at next-to-leading order (ME+PS@NLO) prescription [145]. Parton showering, hadronisation, and multiple parton interaction algorithms are used to generate the fully-hadronic final state. A dedicated SHERPA parton shower tuning is used alongside the NNPDF3.0nnlo PDF set [146]. Next-to-next-to-leading order (NNLO) accuracy is used for the normalisation of the samples to the cross-sections [147]. Event generation speed is improved by producing the samples with a simplified scale setting prescription when building the multi-parton matrix elements. The jet multiplicity distribution is re-weighted at event-level based on theoretical assumptions which are derived from the strict scale prescription of the event generation.

In order to cross-check $V+$jets samples, the process is also generated using MADGRAPH5 aMC@NLO v2.2.2 for leading order. Parton showering, hadronisation and underlying-event modeling is executed by PYTHIA v8.186. The A14 tune and NNPDF3.0nlo PDF set are used and the normalisation follows the same methodology as that of the SHERPA $V+$jets samples.

$V+$jets samples are also produced for purely electroweak events at leading order accuracy using SHERPA v2.1.1 with the dedicated SHERPA parton shower tuning and the CT10nlo PDF set [96]. These events include vector boson fusion producing a Z boson, as well as semi-leptonic VV processes with the hadronic decay of one of the weak bosons. This combination of event-generation stages is also used for the next-to-leading order production of samples of dibosons decaying leptonically [148].

The POWHEGBOX v2 [95] generator is used alongside the CT10nlo PDF set to produce samples of: top-antitop pairs, and single tops. PYTHIA v6.428 is then used for parton showering, hadronisation, and underlying-event modeling, by employing the CTEQ6L1 PDF set [149] and the Perugia 2012 tune [150].

PYTHIA v8.186 is used to generate leading order multijet processes. The A14 tune is again used, this time with the NNPDF2.3lo PDF set [151]. Modeling the properties of the bottom and charm hadron decays in all samples is executed by the EvtGen v1.2.0 program [152].

The POWHEGBOX v2 is used to generate samples for the simplified WIMP dark matter model in association with an axial-vector mediator particle, described in Section 2.2.2. The samples are then showered, hadronised, and modeled for the underlying event using PYTHIA v8.205 alongside the A14 tuning and NNPDF3.0nlo PDF set. Of the four parameters, two are fixed: the coupling of Standard Model quarks to the mediator particle, $g_q = 0.25$, and the coupling of the dark matter particles to the mediator particle $g_\chi = 1$. Samples are produced in a grid for dark matter masses in the range 1 GeV–1 TeV, and mediator particle masses in the range 10 GeV–2 TeV.

POWHEGBOX v1 is used for the generation of the process $H \to ZZ \to \nu\bar{\nu}\nu\bar{\nu}$ for the invisible decay of the Higgs boson, again described in Section 2.2.2. The CT10nlo PDF set and PYTHIA v8.212 are also used. The contributing signal cross-sections are calculated at the following accuracies: vector boson fusion at next-to-leading order; and the gluon fusion at next-to-next-to-leading order. These and the associated productions are taken from Reference [131].

The samples for the effective field theory model also described in Section 2.2.2 are generated using FEYNRULES [74, 153] and MADGRAPH5 aMC@NLO v2.2.3 alongside the NNPDF2.3lo PDF set, PYTHIA v8.212, and the A14 tune.

GEANT4 simulates the ATLAS detector for particle-level samples. All the Standard Model MC samples undergo this process, as well as the simplified WIMP dark matter model in order to cross-check the detector corrections. The effective field theory and Higgs samples are only produced at particle-level.

7.3 Object and event selection

Due to detector corrections being performed with a bin-by-bin methodology, both particle-level and detector-level selections are required. Implementing these detector corrections, or *unfolding* the data back to particle-level, is achieved using MC-simulated data and uncertainties. Bin-by-bin methodology assumes any bin migrations are small and so can be corrected by a *correction factor*. This is elaborated on in Section 7.5. In this section, the selections are discussed for the two kinematic regions outlined above.

7.3.1 Particle-level event selection

The particles measured in an event are defined as final state particles if they have a mean lifetime of $>10\,\mathrm{mm/c}$, where c is the speed of light. Visible particles interact via the strong and electromagnetic force; invisible particles do not interact via these forces and so can escape the detector unseen. The selection criteria for both types of particles are detailed in Table 7.2 and discussed below.

Numerator and denominator	≥ 1 jet	VBF
$p_{\mathrm{T}}^{\mathrm{miss}}$	$> 200\,\mathrm{GeV}$	
(Additional) lepton veto	No e,μ with $p_{\mathrm{T}} > 7\,\mathrm{GeV}$, $\lvert\eta\rvert < 2.5$	
Jet $\lvert y\rvert$	< 4.4	
Jet p_{T}	> 25 GeV	
$\Delta\phi_{p_{\mathrm{T}}^{\mathrm{miss}},\mathrm{jet}}$	> 0.4, for the four leading jets with $p_{\mathrm{T}} > 30$ GeV	
Leading jet p_{T}	> 120 GeV	> 80 GeV
Subleading jet p_{T}	–	> 50 GeV
Leading jet $\lvert\eta\rvert$	< 2.4	–
m_{jj}	–	> 200 GeV
Central-jet veto	–	No jets with $p_{\mathrm{T}} > 25$ GeV
Denominator only	≥ 1 jet and VBF	
Leading lepton p_{T}	> 80 GeV	
Subleading lepton p_{T}	> 7 GeV	
Lepton $\lvert\eta\rvert$	< 2.5	
m_{ll}	66–116 GeV	
ΔR (jet, lepton)	> 0.5, otherwise jet is removed	

Table 7.2: Overview of the selection criteria for particle-level events. The selections for the numerator and denominator for both kinematic regions are shown. Differences with the detector-level selection criteria are minimal and further described in Section 7.3.2. [141]

Leptons produced in the ($\ell^+\ell^- + \text{jets}$) process, used in the denominator of the ratio, are *dressed* leptons: meaning that the four-momenta of any radiated photons found within a cone of $\Delta R < 0.1$ around a central lepton are added into the calculation of the four-momentum of that lepton. The requirement of leptons to not be produced in the decay of a hadron or a tau gives them the descriptor *prompt* leptons.

The $p_{\mathrm{T}}^{\mathrm{miss}}$ variable is critical to this analysis due to its role as the standard signature in the detector for invisible particles. It is defined as the value of the negative vector sum of the transverse momenta of all visible final-state particles in the event with $\eta < 4.9$. The momentum of the lepton pair is excluded from this negative vector sum in the calculation of the denominator. This is in order to ensure the signatures of the numerator and denominator are as similar as possible. Jets are built using the anti-k_t jet algorithm, discussed in Chapter 4, with a jet radius parameter of 0.4. Due to their lack of interaction with the calorimeter, muons and invisible particles are excluded in this reconstruction.

The principle measurement of the ratio R^{miss} is constructed from a fiducial cross-section, influenced by the acceptances of the ATLAS detector, optimum background suppression, and the consideration of specific VBF contributions. The reasons for the specific construction of the kinematic region specialised for VBF contributions are summarised below.

Various selection criteria are motivated by the suppression of specific backgrounds. The number of events containing leptonically decaying W bosons is significantly reduced by placing a veto on charged leptons and additional charged leptons in the numerator and denominator respectively. However, due to the challenging nature of defining hadronically decaying taus, this veto is only applied to electrons and muons at particle-level. The multijet background contribution is reduced by the addition of the requirement on $\Delta\phi(p_{\text{T}}^{\text{miss}},\text{jet})$.

The $m_{\ell\ell}$ selection on the denominator ensures the lepton pair originates from the decay of a Z boson and limits any contributions from processes with a γ mediator. The p_{T} requirements on the lepton pairs guarantees both a large $p_{\text{T}}^{\text{miss}}$ and also incidentally minimises contributions from $t\bar{t}$ production, where leading leptons typically have smaller p_{T}.

The selection criteria motivated for VBF enhancement requires at least two jets in the final state, with a central-jet veto (no jets with $p_{\text{T}} > 25$ GeV) to combat hadronic activity in the rapidity gap between the two leading jets. In order to restrict the leading jets to the forward region in opposite directions, the requirement on m_{jj} is applied. Due to an expected small m_{jj} from vector bosons decaying hadronically, this selection has the double benefit of also reducing the background contribution from diboson events decaying in this way.

7.3.2 Detector-level event selection

Events used in the numerator are selected using the high level trigger requiring a $p_{\text{T}}^{\text{miss}} > 70$ GeV. This trigger is also used for the denominator in the case of muons as they are invisible to its selection. Electrons in the denominator are selected using a combination of different triggers that require at least one final state electron.

Events are also required to contain at least one primary vertex with at least two associated tracks with $p_{\text{T}} > 400$ MeV each. Events collected when the detector was not operating properly are rejected. If jets are considered *bad* (i.e. if jets with $p_{\text{T}} > 20$ GeV do not originate from proton-proton collisions), the associated events are also rejected.

The selection criteria for detector-level events is identical to that of the particle-level events with a number of additions and exceptions. Electrons in the regions $1.37 < |\eta| < 1.52$ and $2.47 < |\eta| < 2.50$ are excluded due to the first being the end-cap transition region, and the second not possessing sufficient electron identification capability. All leptons are required to be isolated and use the *LooseTrackOnly* isolation requirements described in References [82, 154]. In order to reduce $W \to \tau\nu$ background events, a veto on events containing hadronically decaying taus is applied when the total p_{T} of the decay products > 20 GeV. Photons are treated as jets as there is no dedicated selection.

7.4 Backgrounds

The dominant background contribution to the numerator is from events containing a neutrino produced by a leptonically decaying W boson. The final state of one lepton produced in association with jets and large $p_{\mathrm{T}}^{\mathrm{miss}}$ implies invisible particles: a neutrino in this case. If the charged lepton produced in this process is missed (not reconstructed or outside of acceptance of the fiducial volume defined in the previous section), this event would pass the lepton veto and be reconstructed as a signal event. The $W+$jets process is contributed to most heavily by top-quark decays ($\sim$18 % for ≥ 1 jet kinematic region, $\sim$14 % VBF kinematic region), and secondly by diboson events. This background is split into its decay channels ($\mu\nu$, $\tau\nu$, and $e\nu$) in Figures 7.2 and 7.3. The estimation of this background is on par in size with the Standard Model $Z \to \nu\bar{\nu}$ contribution to the numerator.

Another background of the numerator influenced by lepton misidentification or misacceptance takes the form of Z boson decay into two charged leptons. It is more unlikely that this process passes the selection criteria for the signal due to the lack of neutrinos (notable quantities of $p_{\mathrm{T}}^{\mathrm{miss}}$) and the necessity for the misidentification of two, rather than just one, charged leptons. This background is therefore smaller than the previously mentioned W boson process and only accounts for $\sim$0.5 % of the Standard Model signal.

A smaller background contribution to the numerator emerges from multijet events. These events are misidentified when one or more jets is missed or mismeasured, which causes the event to pass the selection criteria of large $p_{\mathrm{T}}^{\mathrm{miss}}$. The majority of the contribution from these events can be mitigated by the requirement on $\Delta\phi(p_{\mathrm{T}}^{\mathrm{miss}},\mathrm{jet})$ as the $p_{\mathrm{T}}^{\mathrm{miss}}$ direction will often point towards one of the jets. The multijet background accounts for 2 % of the total background in the first $p_{\mathrm{T}}^{\mathrm{miss}}$ bin, but falls rapidly to become negligible at high $p_{\mathrm{T}}^{\mathrm{miss}}$.

The background for the denominator signal of $\ell^+\ell^- +$jets is largely composed of top-antitop quark pairs, along with smaller contributions from $W+$jet (excluding contributions from top decays), $Z \to \tau^+\tau^-$, single-top, and diboson events.

The detector-level distributions of the numerator and denominator in the signal regions, including the relative background contributions, are given in Figures 7.2, 7.3 and 7.4, 7.5 respectively. The predictions and data can be seen to be consistent within uncertainties for both components of the ratio.

7.5 Detector corrections

The effect of detector inefficiencies on the dataset is corrected for in order to produce distributions of particle-level data. As the numerator and denominator are similar in structure, nearly complete cancellation can be achieved in the ratio for corrections of $p_{\mathrm{T}}^{\mathrm{miss}}$ and jet-based variables. Lepton veto efficiency corrections also cancel in the ratio.

The primary correction factor necessary after the various possible cancellations is due to the reconstruction efficiency for the charged leptons in the denominator. Bin-by-bin unfolding was used in this analysis and can be verified by comparing two options for correction factors. The first is constructed from the ratio of the R^{miss} distribution at particle-level to that at detector-level. This uses MC simulations of $Z \to \nu\bar{\nu}$ and $Z/\gamma^* \to \ell^+\ell^-$ as a function of the measured distributions, which takes into account all possible differences and corrects for them. The second option only considers the corrections in the denominator for the difference between the particle- and detector-level. Truth leptons and reconstructed leptons are both used separately to produce two event selections; the ratio of event yield from these two selections gives the correction factor C_Z. Figure 7.6 shows the comparison of these two scenarios for a $p_{\mathrm{T}}^{\mathrm{miss}}$ distribution only, but all distributions and bins are used in this calculation. The green curve displays the behaviour of the double ratio of R^{miss} at particle-level versus at detector-level. The second approach, which creates the correction factor C_Z, is shown in blue on the left and red on the right. The two options largely agree and any small differences are consistent within statistical fluctuations.

C_Z is used as the correction factor for this analysis as it provides simpler methodology to deal with systematic uncertainties: only lepton efficiency uncertainties require consideration. C_Z is 0.9 at low $p_{\mathrm{T}}^{\mathrm{miss}}$ but decreases to 0.85 at higher $p_{\mathrm{T}}^{\mathrm{miss}}$ if the leptons are muons, but increases with $p_{\mathrm{T}}^{\mathrm{miss}}$ for electrons from 0.7 to 0.8. This difference is due to the higher value of muon reconstruction efficiency with respect to that of electrons for the specific selection

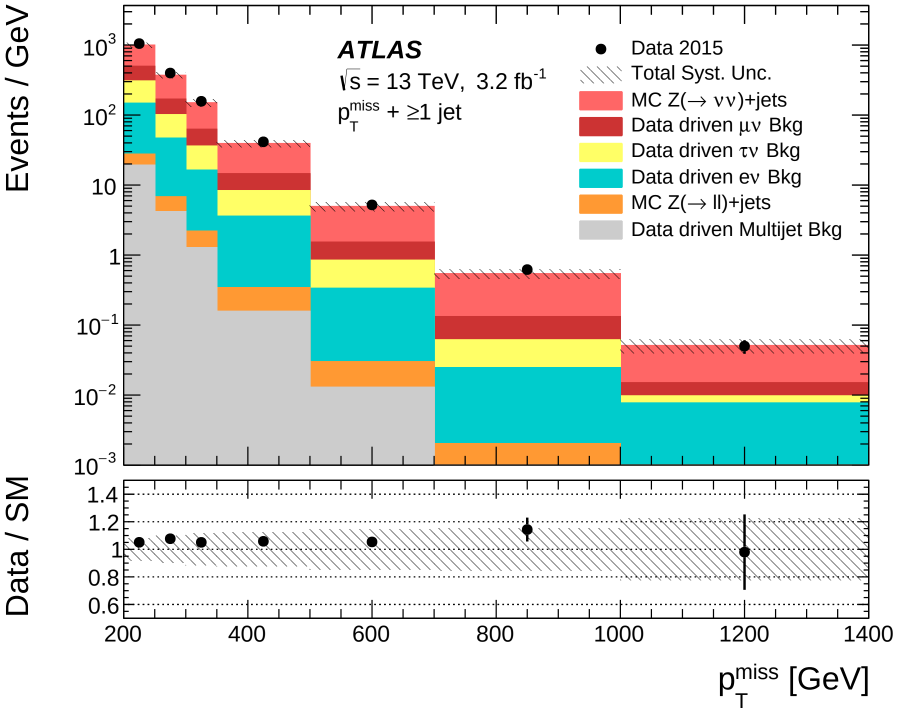

(a)

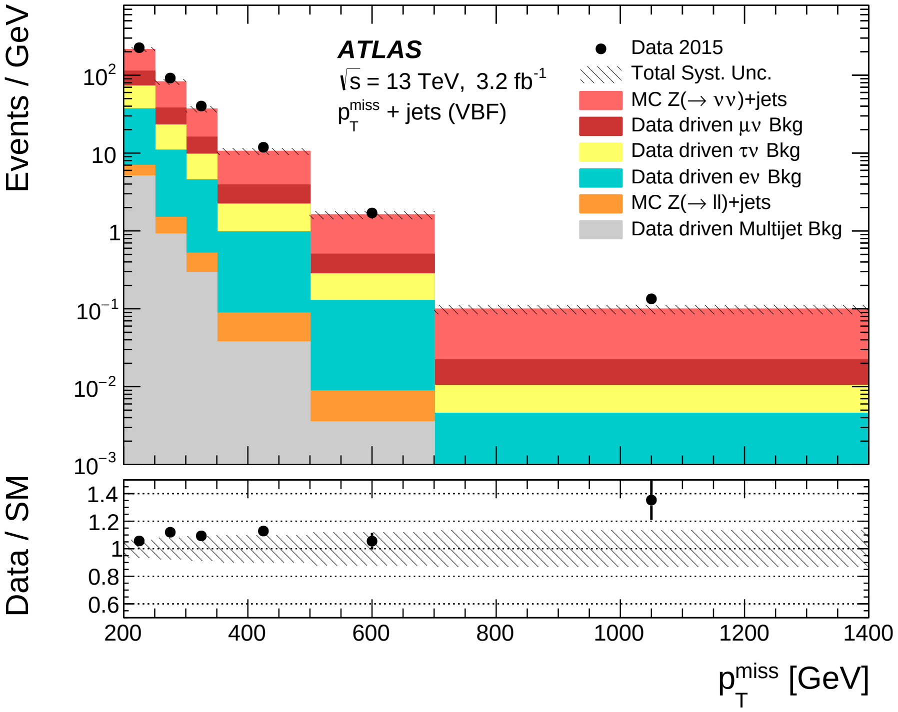

(b)

Figure 7.2: The composition of the detector-level combined numerators including all background predictions. These figures show the first two measured distributions for this analysis: $p_{\mathrm{T}}^{\mathrm{miss}}$ for (a) the ≥ 1 jet region, and (b) the VBF region. The predictions and data are compared—the ratio panel details this relationship. The statistical uncertainties of the data, and the systematic uncertainties (discussed in Section 7.6.1) are represented by error bars and bands respectively.

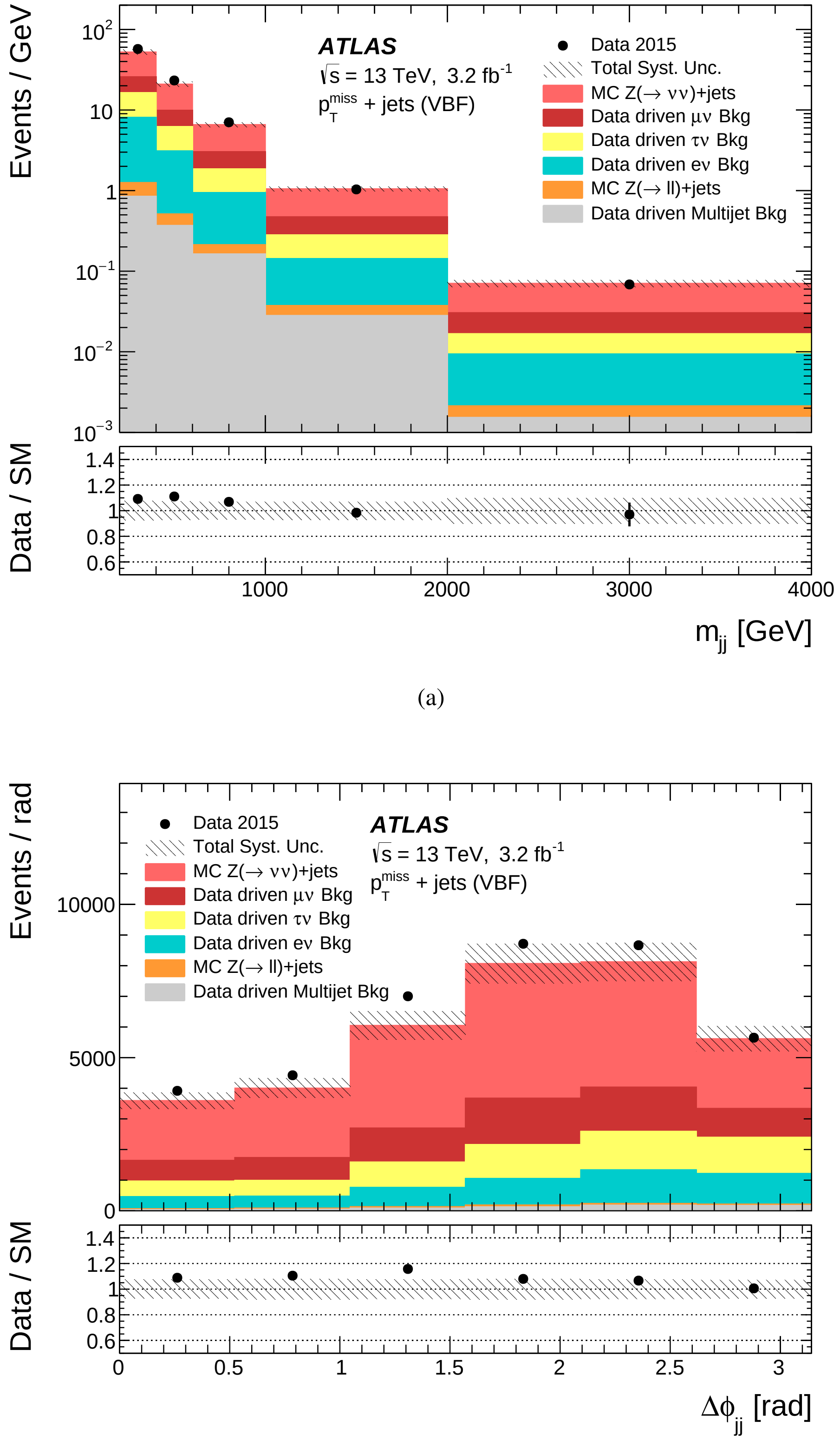

(a)

(b)

Figure 7.3: The composition of the detector-level combined numerators including all background predictions. These figures show the final two measured distributions for this analysis: (a) m_{jj}, and (b) $\Delta\phi_{jj}$ for the VBF region. The predictions and data are compared—the ratio panel details this relationship. The statistical uncertainties of the data, and the systematic uncertainties (discussed in Section 7.6.1) are represented by error bars and bands respectively.

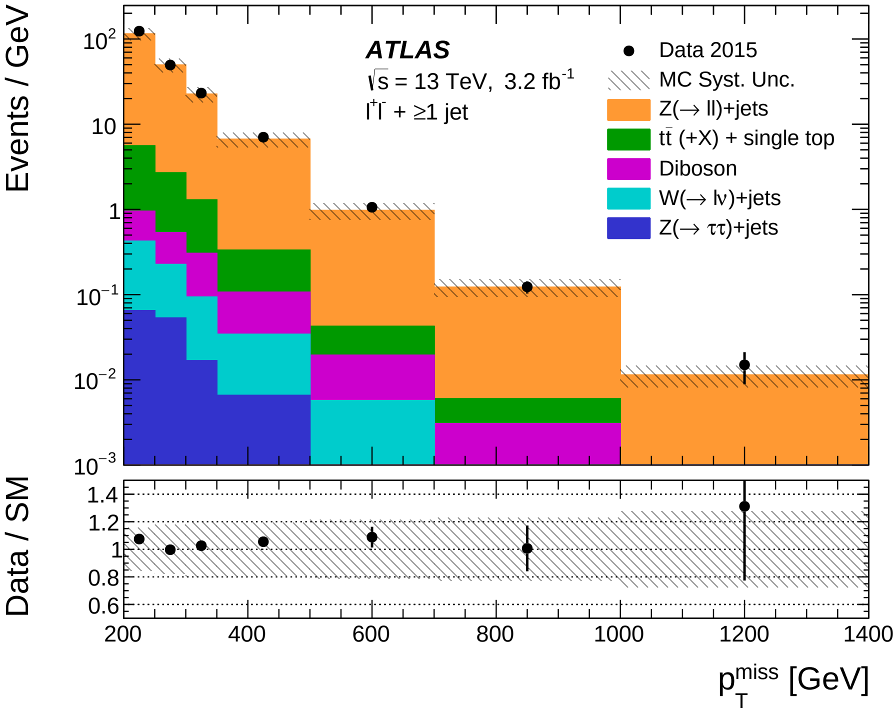

(a)

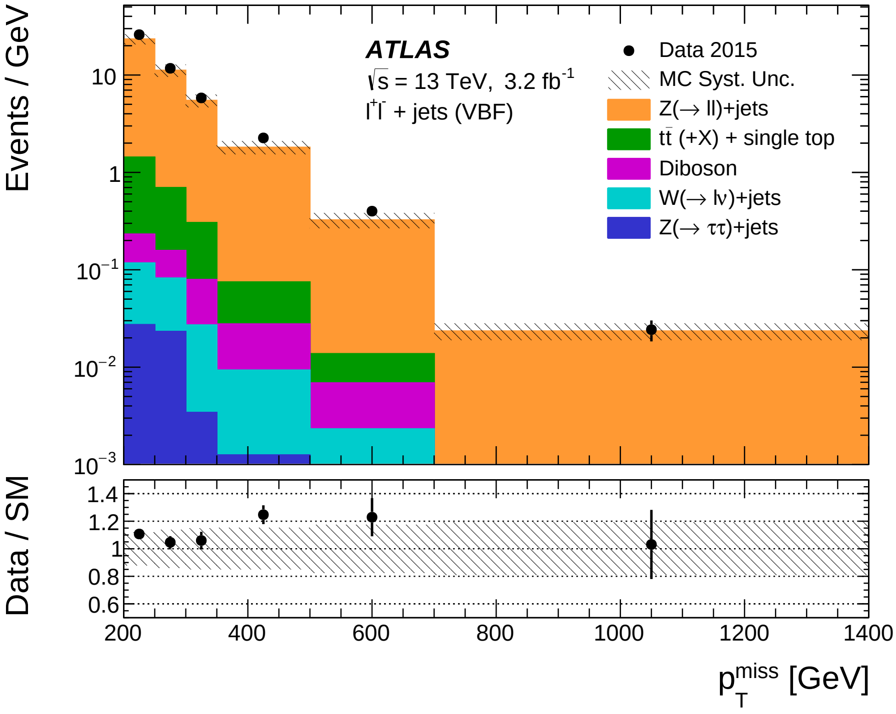

(b)

Figure 7.4: The composition of the detector-level combined denominators including all background predictions. These figures show the first two measured distributions for this analysis: $p_{\mathrm{T}}^{\mathrm{miss}}$ for (a) the ≥ 1 jet region, and (b) the VBF region. The predictions and data are compared—the ratio panel details this relationship. The statistical uncertainties of the data, and the systematic uncertainties (discussed in Section 7.6.1) are represented by error bars and bands respectively.

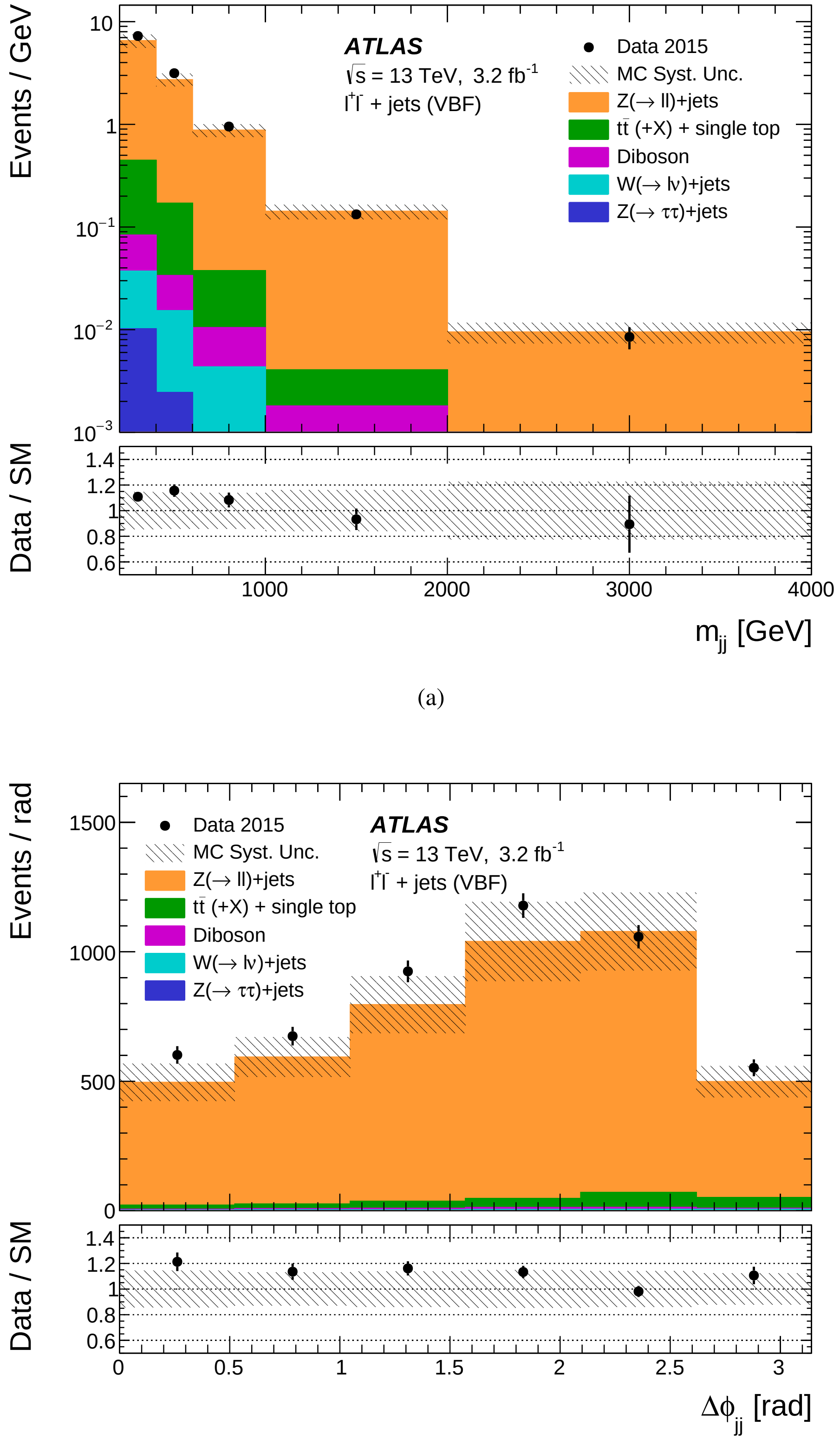

(a)

(b)

Figure 7.5: The composition of the detector-level combined denominators including all background predictions. These figures show the final two measured distributions for this analysis: (a) m_{jj}, and (b) $\Delta\phi_{jj}$ for the VBF region. The predictions and data are compared—the ratio panel details this relationship. The statistical uncertainties of the data, and the systematic uncertainties (discussed in Section 7.6.1) are represented by error bars and bands respectively.

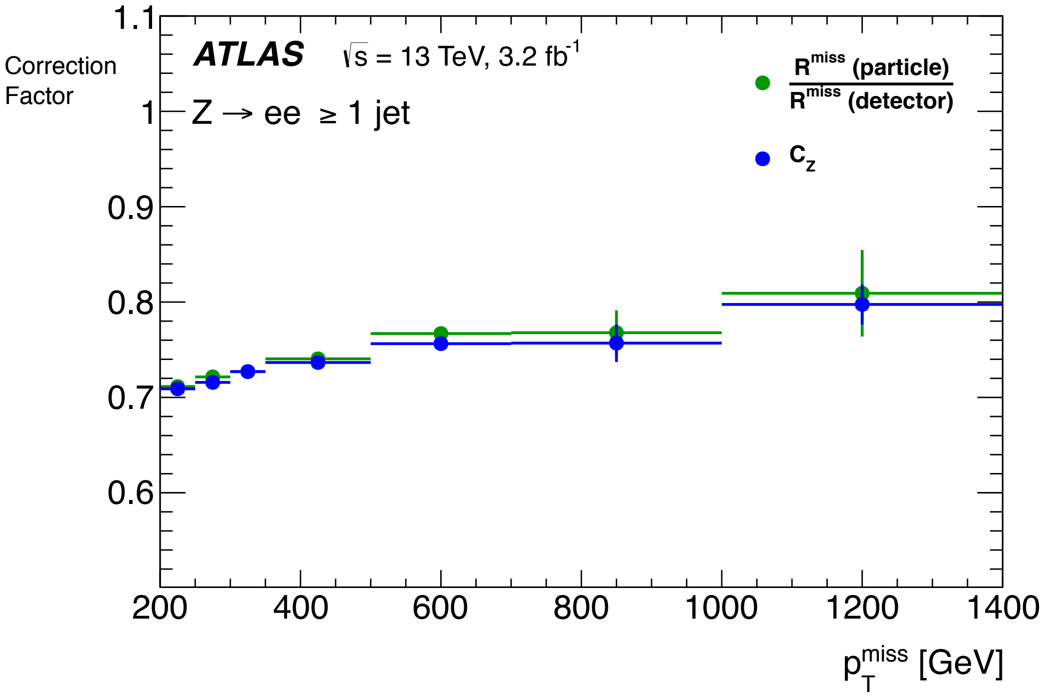

(a)

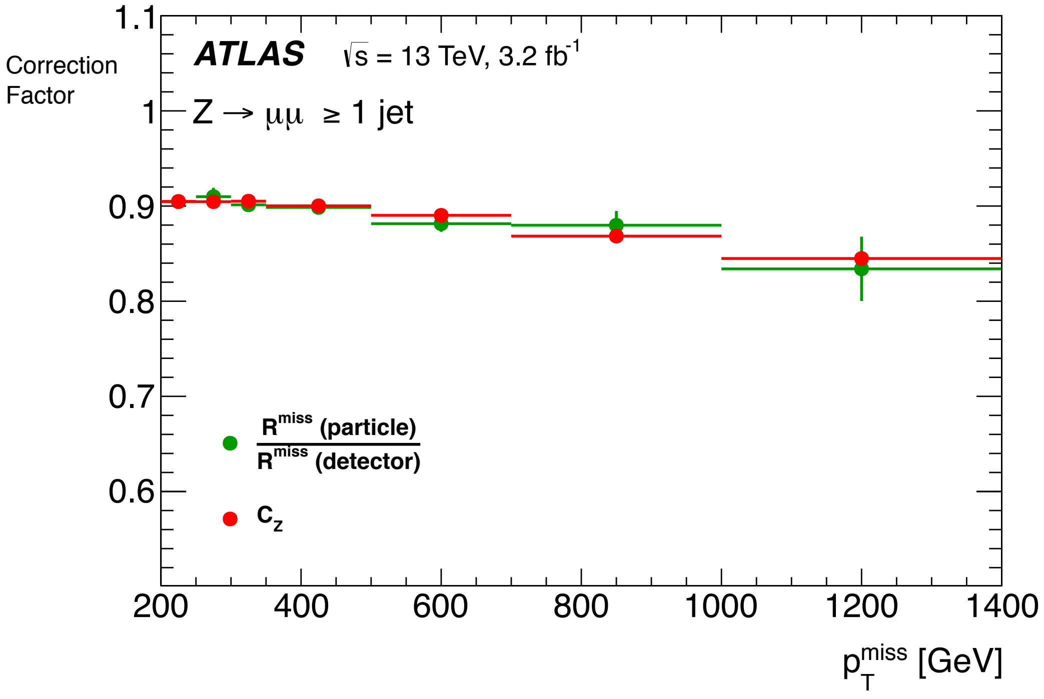

(b)

Figure 7.6: Two options for correction factors as a function of p_T^{miss}. These curves are calculated in the $\geq$ 1jet kinematic region and use in the denominator the fiducial cross-section of: (a) $Z \to ee$, and (b) $Z \to \mu\mu$. The two options are consistent within statistical uncertainties.

criteria used. The shape difference between the two distributions is due to isolation criteria differences for electrons and muons, as well as the differences in efficiencies.

Figure 7.7 shows the case where a strong dark matter signal is injected into the distribution. The impact of the detector correction factor on the final results is minimal. Figure 7.7 (a) shows the detector-level ratio with and without the injected dark matter signal of the simplified WIMP model discussed in Section 2.2.2. Here, the parameters are set at: $g_q = 0.25$, $g_\chi = 1$, $m_\chi = 150$ TeV, $m_\mathrm{A} = 1$ TeV. The two ratios are significantly different. Figure 7.7 (b) shows the correction factors produced for each of these R^{miss} distributions. Little difference can be seen, which indicates that the detector-correction process is largely independent of whether the signal used to drive the correction calculations is Standard Model or BSM physics.

7.6 Construction of the ratio

7.6.1 Sources of uncertainty

A number of sources of uncertainty in the measured ratios are examined in this section and a summary is given in Table 7.3. The final systematic uncertainties are calculated from the contributions of each individual source added in quadrature.

The primary sources of experimental systematic uncertainty arise from lepton (muon and electron) reconstruction and isolation efficiencies, and electron trigger efficiencies. These sources of uncertainty affect the detector corrections and various background predictions. The tau reconstruction efficiency is also considered and included under *lepton efficiency* in the table, but contributes significantly less to the overall uncertainty. Uncertainties labelled *jet energy scale and resolution* in the table affect both background predictions and detector corrections. The latter is affected due to small differences in numerator and denominator event selection. The $W \to \tau\nu$ source of uncertainty arises due to the choice of control region in the associated background estimation. The uncertainty associated with the estimation of the multijet background also features in the table and takes into account the uncertainty in the number of events predicted as well as uncertainties attributed to the chosen selection criteria. Both named statistical uncertainties (*correction factor* and W) arise from the finite size of the MC samples when the detector-correction factors and W background estimates

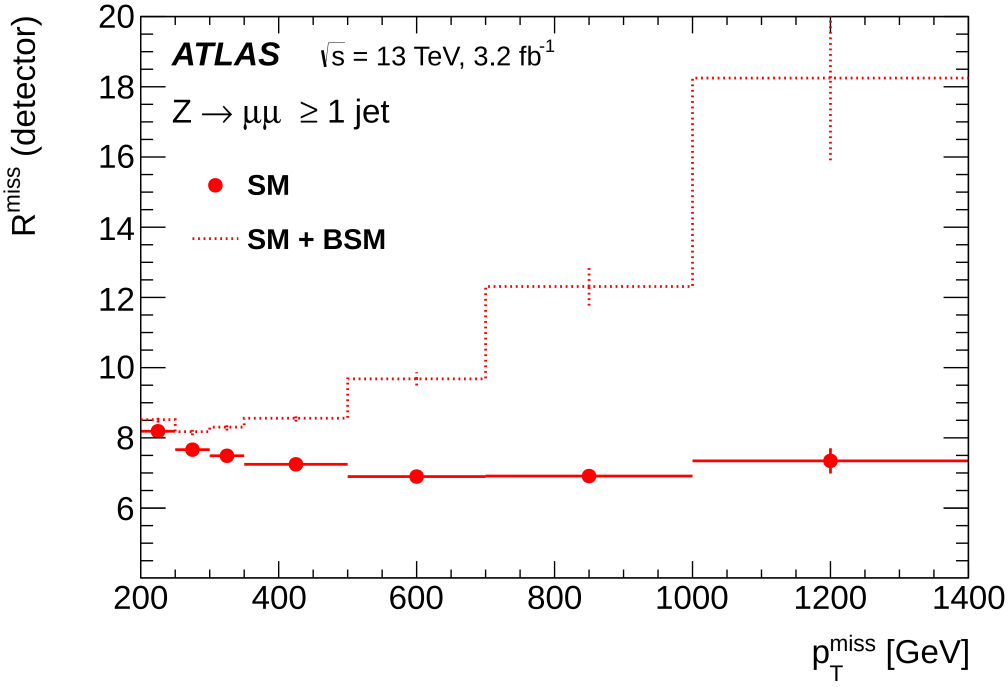

(a)

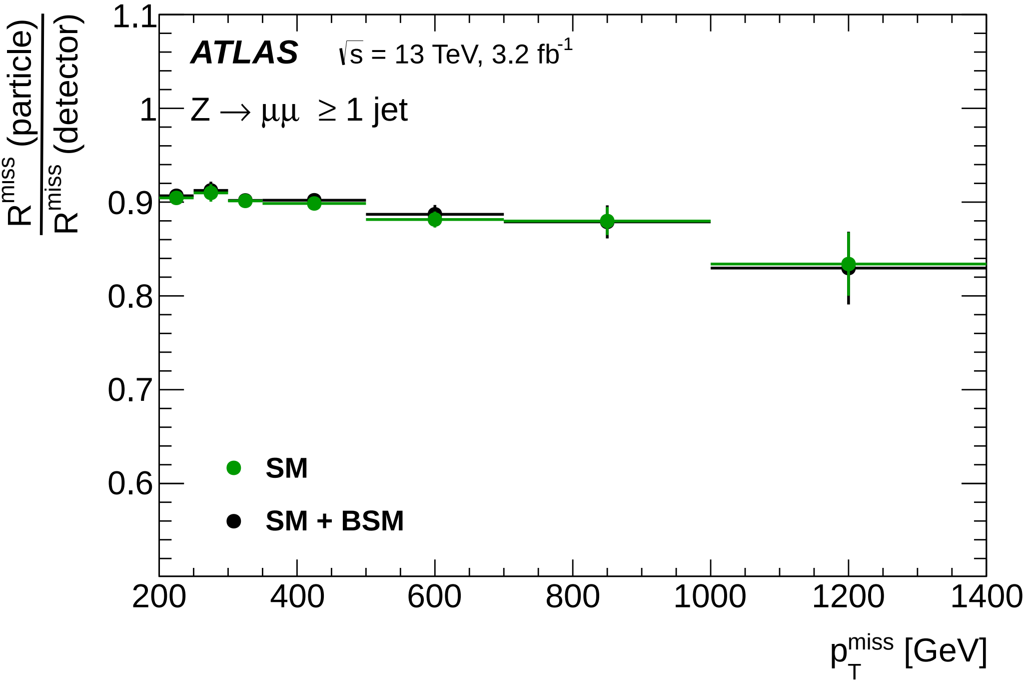

(b)

Figure 7.7: The effect of injecting a dark matter signal into the numerator of R^{miss} on the (a) R^{miss}, and (b) correction factor distributions. The dark matter signal is a simplified WIMP dark matter model with an associated axial-vector mediator particle, with parameters: $g_q = 0.25$, $g_\chi = 1$, $m_\chi = 150$ TeV, $m_\text{A} = 1$ TeV.

Systematic uncertainty source	Low $p_{\mathrm{T}}^{\mathrm{miss}}$ [%]	High $p_{\mathrm{T}}^{\mathrm{miss}}$ [%]	Low m_{jj} [%]	High m_{jj} [%]
Lepton efficiency	+3.5, −3.5	+7.6, −7.1	+3.7, −3.6	+4.6, −4.4
Jet energy scale and resolution	+0.8, −0.7	+2.2, −2.8	+1.1, −1.0	+9.0, −0.5
$W \to \tau\nu$ from control region	+1.2, −1.2	+4.6, −4.6	+1.3, −1.3	+3.9, −3.9
Multijet	+1.8, −1.8	+0.9, −0.9	+1.4, −1.4	+2.5, −2.5
Correction factor statistical	+0.2, −0.2	+2.0, −1.9	+0.4, −0.4	+3.8, −3.6
W statistical	+0.5, −0.5	+24, −24	+1.1, −1.1	+6.8, −6.8
W theory	+2.4, −2.3	+6.0, −2.3	+3.1, −3.0	+4.9, −5.1
Top cross-section	+1.5, −1.8	+1.3, −0.1	+1.1, −1.2	+0.5, −0.4
$Z \to ll$ backgrounds	+0.9, −0.8	+1.1, −1.1	+1.0, −1.0	+0.1, −0.1
Total systematic uncertainty	+5.2, −5.2	+27, −26	+5.6, −5.5	+14, −11
Statistical uncertainty	+1.7, −1.7	+83, −44	+3.5, −3.4	+35, −25
Total uncertainty	+5.5, −5.4	+87, −51	+6.6, −6.5	+38, −27

Table 7.3: Summary of the contributions of each uncertainty described in this section. The table gives the various uncertainties in terms of the lowest and highest $p_{\mathrm{T}}^{\mathrm{miss}}$ bin for the ≥ 1 jet kinematic region and the lowest and highest m_{jj} bin for the VBF kinematic region [141].

are calculated.

There are three groups of theoretical uncertainty taken into account and named in the table: W, *top cross-section*, and $Z \to ll$ *backgrounds*. The contribution under W *theory* covers a number of sources that affect the extrapolation of the W background prediction from control region to signal region. The *top cross-section* contribution originates from the disagreement of data and MC for the top-enriched control region. The $Z \to ll$ *backgrounds* uncertainty arises from the method of estimation used for the denominator background predictions.

7.6.2 Combination

Once all the estimated backgrounds have been subtracted from the two denominator distributions ($e^+e^- +$jets and $\mu^+\mu^- +$jets) and the detector correction factors have been applied to each, they are statistically combined to produce an average $\ell^+\ell^- +$jets. This is done using the best linear unbiased estimate (BLUE) combination method [155], which takes the relative precision of each contribution into consideration. This tool provides the minimum variance possible if the true uncertainties and correlations between them are known. It is equivalent to a maximum-likelihood estimate when the distributions are Gaussian, and a χ^2-minimisation for all distributions. In order to counteract a potential bias in the combination, the statistical uncertainties on the data of the two distributions are replaced and the combination is iterated again. A probability value (p-value) is used as a measure of the compatibility of two compared distributions, and to find the probability that, given the null hypothesis is true, the data would produce deviations from the null hypothesis at the observed level or larger. For this analysis, a rejection of similarity between two distributions requires the restriction of p-value $< 5\,\%$. The p-value for the compatibility of the two denominator distributions is found to be $74\,\%$. This shows high levels of similarity between the two distributions.

The estimated backgrounds of the numerator are then subtracted from the $p_{\mathrm{T}}^{\mathrm{miss}} + \mathrm{jets}$ data event sample, which is then divided by the combined denominator.

Figures 7.8 and 7.9 show the four combined differential distributions of R^{miss} for data, Standard Model simulation of particle-level lepton channels, and a number of dark matter model samples. These are the main results of this analysis and they have been uploaded to the online HEPData database alongside their correlation matrices for the use of others to compare with new particle-level physics models.

The Standard Model simulated samples are shown in Figure 7.8 as a function of $p_{\mathrm{T}}^{\mathrm{miss}}$ for both kinematic regions. These distributions show a downward trend with increasing $p_{\mathrm{T}}^{\mathrm{miss}}$ tending towards a ratio value of 5.9. This behaviour is due to the specific lepton acceptances in the selection criteria contributing the denominator: charged leptons are only measured in the central region ($\eta \leq 2.5$) of the detector and a larger p_{T} corresponds with more decay products of the Z boson in the central region, which increases the value of the denominator and reduces that of the ratio. The measured data and Standard Model simulated samples have a p-value consistency measure of $22\,\%$. Although this shows some tension with the Standard Model, it cannot be ruled out as the p-value $> 5\,\%$.

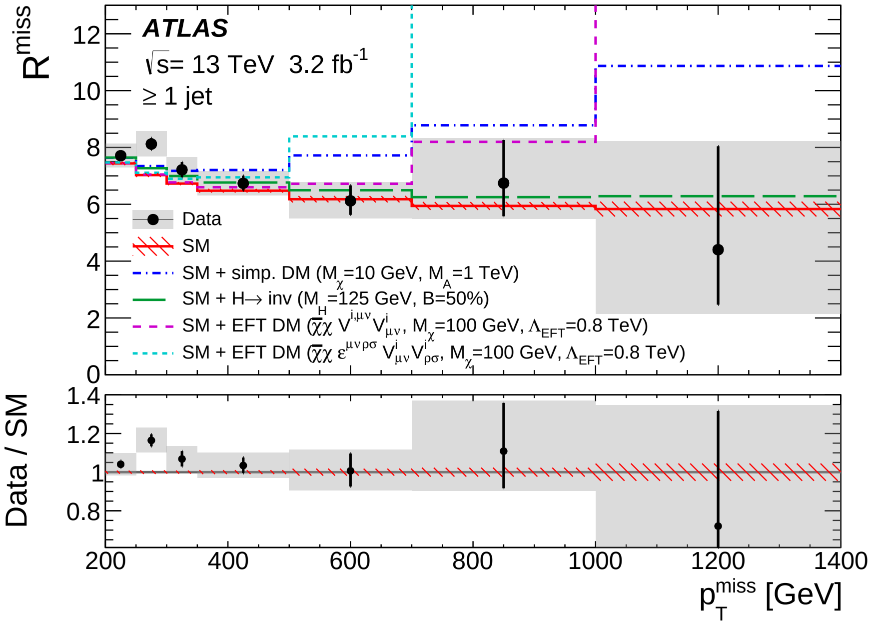

(a)

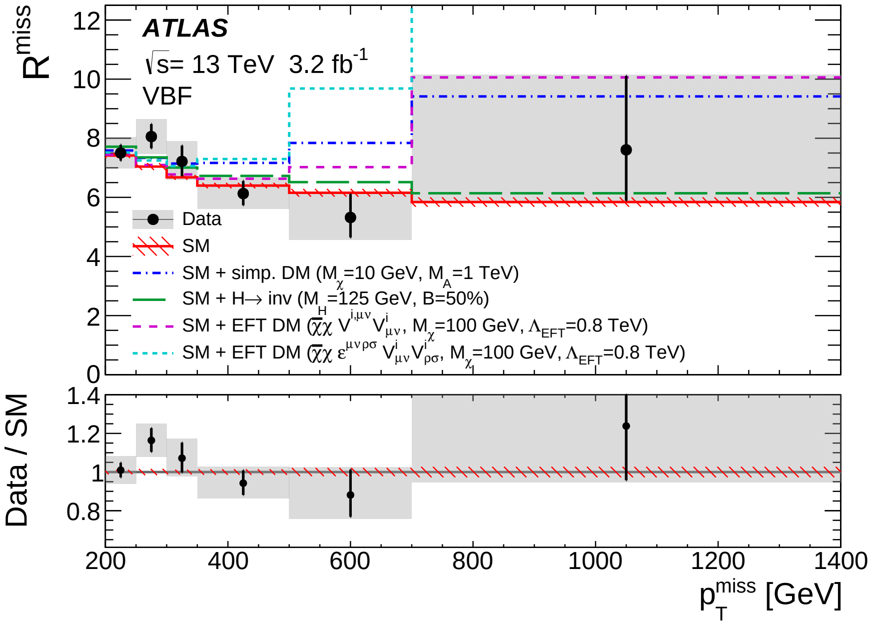

(b)

Figure 7.8: The final detector-corrected combined ratios. These figures show the first two measured distributions of R^{miss}: $p_{\text{T}}^{\text{miss}}$ for (a) the ≥ 1 jet region, and (b) the VBF region. Both data and simulated predictions for the Standard Model and some BSM theoretical models are included in the figures. The statistical uncertainties of the data, and the systematic uncertainties (discussed in Section 7.6.1) are represented by error bars and bands respectively.

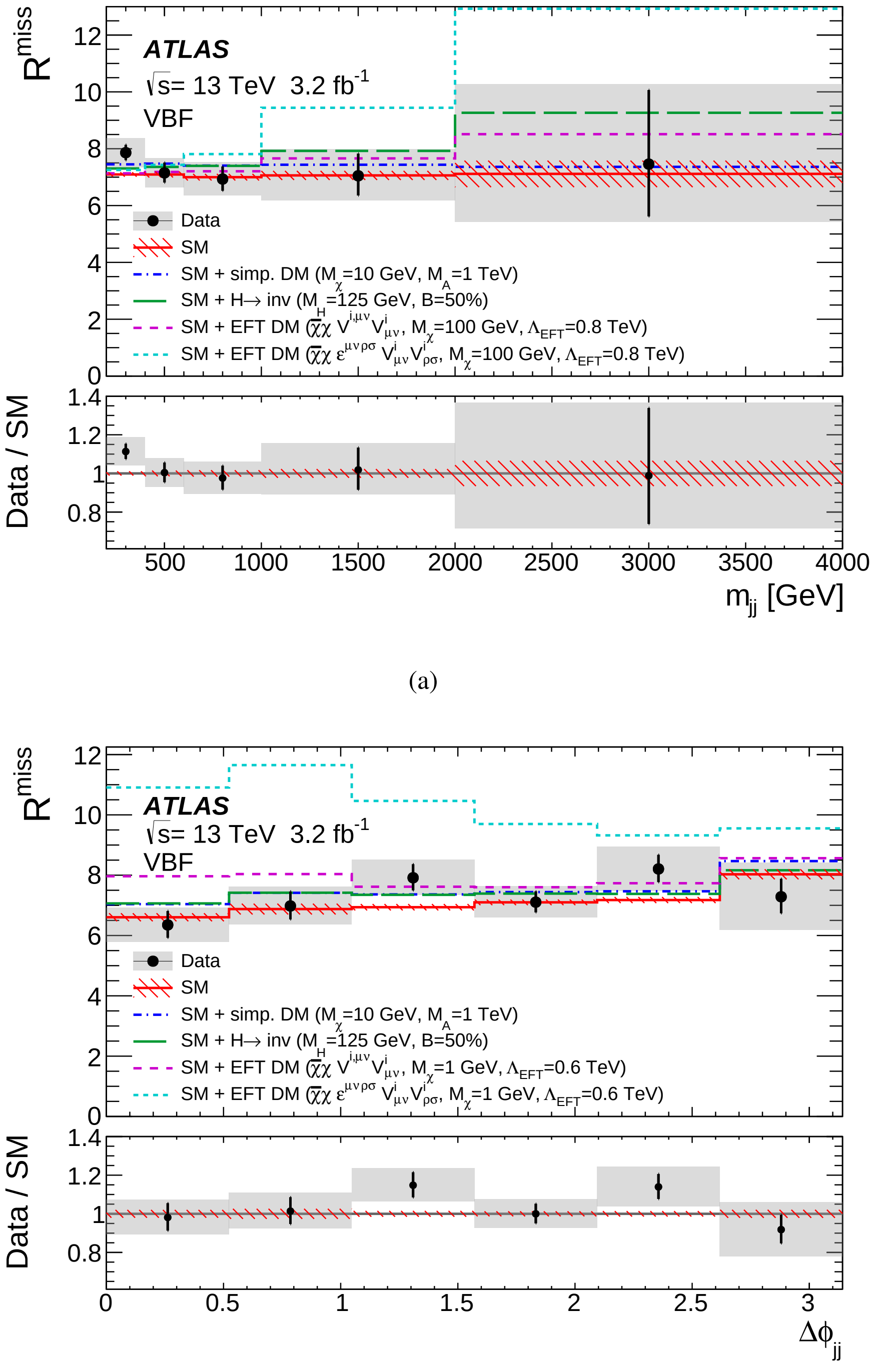

(a)

(b)

Figure 7.9: The final detector-corrected combined ratios. These figures show the final two measured distributions of R^{miss}: (a) m_{jj}, and (b) $\Delta\phi_{jj}$ for the VBF region. Both data and simulated predictions for the Standard Model and some BSM theoretical models are included in the figures. The statistical uncertainties of the data, and the systematic uncertainties (discussed in Section 7.6.1) are represented by error bars and bands respectively.

Chapter 8

Interpretation

Each of the four distributions in Figures 7.8 and 7.9 display varying degrees of constraining power over different dark matter models: the greater the difference in shape and magnitude of the dark matter model and the expected Standard Model distributions, the greater the constraining power that distribution has.

In order to set limits on these, and other dark matter models, a χ^2 quantity is constructed as the initial measure:

$$\chi^2 = (\mathbf{y}_{\text{data}} - \mathbf{y}_{\text{pred}})^T C^{-1} (\mathbf{y}_{\text{pred}} - \mathbf{y}_{\text{data}}), \tag{8.1}$$

where $\mathbf{y}_{\text{data}}$ and $\mathbf{y}_{\text{pred}}$ are the vectors of the measured and predicted R^{miss} values respectively. C is the total covariance matrix which comprises the sum of the statistical and systematic (both experimental and theoretical) uncertainty covariance matrices. A covariance matrix is built for each the four individual distributions, discussed in Section 7.6.2, before the final covariance matrix including all distributions and correlations is produced. Figures 8.1 and 8.2 give these statistical and total correlation matrices. The constituents of the statistical correlation matrix are generated by producing variations of the expected data distributions (toys) and assessing the statistical uncertainties. The systematic components are produced on a bin-by-bin basis, where the uncertainty is extracted per bin for each source. The correlations between the bins in the covariance matrix provide more information and so stronger expected exclusion limits for models which have contributions in more than one kinematic bin.

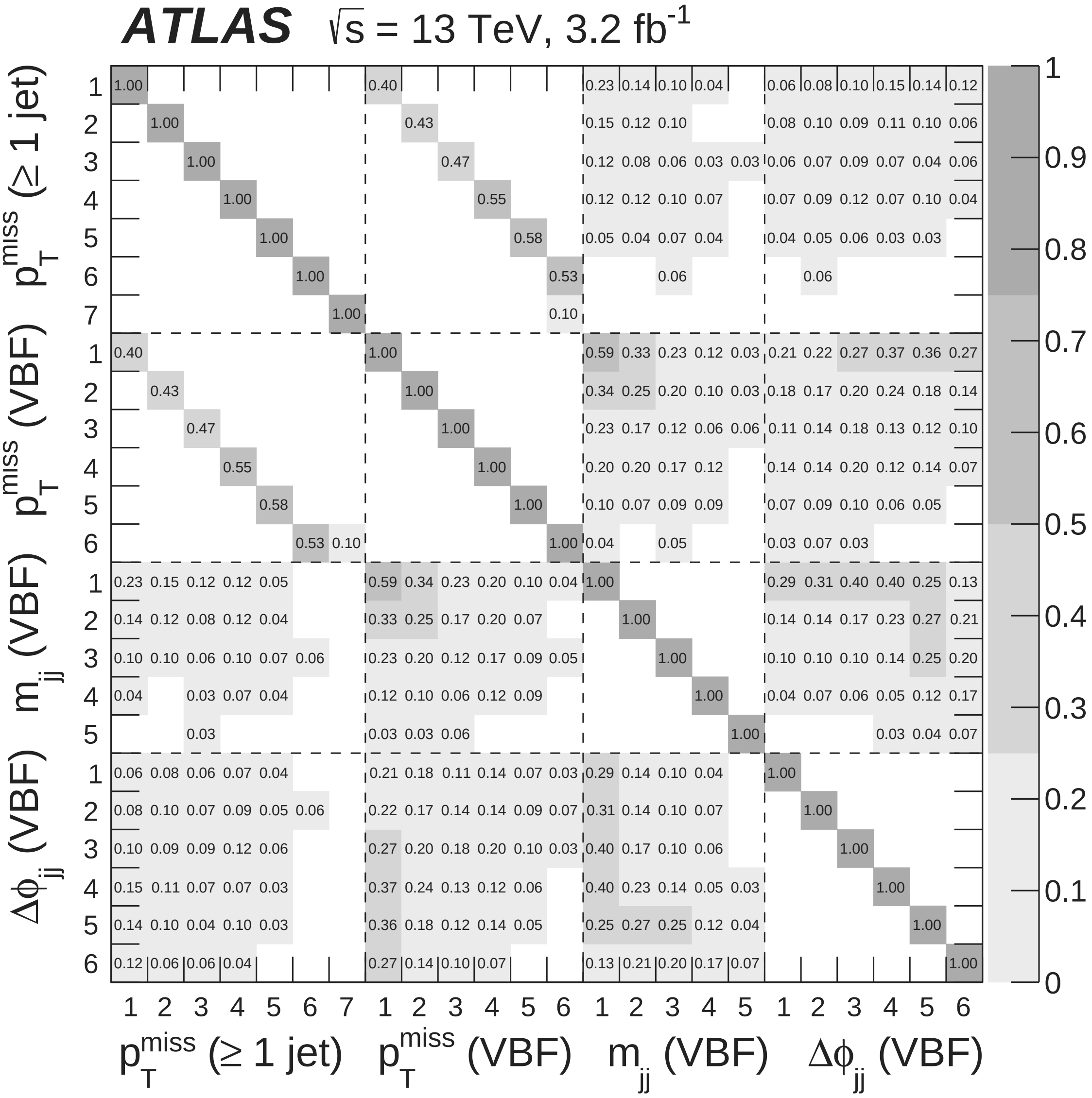

	p_T^{miss} (≥ 1 jet) 1	p_T^{miss} (≥ 1 jet) 2	p_T^{miss} (≥ 1 jet) 3	p_T^{miss} (≥ 1 jet) 4	p_T^{miss} (≥ 1 jet) 5	p_T^{miss} (≥ 1 jet) 6	p_T^{miss} (≥ 1 jet) 7	p_T^{miss} (VBF) 1	p_T^{miss} (VBF) 2	p_T^{miss} (VBF) 3	p_T^{miss} (VBF) 4	p_T^{miss} (VBF) 5	p_T^{miss} (VBF) 6	m_{jj} (VBF) 1	m_{jj} (VBF) 2	m_{jj} (VBF) 3	m_{jj} (VBF) 4	m_{jj} (VBF) 5	$\Delta\phi_{jj}$ (VBF) 1	$\Delta\phi_{jj}$ (VBF) 2	$\Delta\phi_{jj}$ (VBF) 3	$\Delta\phi_{jj}$ (VBF) 4	$\Delta\phi_{jj}$ (VBF) 5	$\Delta\phi_{jj}$ (VBF) 6
p_T^{miss} (≥ 1 jet) 1	1.00							0.40						0.23	0.14	0.10	0.04		0.06	0.08	0.10	0.15	0.14	0.12
p_T^{miss} (≥ 1 jet) 2		1.00							0.43					0.15	0.12	0.10			0.08	0.10	0.09	0.11	0.10	0.06
p_T^{miss} (≥ 1 jet) 3			1.00							0.47				0.12	0.08	0.06	0.03	0.03	0.06	0.07	0.09	0.07	0.04	0.06
p_T^{miss} (≥ 1 jet) 4				1.00							0.55			0.12	0.12	0.10	0.07		0.07	0.09	0.12	0.07	0.10	0.04
p_T^{miss} (≥ 1 jet) 5					1.00							0.58		0.05	0.04	0.07	0.04		0.04	0.05	0.06	0.03	0.03	
p_T^{miss} (≥ 1 jet) 6						1.00							0.53			0.06				0.06				
p_T^{miss} (≥ 1 jet) 7							1.00						0.10											
p_T^{miss} (VBF) 1	0.40							1.00						0.59	0.33	0.23	0.12	0.03	0.21	0.22	0.27	0.37	0.36	0.27
p_T^{miss} (VBF) 2		0.43							1.00					0.34	0.25	0.20	0.10	0.03	0.18	0.17	0.20	0.24	0.18	0.14
p_T^{miss} (VBF) 3			0.47							1.00				0.23	0.17	0.12	0.06	0.06	0.11	0.14	0.18	0.13	0.12	0.10
p_T^{miss} (VBF) 4				0.55							1.00			0.20	0.20	0.17	0.12		0.14	0.14	0.20	0.12	0.14	0.07
p_T^{miss} (VBF) 5					0.58							1.00		0.10	0.07	0.09	0.09		0.07	0.09	0.10	0.06	0.05	
p_T^{miss} (VBF) 6						0.53	0.10						1.00	0.04		0.05			0.03	0.07	0.03			
m_{jj} (VBF) 1	0.23	0.15	0.12	0.12	0.05			0.59	0.34	0.23	0.20	0.10	0.04	1.00					0.29	0.31	0.40	0.40	0.25	0.13
m_{jj} (VBF) 2	0.14	0.12	0.08	0.12	0.04			0.33	0.25	0.17	0.20	0.07			1.00				0.14	0.14	0.17	0.23	0.27	0.21
m_{jj} (VBF) 3	0.10	0.10	0.06	0.10	0.07	0.06		0.23	0.20	0.12	0.17	0.09	0.05			1.00			0.10	0.10	0.10	0.14	0.25	0.20
m_{jj} (VBF) 4	0.04		0.03	0.07	0.04			0.12	0.10	0.06	0.12	0.09					1.00		0.04	0.07	0.06	0.05	0.12	0.17
m_{jj} (VBF) 5			0.03					0.03	0.03	0.06								1.00				0.03	0.04	0.07
$\Delta\phi_{jj}$ (VBF) 1	0.06	0.08	0.06	0.07	0.04			0.21	0.18	0.11	0.14	0.07	0.03	0.29	0.14	0.10	0.04		1.00					
$\Delta\phi_{jj}$ (VBF) 2	0.08	0.10	0.07	0.09	0.05	0.06		0.22	0.17	0.14	0.14	0.09	0.07	0.31	0.14	0.10	0.07			1.00				
$\Delta\phi_{jj}$ (VBF) 3	0.10	0.09	0.09	0.12	0.06			0.27	0.20	0.18	0.20	0.10	0.03	0.40	0.17	0.10	0.06				1.00			
$\Delta\phi_{jj}$ (VBF) 4	0.15	0.11	0.07	0.07	0.03			0.37	0.24	0.13	0.12	0.06		0.40	0.23	0.14	0.05	0.03				1.00		
$\Delta\phi_{jj}$ (VBF) 5	0.14	0.10	0.04	0.10	0.03			0.36	0.18	0.12	0.14	0.05		0.25	0.27	0.25	0.12	0.04					1.00	
$\Delta\phi_{jj}$ (VBF) 6	0.12	0.06	0.06	0.04				0.27	0.14	0.10	0.07			0.13	0.21	0.20	0.17	0.07						1.00

Figure 8.1: Correlation matrix containing the statistical uncertainty information for the four R^{miss} distributions under investigation. Each value corresponds to the level of correlation between each of the bins in each distribution.

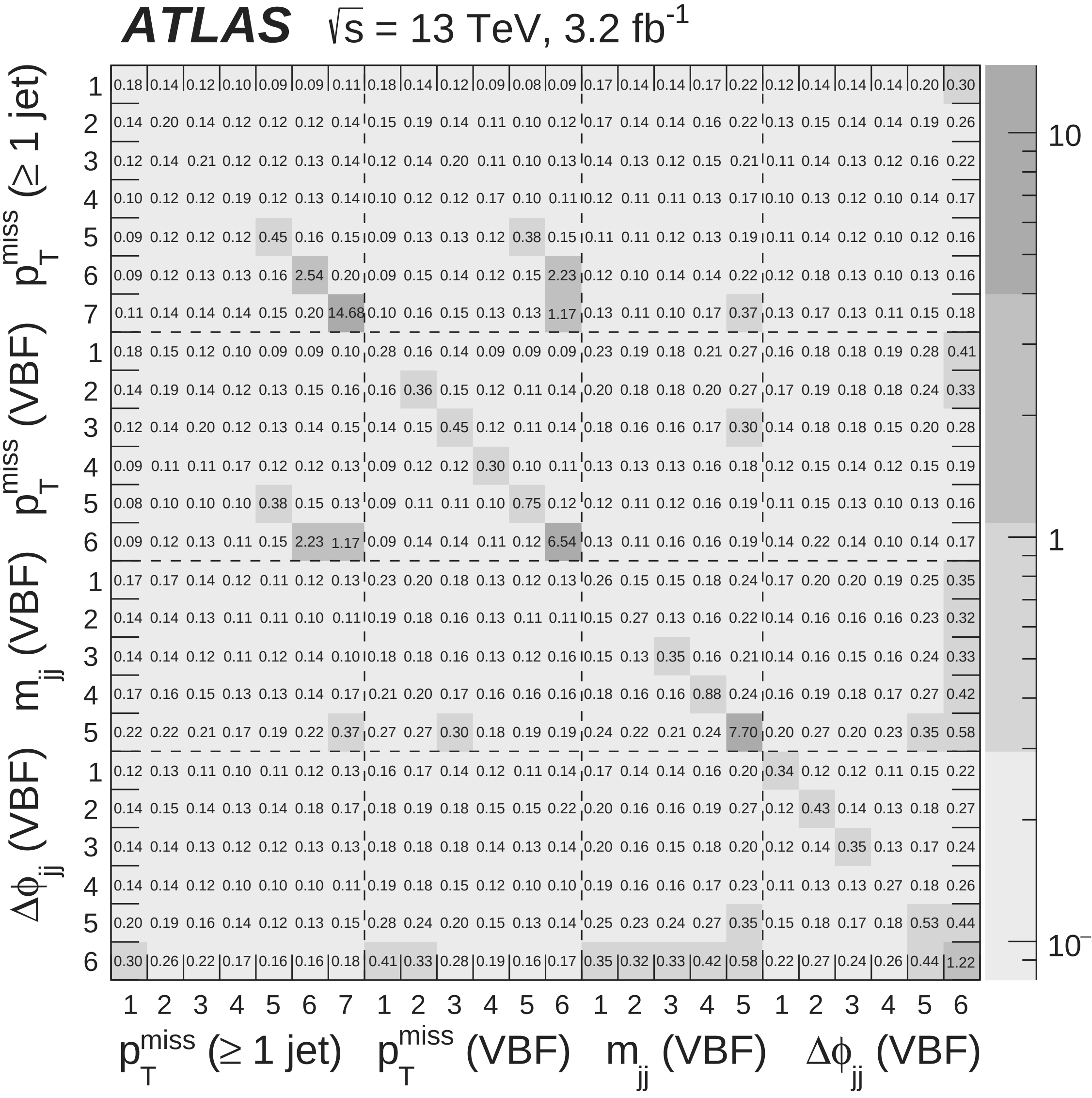

Figure 8.2: Correlation matrix containing the total uncertainty information for the four R^{miss} distributions under investigation. Each value corresponds to the level of correlation between each of the bins in each distribution.

The p-value compatibility of the Standard Model prediction and the data is then calculated using:

$$p_{\mathrm{SM}} = \int_{\chi^2_{\mathrm{SM,obs}}}^{\infty} \chi^2(x; n \text{ d.o.f}), \tag{8.2}$$

where n is the number of bins used in the distribution of interest. A similar probability may be formed to study the compatibility of the data with the dark matter scenario:

$$p_{\mathrm{DM}} = \int_{\chi^2_{\mathrm{DM,obs}}}^{\infty} \chi^2(x; n \text{ d.o.f}). \tag{8.3}$$

The upper limits of each model are derived using the $\mathrm{CL_s}$ technique [156, 157], which uses interval estimation for parameters that can only take non-negative values. It is a variation of frequentist methodology in that the limits are designed to be greater than the true value of the parameter. By convention, this limit has the probability of 95 %, which is at least equal to the confidence level (CL) [158]. In practice, this means that the ratio of the signal and background $(\mathrm{s}+\mathrm{b})$ p-value to the $1-p$-value of the background only, is required to be smaller than $1-\mathrm{CL}$:

$$\mathrm{CL_s} = \frac{p_{(\mathrm{s+b})}}{1-p_{\mathrm{b}}} < 1-\mathrm{CL}. \tag{8.4}$$

This is used to ensure robustness against fluctuations in the background and removes the possibility of setting limits in regions where the analysis has no sensitivity.

In the context of dark matter models, the exclusion power of the signal + background $(\mathrm{DM}+\mathrm{SM})$ can be quantified relative to the background (SM) by calculating:

$$1-\mathrm{CL} = \int_{\chi^2_{\mathrm{DM+SM}}-\chi^2_{\mathrm{SM}}}^{\infty} \chi^2(x; m \text{ d.o.f}). \tag{8.5}$$

where m is the number of parameters in the model. Three different types of dark matter model are studied in this analysis: a simplified WIMP model with an axial-vector mediator particle, an effective field theory model using vector boson fusion, and an invisible Higgs-boson decay model. The model samples are produced as discussed in Section 7.2, before they are subjected to the Rivet analysis ATLAS_2017_I1609448 [78, 141] like the Standard Model samples. The selection criteria is applied at this stage and the R^{miss} distributions are formed. The values of $1-\mathrm{CL}$ are calculated for each parameter point for these models in the following sections.

8.1 Simplified WIMP axial-vector mediator model

The simplified axial-vector mediator WIMP model is defined by four parameters: the dark matter mass m_χ, the mediator mass m_A, the coupling of the mediator to quarks (g_q fixed at 0.25), and the coupling of the mediator to dark matter (g_χ fixed at 1). The Lagrangian is given by:

$$\mathcal{L}_{\mathrm{axial-vector}} = g_q \sum_{q=u,d,s,c,t,b} A_\mu \bar{q}\gamma^\mu \gamma^5 q + g_\chi A_\mu \bar{\chi}\gamma^\mu \gamma^5 \chi. \tag{8.6}$$

The limits discussed in this study are set on the m_χ–m_A plane. This plane encompasses a number of points in a grid-like system. In places of discriminatory power, more points are created by scaling along the mediator mass axis using the ratio of the target width to that of the original width of the mediator particle. This scaling is only valid at high mediator mass.

8.1.1 Kinematic variations for mass changes

Figures 8.3 and 8.4 illustrate the dependence of the dark matter distributions in the ≥ 1 jet and VBF kinematic regions on the WIMP axial-vector mediator model for a number of different dark matter mass and mediator mass working points. On the left are the differential distributions with no added Standard Model contribution, and on the right are the R^{miss} distributions for each mass working point. All four observables under investigation for this measurement are shown. The shape information of these distributions is vital for this analysis due to the reliance on the uncertainty correlations between bins. It can be seen that some mass working points give stronger distinguishing power from the Standard Model than others: lower dark matter and mediator masses appear to give the largest difference in shape in all the given distributions for example. The Standard Model numerator can be seen in Figures 7.2 and 7.3 for a comparison with the BSM model shown here. As can be seen the BSM signal is of similar shape, but different magnitude, to that of the Standard Model.

8.1.2 Setting limits

Figure 8.5 shows the expected and observed 95 % confidence level exclusion limits for this model. These constraints are calculated from the four distributions, described previously, and the correlations between them. The figure also displays a conventional ATLAS

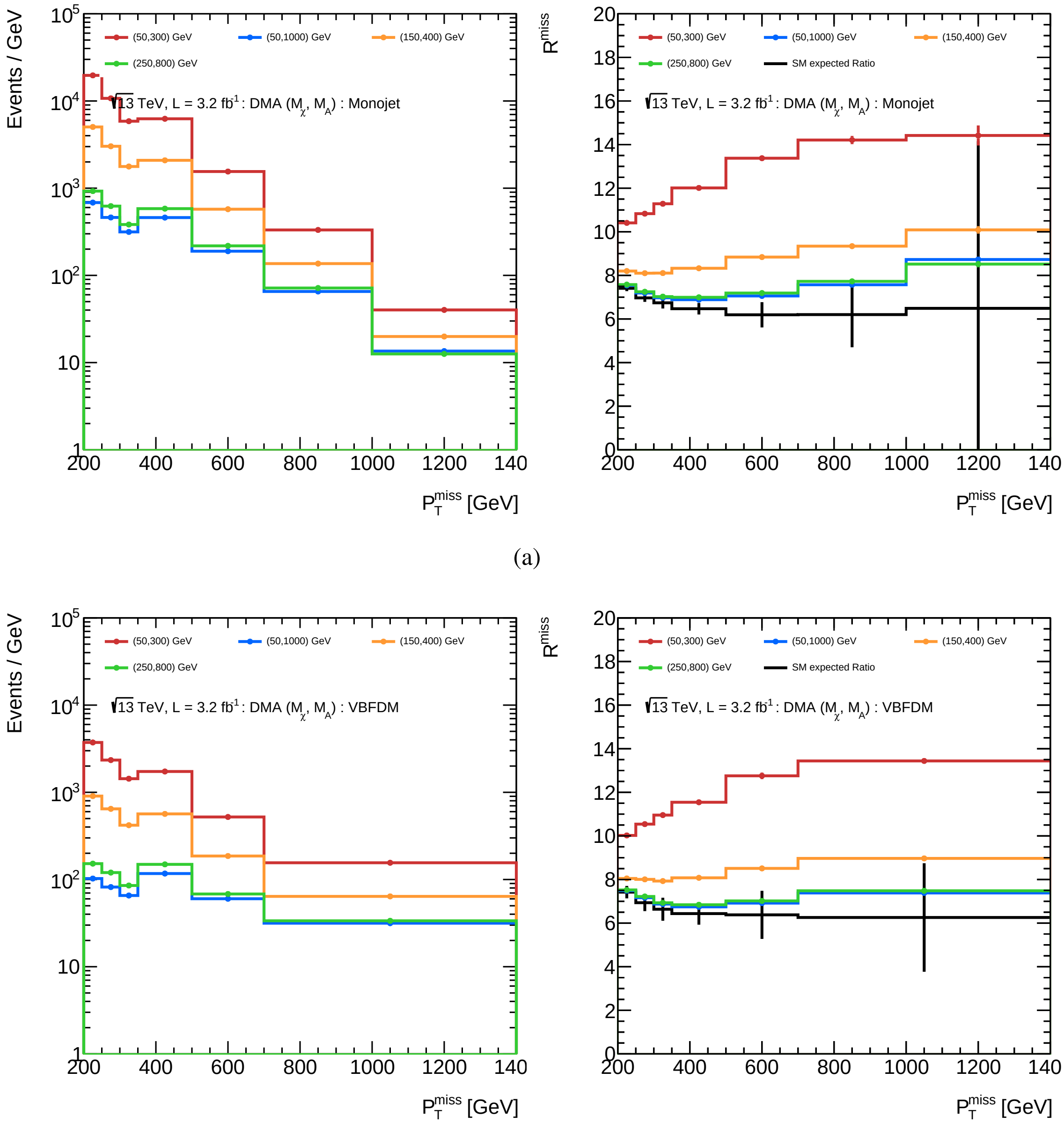

(a)

(b)

Figure 8.3: Missing transverse momentum distributions for a simplified axial-vector mediator WIMP model in the (a) ≥ 1 jet, and (b) VBF kinematic regions. A number of different mass variations under investigation are shown. The distributions on the left are kinematic distributions which are normalised by the cross-section and the luminosity from data collected in this analysis. The right gives the R^{miss} distribution for the Standard Model expected and BSM samples. The Standard Model numerator can be seen in Figures 7.2 and 7.3 to compare with the figures on the left.

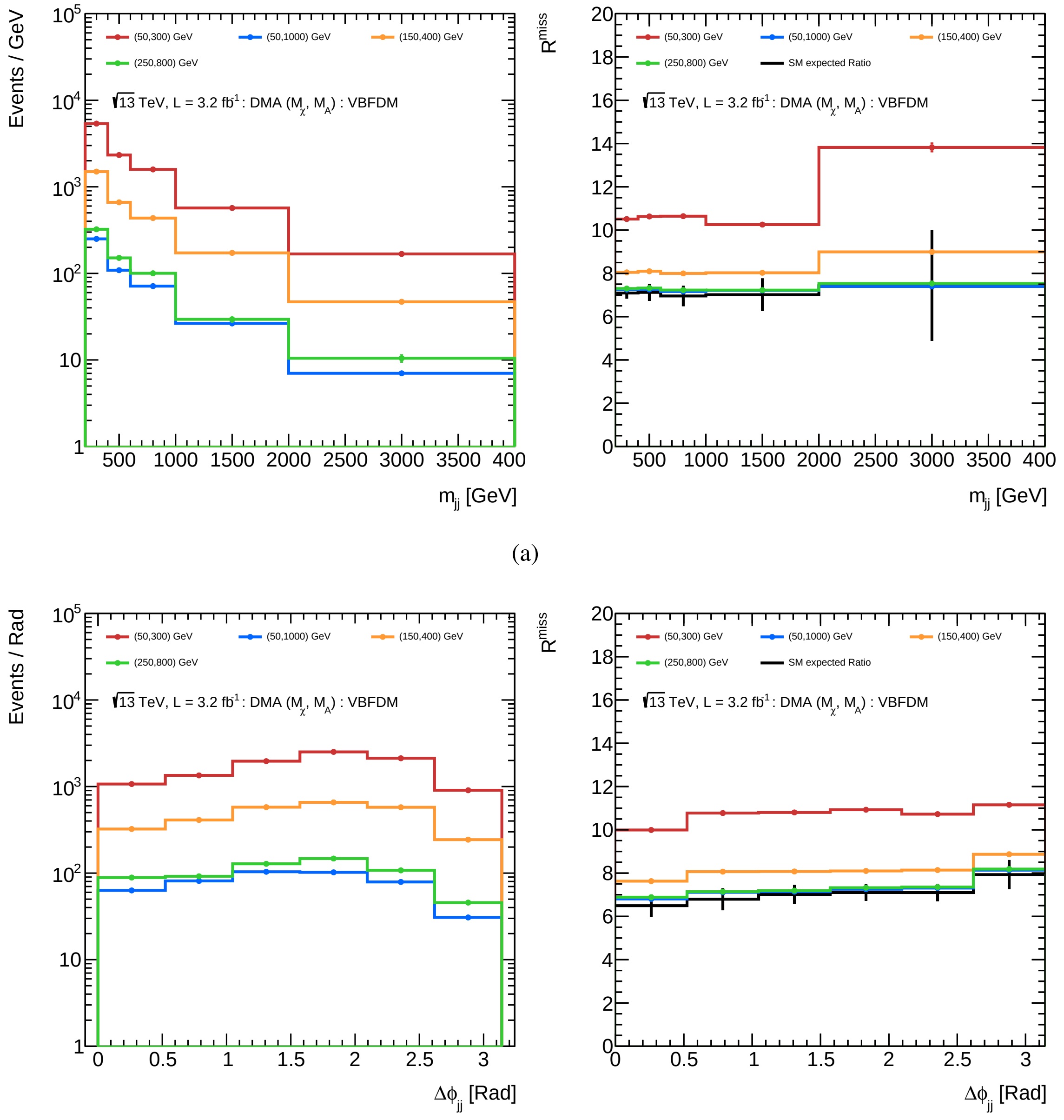

(a)

(b)

Figure 8.4: Dijet invariant mass and $\Delta\phi_{jj}$ distributions for a simplified axial-vector mediator WIMP model in the VBF kinematic region. A number of different mass variations under investigation are shown. The distributions on the left are kinematic distributions which are normalised by cross-section and the luminosity from data collected in this analysis. The right gives the R^{miss} distribution for the Standard Model expected and BSM samples. The Standard Model numerator can be seen in Figures 7.2 and 7.3 to compare with the figures on the left.

$p_{\mathrm{T}}^{\mathrm{miss}}+\text{jets}$ search for comparison—which does not utilise the correlations between multiple distributions to set limits. The range of the expected limit is shown with $\pm 1\sigma$ bands. These bands are created using 1000 statistically fluctuated Standard Model R^{miss} distributions (toys). As four distributions are under study, it is necessary to also fluctuate related bins in each toy. For example, a statistical fluctuation in the m_{jj} distribution may also appear in the $\Delta\phi_{jj}$ distribution due to shared data. Thus, only shifting one bin in one distribution would not reflect the reality of a statistical fluctuation in the dataset. The correlation information between bins can be used to evaluate the effect of a fluctuation in one bin, on all other bins across all distributions. Figure 8.1 gives this statistical correlation information. The exclusion limit calculations are then run on each of the Standard Model toys that surround the expected Standard Model distribution, and the 95 % confidence level coverage is found. The bands represent this coverage.

The band surrounding the observed limits includes the effect of theoretical uncertainties associated with the cross-section of the dark matter model. A red curve is also shown to indicate agreement with the relic density observed by WMAP and Planck [29, 159]. The grey shaded region gives the perturbativity limit, where $m_\chi > \sqrt{\pi/2}m_A$ [160]. This constraint arises as perturbative unitarity can be violated by this type of model at large energies; the expansion of the effective operator is no longer perturbative if the effective coupling is larger than one. The presence of more new physics would be necessary to restore unitarity. This constraint ensures that higher order terms converge, rather than diverge.

A final constraint is given with the blue curve indicating the region where $m_A = 2m_\chi$, above which dark matter particles are too heavy for the mediator to decay via on-shell pair production.

Stronger expected and observed limits than the conventional $p_{\mathrm{T}}^{\mathrm{miss}}+\text{jets}$ analysis can be seen along the $m_A = 2m_\chi$ line. This is due to the inclusion of the low $p_{\mathrm{T}}^{\mathrm{miss}}$ region in the fit and the utilisation of the correlation information between bins. Often, similar analyses to the one discussed in this chapter restrict their search area to a high p_{T} region. However, as can be seen, the information extracted from the low $p_{\mathrm{T}}^{\mathrm{miss}}$ region provides useful shape-constraining power. The R^{miss} ($p_{\mathrm{T}}^{\mathrm{miss}}$) distributions in both kinematic regions (in red and orange) in Figure 8.3 show the lowest mass curves deviating in shape from the Standard Model. In contrast, the conventional analysis is able to set stronger expected limits at high mediator mass. This is attributed to the smaller cross-section of the denominator in the ratio,

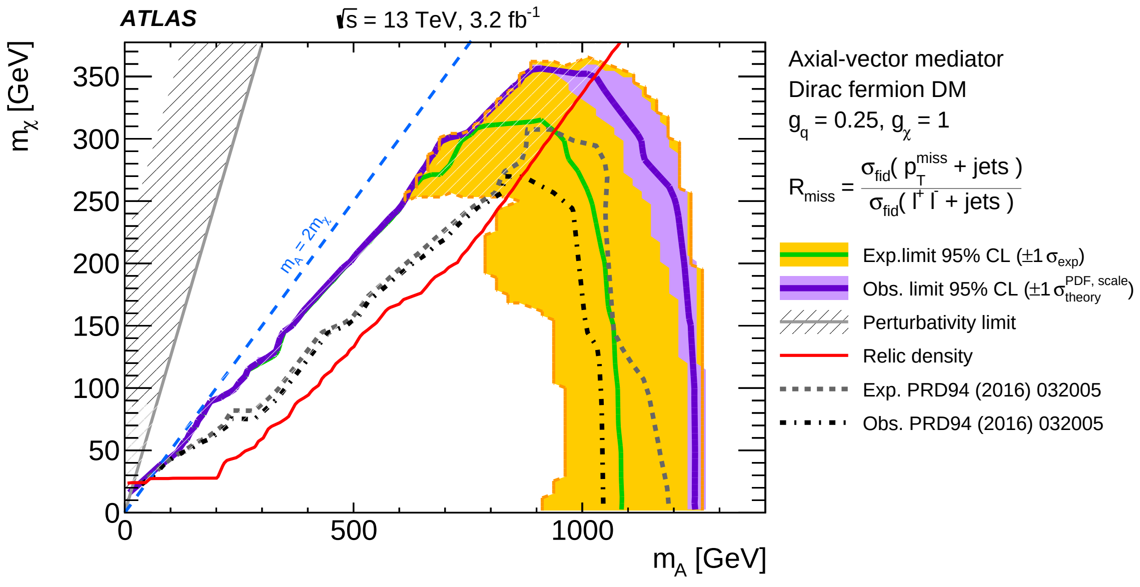

Figure 8.5: Exclusion 95 % CL limits set on the simplified WIMP axial-vector mediator model [141]. The limits found by the previous conventional $p_{\mathrm{T}}^{\mathrm{miss}}$ + jets analysis are shown for comparison. A number of other constraints are also provided for further information.

which gives rise to the statistical limitations seen in this analysis.

As such, the large discrepancy between the expected and observed limits at high mediator mass is driven by statistical fluctuations when taking measurements of large $p_{\mathrm{T}}^{\mathrm{miss}}$. The observed limit here fluctuates up $\sim 1\sigma$ due to anticorrelations, however, it could have fluctuated down instead. Any weaker limits would only be for the observed and would likely be no further than one or two σ away from the expected limit.

8.1.3 Exclusion limit variations

A number of different contributions were necessary to produce the final 95 % confidence level exclusion limits: each distribution for both expected, observed, dark matter and Standard Model; and the statistical, systematic, and theoretical uncertainties for each. These contributions were evaluated in order to investigate discrepancies in the final expected and observed limits, as well as to understand the difference in sensitivity between the presented and dedicated analyses.

The first study investigates the contribution of each of the four R^{miss} distributions. Figures 8.6 and 8.7 show that the strongest constraining power belongs to the $p_{\mathrm{T}}^{\mathrm{miss}}$ distribution in the ≥ 1 jet kinematic region. This result is expected due to the use of the ≥ 1 jet kinematic region in the dedicated analysis, also shown on each figure for comparison.

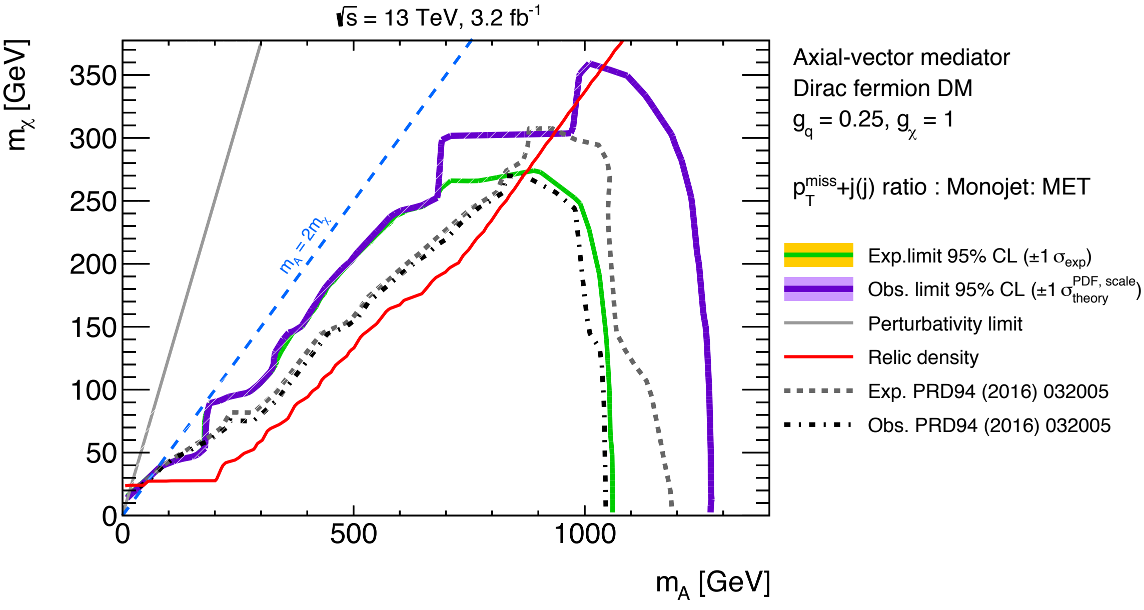

(a) p_T^{miss} ($\geq$ 1jet)

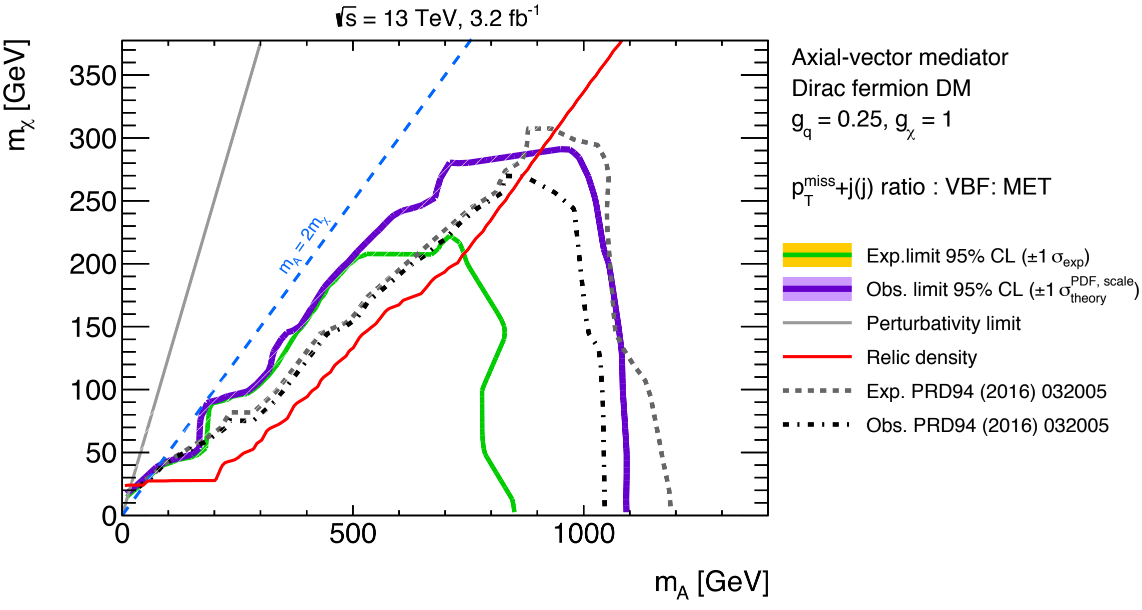

(b) p_T^{miss} (VBF)

Figure 8.6: Expected and observed 95 % confidence level exclusion limits are shown for a simplified WIMP dark matter model with an axial-vector mediator particle for the first two distributions of R^{miss}: p_T^{miss} for (a) the $\geq$ 1jet kinematic region, and (b) the VBF kinematic region.

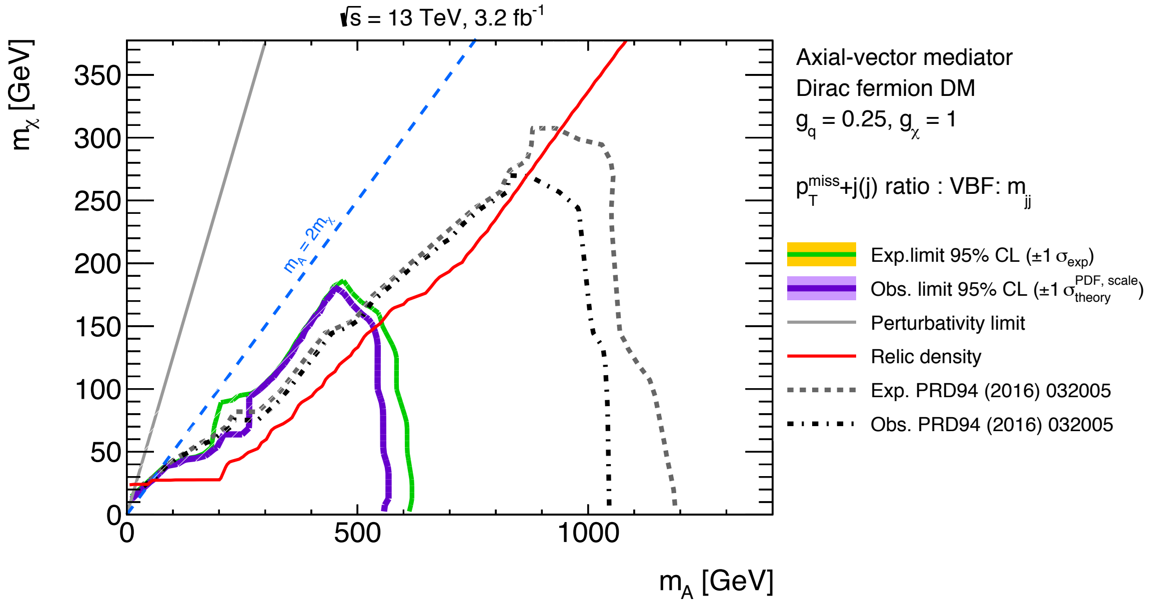

(a) m_{jj} (VBF)

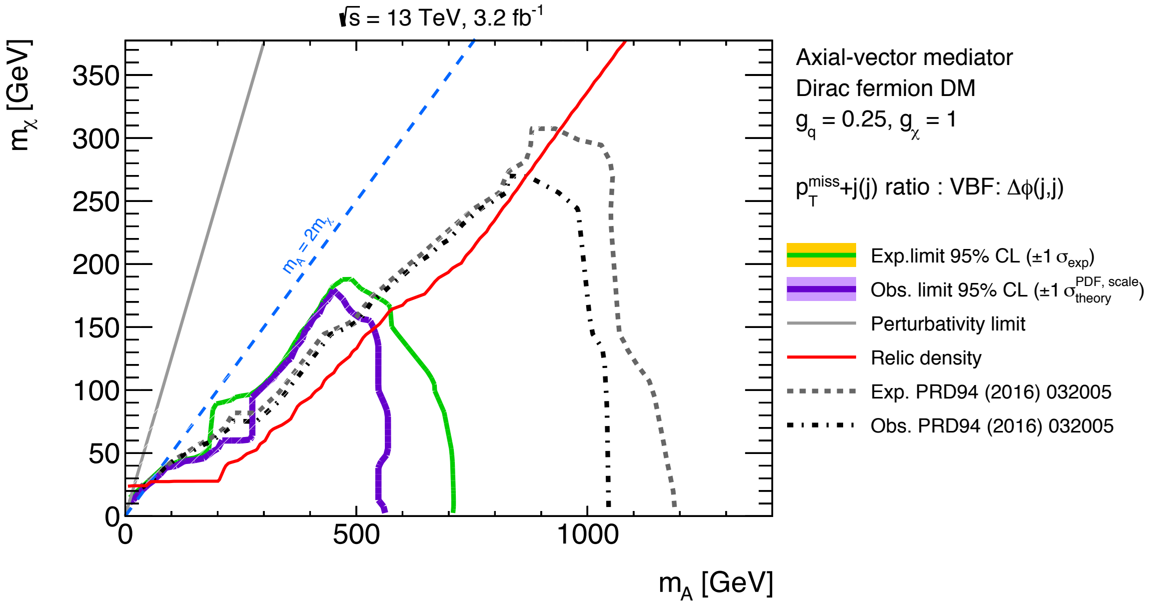

(b) $\Delta\phi_{jj}$ (VBF)

Figure 8.7: Expected and observed 95 % confidence level exclusion limits are shown for a simplified WIMP dark matter model with an axial-vector mediator particle for the final two distributions of R^{miss}: (a) m_{jj} (VBF), and (b) $\Delta\phi_{jj}$ (VBF).

The effect of systematically adding in each type of uncertainty and then including correlations between bins in the covariance matrix is displayed in Figures 8.8 and 8.9.

Figure 8.8 (a) gives the expected and observed 95 % confidence level exclusion limits for a covariance matrix with only statistical uncertainties included and no correlations between bins. The observed limit is vastly weakened. This behaviour is due to p-values for the SM+DM ratio, with a mediator mass of $\sim$ 1 TeV representing a closer description of the data than the Standard Model ratio alone; the $\chi^2_{\text{SM+DM}}$ at a mediator mass of 1.2 TeV in observed data is 28, while $\chi^2_{\text{SM}} = 32$. As our statistical procedure penalised the observed $p_{\text{s+b}}$ against the p_{b}, dark matter frameworks that are a better, or equivalent, fit to the data as the Standard Model cannot be excluded.

Figure 8.8 (b), which again shows 95 % confidence level exclusion limits with statistical uncertainties, additionally includes the theoretical uncertainties. A reduction in the expected sensitivity can be seen due to this inclusion, however, there is little change in the observed sensitivity. The small step difference at the approximate point (750, 150) GeV, on the observed contour, is due to the discrete grid system on which the test contours are drawn. This step only requires one or two of these discrete points to have a slight change in sensitivity to produce this effect. Structures at the size of $\sim$ 100 GeV steps therefore are not significant.

The effect of the systematic uncertainties in the covariance matrix is shown in Figure 8.9 (a). The expected exclusion limits again slightly degrade relative to the limits with statistical and theoretical uncertainties only. The observed limit is still weaker than the expected. However, the additional systematic uncertainty contributions cause the observed limit to approach the expected. This occurs as dark matter frameworks with mediator masses near 800 GeV begin to become a worse description of the data than the Standard Model. This stage is the last before systematic correlations within the $p_{\text{T}}^{\text{miss}}$ ($\geq$ 1jet) distribution are included in the fit, and the exclusion limits return to the nominal case. The shape of the observed data distribution therefore drives the $\sim 1\sigma$ shift upward in the observed limit shown in Figure 8.9 (b).

The exclusion limits were further probed by progressively removing the first three bins of the $p_{\text{T}}^{\text{miss}}$ distribution in the $\geq$ 1 jet kinematic region from the fit. Figures 8.10 and 8.11 show how the shape of this distribution (Figure 7.8 (a)) has influenced the results, with all uncertainties and correlations still included. It can be seen that both limits progressively degrade, with the largest difference occurring in the observed limit when the second bin

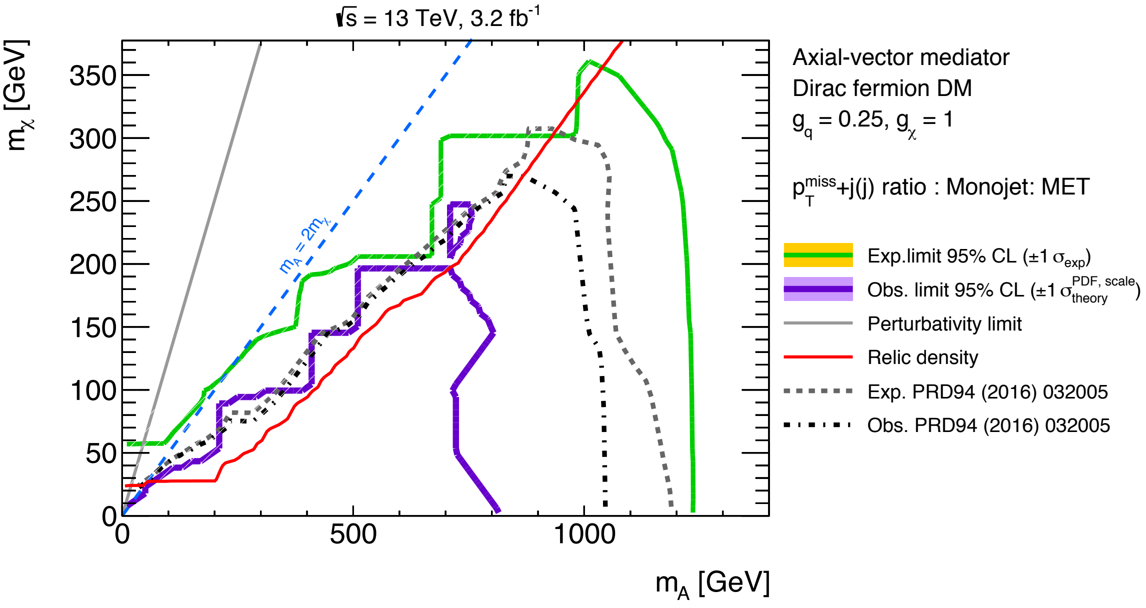

(a) Statistical uncertainties only.

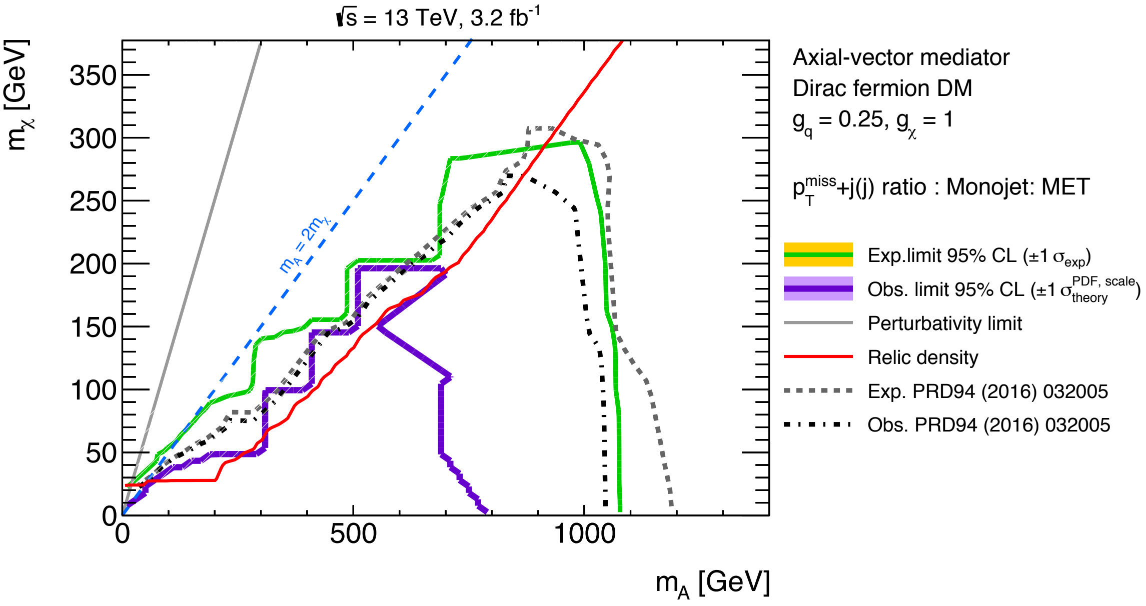

(b) Statistical and theoretical uncertainties.

Figure 8.8: Expected and observed 95 % confidence level exclusion limits are shown for a simplified WIMP dark matter model with an axial-vector mediator particle, including in the covariance matrix: (a) only statistical uncertainties, and (b) statistical and theoretical uncertainties.

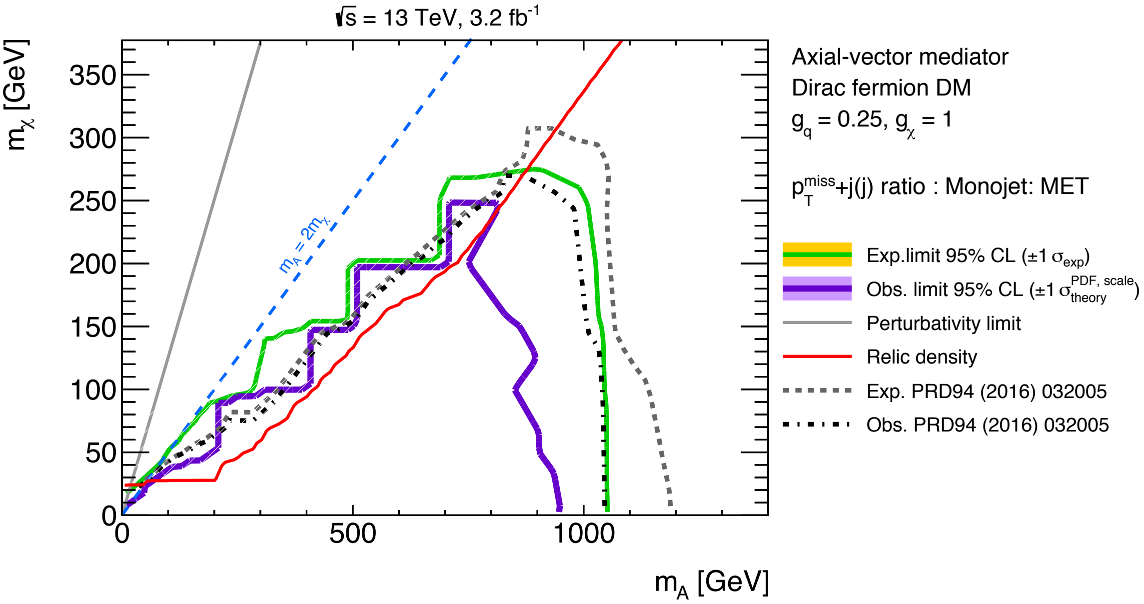

(a) All uncertainties, no correlations.

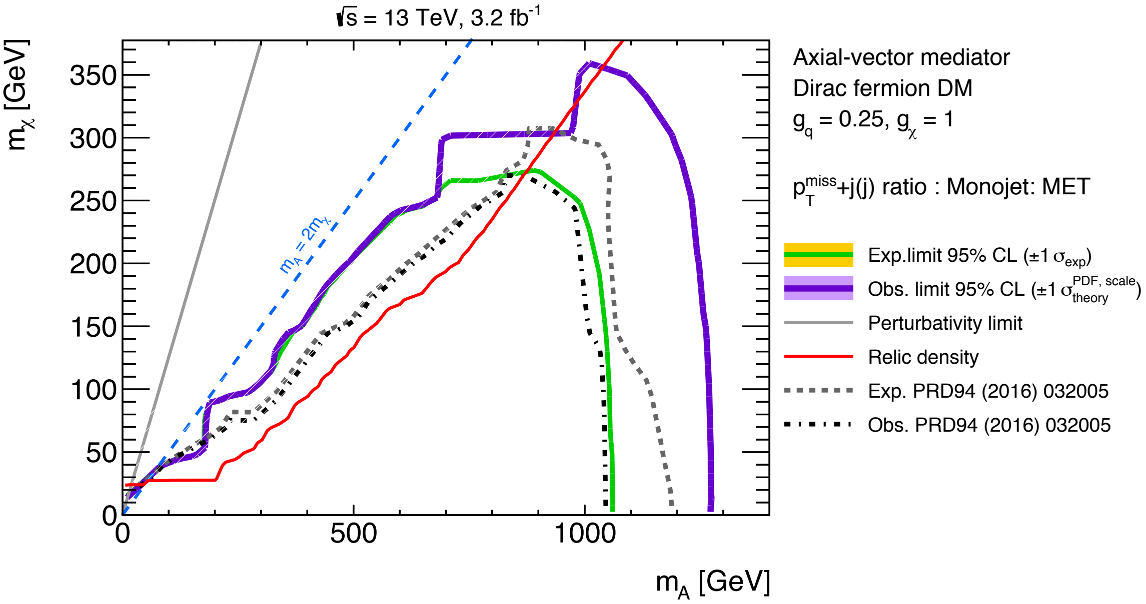

(b) All uncertainties and correlations.

Figure 8.9: Expected and observed 95 % confidence level exclusion limits are shown for a simplified WIMP dark matter model with an axial-vector mediator particle, including in the covariance matrix: (a) all uncertainties, but no correlations between bins, and (b) all uncertainties and correlations.

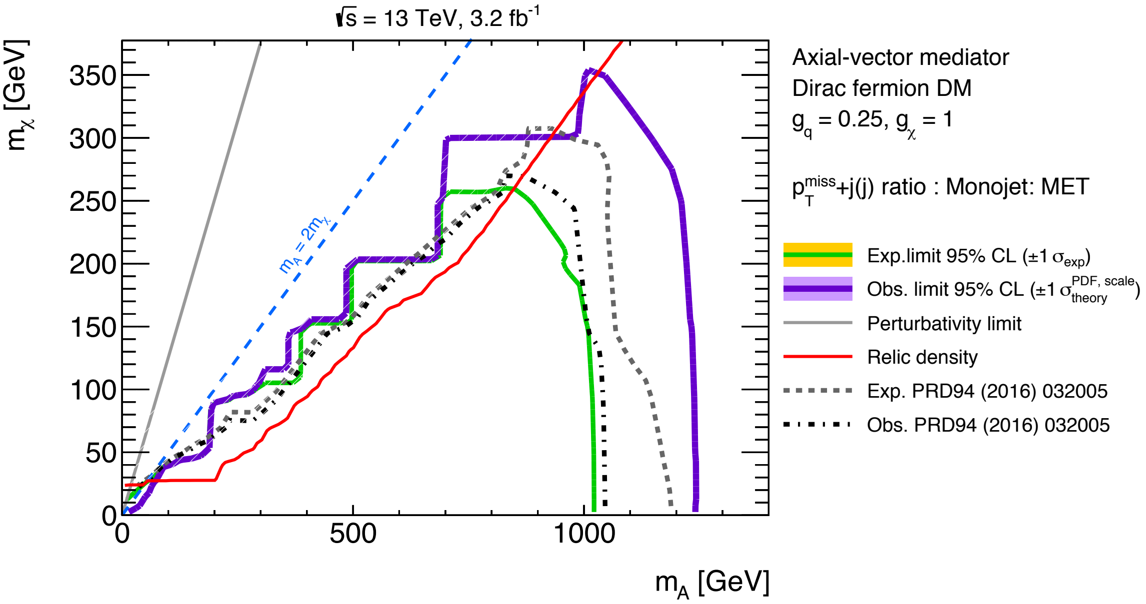

(a) 1st bin removed.

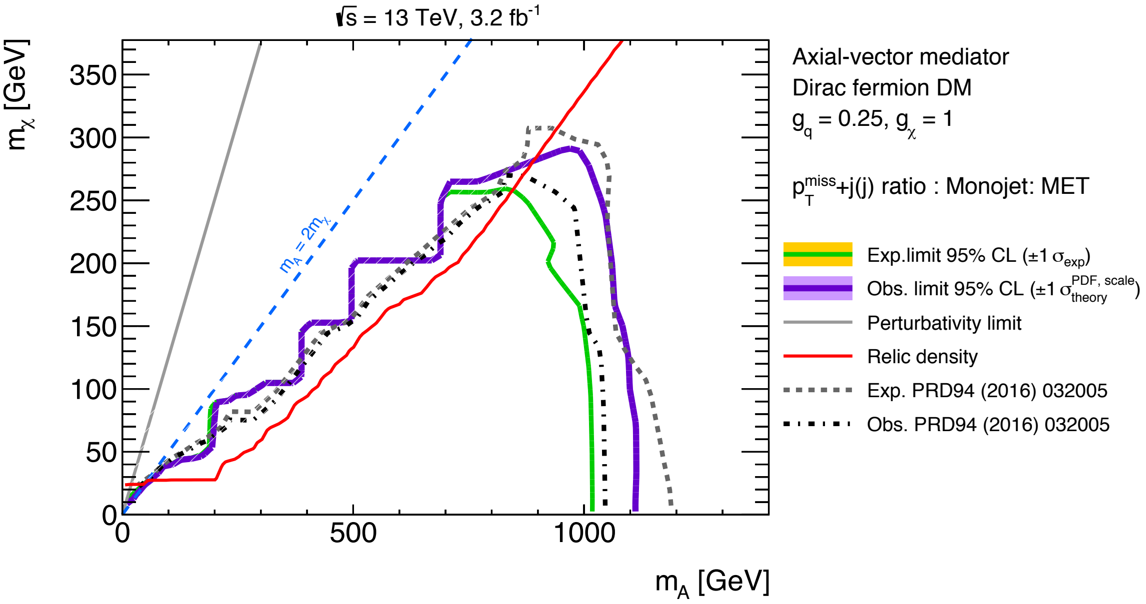

(b) 1st and 2nd bins removed.

Figure 8.10: Expected and observed 95 % CL exclusion limits are shown for a simplified WIMP dark matter model with an axial-vector mediator particle for distributions with the (a) first, and (b) second bins progressively removed.

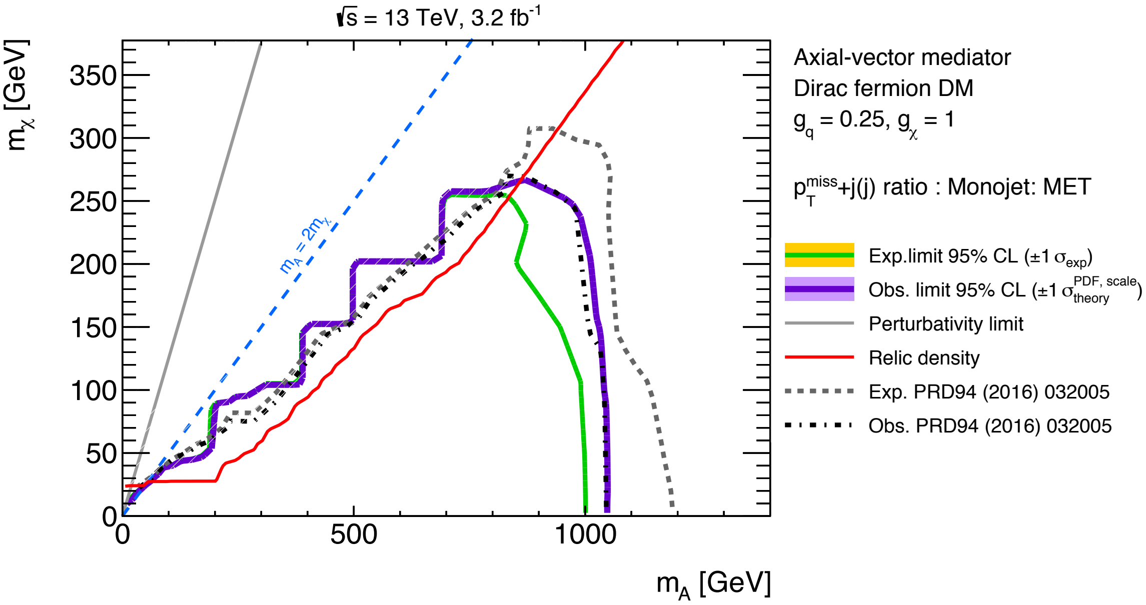

(a) 1st, 2nd, and 3rd bins removed.

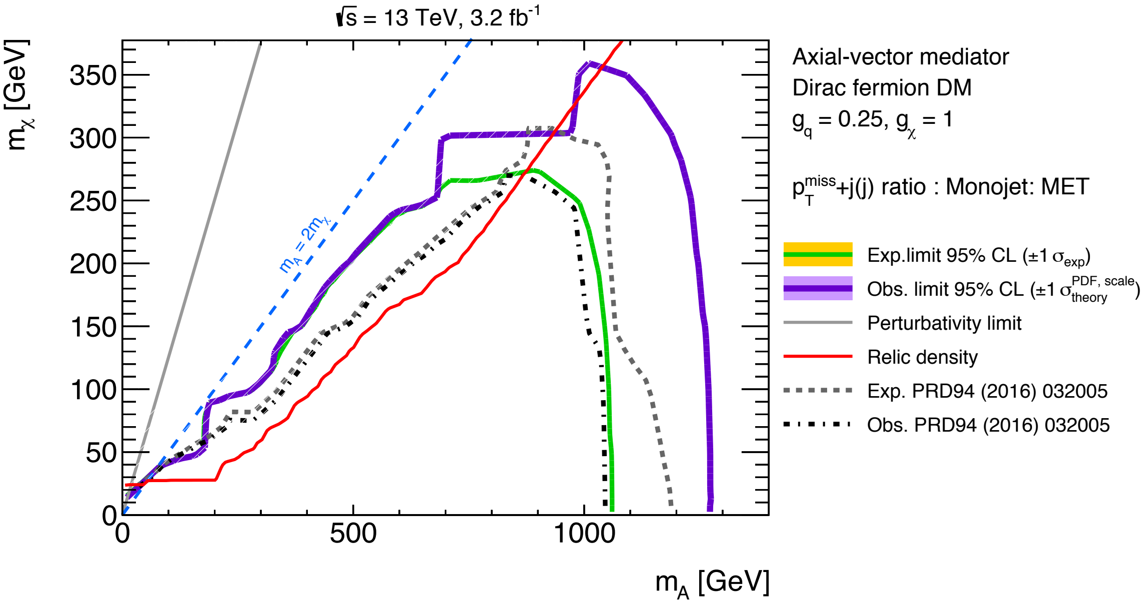

(b) All bins included.

Figure 8.11: Expected and observed 95 % CL exclusion limits are shown for a simplified WIMP dark matter model with an axial-vector mediator particle for distributions with the (a) first, second, and third bins removed. (b) includes all bins.

is removed. This approach of the observed limit to the expected is due to the upwards statistical fluctuation of the data in the named bin. This is consistent with the conclusion that the stronger limits arise from the shape information included in the correlations between bins.

As a final study, the effect on the exclusion limits of shifts in single bins is investigated. Figures 8.12 and 8.13 show the results of shifting single bins in the observed R^{miss} ($p_{\text{T}}^{\text{miss}}$, ≥ 1 jet kinematic region) distribution to the Standard Model expectation value. All uncertainty and correlation information is included throughout this study. It can be seen that any single shift of one of the more divergent bins is enough to remove most of the 1σ observed-expected limit discrepancy.

8.2 A weak boson fusion effective field theory

The four detector-corrected R^{miss} distributions are, in addition, used to set 95 % CL exclusion limits on two generalised effective field theory Dirac fermion dark matter models. In these models, dark matter is produced via the interactions of electroweak bosons. They adopt Dirac fermion dark matter candidates as a standard benchmark for study. Assuming that BSM physics is at a higher energy scale than the Standard Model, the effective field theory Lagrangians can be constructed for dimensions > 4 with only minor model dependence. This general Lagrangian is given by:

$$\mathcal{L} = \mathcal{L}^{\text{SM}} + \frac{f^{(5)}}{\Lambda} \sum O^{(5)} + \frac{f^{(6)}}{\Lambda^2} \sum O^{(6)} + \frac{f^{(7)}}{\Lambda^3} \sum O^{(7)} + ..., \tag{8.7}$$

where $\mathcal{L}^{\text{SM}}$ is the dimension 4 Standard Model Lagrangian. The following terms are higher-dimension extensions. The $f^{(5,6,7,etc.)}$ terms are the Wilson coefficients—set to 1 for this analysis—for the relative effective operators, $O^{(5,6,7,etc.)}$. Λ is the energy scale used to suppress this set of operators. This, and the dark matter mass m_χ give the plane on which the limits are set. The energy suppression scale places limits on which interactions can occur. The different effective operators associated with different energy suppression scales are detailed in Table 8.1. For all operators, a minimum scale of 100 GeV is used as a common baseline reference for all event generation. However, certain operators have stronger constraints on the effective field theory scale arising from the Z invisible width [161, 162]. The D5c effective operator, for example, allows a new decay channel for the Z if dark matter

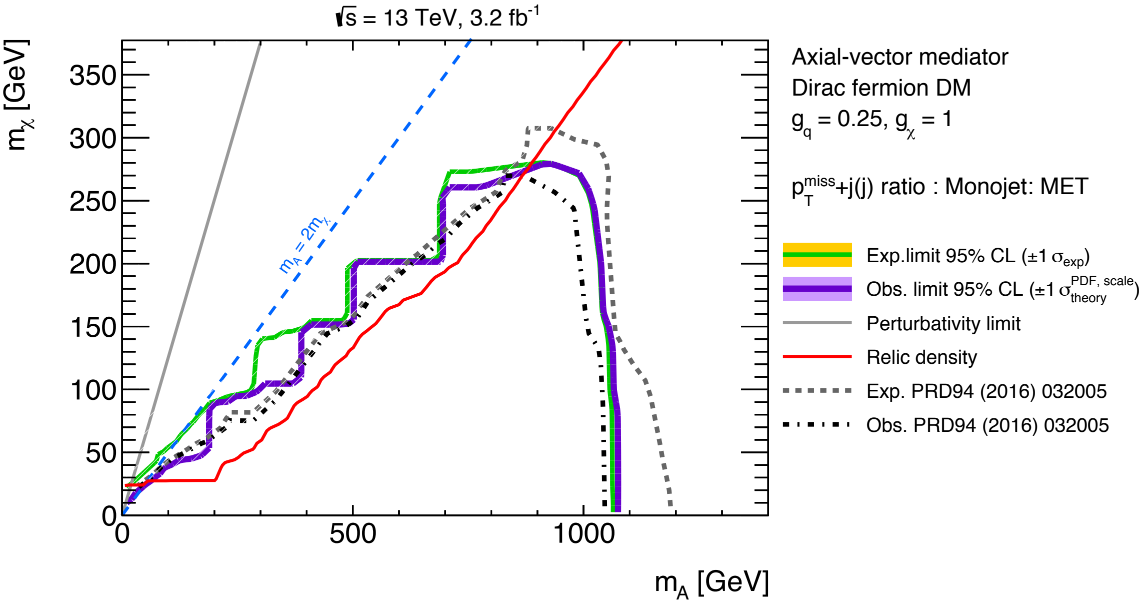

(a) 2^{nd} bin shifted.

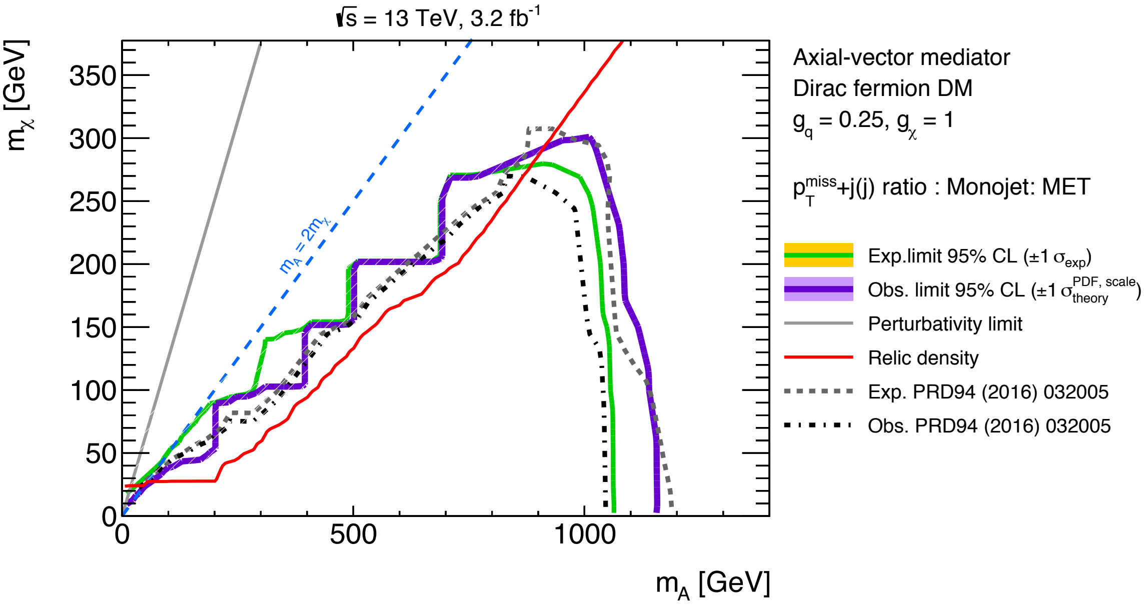

(b) 3^{rd} bin shifted.

Figure 8.12: Expected and observed 95 % CL exclusion limits are shown for a simplified WIMP dark matter model with an axial-vector mediator particle for distributions with the (a) second, and (b) third bins each shifted to the Standard Model expectation value in turn.

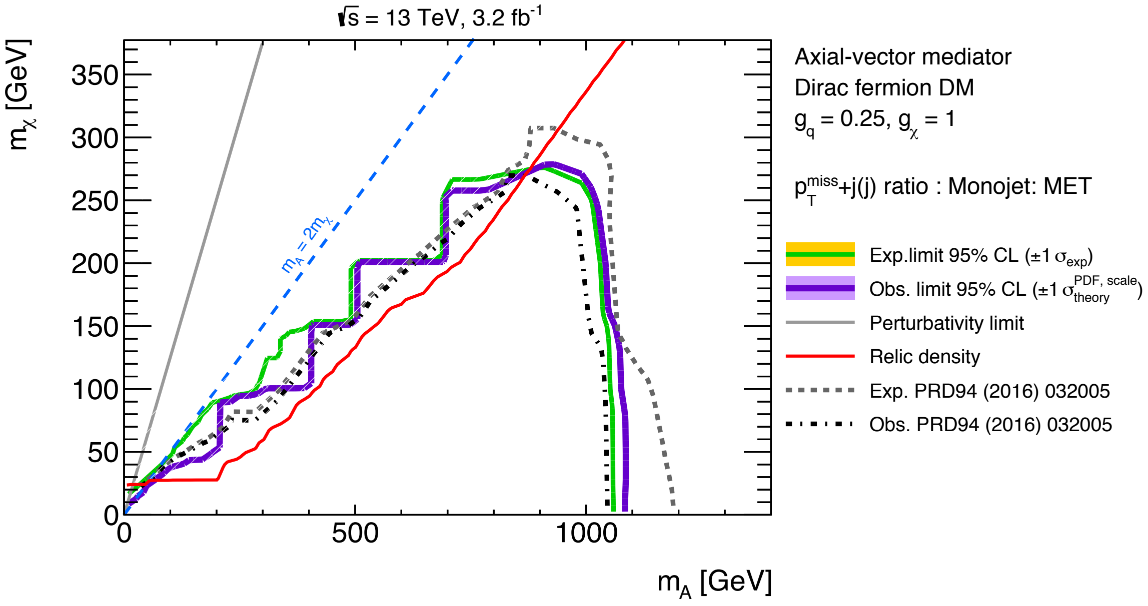

(a) 4th bin shifted.

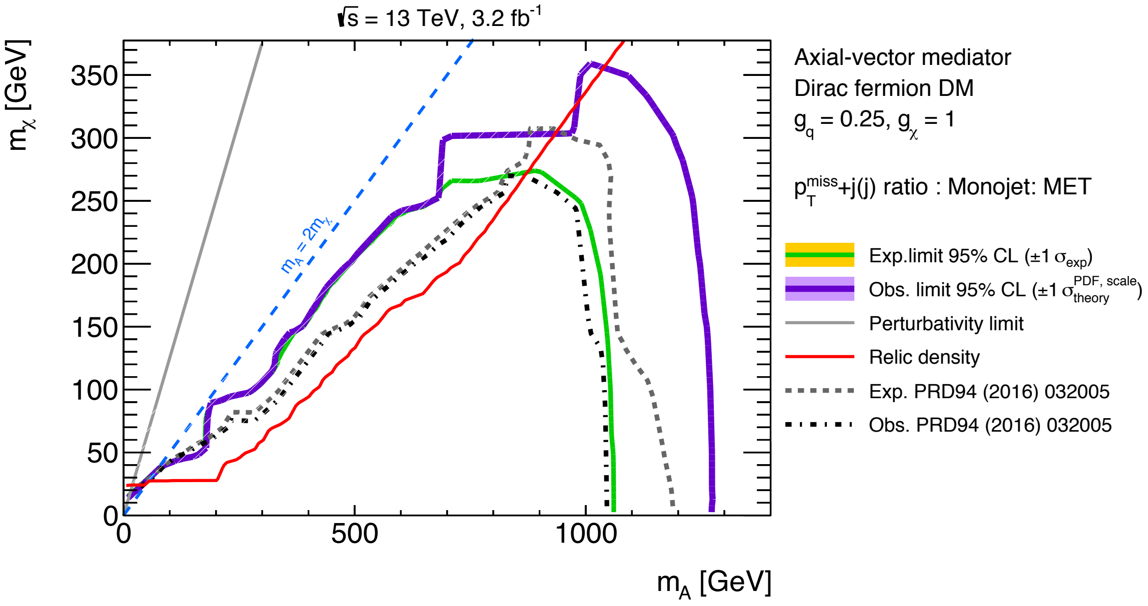

(b) No bins shifted.

Figure 8.13: Expected and observed 95 % CL exclusion limits are shown for a simplified WIMP dark matter model with an axial-vector mediator particle for distributions with the (a) fourth bin shifted to the Standard Model expectation value. (b) is the nominal distribution with no bins shifted.

particles are produced on-shell. For $m_\chi < m_Z/2$ the decay width is given by:

$$\Gamma(Z \to \chi\bar{\chi}) = \frac{2\alpha m_Z^3}{3\Lambda^2 \cos^2\theta_W \sin^2\theta_W}\left(1+\frac{8m_\chi^2}{m_Z^2}\right)\sqrt{1-\frac{4m_\chi^2}{m_Z^2}} \tag{8.8}$$

$$= (2.2\text{ GeV})\left(\frac{\Lambda}{100\text{ GeV}}\right)^{-2}\left(1+\frac{8m_\chi^2}{m_Z^2}\right)\sqrt{1-\frac{4m_\chi^2}{m_Z^2}}, \tag{8.9}$$

and as the Z invisible width is measured to a resolution of $\delta Z \sim 2$ MeV, massless dark matter would impose a minimum scale of 3.3 TeV. The D5d and D6 operators are limited in a similar way. These limitations are only valid for the on-shell pair production of dark matter particles. Therefore only dark matter particles with masses $< m_Z/2$ are excluded.

The effective field theory model studied here makes the assumption that the dark matter (χ) is either a Dirac or Majorana fermion, and that effective operators facilitating the coupling of the χ to Standard Model bosons ($V = \gamma$, W, or Z) are of dimension D ≤ 7 with either three $V\chi\chi$ or four $VV\chi\chi$ point couplings. D5 operators arise from exchanges mediated by new heavy scalar (D5a) or pseudoscalar (D5b) bosons, or interactions related to models with dark magnetic (D5c) or electric (D5d) dipole moments [163–170]. D6 operators can arise from the exchange of a new neutral vector boson. D7 operators are related to 1-loop diagrams.

For a UV-complete theory, Λ is related to the mediator mass as $1/\Lambda^2 \sim (g_{\mathrm{SM}} g_\chi)/m_{\mathrm{A}}^2$ where g_{SM} and g_χ are the Standard Model and dark matter particle coupling constants. The effective field theory scale also dictates the rate at which a process occurs under the studied dark matter model framework. This rate is proportional to $\Lambda^{-2(D-4)}$, where D is the dimension of the operator. In order to produce working points across the effective field theory scale range, each dark matter mass point is scaled by $(\Lambda'/\Lambda)^{-2(D-4)}$.

For this study, it is assumed that the particular operator under study is the dominant interaction channel at that dimensionality. Although this is an approximately model-independent approach to represent electroweak boson–dark matter interactions, weak boson fusion interactions are expected to be optimised for LHC searches.

8.2.1 Production rates

The ten contact-interaction Lagrangians detailed in Table 8.1 allow for the generation of parton-level rate predictions within a vector boson fusion kinematic region. Table 8.2 summarises the cross-sections for the pair production of dark matter particles at $\Lambda = 100$ GeV

Name	Operator	Dimension	Minimum EFT Scale (GeV)
D5a	$\bar{\chi}\chi\left[\frac{Z_\mu Z^\mu}{2}+W^+_\mu W^{-\mu}\right]$	5	100
D5b	$\bar{\chi}\gamma^5\chi\left[\frac{Z_\mu Z^\mu}{2}+W^+_\mu W^{-\mu}\right]$	5	100
D5c	$\frac{g}{2\cos\theta_W}\bar{\chi}\sigma^{\mu\nu}\chi\left[\delta_\mu Z_\nu-\delta_\nu Z_\mu\right]$	5	3300
D5d	$\frac{g}{2\cos\theta_W}\bar{\chi}\sigma^{\mu\nu}\chi\varepsilon^{\mu\nu\sigma\rho}\left[\delta_\rho Z_\sigma-\delta_\sigma Z_\rho\right]$	5	6600
D6a	$\frac{g}{2\cos\theta_W}\bar{\chi}\gamma^\mu\delta^\nu\chi\left[\delta_\mu Z_\nu-\delta_\nu Z_\mu\right]$	6	230
D6b	$\frac{g}{2\cos\theta_W}\bar{\chi}\gamma_\mu\delta_\nu\chi\varepsilon^{\mu\nu\sigma\rho}\left[\delta_\rho Z_\sigma-\delta_\sigma Z_\rho\right]$	6	330
D7a	$\bar{\chi}\chi W^{i,\mu\nu}W^i_{\mu\nu}$	7	100
D7b	$\bar{\chi}\gamma^5\chi W^{i,\mu\nu}W^i_{\mu\nu}$	7	100
D7c	$\bar{\chi}\chi\varepsilon^{\mu\nu\sigma\rho}W^{i,\mu\nu}W^i_{\rho\sigma}$	7	100
D7d	$\bar{\chi}\gamma^5\chi\varepsilon^{\mu\nu\sigma\rho}W^{i,\mu\nu}W^i_{\rho\sigma}$	7	100

Table 8.1: Effective operators as defined in Reference [171], where χ and $\bar{\chi}$ are Dirac or Majorana fermionic dark matter particles and Z and W are Standard Model boson operators.

	Cross-section (pb)				
Operator	DM mass (GeV)				
	10	100	400	700	1000
D5a	102.6 ± 0.2	94.7 ± 0.3	51.0 ± 0.14	22.5 ± 0.08	9.1 ± 0.02
D5b	101.8 ± 0.3	99.7 ± 0.3	68.3 ± 0.2	37.7 ± 0.13	18.66 ± 0.03
D5c	4361.7 ± 9.1	60.8 ± 0.1	5.8 ± 0.02	1.34 ± 0.005	0.37 ± 0.001
D5d	15221 ± 32	94.6 ± 0.2	6.49 ± 0.08	1.14 ± 0.01	0.26 ± 0.0007
D6a	151.1 ± 0.3	44.5 ± 0.1	22.7 ± 0.03	10.88 ± 0.009	4.99 ± 0.02
D6b	562 ± 1	139.0 ± 0.3	41.76 ± 0.1	13.27 ± 0.02	4.25 ± 0.01
D7a	42428 ± 108	41530 ± 115	37468 ± 93	29801 ± 49	10288 ± 29
D7b	41855 ± 79	42372 ± 115	36366 ± 72	26846 ± 59	17610 ± 47
D7c	$1.67 \times 10^5 \pm 301$	$1.63 \times 10^5 \pm 490$	$1.39 \times 10^5 \pm 381$	$1.03 \times 10^5 \pm 214$	40920 ± 115
D7d	$1.67 \times 10^5 \pm 295$	$1.66 \times 10^5 \pm 450$	$1.44 \times 10^5 \pm 403$	$1.06 \times 10^5 \pm 198$	69975 ± 185

Table 8.2: Dark matter effective field theory VBF model production rates for dark matter pair production in association with exactly two jets from Madgraph *before* kinematic acceptance criteria. These cross-sections use a baseline effective field theory scale of 100 GeV for all values quoted, which in some cases can be excluded from $Z \to$ invisibles measurements. Cross-sections can be re-calculated at an arbitary scale Λ' by multiplying quoted values by $(\Lambda'/100\text{ GeV})^{-2(D-4)}$.

for each operator before the VBF selection criteria has been applied. After applying the VBF selection criteria, the total rate is reduced by that detailed in Table 8.3. Acceptance is defined as the fraction of generated events passing the VBF kinematic region selections defined in Section 7.3, at parton-level. Table 8.4 gives the new cross-sections after the kinematic selections have been applied.

These cross-sections do not take into account the constraints arising from the Z invisible width measurement. The D5c, D5d, D6a, and D6b operator processes are all suppressed up to their individual effective field theory scales: 3.3 TeV, 6.6 TeV, 230 GeV, and 330 GeV respectively. However, this supression is only known to be valid for the on-shell pair production of dark matter particles—at $m_\chi < m_Z/2$.

8.2.2 Kinematic variations between models

Figures 8.14 and 8.15 illustrate the dependence of the dark matter distributions in the ≥ 1 jet and VBF kinematic regions on each operator. The dark matter mass and effective field theory scale are fixed at 400 GeV and 100 GeV, respectively. On the left are the differential distributions, and on the right are the R^{miss} distributions for all operators under investigation. All four observables being used for this measurement are shown. The shape information of these distributions is vital for this analysis due to the reliance on the uncertainty correlations

	Acceptance (%)				
Operator	DM mass (GeV)				
	10	100	400	700	1000
D5a	7.9	8.5	7.7	6.5	5.9
D5b	7.5	8.3	7.5	6.9	6.4
D5c	5.5	3.9	8.0	9.2	10.0
D5d	5.1	5.3	8.9	9.7	10.1
D6a	2.0	7.6	8.4	9.6	9.8
D6a	2.1	7.4	9.8	9.8	10.2
D7a	44.2	44.2	43.8	43.5	43.1
D7b	44.5	44.1	43.6	43.4	43.3
D7c	46.2	45.7	45.4	44.9	43.4
D7d	46.6	46.5	46.4	44.7	43.6

Table 8.3: Kinematic acceptance for each effective field theory operator and dark matter mass combination when applying the VBF fiducial region selection criteria to the parton-level events.

	Cross-section (pb)				
Operator	DM mass (GeV)				
	10	100	400	700	1000
D5a	8.17 ± 0.02	8.08 ± 0.03	3.93 ± 0.01	1.46 ± 0.005	0.51 ± 0.001
D5b	7.66 ± 0.02	8.25 ± 0.03	5.11 ± 0.02	2.61 ± 0.009	1.19 ± 0.002
D5c	23.99 ± 0.50	2.37 ± 0.004	0.47 ± 0.002	0.12 ± 0.0005	0.04 ± 0.0001
D5d	77.63 ± 1.63	5.06 ± 0.01	0.57 ± 0.007	0.11 ± 0.001	0.03 ± 0.0001
D6a	3.06 ± 0.01	3.37 ± 0.008	1.91 ± 0.003	1.04 ± 0.0009	0.48 ± 0.002
D6b	11.98 ± 0.02	10.39 ± 0.02	4.10 ± 0.01	1.30 ± 0.002	0.43 ± 0.001
D7a	18753 ± 47	18356 ± 50	16410 ± 40	12963 ± 21	4434 ± 12
D7b	18634 ± 35	18703 ± 50	15862 ± 31	11640 ± 25	7604 ± 20
D7c	77154 ± 139	75862 ± 224	65376 ± 159	47594 ± 96	17759 ± 49
D7d	77998 ± 137	77547 ± 209	66947 ± 187	47485 ± 88	30516 ± 80

Table 8.4: Dark matter effective field theory VBF model production rates for dark matter pair production in association with exactly two jets *after* the application of kinematic acceptance criteria. These cross-sections use a baseline effective field theory scale of 100 GeV for all values quoted.

between bins. It can be seen that some operators give stronger distinguishing power from the Standard Model than others: D5a, D5b and D7 effective operators give the largest difference in shape in the m_{jj} distribution for example. Most effective operators also differ in shape in the $p_{\mathrm{T}}^{\mathrm{miss}}$ and $\Delta\phi_{jj}$ distributions at high $p_{\mathrm{T}}^{\mathrm{miss}}$ and low $\Delta\phi_{jj}$ respectively. This influences the decision to choose these observables to set limits on the given dark matter models.

Figures 8.16 and 8.17 compare the same distributions for the D5a operator at a spread of different dark matter masses. The effective field theory scale is set at 100 GeV for this comparison. Again, the differential distributions are on the left, with the R^{miss} distributions on the right. In all cases of the R^{miss} distribution, the discrepancy from the Standard Model decreases with increasing dark matter mass. All masses produce the largest difference in shape at high $p_{\mathrm{T}}^{\mathrm{miss}}$, high m_{jj} and low $\Delta\phi_{jj}$. However, low dark matter masses still have a significant discrepancy from the Standard Model at low $p_{\mathrm{T}}^{\mathrm{miss}}$ in the VBF kinematic region.

8.2.3 Correlations in dark matter models

Studying more than one differential observable, and accounting for correlations between them, offers the potential for greater sensitivity to the presence of dark matter particles. A number of examples of the correlations between the observables $\Delta\phi_{jj}$ and m_{jj} are given in Figures 8.18 and 8.19 for all effective operators previously mentioned in this section. A Standard Model background is also included to illustrate the regions for optimum sensitivity to a dark matter signal above the Standard Model.

Due to the large value of the effective field theory scale suppression for D5c to D6b operators, the dark matter signal observed in these channels would not be seen at the set scale of $\Lambda = 100$ GeV. The suppression scale has not been applied here as it is only valid for values of dark matter mass less than half the mass of the Z boson. These operators show the largest production rate at high $\Delta\phi_{jj}$ and low m_{jj}; this kinematic region appears to be the same area in which the Standard Model process mostly operates, and as such, the sensitivity will be reduced. The remaining operators show sensitivity to regions of the plane of the two observables that the Standard Model does not. This allows discriminating power at largely high m_{jj} and all regions of $\Delta\phi_{jj}$ when all the remaining operators are considered. Effective operators D7a and D7c give close to opposite discriminating power at high m_{jj}; D7a shows the most sensitivity at low and high $\Delta\phi_{jj}$ and D7c shows the most sensitivity to central values of $\Delta\phi_{jj}$. This aided in the decision to utilise them for limit setting in the first

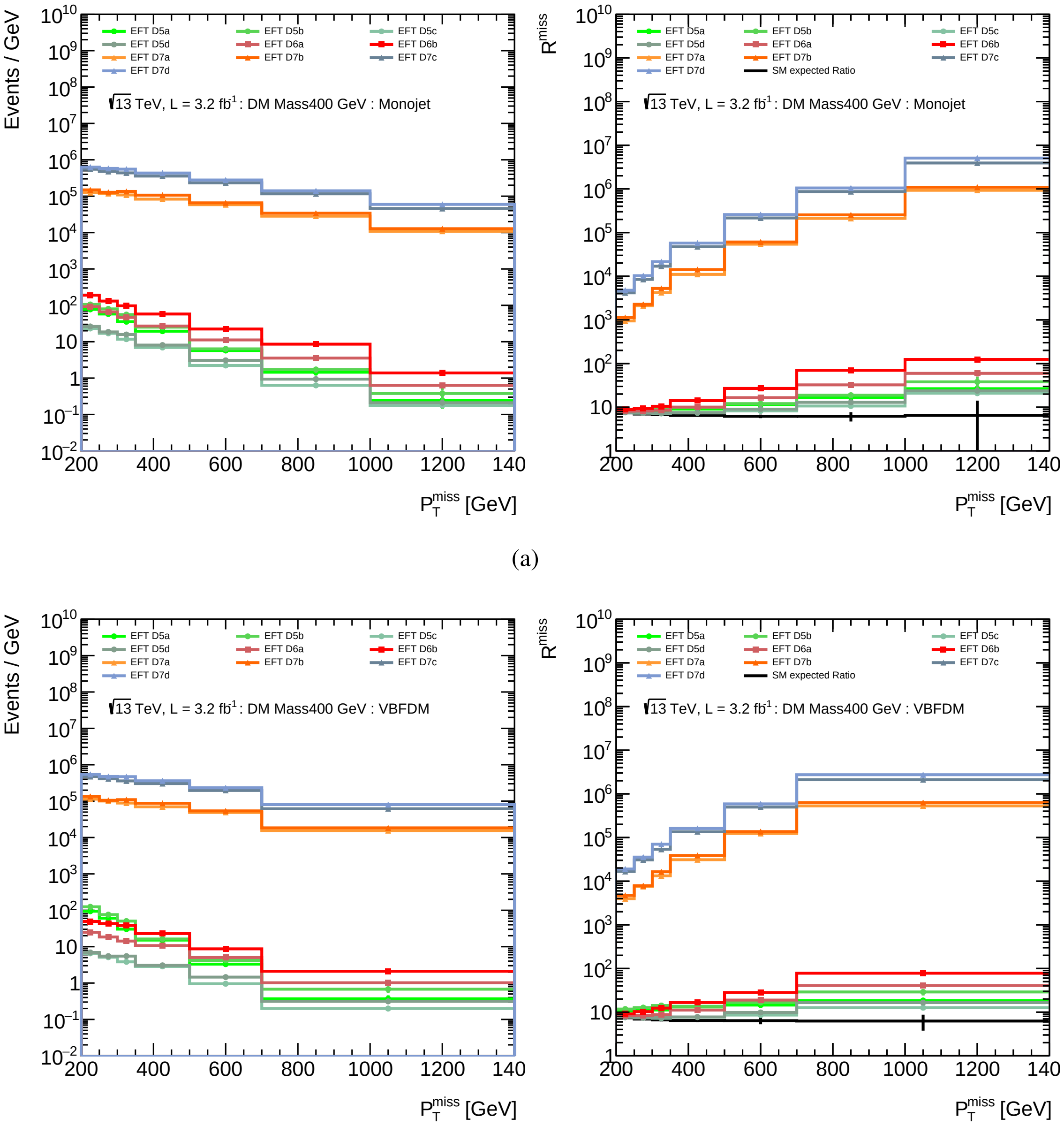

(a)

(b)

Figure 8.14: Missing transverse momentum distributions for effective field theory dark matter models with a dark matter particle mass of 400 GeV and an effective field theory scale of 100 GeV, measured in the (a) ≥ 1 jet, and (b) VBF kinematic regions. All effective operators under investigation are shown. The distributions on the left are kinematic distributions which are normalised by cross-section and the luminosity from data collected in this analysis. The right gives the R^{miss} distribution for the Standard Model expected and BSM samples.

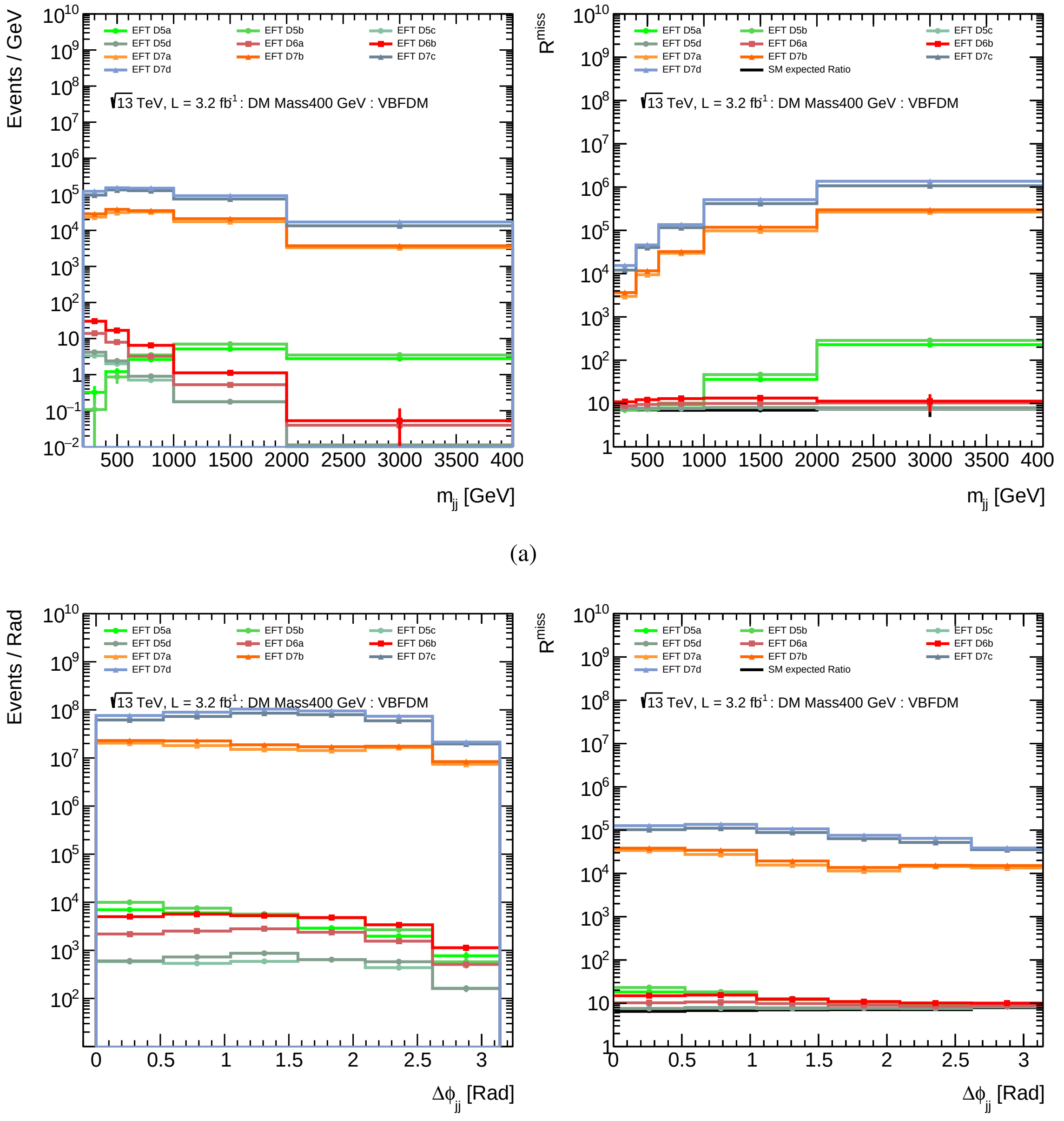

(a)

(b)

Figure 8.15: Dijet invariant mass and $\Delta\phi_{jj}$ distributions for effective field theory dark matter models with a dark matter particle mass of 400 GeV and an effective field theory scale of 100 GeV, measured in the VBF kinematic region. All effective operators under investigation are shown. The distributions on the left are kinematic distributions which are normalised by cross-section and the luminosity from data collected in this analysis. The right gives the R^{miss} distribution for the Standard Model expected and BSM samples.

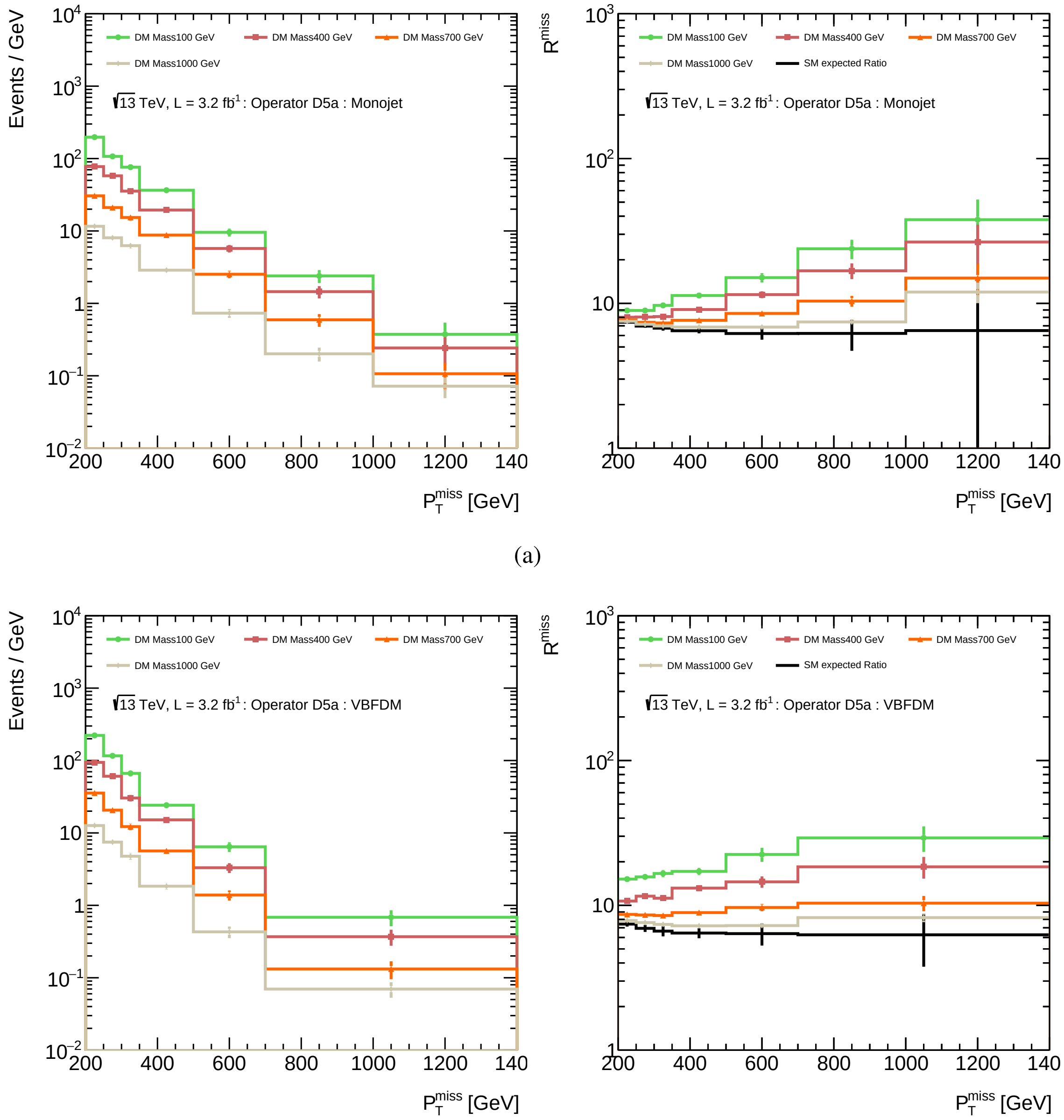

(a)

(b)

Figure 8.16: Missing transverse momentum distributions for effective field theory dark matter models with an effective field theory scale of 100 GeV for the D5a operator, measured in the (a) ≥ 1 jet, and (b) VBF kinematic regions. Various representative dark matter mass points are shown for this operator. The distributions on the left are kinematic distributions which are normalised by cross-section and the luminosity from data collected in this analysis. The right gives the R^{miss} distribution for the Standard Model expected and BSM samples.

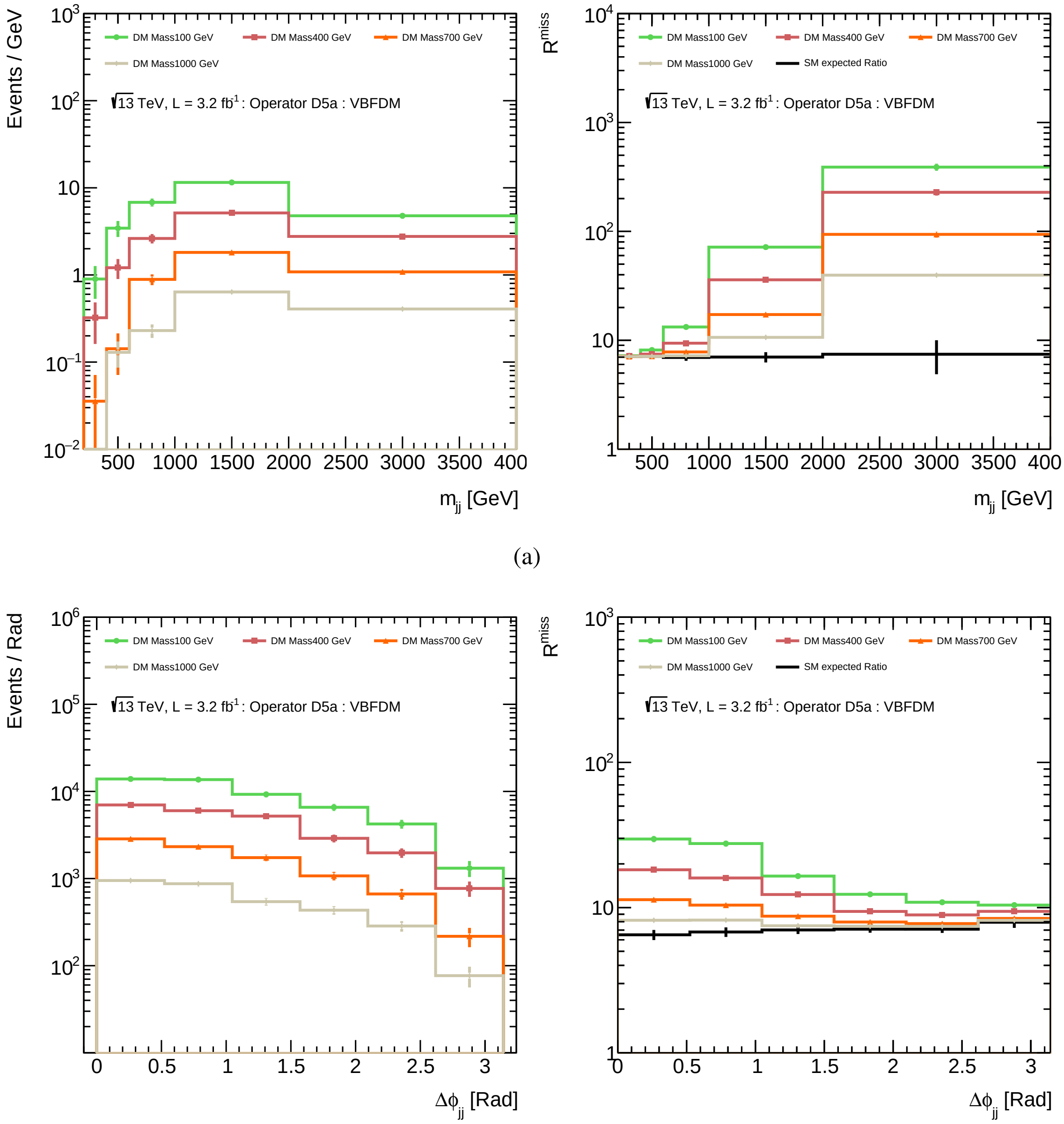

(a)

(b)

Figure 8.17: Dijet invariant mass and $\Delta\phi_{jj}$ distributions for effective field theory dark matter models with an effective field theory scale of 100 GeV for the D5a operator, measured in the VBF kinematic region. Various representative dark matter mass points are shown for this operator. The distributions on the left are kinematic distributions which are normalised by cross-section and the luminosity from data collected in this analysis. The right gives the R^{miss} distribution for the Standard Model expected and BSM samples.

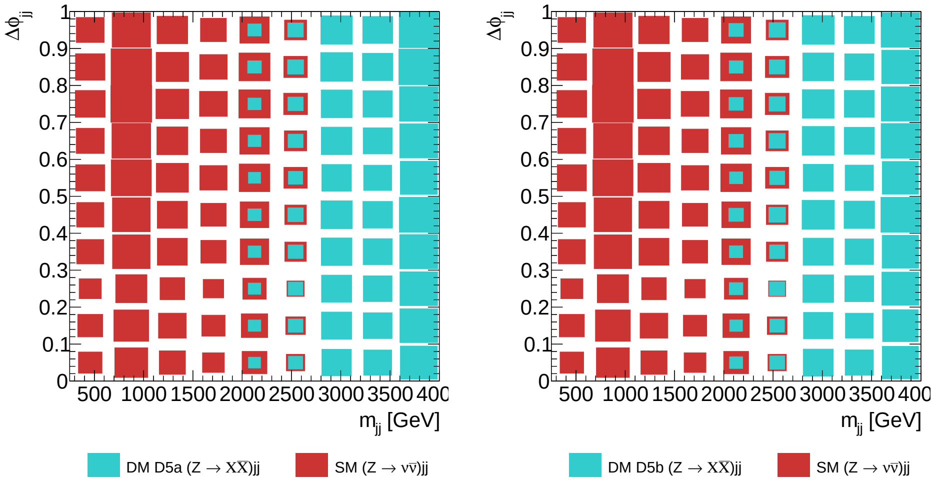

(a) D5a

(b) D5b

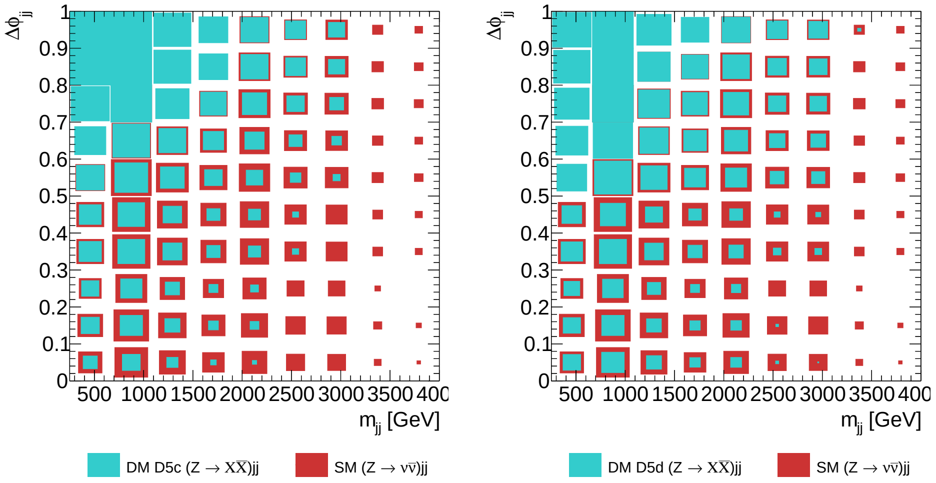

(c) D5c

(d) D5d

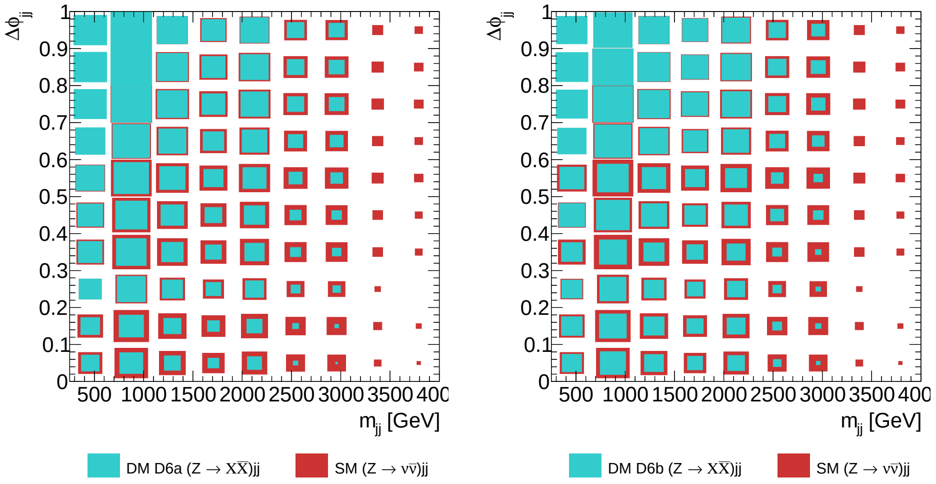

(e) D6a

(f) D6b

Figure 8.18: Two-dimensional cross-section distributions for m_{jj} versus $\Delta\phi_{jj}$, where $\Delta\phi_{jj}$ has been normalised to one. All dark matter models are shown in blue, with a dark matter particle mass of 100 GeV, and an effective field theory scale of 100 GeV. From top left to bottom right are D5a, D5b, D5c, D5d, D6a, D6b. The Standard Model background of $(Z \rightarrow \nu\bar{\nu})$jj is also highlighted in red.

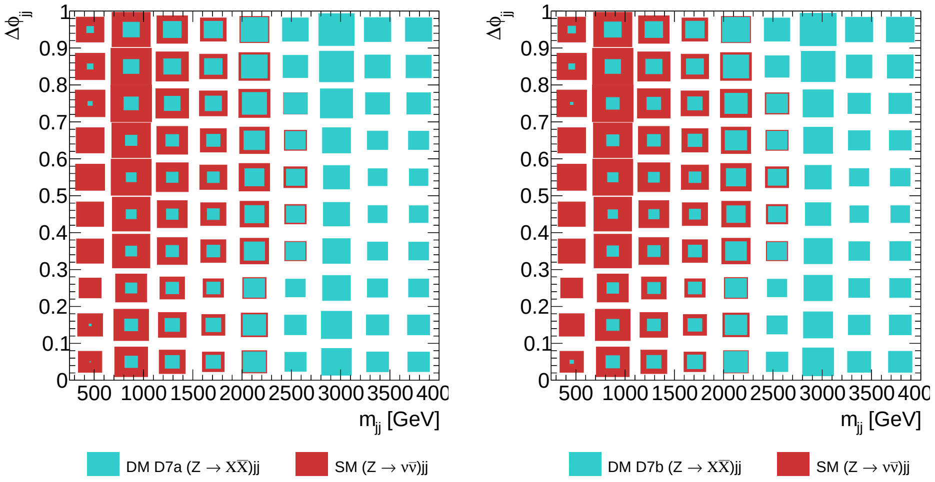

(a) D7a

(b) D7b

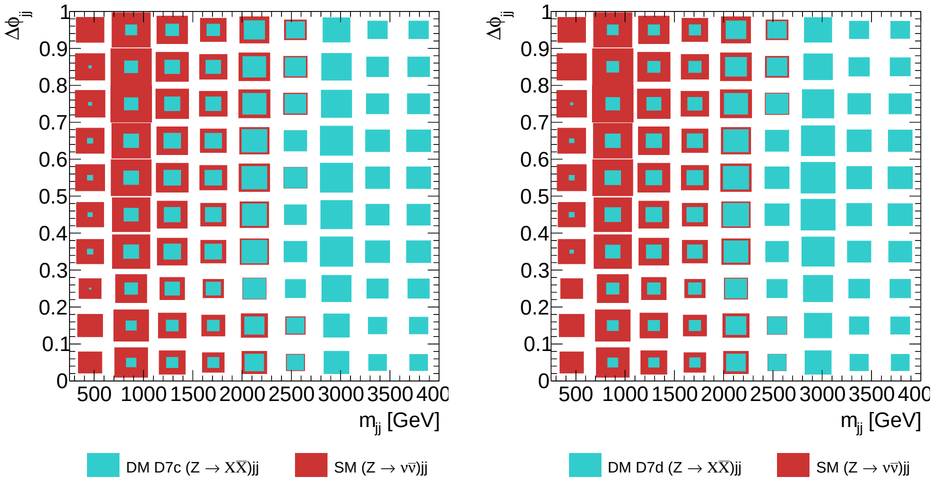

(c) D7c

(d) D7d

Figure 8.19: Two-dimensional cross-section distributions for m_{jj} versus $\Delta\phi_{jj}$, where $\Delta\phi_{jj}$ has been normalised to one. All dark matter models are shown in blue, with a dark matter particle mass of 100 GeV, and an effective field theory scale of 100 GeV. From top left to bottom right are D7a, D7b, D7c, and D7d. The Standard Model background of $(Z \to \nu\bar{\nu})$jj is also highlighted in red.

iteration of the analysis.

8.2.4 Setting limits

In this search, two operators are considered: D7a ($\bar{\chi}\chi V^{\mu\nu}V_{\mu\nu}$) and D7c ($\bar{\chi}\chi\varepsilon^{\mu\nu\rho\sigma}V^{\mu\nu}V_{\rho\sigma}$) where V represents W/Z bosons. The operators vary in charge parity: the first conserves CP and the latter violates it.

Figure 8.20 shows the 95 % confidence level exclusion limits for the observed and expected distributions. Figure 8.20 (a) gives limits set on the CP-conserving operator, showing a range in the effective field theory scale of $\sim$ 600–800 GeV, and $\sim$ 700–900 GeV for expected and observed limits respectively. For the CP-violating operator, limits have a range of $\sim$ 800–1000 GeV at the effective field theory scale for expected results, and $\sim$ 100 GeV greater for the observed results, as shown in Figure 8.20 (b). The observed and expected limits are consistent within uncertainties. Indirect detection limits are also shown in the figures for comparison; these were taken from Reference [140] and represent limits set by the Fermi-LAT experiment, the VERITAS experiment [117], and the PAMELA experiment [113]—all discussed in Section 6.2. These bounds are obtained from observations of dwarf spheroidal galaxies, mono-chromatic γ-ray searches, and cosmic-ray antiproton spectrum measurements.

8.2.5 Additional effective operators

During the analysis described in this chapter, only two operators of the effective field theory dark matter model are investigated. This is due to the *proof-of-principle* nature of the publication. However, as all the data, distributions and correlations are published for reinterpretation, it is possible to study the remaining operators from Table 8.1.

It is previously stated that the Z invisible width places limitations on a number of these operators. These limitations are also included in Table 8.1 as the minimum effective field theory scale. However, as the Z invisible width measurement only constrains values of the dark matter mass below $m_Z/2$, limits can still be improved at larger dark matter masses. Figures 8.21–8.24 show the limits placed on the remaining operators from the effective field theory discussed previously. The limits provided by the Z invisible width measurement are also included in these figures. In the relevant figures, the $m_Z/2$ limits are shown up to where

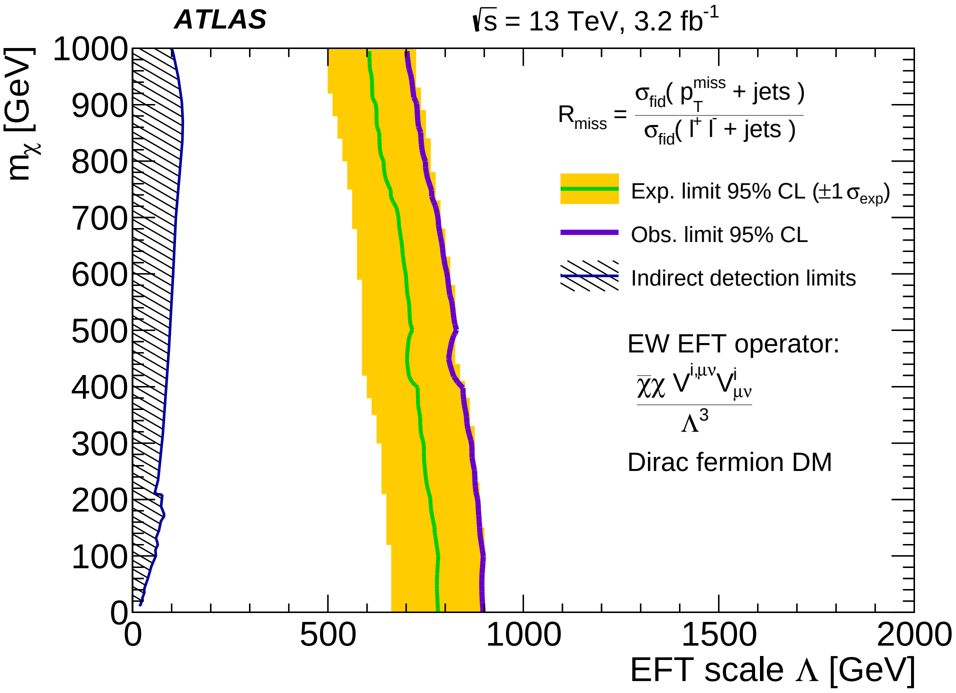

(a) D7a

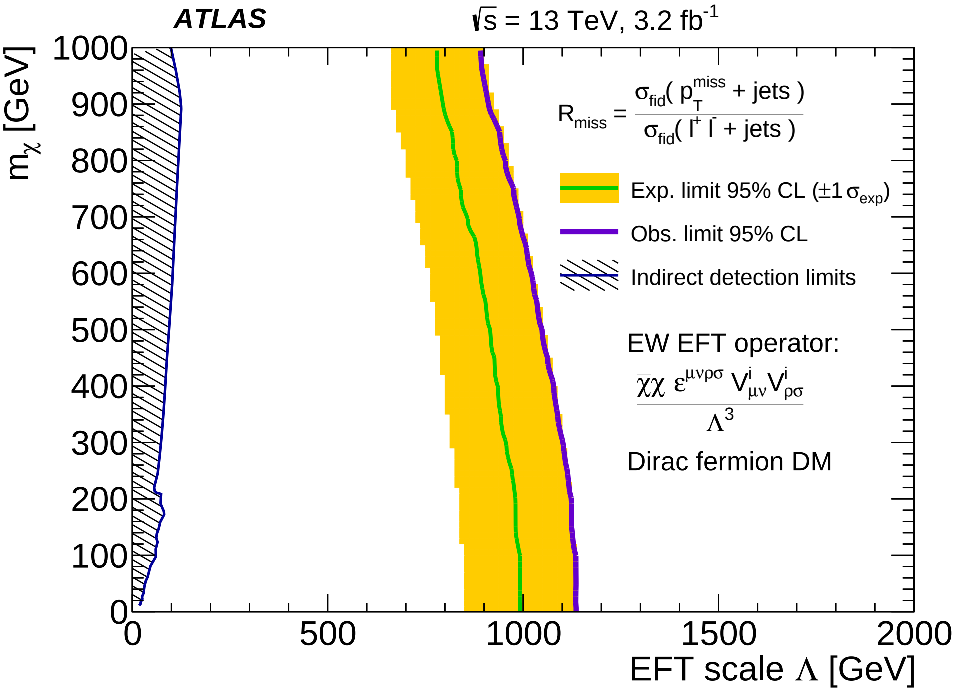

(b) D7c

Figure 8.20: Exclusion 95 % CL limits on two EFT operators with Dirac fermion dark matter particles are shown [141]. These operators are (a) CP-conforming and (b) CP-violating. The limits are set in the dark matter mass, m_χ–Λ (EFT scale) plane. Limits set by indirect detection experiments are also shown for comparison [117, 140, 172].

they are valid—below their relative effective field theory scales.

The dashed area in blue in the figures represents the exclusion due to indirect detection experiments. These originate from the same constraints illustrated on the D7a and D7c exclusion limit figures. With the exception of the D5a operator, the indirect detection limits almost completely exclude the regions of sensitivity of this analysis. The dominant contribution to the indirect limit on the D5b arises from measurements of the production of WW pairs in dwarf spheroidal galaxies, with smaller contributions from cosmic-ray antiproton spectrum measurements. This indirect limit covers most of the sensitive regions of this analysis, with the exception at very low ($<$ 100 GeV) and very high ($>$ 950 GeV) dark matter mass. The sensitivity of D5c and D5d is almost completely removed due to this limit; D5d may still hold some potential at low dark matter mass, above the constraint from the Z invisible measurement. The main contribution to the indirect limits on these two operators is due to the production of $b\bar{b}$ and WW pairs in dwarf spheroidal galaxies, respectively. The D6a and D6b operators are mostly limited by the production of $b\bar{b}$ pairs in dwarf spheroidal galaxies and the cosmic-ray antiproton spectrum, respectively. The sensitivity achieved by this analysis for the D6a operator is not affected by these indirect limits due to their exclusion at low effective field theory scale. In contrast, the indirect limits set on D6b entirely exclude the sensitivity of this analysis. All of the previously mentioned contributions to indirect limits arise for the D7b and D7d operators. These limits drown the sensitivity of this analysis at high dark matter mass, but only reach low values of effective field theory scale at low dark matter mass. The reach of the limits set by indirect detection experiments varies significantly between the effective operators. These differences can be explained according to the relative velocity suppression in the non-relativistic limit of each operator. Operators D5a, D6b, D7a, D7d are all difficult to exclude as they are all velocity suppressed to different extents. The prominent peak in sensitivity for the indirect detection limits near $m_\chi \sim m_Z/2$ for some operators is due to the three-point couplings these operators make with the Z boson.

For the collider limits set by this analysis, the variations in reach for the different operators arise for two reasons: they have different scaling dimensions; and their kinematic differences influence the effectiveness of the selection criteria for the VBF topology. Operators D5c–D6b have both three- and four-point contact interactions. The Standard Model backgrounds have similar kinematic diagrams to the three-point interactions, which causes

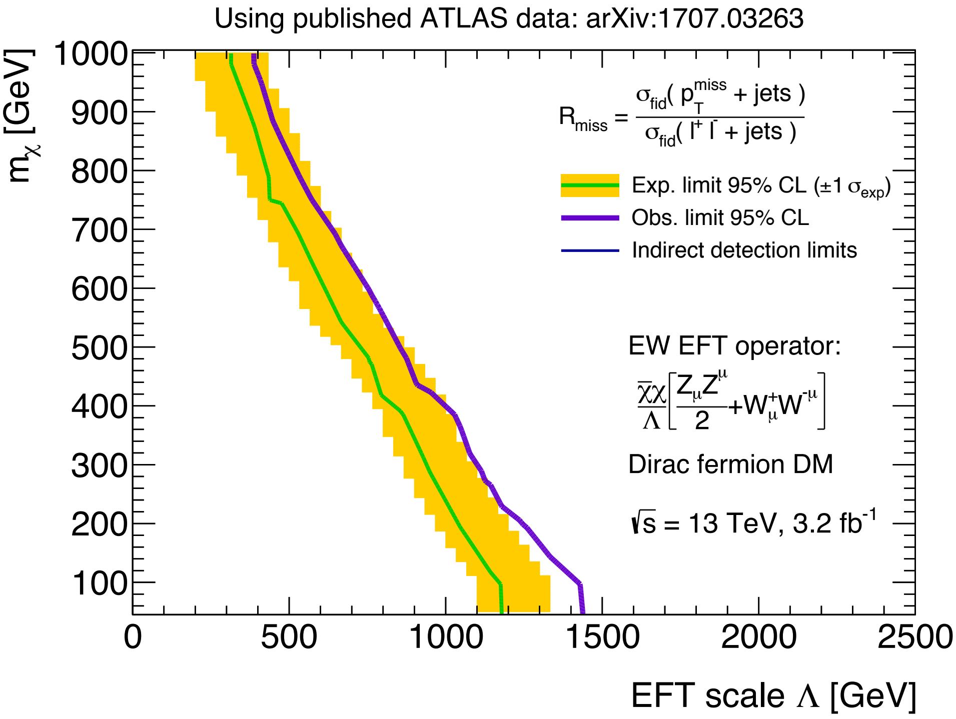

(a) D5a

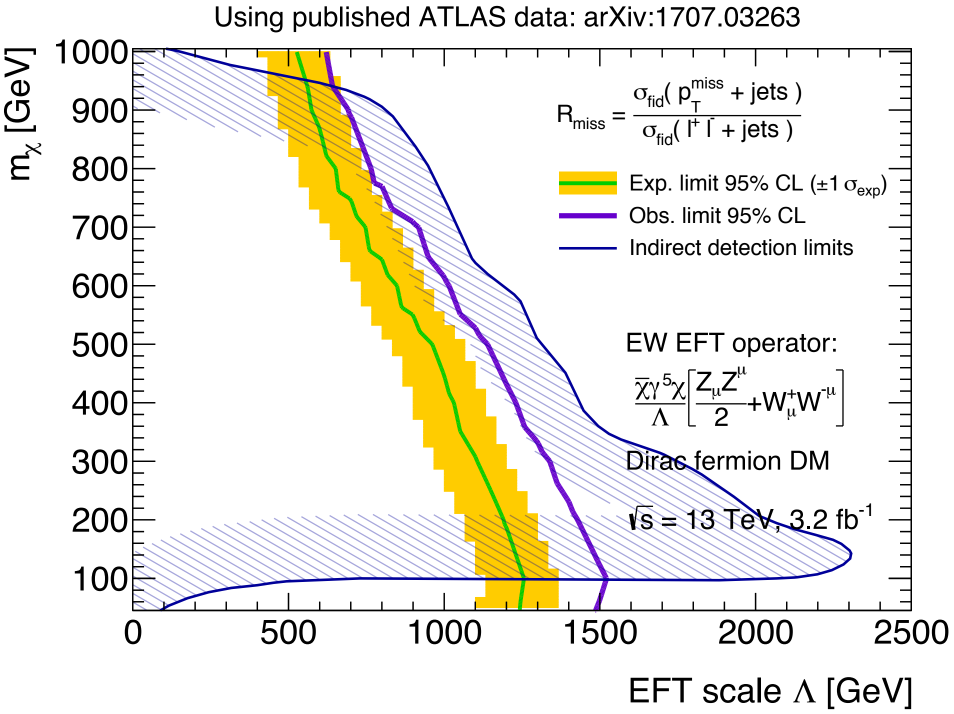

(b) D5b

Figure 8.21: Exclusion 95 % CL limits on the D5a and D5b effective field theory operators with Dirac fermion dark matter particles are shown. The limits are set in the dark matter mass, m_χ–Λ (EFT scale) plane. Limits set by indirect detection experiments are also shown for comparison [117, 140, 172].

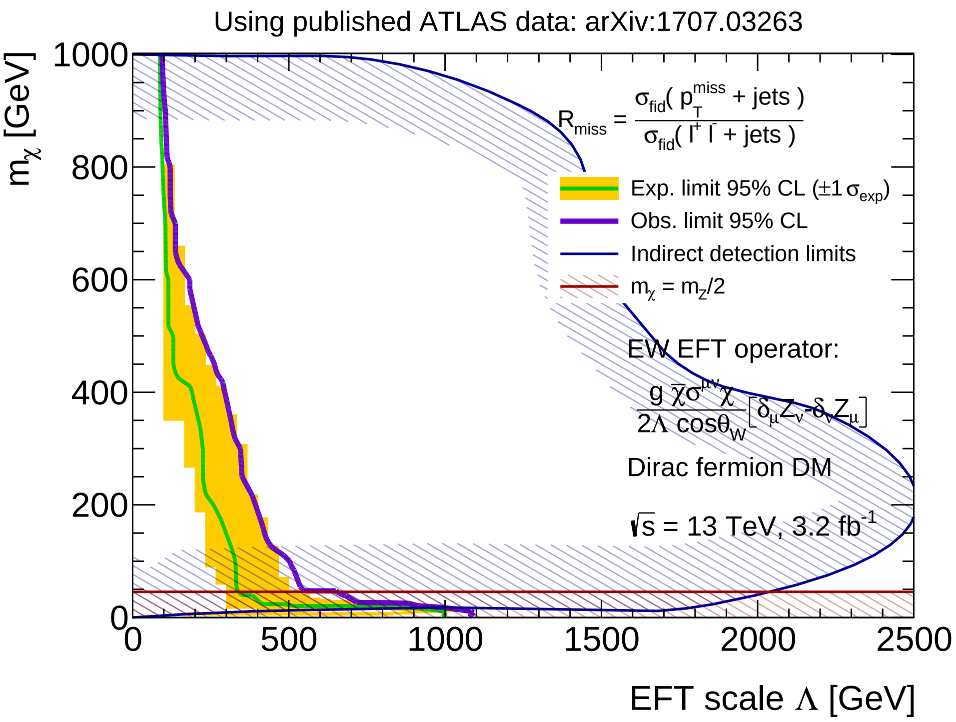

(a) D5c

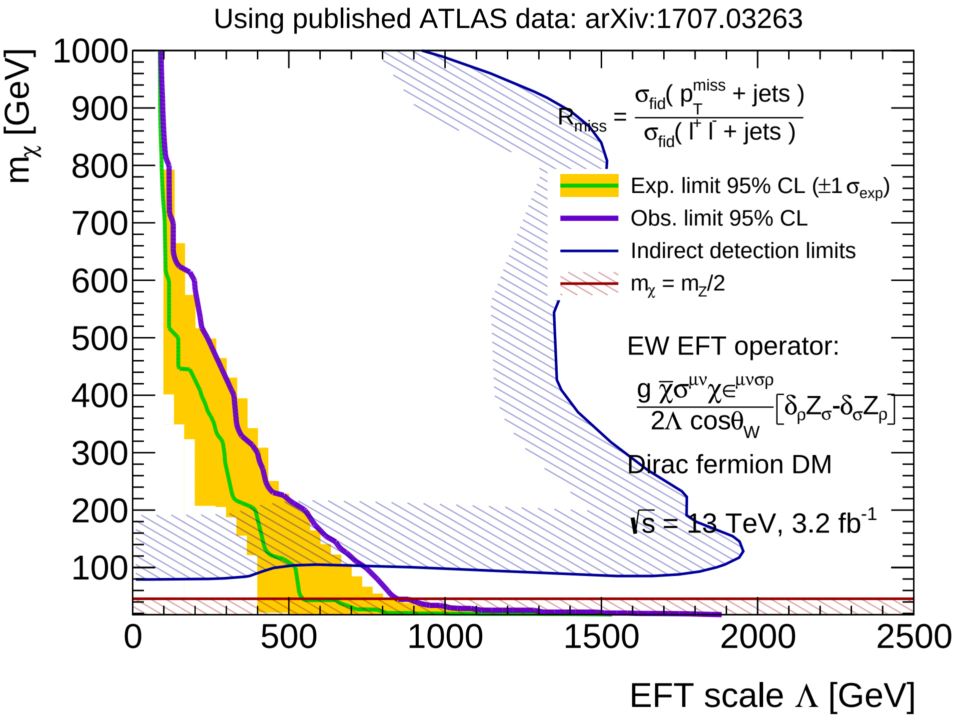

(b) D5d

Figure 8.22: Exclusion 95 % CL limits on the D5c and D5d effective field theory operators with Dirac fermion dark matter particles are shown. The limits are set in the dark matter mass, m_χ–Λ (EFT scale) plane. Limits set by indirect detection experiments [117, 140, 172] and the Z invisible width measurement are also shown for comparison. The Z invisible width measurement is only valid below the relative EFT scales of each operator: Λ = (a) 3300 GeV, and (b) 6600 GeV.

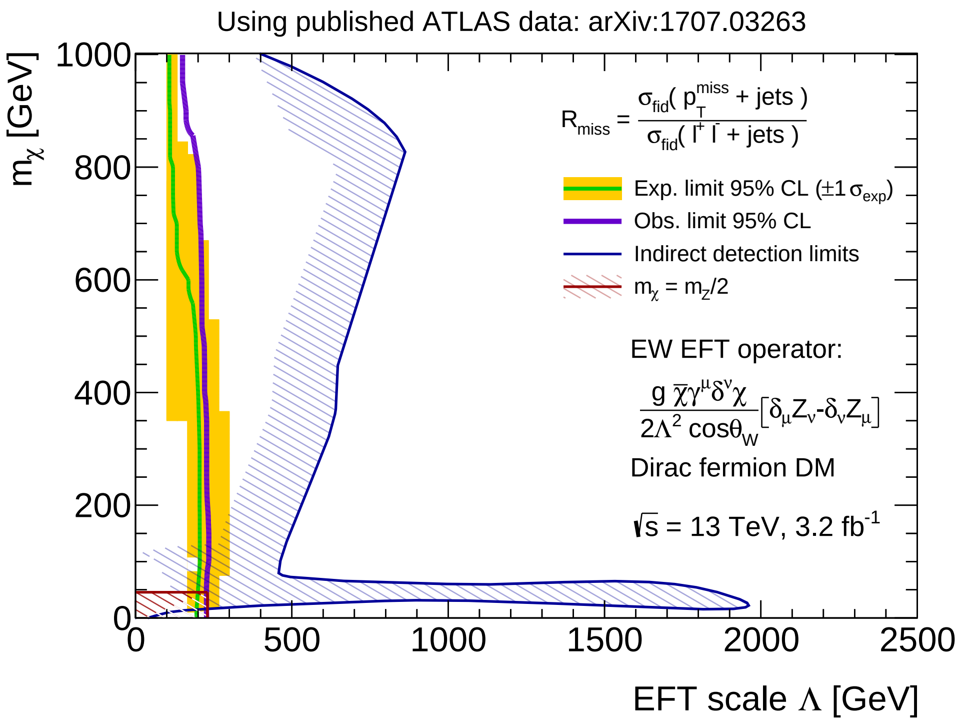

(a) D6a

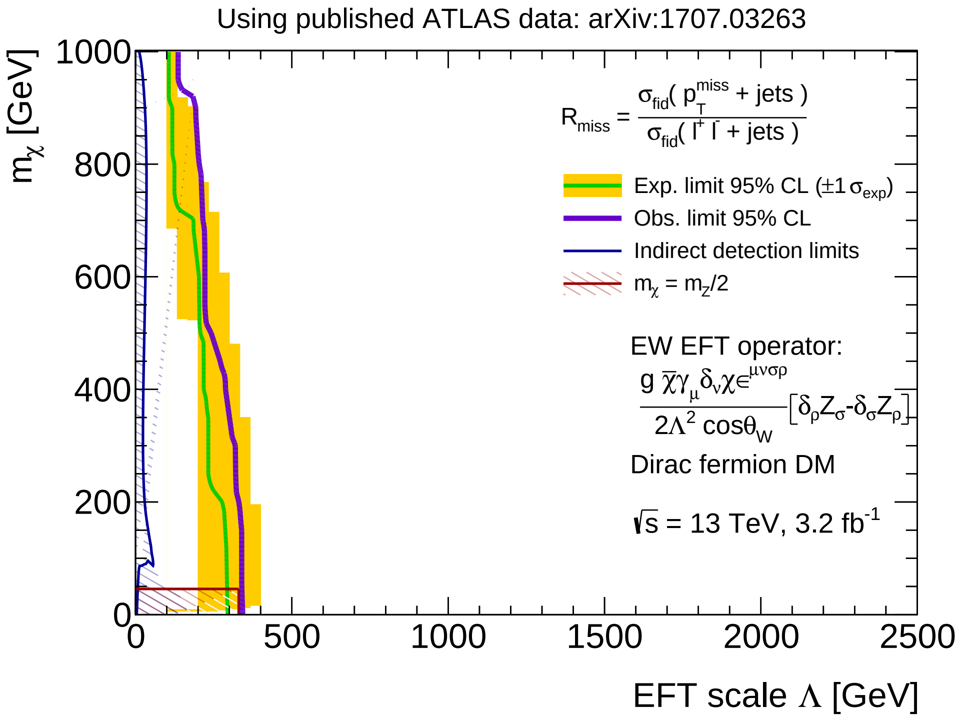

(b) D6b

Figure 8.23: Exclusion 95 % CL limits on the D6 effective field theory operators with Dirac fermion dark matter particles are shown. The limits are set in the dark matter mass, m_χ–Λ (EFT scale) plane. Limits set by indirect detection experiments [117, 140, 172] and the Z invisible width measurement are also shown for comparison. The Z invisible width measurement is only valid below the relative EFT scales of each operator: $\Lambda =$ (a) 230 GeV, and (b) 330 GeV.

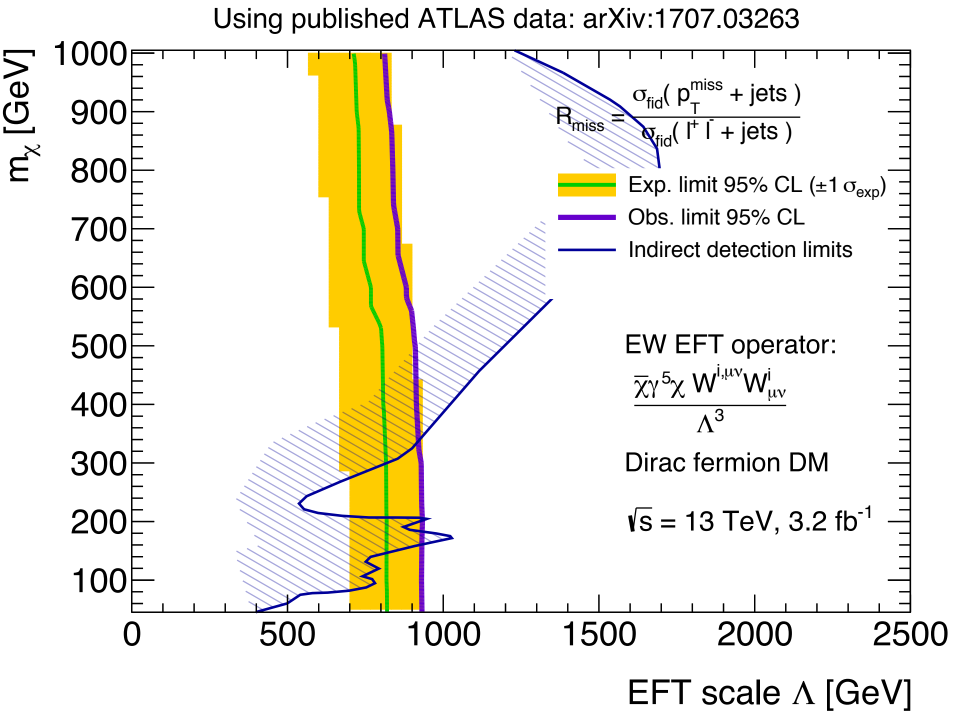

(a) D7b

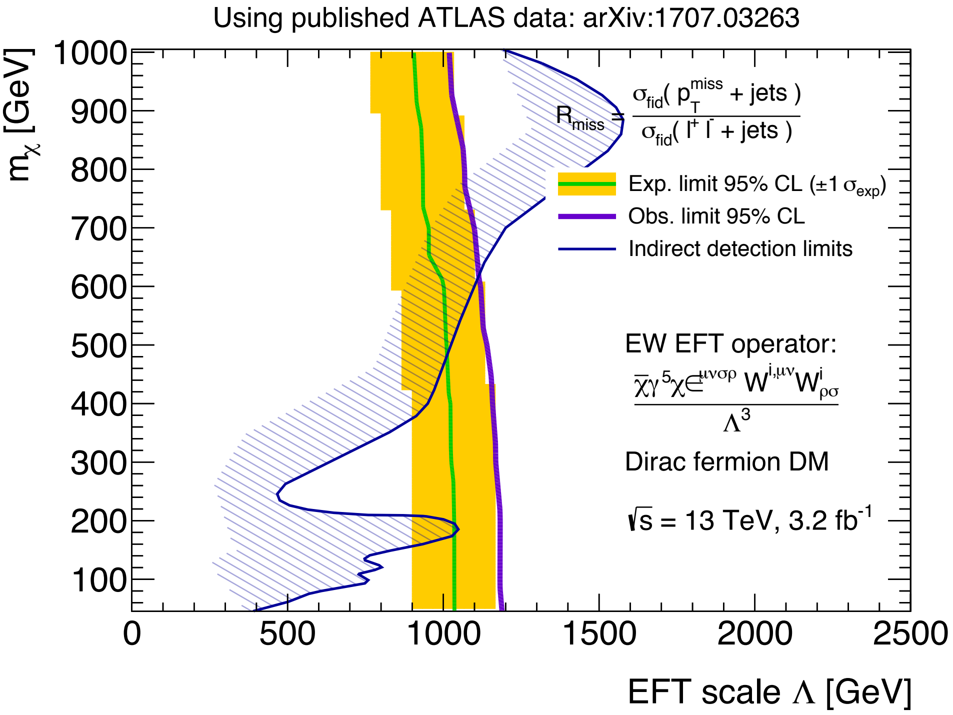

(b) D7d

Figure 8.24: Exclusion 95 % CL limits on the remaining D7 effective field theory operators with Dirac fermion dark matter particles are shown. The limits are set in the dark matter mass, m_χ–Λ (EFT scale) plane. Limits set by indirect detection experiments are also shown for comparison [117, 140, 172].

markedly worse sensitivity for the VBF side of this analysis. This is due to the selection criteria encountering problems when attempting to separate the signal from the background. The D7 operators do not suffer from this issue. However, the VBF signal events are, to a lesser extent, still difficult to distinguish from the background. The D7 operators are not typically generated from longitudinally-polarized W bosons, which are the largest component of electroweak bosons produced from the protons in the beam, and generally have low p_{T}. Therefore, the rates of signal are lower and the signature leading jets are produced more centrally from the VBF process, causing worse signal criteria efficiencies.

As can be seen, the analysis has good constraining power for the D5a and D5b operators at low dark matter mass: the 95 % confidence level exclusion limits reach up to an effective field theory scale of approximately 1500 GeV. This is consistent with the large deviation of the BSM R^{miss} from that of the Standard Model at low dark matter mass. The D5c and D5d operators follow a similar trend with more sensitivity at low dark matter mass. However, both the expected and observed data displays much less sensitivity than for those previously mentioned. This analysis appears to have very little sensitivity to effective operators D6a and D6b—the 95 % confidence level exclusion limits only reaching an effective field theory scale of 200–300 GeV. However, the indirect detection limits are only able to exclude working points at very low effective field theory scale for the D6b operator, which may offer more potential for new limit setting in the future. The D7 operators shown here in Figure 8.24 display similar constraints to those on the other D7 operators published with the analysis in Figure 8.20. However, the indirect detection limits are much larger for these operators. As the decay rate scales as $(\Lambda'/100\ \mathrm{GeV})^{-2(D-4)}$ with the effective field theory scale, it is not unexpected that the analysis has limited distinguishing power on the D7 operators, despite the relatively large cross-sections given in Table 8.4.

These limits are set on the presumption of that particular operator predominantly contributing to (a) dark matter production in the Universe, and (b) dark matter production at the Large Hadron Collider. This allows the comparison of limits from different sources, such as indirect detection to collider measurements. However, this assumption could be incorrect and dark matter production could arise from a complex mix of these operators (eg. 30 % D5a, 30 % D6a, 40 % D7a). The proportions in this mix could also vary with energy scale; the mix of operators causing dark matter production in space versus at a collider may be different. Therefore, a more detailed analysis could study limits set on all of these operators simultaneously—made possible with the publication of the data from this analysis. This would provide complementary information to the study of dark matter production due to the difference in the initial states of the two types of limits.

8.3 Invisible Higgs-boson decay model

Further 95 % confidence level exclusion limits are set on a model of Higgs boson decay to invisible particles using the detector-corrected distributions and their correlations. This model, assuming a scalar singlet dark matter particle, produces the BSM extension to the Standard Model [173]:

$$\mathcal{L}_{\mathrm{Higgs-DM}} = -\frac{1}{2}\mu_{\chi}^{2}\chi^{2} - \frac{1}{2}\lambda_{h_{\chi}}\chi^{2}H^{\dagger}H. \tag{8.10}$$

This model is considered a benchmark by the ATLAS collaboration and has previously had limits set by a dedicated analysis using 20 fb^{-1} of $\sqrt{s} = 8$ TeV data collected by the ATLAS experiment [40] during Run 1 (2009–2013), and more recently with 36.1 fb^{-1} of $\sqrt{s} = 13$ TeV data collected by the ATLAS experiment [131] during 2015–2016.

The distributions of this model are shown in Figures 7.8 and 7.9 as the green dashed line. The m_{jj} distribution in the VBF kinematic region offers the most discrimination power for this particular model. The limit is also strengthened slightly by the $\Delta\phi_{jj}$ distribution, but unlike the other models, the $p_{\mathrm{T}}^{\mathrm{miss}}$ distributions offer close to no impact. The production rate of the Higgs boson is multiplied by a range of possible branching fractions of the Higgs boson to invisible particles in order to find an upper limit. The 95 % CL upper expected and observed limits for a Higgs boson of mass 125 GeV are calculated to be $0.59^{+0.54}_{-0.12}$ and 0.46 respectively. Systematic uncertainty correlations between bins in the detector-corrected distributions produce stronger observed limits than expected. The previous ATLAS analysis to investigate this model used 20 fb^{-1} of 8 TeV data to set an observed exclusion limit of 0.28 [40]. The previous analysis used a dataset size significantly larger than the presented analysis. However, for data collected by the ATLAS experiment at $\sqrt{s} = 13$ TeV , the presented analysis gave the best limits at the time of publication. Both the results discussed here and other studies and projections of this measurement are shown in Figure 8.25. Another *Higgs-to-invisibles* dedicated analysis has since been published with 36.1 fb^{-1} of $\sqrt{s} = 13$ TeV and gives a 95 % CL upper limit of 0.37 [131].

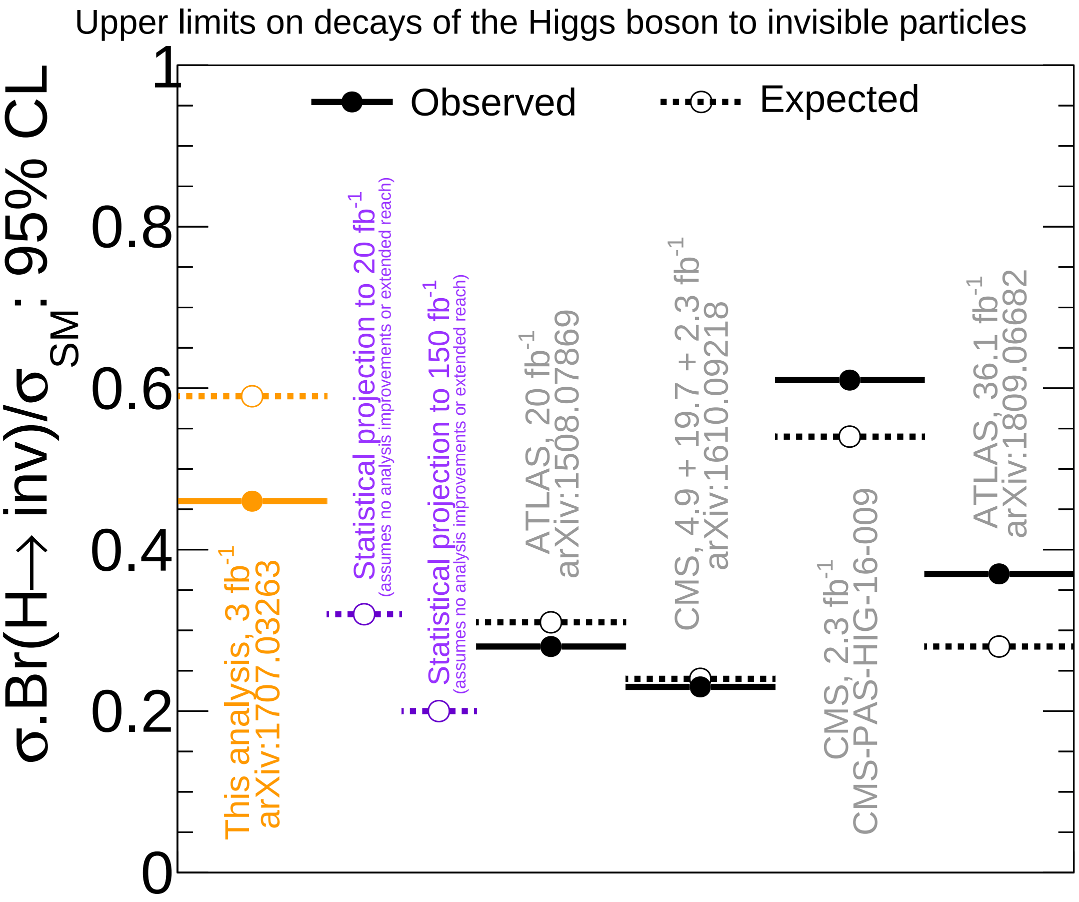

Figure 8.25: Exclusion 95 % CL exclusion limits on the Higgs boson decay to dark matter particles are shown. (Orange) This analysis is compared with statistical projections to (purple) 20 fb^{-1} and 150 fb^{-1}, and (black) other published analyses [40, 131, 132, 174].

Chapter 9

Future outlook

The analysis described in the previous two chapters will be iterated upon again; it will be extended with a number of adjustments to the analysis strategy and will investigate a much larger dataset. The analysis will again be published with all data, distribution, and calibration information for the purpose of future reinterpretation as new BSM models present themselves.

This next iteration will use data collected by the ATLAS detector throughout the whole period of Run 2 (2015–2018). These datasets contain a total of $140\,\text{fb}^{-1}$ of integrated luminosity. The ideology of the detector-corrected ratio measurement as a method for probing beyond-the-Standard-Model physics remains within the analysis strategy. However, now the principle of the method has been proven, more channels for the numerator and denominator can be investigated—Table 9.1 gives these new signal regions which will be under investigation for this iteration of the analysis.

Corrections for detector effects will also be performed using alternative methodology: *topology unfolding* [175] will be utilised for this strategy point. In contrast to the previous procedures, this method unfolds an inclusive event topology rather than unfolding the data for a specific process; there is no distinction between signal and background, and consequently most background subtractions are unnecessary. This eliminates the need to consider uncertainties associated with the estimation of background contributions. Only background contributions associated with the misidentification of objects in the detector are accounted for and removed before the unfolding procedure.

Lepton multiplicity		Final state
$\mathrm{N}_l = 2$	$\rightarrow$ SFOS $\rightarrow$	$p_{\mathrm{T}}^{\mathrm{miss}} + Z$
		$p_{\mathrm{T}}^{\mathrm{miss}} + t\bar{t}$
$\mathrm{N}_l = 1$	$\rightarrow$	$p_{\mathrm{T}}^{\mathrm{miss}} + W$
$\mathrm{N}_l = 0$	$\rightarrow \mathrm{N}_{b-\mathrm{jet}} = 0 \rightarrow$	$p_{\mathrm{T}}^{\mathrm{miss}} + \mathrm{hf}$
		$p_{\mathrm{T}}^{\mathrm{miss}} + \mathrm{jets}$

Table 9.1: Signal regions for the second iteration of the analysis discussed in this thesis. Where SFOS represents the selection of same-flavour opposite-sign pairs of leptons, and hf stands for heavy flavour and refers to the 3^{rd} generation of quarks. $p_{\mathrm{T}}^{\mathrm{miss}} + \mathrm{jets}$ is the signal channel for the previous iteration of the analysis and can be split into the three categories: VBF, VH, and untagged.

Chapter 10

Summary and conclusions

The work presented in this thesis covers the calibration of the energy resolution of forward jets in the ATLAS calorimeter, a novel approach for collider searches for dark matter, and the interpretation of the subsequent measurements. The calibration of the energy resolution of forward jets is vital in a large number of ATLAS analyses, including the search discussed in this thesis. The measurement of the detector-corrected, differential cross-sections of final states with $p_{\mathrm{T}}^{\mathrm{miss}}$ and hadronic jets as a function of different observables and kinematic regions, allows for the predictions of the Standard Model to be compared with a variety of dark matter models. Improvements made to $p_{\mathrm{T}}^{\mathrm{miss}}+$jets searches are discussed: publishing unfolded results in order to reduce the difficulty of reinterpretation with new models.

The in-situ calibration of the forward jet energy resolution for dijet events in the ATLAS calorimeter was performed using $36.1\,\mathrm{fb}^{-1}$ of $\sqrt{s} = 13$ TeV data collected in 2015 and 2016. The jet energy resolution calibration for dijet events in data is calculated to reside in the range 0.15 to 0.40, varying as a function of the transverse momentum and pseudorapidity of the jet. The resolution in data is consistent with the jet energy resolution observed in MC-simulated samples within systematic uncertainties.

The analysis discussed in Chapters 7 and 8 presents the fiducial cross-section ratio of the final state of $p_{\mathrm{T}}^{\mathrm{miss}}+$jets to $\ell^{+}\ell^{-}+$jets for $3.2\,\mathrm{fb}^{-1}$ of proton-proton collision data collected by the ATLAS detector in 2015 at a centre-of-mass energy of $\sqrt{s} = 13$ TeV . In the Standard Model this ratio corresponds to a numerator of $Z \rightarrow \nu\bar{\nu}+$jets events, and a denominator of $Z \rightarrow \ell^{+}\ell^{-}+$jets events where electron and muon channels are measured independently and then combined. Two different kinematic regions are used to measure the unfolded cross-section ratio for four differential distributions: $p_{\mathrm{T}}^{\mathrm{miss}}$ in both an inclusive $\geq$ 1jet region and

VBF-like region, and m_{jj} and $\Delta\phi$ in a VBF-like region. These distributions are used to set limits on three categories of beyond-the-Standard-Model theoretical framework: a simplified dark matter WIMP model with an axial-vector mediator particle, an effective field theory in which the Standard Model and dark matter interact via electroweak bosons, and an invisible Higgs boson decay model. The detector-corrected distributions are published alongside all uncertainty information to improve the longevity of the data and to set limits on future models without the necessity of detector simulations.

Bibliography

[1] David Griffiths. *Introduction to elementary particles*. 2008. ISBN: 9783527406012.

[2] ATLAS Collaboration. “Observation of a new particle in the search for the Standard Model Higgs boson with the ATLAS detector at the LHC”. In: *Phys. Lett.* B716 (2012), pp. 1–29. DOI: `10.1016/j.physletb.2012.08.020`. arXiv: `1207.7214 [hep-ex]`.

[3] CMS Collaboration. “Observation of a new boson at a mass of 125 GeV with the CMS experiment at the LHC”. In: *Phys. Lett.* B716 (2012), pp. 30–61. DOI: `10.1016/j.physletb.2012.08.021`. arXiv: `1207.7235 [hep-ex]`.

[4] J. Silk et al. *Particle Dark Matter: Observations, Models and Searches*. Ed. by Gianfranco Bertone. Cambridge: Cambridge Univ. Press, 2010. ISBN: 9781107653924. DOI: `10.1017/CBO9780511770739`. URL: `http://www.cambridge.org/uk/catalogue/catalogue.asp?isbn=9780521763684`.

[5] Lyndon Evans and Philip Bryant. “LHC Machine”. In: *JINST* 3 (2008), S08001. DOI: `10.1088/1748-0221/3/08/S08001`.

[6] ATLAS Collaboration. “The ATLAS Experiment at the CERN Large Hadron Collider”. In: *JINST* 3 (2008), S08003. DOI: `10.1088/1748-0221/3/08/S08003`.

[7] Matthew B. Robinson et al. *A Simple Introduction to Particle Physics. Part I - Foundations and the Standard Model*. BU-HEPP-08-20. 2008. arXiv: `0810.3328 [hep-th]`.

[8] F. Englert and R. Brout. “Broken Symmetry and the Mass of Gauge Vector Mesons”. In: *Phys. Rev. Lett.* 13 (1964). [,157(1964)], pp. 321–323. DOI: `10.1103/PhysRevLett.13.321`.

[9] Peter W. Higgs. "Broken symmetries, massless particles and gauge fields". In: *Phys. Lett.* 12 (1964), pp. 132–133. DOI: `10.1016/0031-9163(64)91136-9`.

[10] Peter W. Higgs. "Broken Symmetries and the Masses of Gauge Bosons". In: *Phys. Rev. Lett.* 13 (1964), pp. 508–509. DOI: `10.1103/PhysRevLett.13.508`.

[11] G. S. Guralnik, C. R. Hagen, and T. W. B. Kibble. "Global Conservation Laws and Massless Particles". In: *Phys. Rev. Lett.* 13 (1964), pp. 585–587. DOI: `10.1103/PhysRevLett.13.585`.

[12] T. W. B. Kibble. "Symmetry breaking in nonAbelian gauge theories". In: *Phys. Rev.* 155 (1967). [,165(1967)], pp. 1554–1561. DOI: `10.1103/PhysRev.155.1554`.

[13] Peter W. Higgs. "Spontaneous Symmetry Breakdown without Massless Bosons". In: *Phys. Rev.* 145 (1966), pp. 1156–1163. DOI: `10.1103/PhysRev.145.1156`.

[14] Franz Mandl and Graham Shaw. *QUANTUM FIELD THEORY*. 1985. URL: `http://eu.wiley.com/WileyCDA/WileyTitle/productCd-0471496839.html`.

[15] Antonio Pich. "The Standard model of electroweak interactions". In: *The Standard model of electroweak interactions*. [,1(2007)]. 2008, pp. 1–49. arXiv: `0705.4264 [hep-ph]`. URL: `http://doc.cern.ch/yellowrep/2007/2007-005/cern-2007-005.pdf`.

[16] Michael E. Peskin and Daniel V. Schroeder. *An Introduction to quantum field theory*. Reading, USA: Addison-Wesley, 1995. URL: `http://www.slac.stanford.edu/~mpeskin/QFT.html`.

[17] L Alvarez-Gaume and J Ellis. "Eyes on a prize particle". In: *Nature Phys.* 7.1 (2011). Editorial Material, pp. 2–3. URL: `https://cds.cern.ch/record/1399903`.

[18] Planck Collaboration. "Planck 2018 results. I. Overview and the cosmological legacy of Planck". In: *Planck Collaboration* (2018). arXiv: `1807.06205 [astro-ph.CO]`.

[19] Katherine Freese. "Review of Observational Evidence for Dark Matter in the Universe and in upcoming searches for Dark Stars". In: *EAS Publ. Ser.* 36 (2009), pp. 113–126. DOI: `10.1051/eas/0936016`. arXiv: `0812.4005 [astro-ph]`.

[20] J H Oort. "The force exerted by the stellar system in the direction perpendicular to the galactic plane and some related problems". In: *Bull. Astron. Inst. Netherlands* 6 (1932), pp. 249–287. URL: `http://cds.cern.ch/record/436532`.

[21] F. Zwicky. “Republication of: The redshift of extragalactic nebulae”. In: *General Relativity and Gravitation* 41 (2009). DOI: `10.1007/s10714-008-0707-4`. URL: `https://doi.org/10.1007/s10714-008-0707-4`.

[22] Yoshiaki Sofue and Vera Rubin. “Rotation curves of spiral galaxies”. In: *Ann. Rev. Astron. Astrophys.* 39 (2001), pp. 137–174. DOI: `10.1146/annurev.astro.39.1.137`. arXiv: `astro-ph/0010594 [astro-ph]`.

[23] B. Fuchs. “Dynamics of the Disks of Nearby Galaxies”. In: *Astron. Nachr.* 329 (2008), p. 916. DOI: `10.1002/asna.200811047`. arXiv: `0810.3503 [astro-ph]`.

[24] Matthias Bartelmann and Peter Schneider. “Weak gravitational lensing”. In: *Phys. Rept.* 340 (2001), pp. 291–472. DOI: `10.1016/S0370-1573(00)00082-X`. arXiv: `astro-ph/9912508 [astro-ph]`.

[25] Douglas Clowe et al. “A direct empirical proof of the existence of dark matter”. In: *Astrophys. J.* 648 (2006), pp. L109–L113. DOI: `10.1086/508162`. arXiv: `astro-ph/0608407 [astro-ph]`.

[26] COBE Collaboration. “The COBE normalization of CMB anisotropies”. In: *Astrophys. J.* 450 (1995). [Erratum: Astrophys. J.477, 460(1995)], p. 477. DOI: `10.1086/176158`. arXiv: `astro-ph/9503054 [astro-ph]`.

[27] D. Larson et al. “Seven-Year Wilkinson Microwave Anisotropy Probe (WMAP) Observations: Power Spectra and WMAP-Derived Parameters”. In: *Astrophys. J. Suppl.* 192 (2011), p. 16. DOI: `10.1088/0067-0049/192/2/16`. arXiv: `1001.4635 [astro-ph.CO]`.

[28] Andrew R. Liddle. *An introduction to modern cosmology*. 1998.

[29] Planck Collaboration. “Planck 2015 results. I. Overview of products and scientific results”. In: *Astron. Astrophys.* 594 (2016), A1. DOI: `10.1051/0004-6361/201527101`. arXiv: `1502.01582 [astro-ph.CO]`.

[30] R. D. Peccei and Helen R. Quinn. “CP Conservation in the Presence of Instantons”. In: *Phys. Rev. Lett.* 38 (1977). [,328(1977)], pp. 1440–1443. DOI: `10.1103/PhysRevLett.38.1440`.

[31] ADMX Collaboration. “A SQUID-based microwave cavity search for dark-matter axions”. In: *Phys. Rev. Lett.* 104 (2010), p. 041301. DOI: `10.1103/PhysRevLett.104.041301`. arXiv: `0910.5914 [astro-ph.CO]`.

[32] B. J. Carr et al. “New cosmological constraints on primordial black holes”. In: *Phys. Rev.* D81 (2010), p. 104019. DOI: `10.1103/PhysRevD.81.104019`. arXiv: `0912.5297 [astro-ph.CO]`.

[33] Matias Zaldarriaga and Diego D. Harari. “Analytic approach to the polarization of the cosmic microwave background in flat and open universes”. In: *Phys. Rev.* D52 (1995), pp. 3276–3287. DOI: `10.1103/PhysRevD.52.3276`. arXiv: `astro-ph/9504085 [astro-ph]`.

[34] Carlos Munoz. “Models of Supersymmetry for Dark Matter”. In: *EPJ Web Conf.* 136 (2017), p. 01002. DOI: `10.1051/epjconf/201713601002`. arXiv: `1701.05259 [hep-ph]`.

[35] Daniel Abercrombie et al. “Dark Matter Benchmark Models for Early LHC Run-2 Searches”. In: *Report of the ATLAS/CMS Dark Matter Forum* (2015). Ed. by Antonio Boveia et al. arXiv: `1507.00966 [hep-ex]`.

[36] LHC New Physics Working Group. “Simplified Models for LHC New Physics Searches”. In: *J. Phys.* G39 (2012). Ed. by Nima Arkani-Hamed et al., p. 105005. DOI: `10.1088/0954-3899/39/10/105005`. arXiv: `1105.2838 [hep-ph]`.

[37] Motoi Endo and Yasuhiro Yamamoto. “Unitarity Bounds on Dark Matter Effective Interactions at LHC”. In: *JHEP* 06 (2014), p. 126. DOI: `10.1007/JHEP06(2014)126`. arXiv: `1403.6610 [hep-ph]`.

[38] S. Dittmaier et al. “Handbook of LHC Higgs Cross Sections: 1. Inclusive Observables”. In: *LHC Higgs Cross Section Working Group* (2011). DOI: `10.5170/CERN-2011-002`. arXiv: `1101.0593 [hep-ph]`.

[39] S. Dittmaier et al. “Handbook of LHC Higgs Cross Sections: 2. Differential Distributions”. In: *LHC Higgs Cross Section Working Group* (2012). DOI: `10.5170/CERN-2012-002`. arXiv: `1201.3084 [hep-ph]`.

[40] ATLAS Collaboration. "Search for invisible decays of a Higgs boson using vector-boson fusion in pp collisions at $\sqrt{s} = 8$ TeV with the ATLAS detector". In: *JHEP* 01 (2016), p. 172. DOI: `10.1007/JHEP01(2016)172`. arXiv: `1508.07869 [hep-ex]`.

[41] Oliver S. Bruning et al. *LHC Design Report Vol.1: The LHC Main Ring*. Tech. rep. CERN-2004-003-V1, CERN-2004-003, CERN-2004-003-V-1. 2004.

[42] ATLAS Collaboration. *The timeline of the large hadron collider*. `http://timeline.web.cern.ch/timelines/The-Large-Hadron-Collider`. Accessed = 11/09/2018.

[43] Christiane Lefèvre. *The CERN accelerator complex. Complexe des accélérateurs du CERN*. Tech. rep. CERN-DI-0812015. Dec. 2008. URL: `http://cds.cern.ch/record/1260465`.

[44] M. Benedikt et al. *LHC Design Report Vol.3: The LHC injector chain*. Tech. rep. CERN-2004-003-V-3, CERN-2004-003. 2004.

[45] CMS Collaboration. "The CMS Experiment at the CERN LHC". In: *JINST* 3 (2008), S08004. DOI: `10.1088/1748-0221/3/08/S08004`.

[46] A. Augusto Alves Jr. et al. "The LHCb Detector at the LHC". In: *JINST* 3 (2008), S08005. DOI: `10.1088/1748-0221/3/08/S08005`.

[47] ALICE Collaboration. "The ALICE experiment at the CERN LHC". In: *JINST* 3 (2008), S08002. DOI: `10.1088/1748-0221/3/08/S08002`.

[48] ATLAS Collaboration. *Total Integrated Luminosity and Data Quality in 2015–2018*. `https://twiki.cern.ch/twiki/bin/view/AtlasPublic/LuminosityPublicResultsRun2`. Accessed = 20/02/2019.

[49] *LEP Design Report Vol.1*. Tech. rep. CERN-LEP-TH-83-29, CERN-PS-DL-83-31, CERN-SPS-83-26, LAL-RT-83-09. 1983.

[50] *LEP Design Report: Vol.2. The LEP Main Ring*. Tech. rep. CERN-LEP-84-01. 1984.

[51] Mark Thomson. *Modern particle physics*. New York: Cambridge University Press, 2013. ISBN: 9781107034266. URL: `http://www-spires.fnal.gov/spires/find/books/www?cl=QC793.2.T46::2013`.

[52] ATLAS Collaboration. *ATLAS magnet system: Technical design report*. Tech. rep. CERN-LHCC-97-18. 1997.

[53] ATLAS Collaboration. *ATLAS inner detector: Technical design report. Vol. 1*. Tech. rep. CERN-LHCC-97-16, ATLAS-TDR-4. 1997.

[54] ATLAS Collaboration. *ATLAS inner detector: Technical design report. Vol. 2*. Tech. rep. CERN-LHCC-97-17. 1997.

[55] ATLAS Collaboration. *Track Reconstruction Performance of the ATLAS Inner Detector at $\sqrt{s} = 13$ TeV*. Tech. rep. ATL-PHYS-PUB-2015-018. Geneva: CERN, July 2015. URL: `http://cds.cern.ch/record/2037683`.

[56] ATLAS Collaboration. "The Pixel Detector of the ATLAS experiment for the Run 2 at the Large Hadron Collider". In: *JINST* 10.02 (2015), p. C02001. DOI: `10.1088/1748-0221/10/02/C02001, 10.1088/1748-0221/10/12/C12001`. arXiv: `1411.5338 [physics.ins-det]`.

[57] ATLAS Collaboration. *ATLAS Insertable B-Layer Technical Design Report*. Tech. rep. CERN-LHCC-2010-013, ATLAS-TDR-19. 2010.

[58] ATLAS Collaboration. "The ATLAS transition radiation tracker". In: *Astroparticle, particle and space physics, detectors and medical physics applications. Proceedings, 8th Conference, ICATPP 2003, Como, Italy, October 6-10, 2003*. 2003, pp. 497–501. DOI: `10.1142/9789812702708_0073`. arXiv: `hep-ex/0311058 [hep-ex]`. URL: `http://weblib.cern.ch/abstract?ATL-CONF-2003-012`.

[59] ATLAS Collaboration. *ATLAS liquid argon calorimeter: Technical design report*. Tech. rep. CERN-LHCC-96-41. 1996.

[60] ATLAS Collaboration. "Readiness of the ATLAS Liquid Argon Calorimeter for LHC Collisions". In: *Eur. Phys. J.* C70 (2010), pp. 723–753. DOI: `10.1140/epjc/s10052-010-1354-y`. arXiv: `0912.2642 [physics.ins-det]`.

[61] ATLAS Collaboration. "Performance of the electronic readout of the ATLAS liquid argon calorimeters". In: *JINST* 5 (2010), P09003. DOI: `10.1088/1748-0221/5/09/P09003`.

[62] ATLAS Collaboration. "Readiness of the ATLAS Tile Calorimeter for LHC collisions". In: *Eur. Phys. J.* C70 (2010), pp. 1193–1236. DOI: `10.1140/epjc/s10052-010-1508-y`. arXiv: `1007.5423 [physics.ins-det]`.

[63] ATLAS Collaboration. *ATLAS muon spectrometer: Technical design report*. Tech. rep. CERN-LHCC-97-22, ATLAS-TDR-10. 1997.

[64] ATLAS Collaboration. "Muon reconstruction performance of the ATLAS detector in proton–proton collision data at $\sqrt{s} = 13$ TeV". In: (2016). arXiv: `1603.05598 [hep-ex]`.

[65] ATLAS Collaboration. "Commissioning of the ATLAS Muon Spectrometer with Cosmic Rays". In: *Eur. Phys. J.* C70 (2010), pp. 875–916. DOI: `10.1140/epjc/s10052-010-1415-2`. arXiv: `1006.4384 [physics.ins-det]`.

[66] ATLAS Collaboration. "Large-Scale Production of Monitored Drift Tube Chambers for the ATLAS Muon Spectrometer". In: *Nucl. Instrum. Meth.* A518 (2004), pp. 69–72. DOI: `10.1016/j.nima.2003.10.026`. arXiv: `1604.00240 [physics.ins-det]`.

[67] ATLAS Collaboration. "Cathode strip chambers in ATLAS : Installation, commissioning and in situ performance". In: *Proceedings, 2008 IEEE Nuclear Science Symposium, Medical Imaging Conference and 16th International Workshop on Room-Temperature Semiconductor X-Ray and Gamma-Ray Detectors (NSS/MIC 2008 / RTSD 2008): Dresden, Germany, October 19-25, 2008*. 2008, pp. 2819–2824. DOI: `10.1109/NSSMIC.2008.4774958`.

[68] ATLAS Collaboration. "The Resistive Plate Chambers of the ATLAS experiment: performance studies on Calibration Stream". In: *Proceedings, 13th ICATPP Conference on Astroparticle, Particle, Space Physics and Detectors for Physics Applications (ICATPP 2011): Como, Italy, October 3-7, 2011*. 2012, pp. 869–873. DOI: `10.1142/9789814405072_0131`.

[69] ATLAS Collaboration. "Performance of the ATLAS Trigger System in 2010". In: *Eur. Phys. J.* C72 (2012), p. 1849. DOI: `10.1140/epjc/s10052-011-1849-1`. arXiv: `1110.1530 [hep-ex]`.

[70] ATLAS Collaboration. "Performance of the ATLAS Trigger System in 2015". In: *Eur. Phys. J.* C77.5 (2017), p. 317. DOI: `10.1140/epjc/s10052-017-4852-3`. arXiv: `1611.09661 [hep-ex]`.

[71] ATLAS Collaboration. "The ATLAS Trigger in Run 2: Design, Menu, and Performance". In: *PoS* EPS-HEP2017 (2017), p. 525. DOI: `10.22323/1.314.0525`.

[72] Neil Geddes. "The Large Hadron Collider and Grid computing". In: *Phil. Trans. Roy. Soc. Lond.* A370 (2012), pp. 965–977. DOI: `10.1098/rsta.2011.0465`.

[73] ATLAS Collaboration. "Reconstruction of primary vertices at the ATLAS experiment in Run 1 proton–proton collisions at the LHC". In: *Eur. Phys. J.* C77.5 (2017), p. 332. DOI: `10.1140/epjc/s10052-017-4887-5`. arXiv: `1611.10235 [physics.ins-det]`.

[74] Neil D. Christensen and Claude Duhr. "FeynRules - Feynman rules made easy". In: *Comput. Phys. Commun.* 180 (2009), pp. 1614–1641. DOI: `10.1016/j.cpc.2009.02.018`. arXiv: `0806.4194 [hep-ph]`.

[75] B. R. Webber. "A QCD Model for Jet Fragmentation Including Soft Gluon Interference". In: *Nucl. Phys.* B238 (1984), pp. 492–528. DOI: `10.1016/0550-3213(84)90333-X`.

[76] Bo Andersson et al. "Parton Fragmentation and String Dynamics". In: *Phys. Rept.* 97 (1983), pp. 31–145. DOI: `10.1016/0370-1573(83)90080-7`.

[77] S. Agostinelli et al. "GEANT4: A Simulation toolkit". In: *Nucl. Instrum. Meth.* A506 (2003), pp. 250–303. DOI: `10.1016/S0168-9002(03)01368-8`.

[78] Andy Buckley et al. "Rivet user manual". In: *Comput. Phys. Commun.* 184 (2013), pp. 2803–2819. DOI: `10.1016/j.cpc.2013.05.021`. arXiv: `1003.0694 [hep-ph]`.

[79] ATLAS Collaboration. "Electron efficiency measurements with the ATLAS detector using the 2015 LHC proton-proton collision data". In: *ATLAS Conf. Note* (2016).

[80] ATLAS Collaboration. "Photon identification with the ATLAS detector". In: *PoS* EPS-HEP2017 (2017), p. 760. DOI: `10.22323/1.314.0760`.

[81] ATLAS Collaboration. "Electron and photon energy calibration with the ATLAS detector using 2015-2016 LHC proton-proton collision data". In: *Submitted to: JINST* (2018). arXiv: `1812.03848 [hep-ex]`.

[82] ATLAS Collaboration. "Muon reconstruction performance of the ATLAS detector in proton–proton collision data at $\sqrt{s}$ =13 TeV". In: *Eur. Phys. J.* C76.5 (2016), p. 292. DOI: `10.1140/epjc/s10052-016-4120-y`. arXiv: `1603.05598 [hep-ex]`.

[83] ATLAS Collaboration. "Selection of jets produced in 13 TeV proton-proton collisions with the ATLAS detector". In: *ATLAS Conf. Note* (2015).

[84] ATLAS Collaboration. “Jet energy measurement and its systematic uncertainty in proton-proton collisions at $\sqrt{s} = 7$ TeV with the ATLAS detector”. In: *Eur. Phys. J.* C75 (2015), p. 17. DOI: `10.1140/epjc/s10052-014-3190-y`. arXiv: `1406.0076 [hep-ex]`.

[85] Matteo Cacciari, Gavin P. Salam, and Gregory Soyez. “The anti-k_t jet clustering algorithm”. In: *JHEP* 04 (2008), p. 063. DOI: `10.1088/1126-6708/2008/04/063`. arXiv: `0802.1189 [hep-ph]`.

[86] ATLAS Collaboration. “Monte Carlo Calibration and Combination of In-situ Measurements of Jet Energy Scale, Jet Energy Resolution and Jet Mass in ATLAS”. In: *ATLAS Conf. Note* (2015).

[87] ATLAS Collaboration. “Performance of Missing Transverse Momentum Reconstruction in ATLAS studied in Proton-Proton Collisions recorded in 2012 at 8 TeV”. In: *ATLAS Conf. Note* (2013).

[88] ATLAS Collaboration. “Performance of missing transverse momentum reconstruction with the ATLAS detector using proton-proton collisions at $\sqrt{s}$ = 13 TeV”. In: *Eur. Phys. J.* C78.11 (2018), p. 903. DOI: `10.1140/epjc/s10052-018-6288-9`. arXiv: `1802.08168 [hep-ex]`.

[89] ATLAS Collaboration. “Data-driven determination of the energy scale and resolution of jets reconstructed in the ATLAS calorimeters using dijet and multijet events at $\sqrt{s} = 8\ TeV$”. In: (2015).

[90] ATLAS Collaboration. “Jet energy scale measurements and their systematic uncertainties in proton proton collisions at $\sqrt{s} = 13$ TeV with the ATLAS detector”. In: *ATLAS Conf. Note* (2017). arXiv: `1703.09665 [hep-ex]`.

[91] ATLAS Collaboration. “Luminosity determination in pp collisions at $\sqrt{s}$ = 8 TeV using the ATLAS detector at the LHC”. In: *Eur. Phys. J.* C76.12 (2016), p. 653. DOI: `10.1140/epjc/s10052-016-4466-1`. arXiv: `1608.03953 [hep-ex]`.

[92] Andy Buckley and Debottam Bakshi Gupta. “Powheg Pythia matching scheme effects in NLO simulation of dijet events”. In: *hep-ph MCNET* MCNET-16-34 (2016). arXiv: `1608.03577 [hep-ph]`.

[93] T. Gleisberg et al. “Event generation with SHERPA 1.1”. In: *JHEP* 02 (2009), p. 007. DOI: `10.1088/1126-6708/2009/02/007`. arXiv: `0811.4622 [hep-ph]`.

[94] Torbjorn Sjostrand, Stephen Mrenna, and Peter Z. Skands. “A Brief Introduction to PYTHIA 8.1”. In: *Comput. Phys. Commun.* 178 (2008), pp. 852–867. DOI: `10.1016/j.cpc.2008.01.036`. arXiv: `0710.3820 [hep-ph]`.

[95] Carlo Oleari. “The POWHEG-BOX”. In: *Nucl. Phys. Proc. Suppl.* 205-206 (2010), pp. 36–41. DOI: `10.1016/j.nuclphysbps.2010.08.016`. arXiv: `1007.3893 [hep-ph]`.

[96] Hung-Liang Lai et al. “New parton distributions for collider physics”. In: *Phys. Rev.* D82 (2010), p. 074024. DOI: `10.1103/PhysRevD.82.074024`. arXiv: `1007.2241 [hep-ph]`.

[97] Stefano Carrazza, Stefano Forte, and Juan Rojo. “Parton Distributions and Event Generators”. In: *Proceedings, 43rd International Symposium on Multiparticle Dynamics (ISMD 13)*. 2013, pp. 89–96. arXiv: `1311.5887 [hep-ph]`. URL: `https://inspirehep.net/record/1266070/files/arXiv:1311.5887.pdf`.

[98] ATLAS Collaboration. *Summary of ATLAS Pythia 8 tunes*. Tech. rep. ATL-PHYS-PUB-2012-003, ATL-COM-PHYS-2012-738. 2012.

[99] Laura Baudis. “Dark matter searches”. In: *Annalen Phys.* 528 (2016), pp. 74–83. DOI: `10.1002/andp.201500114`. arXiv: `1509.00869 [astro-ph.CO]`.

[100] Max-Planck-Institut fur Kernphysik. *Research: Dark Matter*. `https://www.mpi-hd.mpg.de/lin/research_DM.en.html`. Accessed = 26/02/2019.

[101] XENON Collaboration. “First dark matter search results of the XENON1T experiment”. In: *Nuovo Cim.* C41.3 (2018), p. 109. DOI: `10.1393/ncc/i2018-18109-5`.

[102] LUX Collaboration. “First Searches for Axions and Axionlike Particles with the LUX Experiment”. In: *Phys. Rev. Lett.* 118.26 (2017), p. 261301. DOI: `10.1103/PhysRevLett.118.261301`. arXiv: `1704.02297 [astro-ph.CO]`.

[103] Mengjiao Xiao et al. “First dark matter search results from the PandaX-I experiment”. In: *Sci. China Phys. Mech. Astron.* 57 (2014), pp. 2024–2030. DOI: `10.1007/s11433-014-5598-7`. arXiv: `1408.5114 [hep-ex]`.

[104] D. Franco et al. "First results from DarkSide-50". In: *Proceedings, 50th Rencontres de Moriond Electroweak Interactions and Unified Theories: La Thuile, Italy, March 14-21, 2015*. 2015, pp. 451–456.

[105] C. Amole et al. "Dark matter search results from the PICO-60 CF_3I bubble chamber". In: *Phys. Rev.* D93.5 (2016), p. 052014. DOI: `10.1103/PhysRevD.93.052014`. arXiv: `1510.07754 [hep-ex]`.

[106] C. E. Aalseth et al. "CoGeNT: A Search for Low-Mass Dark Matter using p-type Point Contact Germanium Detectors". In: *Phys. Rev.* D88 (2013), p. 012002. DOI: `10.1103/PhysRevD.88.012002`. arXiv: `1208.5737 [astro-ph.CO]`.

[107] G. Angloher et al. "Results on low mass WIMPs using an upgraded CRESST-II detector". In: *Eur. Phys. J.* C74.12 (2014), p. 3184. DOI: `10.1140/epjc/s10052-014-3184-9`. arXiv: `1407.3146 [astro-ph.CO]`.

[108] R. Agnese et al. "Search for Low-Mass Weakly Interacting Massive Particles with SuperCDMS". In: *Phys. Rev. Lett.* 112.24 (2014), p. 241302. DOI: `10.1103/PhysRevLett.112.241302`. arXiv: `1402.7137 [hep-ex]`.

[109] A. Aguilar-Arevalo et al. "First Direct-Detection Constraints on eV-Scale Hidden-Photon Dark Matter with DAMIC at SNOLAB". In: *Phys. Rev. Lett.* 118.14 (2017), p. 141803. DOI: `10.1103/PhysRevLett.118.141803`. arXiv: `1611.03066 [astro-ph.CO]`.

[110] Leszek Roszkowski, Enrico Maria Sessolo, and Sebastian Trojanowski. "WIMP dark matter candidates and searches—current status and future prospects". In: *Rept. Prog. Phys.* 81.6 (2018), p. 066201. DOI: `10.1088/1361-6633/aab913`. arXiv: `1707.06277 [hep-ph]`.

[111] AMS Collaboration. "Constraints on leptophilic dark matter from the AMS−02 experiment". In: *Astrophys. J.* 839.1 (2017). [Erratum: Astrophys. J.869, no.1, 89(2018)], p. 36. DOI: `10.3847/1538-4357/aa624d, 10.3847/1538-4357/aaefea`. arXiv: `1612.06634 [hep-ph]`.

[112] A. Albert et al. "Searching for Dark Matter Annihilation in Recently Discovered Milky Way Satellites with Fermi-LAT". In: *Astrophys. J.* 834.2 (2017), p. 110. DOI: `10.3847/1538-4357/834/2/110`. arXiv: `1611.03184 [astro-ph.HE]`.

[113] O. Adriani et al. “PAMELA results on the cosmic-ray antiproton flux from 60 MeV to 180 GeV in kinetic energy”. In: *Phys. Rev. Lett.* 105 (2010), p. 121101. DOI: `10.1103/PhysRevLett.105.121101`. arXiv: `1007.0821 [astro-ph.HE]`.

[114] ANTARES Collaboration. “Results of dark matter searches with the ANTARES neutrino telescope”. In: *J. Phys. Conf. Ser.* 888.1 (2017), p. 012206. DOI: `10.1088/1742-6596/888/1/012206`. arXiv: `1611.02555 [astro-ph.HE]`.

[115] IceCube Collaboration. “Improved limits on dark matter annihilation in the Sun with the 79-string IceCube detector and implications for supersymmetry”. In: *JCAP* 1604.04 (2016), p. 022. DOI: `10.1088/1475-7516/2016/04/022`. arXiv: `1601.00653 [hep-ph]`.

[116] K. Choi et al. “Search for neutrinos from annihilation of captured low-mass dark matter particles in the Sun by Super-Kamiokande”. In: *Phys. Rev. Lett.* 114.14 (2015), p. 141301. DOI: `10.1103/PhysRevLett.114.141301`. arXiv: `1503.04858 [hep-ex]`.

[117] VERITAS Collaboration. “VERITAS Deep Observations of the Dwarf Spheroidal Galaxy Segue 1”. In: *Phys. Rev.* D85 (2012). [Erratum: Phys. Rev.D91,no.12,129903(2015)], p. 062001. DOI: `10.1103/PhysRevD.85.062001, 10.1103/PhysRevD.91.129903`. arXiv: `1202.2144 [astro-ph.HE]`.

[118] Matthias Danninger. “Review of indirect detection of dark matter with neutrinos”. In: *J. Phys. Conf. Ser.* 888.1 (2017), p. 012039. DOI: `10.1088/1742-6596/888/1/012039`.

[119] ATLAS Collaboration. “Search for new phenomena in final states with an energetic jet and large missing transverse momentum in pp collisions at $\sqrt{s} = 13$ TeV using the ATLAS detector”. In: *Phys. Rev.* D94.3 (2016), p. 032005. DOI: `10.1103/PhysRevD.94.032005`. arXiv: `1604.07773 [hep-ex]`.

[120] CMS Collaboration. “Search for dark matter produced with an energetic jet or a hadronically decaying W or Z boson at $\sqrt{s} = 13$ TeV”. In: *JHEP* 07 (2017), p. 014. DOI: `10.1007/JHEP07(2017)014`. arXiv: `1703.01651 [hep-ex]`.

[121] ATLAS Collaboration. “Search for an invisibly decaying Higgs boson or dark matter candidates produced in association with a Z boson in pp collisions at $\sqrt{s} = 13$ TeV with the ATLAS detector”. In: *Phys. Lett. B* 776.CERN-EP-2017-166 (Aug.

2017), 318–337. 20 p. DOI: `10.1016/j.physletb.2017.11.049`. URL: `https://cds.cern.ch/record/2281451`.

[122] CMS Collaboration. "Search for dark matter and unparticles in events with a Z boson and missing transverse momentum in proton-proton collisions at $\sqrt{s} = 13$ TeV". In: *CMS Conf. Note* (2016).

[123] ATLAS Collaboration. "Search for new phenomena in events with a photon and missing transverse momentum in pp collisions at $\sqrt{s} = 13$ TeV with the ATLAS detector". In: *JHEP* 06 (2016), p. 059. DOI: `10.1007/JHEP06(2016)059`. arXiv: `1604.01306 [hep-ex]`.

[124] CMS Collaboration. "Search for dark matter and graviton produced in association with a photon in pp collisions at $\sqrt{s} = 13$ TeV". In: *CMS Conf. Note* (2016).

[125] ATLAS Collaboration. "Search for new particles in events with one lepton and missing transverse momentum in pp collisions at $\sqrt{s} = 8$ TeV with the ATLAS detector". In: *JHEP* 09 (2014), p. 037. DOI: `10.1007/JHEP09(2014)037`. arXiv: `1407.7494 [hep-ex]`.

[126] CMS Collaboration. "Search for physics beyond the standard model in final states with a lepton and missing transverse energy in proton-proton collisions at $\sqrt{s} = 8$ TeV". In: *Phys. Rev.* D91.9 (2015), p. 092005. DOI: `10.1103/PhysRevD.91.092005`. arXiv: `1408.2745 [hep-ex]`.

[127] ATLAS Collaboration. "Search for dark matter in events with a hadronically decaying vector boson and missing transverse momentum in pp collisions at $\sqrt{s} = 13$ TeV with the ATLAS detector". In: *JHEP* 10 (2018), p. 180. DOI: `10.1007/JHEP10(2018)180`. arXiv: `1807.11471 [hep-ex]`.

[128] ATLAS Collaboration. "Search for dark matter in association with a Higgs boson decaying to b-quarks in pp collisions at $\sqrt{s} = 13$ TeV with the ATLAS detector". In: *Phys. Lett.* B765 (2017), pp. 11–31. DOI: `10.1016/j.physletb.2016.11.035`. arXiv: `1609.04572 [hep-ex]`.

[129] ATLAS Collaboration. "Search for dark matter in association with a Higgs boson decaying to two photons at $\sqrt{s} = 13$ TeV with the ATLAS detector". In: *Phys. Rev.* D96.11 (2017), p. 112004. DOI: `10.1103/PhysRevD.96.112004`. arXiv: `1706.03948 [hep-ex]`.

[130] CMS Collaboration. "Search for associated production of dark matter with a Higgs boson decaying to $b\bar{b}$ or $\gamma\gamma$ at $\sqrt{s} = 13$ TeV". In: *JHEP* 10 (2017), p. 180. DOI: `10.1007/JHEP10(2017)180`. arXiv: `1703.05236 [hep-ex]`.

[131] ATLAS Collaboration. "Search for invisible Higgs boson decays in vector boson fusion at $\sqrt{s} = 13$ TeV with the ATLAS detector". In: *Phys. Lett.* (2018). DOI: `10.1016/j.physletb.2019.04.024`. arXiv: `1809.06682 [hep-ex]`.

[132] CMS Collaboration. "Searches for invisible decays of the Higgs boson in *pp* collisions at $\sqrt{s}$ = 7, 8, and 13 TeV". In: *JHEP* 02 (2017), p. 135. DOI: `10.1007/JHEP02(2017)135`. arXiv: `1610.09218 [hep-ex]`.

[133] ATLAS Collaboration. "Search for new phenomena in dijet mass and angular distributions from *pp* collisions at $\sqrt{s} = 13$ TeV with the ATLAS detector". In: *Phys. Lett.* B754 (2016), pp. 302–322. DOI: `10.1016/j.physletb.2016.01.032`. arXiv: `1512.01530 [hep-ex]`.

[134] ATLAS Collaboration. "Search for new light resonances decaying to jet pairs and produced in association with a photon in proton-proton collisions at $\sqrt{s} = 13$ TeV with the ATLAS detector". In: *ATLAS Conf. Note* (2016).

[135] CMS Collaboration. "Search for dijet resonances in proton–proton collisions at $\sqrt{s}$ = 13 TeV and constraints on dark matter and other models". In: *Phys. Lett.* B769 (2017). [Erratum: Phys. Lett.B772, 882(2017)], pp. 520–542. DOI: `10.1016/j.physletb.2017.09.029,10.1016/j.physletb.2017.02.012`. arXiv: `1611.03568 [hep-ex]`.

[136] ATLAS Collaboration. "Search for heavy particles decaying into top-quark pairs using lepton-plus-jets events in proton–proton collisions at $\sqrt{s} = 13$ TeV with the ATLAS detector". In: *Eur. Phys. J.* C78.7 (2018), p. 565. DOI: `10.1140/epjc/s10052-018-5995-6`. arXiv: `1804.10823 [hep-ex]`.

[137] ATLAS Collaboration. "Search for resonances in the mass distribution of jet pairs with one or two jets identified as *b*-jets in proton-proton collisions at $\sqrt{s} = 13$ TeV with the ATLAS detector". In: *Phys. Rev.* D98 (2018), p. 032016. DOI: `10.1103/PhysRevD.98.032016`. arXiv: `1805.09299 [hep-ex]`.

[138] ATLAS Collaboration. *ATLAS Dark Matter Summary*. `https://atlas.web.cern.ch/Atlas/GROUPS/PHYSICS/CombinedSummaryPlots/EXOTICS/`. Accessed = 06/03/2019.

[139] Andreas Albert et al. "Recommendations of the LHC Dark Matter Working Group: Comparing LHC searches for heavy mediators of dark matter production in visible and invisible decay channels". In: *CERN hep-ex* (2017). arXiv: `1703.05703 [hep-ex]`.

[140] R. C. Cotta et al. "Bounds on Dark Matter Interactions with Electroweak Gauge Bosons". In: *Phys. Rev.* D88 (2013), p. 116009. DOI: `10.1103/PhysRevD.88.116009`. arXiv: `1210.0525 [hep-ph]`.

[141] ATLAS Collaboration. "Measurement of detector-corrected observables sensitive to the anomalous production of events with jets and large missing transverse momentum in *pp* collisions at $\sqrt{\mathbf{s}} = \mathbf{13}$ TeV using the ATLAS detector". In: *Eur. Phys. J.* C77.11 (2017), p. 765. DOI: `10.1140/epjc/s10052-017-5315-6`. arXiv: `1707.03263 [hep-ex]`.

[142] F. Halzen and Alan D. Martin. *Quarks and Leptons: An introductory course in modern particle physics*. 1984. ISBN: 9780471887416.

[143] Tanju Gleisberg and Stefan Hoeche. "Comix, a new matrix element generator". In: *JHEP* 12 (2008), p. 039. DOI: `10.1088/1126-6708/2008/12/039`. arXiv: `0808.3674 [hep-ph]`.

[144] Fabio Cascioli, Philipp Maierhofer, and Stefano Pozzorini. "Scattering Amplitudes with Open Loops". In: *Phys. Rev. Lett.* 108 (2012), p. 111601. DOI: `10.1103/PhysRevLett.108.111601`. arXiv: `1111.5206 [hep-ph]`.

[145] Stefan Hoeche et al. "QCD matrix elements + parton showers: The NLO case". In: *JHEP* 04 (2013), p. 027. DOI: `10.1007/JHEP04(2013)027`. arXiv: `1207.5030 [hep-ph]`.

[146] NNPDF Collaboration. "Parton distributions for the LHC Run II". In: *JHEP* 04 (2015), p. 040. DOI: `10.1007/JHEP04(2015)040`. arXiv: `1410.8849 [hep-ph]`.

[147] Charalampos Anastasiou et al. “High precision QCD at hadron colliders: Electroweak gauge boson rapidity distributions at NNLO”. In: *Phys. Rev.* D69 (2004), p. 094008. DOI: `10.1103/PhysRevD.69.094008`. arXiv: `hep-ph/0312266 [hep-ph]`.

[148] Shu Li. “Monte Carlo modeling of Standard Model multi-boson production processes for $\sqrt{s} = 13$ TeV ATLAS analyses”. In: *5th Large Hadron Collider Physics Conference (LHCP 2017) Shanghai, China, May 15-20, 2017*. 2017. arXiv: `1709.00315 [hep-ex]`.

[149] J. Pumplin et al. “New generation of parton distributions with uncertainties from global QCD analysis”. In: *JHEP* 07 (2002), p. 012. DOI: `10.1088/1126-6708/2002/07/012`. arXiv: `hep-ph/0201195 [hep-ph]`.

[150] Peter Zeiler Skands. “Tuning Monte Carlo Generators: The Perugia Tunes”. In: *Phys. Rev.* D82 (2010), p. 074018. DOI: `10.1103/PhysRevD.82.074018`. arXiv: `1005.3457 [hep-ph]`.

[151] NNPDF Collaboration. “Parton distributions with LHC data”. In: *Nucl. Phys.* B867 (2013), pp. 244–289. DOI: `10.1016/j.nuclphysb.2012.10.003`. arXiv: `1207.1303 [hep-ph]`.

[152] D. J. Lange. “The EvtGen particle decay simulation package”. In: *Nucl. Instrum. Meth.* A462 (2001), pp. 152–155. DOI: `10.1016/S0168-9002(01)00089-4`.

[153] Adam Alloul et al. “FeynRules 2.0 - A complete toolbox for tree-level phenomenology”. In: *Comput. Phys. Commun.* 185 (2014), pp. 2250–2300. DOI: `10.1016/j.cpc.2014.04.012`. arXiv: `1310.1921 [hep-ph]`.

[154] ATLAS Collaboration. “Electron efficiency measurements with the ATLAS detector using 2012 LHC proton˘proton collision data”. In: *Eur. Phys. J.* C77.3 (2017), p. 195. DOI: `10.1140/epjc/s10052-017-4756-2`. arXiv: `1612.01456 [hep-ex]`.

[155] Richard Nisius. “On the combination of correlated estimates of a physics observable”. In: *Eur. Phys. J.* C74.8 (2014), p. 3004. DOI: `10.1140/epjc/s10052-014-3004-2`. arXiv: `1402.4016 [physics.data-an]`.

[156] Alexander L. Read. “Presentation of search results: The CL(s) technique”. In: *J. Phys.* G28 (2002). [,11(2002)], pp. 2693–2704. DOI: `10.1088/0954-3899/28/10/313`.

[157] Thomas Junk. “Confidence level computation for combining searches with small statistics”. In: *Nucl. Instrum. Meth.* A434 (1999), pp. 435–443. DOI: `10.1016/S0168-9002(99)00498-2`. arXiv: `hep-ex/9902006 [hep-ex]`.

[158] Ruth Pottgen. “Search for Dark Matter in events with a highly energetic jet and missing transverse momentum in proton-proton collisions at $\sqrt{s} = 8$ TeV with the ATLAS Detector”. PhD thesis. Cham: Mainz U., 2014-10-09. DOI: `10.1007/978-3-319-41045-6`. URL: `http://www.springer.com/us/book/9783319410449`.

[159] WMAP Collaboration. “Nine-Year Wilkinson Microwave Anisotropy Probe (WMAP) Observations: Cosmological Parameter Results”. In: *Astrophys. J. Suppl.* 208 (2013), p. 19. DOI: `10.1088/0067-0049/208/2/19`. arXiv: `1212.5226 [astro-ph.CO]`.

[160] Felix Kahlhoefer et al. “Implications of unitarity and gauge invariance for simplified dark matter models”. In: *JHEP* 02 (2016), p. 016. DOI: `10.1007/JHEP02(2016)016`. arXiv: `1510.02110 [hep-ph]`.

[161] V. A. Novikov et al. “Theory of Z boson decays”. In: *Rept. Prog. Phys.* 62 (1999), pp. 1275–1332. DOI: `10.1088/0034-4885/62/9/201`. arXiv: `hep-ph/9906465 [hep-ph]`.

[162] Nick Ryder. “Measurement of the Invisible Width of the Z Boson using the ATLAS Detector”. PhD thesis. Oxford U., 2013.

[163] John Bagnasco, Michael Dine, and Scott D. Thomas. “Detecting technibaryon dark matter”. In: *Phys. Lett.* B320 (1994), pp. 99–104. DOI: `10.1016/0370-2693(94)90830-3`. arXiv: `hep-ph/9310290 [hep-ph]`.

[164] Kris Sigurdson et al. “Dark-matter electric and magnetic dipole moments”. In: *Phys. Rev.* D70 (2004). [Erratum: Phys. Rev.D73, 089903(2006)], p. 083501. DOI: `10.1103/PhysRevD.70.083501, 10.1103/PhysRevD.73.089903`. arXiv: `astro-ph/0406355 [astro-ph]`.

[165] Eduard Masso, Subhendra Mohanty, and Soumya Rao. “Dipolar Dark Matter”. In: *Phys. Rev.* D80 (2009), p. 036009. DOI: `10.1103/PhysRevD.80.036009`. arXiv: `0906.1979 [hep-ph]`.

[166] Vernon Barger, Wai-Yee Keung, and Danny Marfatia. “Electromagnetic properties of dark matter: Dipole moments and charge form factor”. In: *Phys. Lett.* B696 (2011), pp. 74–78. DOI: `10.1016/j.physletb.2010.12.008`. arXiv: `1007.4345 [hep-ph]`.

[167] Tom Banks, Jean-Francois Fortin, and Scott Thomas. “Direct Detection of Dark Matter Electromagnetic Dipole Moments”. In: *hep-ph Rep.* (2010). arXiv: `1007.5515 [hep-ph]`.

[168] Jean-Francois Fortin and Tim M. P. Tait. “Collider Constraints on Dipole-Interacting Dark Matter”. In: *Phys. Rev.* D85 (2012), p. 063506. DOI: `10.1103/PhysRevD.85.063506`. arXiv: `1103.3289 [hep-ph]`.

[169] A. Liam Fitzpatrick and Kathryn M. Zurek. “Dark Moments and the DAMA-CoGeNT Puzzle”. In: *Phys. Rev.* D82 (2010), p. 075004. DOI: `10.1103/PhysRevD.82.075004`. arXiv: `1007.5325 [hep-ph]`.

[170] Vernon Barger et al. “Dipole Moment Dark Matter at the LHC”. In: *Phys. Lett.* B717 (2012), pp. 219–223. DOI: `10.1016/j.physletb.2012.09.036`. arXiv: `1206.0640 [hep-ph]`.

[171] James Brooke et al. “Vector Boson Fusion Searches for Dark Matter at the LHC”. In: *Phys. Rev.* D93.11 (2016), p. 113013. DOI: `10.1103/PhysRevD.93.113013`. arXiv: `1603.07739 [hep-ph]`.

[172] Fermi-LAT Collaboration. “Constraining Dark Matter Models from a Combined Analysis of Milky Way Satellites with the Fermi Large Area Telescope”. In: *Phys. Rev. Lett.* 107 (2011), p. 241302. DOI: `10.1103/PhysRevLett.107.241302`. arXiv: `1108.3546 [astro-ph.HE]`.

[173] James M. Cline et al. “Update on scalar singlet dark matter”. In: *Phys. Rev.* D88 (2013). [Erratum: Phys. Rev.D92, no.3, 039906(2015)], p. 055025. DOI: `10.1103/PhysRevD.92.039906, 10.1103/PhysRevD.88.055025`. arXiv: `1306.4710 [hep-ph]`.

[174] CMS Collaboration. “Search for invisible decays of a Higgs boson produced via vector boson fusion at $\sqrt{s} = 13$ TeV.” In: *CMS Conf. Note* (2016).

[175] Bastian Bernarding. “Towards Unfolding Topologies Proof of Concept within a Monojet Analysis”. In: *MSc Thesis, University of Heidelberg* (2016). URL: `http://www.kip.uni-heidelberg.de/Veroeffentlichungen/details.php?id=3475`.